TRANSPORT AND MAGNETIC STUDIES IN γ-$Fe_{80-x}Ni_xCr_{20}$ ($14 \leq x \leq 30$) STAINLESS STEEL ALLOYS AND Cu/Ni-Zr-Al METALLIC GLASSES

by

TAPAN KUMAR NATH

PHY
1997
D
NAT
TRA

DEPARTMENT OF PHYSICS

INDIAN INSTITUTE OF TECHNOLOGY KANPUR
FEBRUARY 1997

TRANSPORT AND MAGNETIC STUDIES IN γ-$Fe_{80-x}Ni_xCr_{20}$ ($14 \leq x \leq 30$) STAINLESS STEEL ALLOYS AND Cu/Ni-Zr-Al METALLIC GLASSES

A Thesis Submitted
in Partial Fulfillment of the Requirements
for the Degree of
Doctor of Philosophy

by

Tapan Kumar Nath

to the
DEPARTMENT OF PHYSICS
INDIAN INSTITUTE OF TECHNOLOGY KANPUR
FEBRUARY, 1997

7 JUL 1998
CENTRAL LIBRARY
I I T. KANPUR
Acc. No. A 125662

PHY-1997-D-NAT-TRA

A125662

7/2/97

CERTIFICATE

It is certified that the work contained in this thesis entitled *Transport and magnetic studies in* γ-$Fe_{80-x}Ni_xCr_{20}$ *(14* $\leq x \leq$ *30) stainless steel alloys and Cu/Ni-Zr-Al metallic glasses* by *Tapan Kumar Nath* has been carried out under my supervision and that this work has not been submitted elsewhere for a degree.

Alok Kumar Majumdar

Dr. A. K. Majumdar
Professor
Department of Physics
Indian Institute of Technology
Kanpur

February, 1997

SYNOPSIS

Name of Student : TAPAN KUMAR NATH *Roll No.* : 8910971
Degree for which submitted : Ph.D., Department of Physics
Thesis Title : **Transport and magnetic studies in γ-$Fe_{80-x}Ni_xCr_{20}$ ($14 \leq x \leq 30$) stainless steel alloys and Cu/Ni-Zr-Al metallic glasses.**
Thesis Supervisor : Dr. A. K. Majumdar, Professor of Physics, Indian Institute of Technology, Kanpur 208016, India.
Month and Year of thesis submission : February 1997

"**Magnetism in Solids**" is a subject which continues to draw attention because of its technological importance. It is a fascinating area by itself and has some role in virtually every branch of *Science and Technology.* Magnetic, thermodynamic, electron– and magneto–transport studies of substitutionally disordered 3d-transitional metal crystalline and amorphous alloys are at the frontline of research in condensed matter physics for the last couple of decades. They have thrown real challenges to both experimentalists and theoreticians, resulting in varieties of experiments and interpretations.

Presence of any kind of disorder, namely, site randomness or bond randomness (together called quenched disorder) is the source of a frustrated state in any magnetic system in which magnetic spins go to a random, yet co-operative frozen state without any long-range spatial magnetic order. So in magnetic materials (either crystalline or amorphous), a random mixture of ferromagnetic (FM) and anti-ferromagnetic (AFM) bonds having strongly competing interactions between them, may lead to a diversity of magnetic structures at low temperatures. There could be a critical concentration range where FM and AFM exchange contributions to the free energy are equal. The ground state in this concentration range may be imagined as a spin-glass (SG) state with short-range FM and AFM orders. Far away from critical concentration a long-range (FM and AFM) magnetic ordering generally sets in (e.g., Fe–Ni, Ni–Mn, Fe-Ni-Mn, Fe–Cr, Au–Cr, etc.).

There could also be a particular regime near the critical concentration which may exhibit double magnetic transitions, one at a higher temperature T_c (PM→FM) and another (FM→Mixed FM and SG) at a lower temperature T_f These are called mixed or re–entrant phase alloys (e.g., Au–Fe, Fe–Cr, Ni–Mn, Al–Fe, Fe–Ni–Mn, Cr–Fe, etc.). Re–entrant transition from an AFM state has been observed in $FeMgCl_2$ and Mn–rich CuMn binary alloys. Although in the last couple of years an extensive research had been carried out on this topic, the exact nature of the re–entrant transition is still unclear and rather controversial.

In the light of the mean-field models of Heisenberg (3d vector spins) systems, Gabay and Toulouse (GT) theoretically predicted the most plausible nature of magnetic transitions in mixed phase alloys. According to them a sequence of three kinds of magnetic transitions are possible with decreasing temperature which are (i) PM→FM followed by (ii) a transition (crossing GT–line) to a mixed phase where FM state coexists with transverse SG ordering and (iii) a crossover from weak to strong irreversibility.

Transport properties, especially the variation of the electrical resistivity with temperature in substitutionally disordered crystalline materials (with short electron mean free paths) are still of interest because of the lack of a complete understanding of the mechanisms involved despite intense theoretical efforts In a disordered metallic alloy, the electrical transport mainly depends on $k_F l$, where l is the mean free path and k_F the Fermi wave number of the conduction electrons. The alloys in the dilute limit generally have $k_F l \gg 1$ and the electronic states remain extended (long mean free paths) throughout the sample. It is assumed that in these alloys Mathiessen's rule holds, the various scattering frequencies are additive, and Boltzmann transport is still valid.

However, in the case of alloys in the weak-disorder limit with large values of electrical resistivity (with short electron mean free paths and $k_F l \sim 1$ which is the *Ioffe - Regel* criterion), the simple Boltzmann transport breaks down. At very low temperatures quantum interference effects become important and as a consequence electron localization and electron – electron interactions (many-body effects) give quantum corrections to the Boltzmann conductivity. At high temperatures, on the other hand, the deviation from linearity (DFL) of the resistivity leads to the so-called "resistivity saturation" and violates the simple Mathiessen's rule as well as the Bloch – Grüneisen theory. This happens in the case of many highly resistive materials as well as in d-band alloys, with intermediate T_c and rare earth superconductors. Over the years, despite a lot of effort to understand this phenomenon theoretically and experimentally, a quantitative, microscopic theory is still a distant goal.

In the case of 3d transition metal alloys, there are additional scattering mechanisms of magnetic origin. Some extensive studies of electrical transport have been done on noble metal - transition metal alloys (e.g., AuFe, CuMn, AuCr, AuMn, etc.,) in the spin-glass (SG), mictomagnetic or cluster-glass and the long-range ferromagnetic (FM) or antiferromagnetic (AFM) phases which exist beyond the Kondo or the dilute non-interacting regime. Sufficient attempts have been made to find out the nature of impurity scattering due to magnetic ions in noble-metal hosts for the entire regime. Despite a number of studies of electrical transport in transition metal - transition metal alloys (e.g., CrFe, NiMn, NiMnPt, CrMn, CrMnV, etc.), a concrete picture of the magnetic contribution to the resistivity is yet to emerge.

In a similar way, magnetoresistance (MR) have been studied in various magnetic phases and they do show characteristic behaviours. However, the normal magnetoresistance (band effect) due to Lorentz force acting on the carriers is superposed on them. In addition to that in any disordered material the dominant low-temperature MR contribution comes from the destruction of back scattering in *weak localization* and from *electron-electron interaction effects* (both of them together called quantum interference effect) with the application of an external magnetic field.

In the present investigation we have chosen a particular series of γ–$\mathrm{Fe}_{80-x}\mathrm{Ni}_x\mathrm{Cr}_{20}$ ($14 \leq x \leq 30$) substitutionally disordered alloys of type–304,308,309 polycrystalline austenitic stainless steel. These isostructural (fcc structure) alloys are the closest realization of γ–Fe, the nature of the ground state of which was highly controversial but later on confirmed to be AFM. These stainless alloys are used for chemical and food processing equipment, recording wire, etc.. Although the f.c.c. γ-Fe (AFM) is unstable at room temperature, the f.c.c allotrope could be obtained by alloying with Ni and the resulting structure stabilized by the addition of Cr, Mn, V or Cu.

They have industrial applications as corrosion-resistant materials. They are also non-toxic and non-magnetic and are used in cryogenics, as sophisticated pharmaceutical euipments, and as creep–resistive and high-resistance materials.

It is known that γ–FeNiCr alloys have competing exchange interactions because of which the local spin orientation is expected to depend on its environment. The effective exchange interaction can be positive, negative or nearly zero. In the Heisenberg local moment picture, the behaviour of the whole sample will be governed by concentration, distribution and the strength of the six different possible exchange interactions J_{ij} between the different magnetic atoms. As a result, a number of exotic magnetic phases are realized at low temperatures.

The magnetic phase diagram had been established in γ–$Fe_{80-x}Ni_xCr_{20}$ ($14 \leq x \leq 30$) through dc–magnetization, magnetic neutron scattering and ac–susceptibility measurements. Due to the strong competing exchange interaction between different kinds of magnetic atoms, this system of alloys undergoes a compositional phase transition from long-range AFM (x = 10-14) to SG (17-21) to mixed FM and SG (23–26) or re–entrant phase and finally to long-range FM (30) order *within the same crystallographic γ-phase.* To our knowledge, so far there is no electronic or magnetic band structure calculation in this series of ternary magnetic alloys having such wide varieties of magnetic phases. The present investigation might lead to band structure calculations.

The motivation behind the present investigation is to seek answers to many questions regarding these substitutionally disordered, highly resistive γ-Fe-Ni-Cr alloys near the critical concentration regime of long-range ordering (either FM or AFM).

1. What distinct features does one observe in electronic transport, magneto-transport and magnetization when the system undergoes a gradual change from one long-range ordered phase (FM) to another (AFM) with intermediate magnetically disordered phases (SG or re-entrant SG or mixed FM and SG) by varying the composition but keeping the crystal structure the same ?

2. At sufficiently high temperatures (where the contribution to the resistivity from magnetic scattering can be neglected), the deviation from linearity (DFL) of the electrical resistivity which might lead to a saturation, gives one an opportunity to investigate thoroughly the long-debated phenomenon of resistivity saturation for highly resistive crystalline magnetic alloys. Several models or theories have been proposed on the DFL of resistivity which ultimately leads to a saturation. In the present work, we have considered some of them which are the most appropriate ones to explain this phenomenon and tested them rigorously with our observed experimental ρ(T) data at high temperatures. The role of magnetic ordering in the electronic transport has also been examined.

3. What are the very high-field magnetic responses (χ_{HF}) of these wide varieties of magnetic phases (FM, mixed, SG and AFM) with strong competing exchange interactions? Also, is it possible to find in them distinct functional relationships between magnetization and magnetic field ?

4. How do the electronic transport properties of amorphous alloys (metallic glasses) compare with those of disordered crystalline alloys ? How do the recent theories of quantum interferrence effects, namely, weak localization and electron-electron interaction provide the quantum corrections to the Boltzmann conductivity in bulk non-magnetic amorphous alloys ?

This thesis consists of two parts. The subdivisions of the 1st part are : (a) studies of electrical resitivity, (b) magneto-transport studies (magnetoresistance) and the correlation between low-field magnetoresistance and magnetization, and (c) very high-field (up to 20 tesla) magnetization and magnetoresistance studies of $Fe_{80-x}Ni_xCr_{20}$ ($14 \leq x \leq 30$), substitutionally disordered austenitic stainless steel alloys near the critical concentration regime. The second part is an independent chapter by itself where we have presented electrical and thermal transport studies of some (Cu/Ni-Zr-Al) Pauli paramagnetic amorphous metallic glass alloys.

In chapter 2 we give details of sample preparation and their characterization through different non-destructive testings. In this chapter we have also described briefly the experimental techniques, cryostat design for low-temperature resistivity measurements, design of high-temperature resistivity set up, etc..In Appendix A a typical software, developed for data acquisition through IEEE interfacable measuring instruments (e.g.,DMM, Temperature Controller, Constant Current Source, Multichannel Scanner, Lock-in-Amplifier, Gauss-meter, Nano-voltmeter, etc.) with PC/AT, has been provided.

Chapter 3 reports a systematic study of the electrical resistivity on substitutionally disordered γ-$Fe_{80-x}Ni_xCr_{20}$ ($14 \leq x \leq 30$) austenitic stainless steel alloys in different magnetic states in the temperature range of 10 K - 600 K. Rigorous and thorough analysis and interpretation of the data have been presented. We observe in each alloy, irrespective of its low - temperature magnetic state, a strong deviation from linearity (DFL) of ρ which is an indication of resistivity saturation at high temperatures. The temperature coefficient of resistivity (TCR $= \rho^{-1}\frac{d\rho}{dT}$) vs ρ curves for all the alloys merge in the temperature range of 100 to 600 K. This behaviour indicates that both thermal and compositional disorders are equally important in determining the resistivity saturation. We have examined several models and find that the parallel-resistor and the ion-displacement models are the most appropriate ones in explaining this DFL of ρ at high temperatures. At low temperatures, in the long-range ferromagnetic and antiferromagnetic as well as in the mixed-phase regimes, the contribution to resistivity from the electron-magnon scattering ($\sim T^2$) dominates. In the spin-glass regime there is an additional T^3 term arising from the electron-phonon s-d scattering. In Appendix B and C the different softwares developed for (1) the evaluation of *Bloch-Wilson* integral using D01AHF NAG-Routine, (2) non-linear least-square fitting programme using the result of the above integral and (3) linear interpolation techniques.

In chapter 4 we have presented the low-field magnetoresistance and magnetization studies and their correlations in the Fe-Ni-Cr alloys. The measurements were done in the temperature range of 10 to 300 K up to a field of 1.65 tesla. High-field magnetoresistance study of some of them has been made in the temperature range of 4.2 to 60 K and up to a field as high as 20 tesla.

We have found distinct field dependence of magnetoresistance $\frac{\Delta\rho}{\rho}$(H) in the different magnetic phases, namely, spin glass, re-entrant spin glass, ferromagnetic and antiferromagnetic below their respective transition temperatures. The negative magnetoresistance (MR) in different magnetic states at low temperatures is found to be of magnetic origin. The MR due to quantum interference effects of these disordered magnetic alloys are rather small, if present at all.

Chapter 5 contains very high-field magnetization M(H,T) studies up to 19 tesla and down to 4.2 K in the Fe-Ni-Cr alloys near the critical concentration regime. Distinct functional relationships M(H) have been found in different magnetic phases below their respective transition temperatures. In the ferromagnetic (FM) alloy with x = 30, contributions from long – wavelength *spin – wave* and *Stoner single-particle excitations* have been found in the temperature – dependent demagnetization process. In the light of the *Rhodes – Wohlfarth* criterion, this alloy is found to be a *weak – itinerant FM.* For the alloys with x = 26 and 23 (mixed or re – entrant phase) the coexistence of long – range FM ordering along with spin – glass (SG) freezing has been established supporting the Gabay – Toulouse model. For x = 21 and 19 (SG), the field – dependent magnetization (after scaling) falls on a single universal curve which implies the same kind of response dynamics of the frozen spins. For the antiferromagnetic (AFM) alloy with x = 14, a *spin – flop* transition has been observed at 1 tesla due to the canting of the AFM spins in the strong external magnetic field. The effective moleclar – field coefficients (γ_i) for the 1st and 2nd nearest neighbour as well as the effective – field exchange interaction J_i between the ith neighbours inside the different sublattices have been estimated. The long – range AFM structure of this alloy is found to be of *type 1* .

In chapter 6 we have presented the electrical and thermal transport studies of Pauli paramagnetic ($\chi \sim 10^{-6}$ emu/mol) Cu/Ni-Zr-Al amorphous metallic glass ribbons. Very high-resolution electrical resistivity data have been presented for Zr-rich $(Cu_{0.36}Zr_{0.64})_{1-x}Al_x$ and $(Ni_{0.5}Zr_{0.5})_{1-x}Al_x$ ($0 \leq x \leq 0.2$) non-magnetic transition-metal-based amorphous metallic glasses in the temperature range of 1.2 to 300 K at every 50 mK.. All the alloys are found to fall into the strong-scattering regime ($\rho_{300} > 165$ $\mu\Omega$ cm) with negative temperature coefficient of resistance even till 300 K. With the addition of Al in both the systems, the value of ρ_{300} increases because of the enhancement of the degree of disorder. In the low-temperature range, all of them show a tendency towards superconductivity with transition temperature $T_c < 4.2$ K and large superconducting fluctuations. They are found to be extreme type-II dirty BCS superconductors with the electron-phonon coupling constant, $\Lambda \sim 0.5$. The data have been analysed in the light of *Quantum Interference Effects* which provide the quantum corrections to Boltzmann conductivity. A quantitative analysis of the electrical resistivity, based on the electron-electron interaction and localization effects, is reported here for all the alloys in the temperature range, $T_c < T < 300$ K. We find three distinct regions, hitherto only theoretically predicted where the conductivity varies in a sequence of $\sqrt{T}$, T and $\sqrt{T}$ at low, intermediate and high temperatures, respectively. The only earlier similar observation was made in a ferromagnetic system where the interpretation in terms of quantum interference effects will always remain controversial. A number of parameters, namely, the coefficient of the $\sqrt{T}$ term at low temperatures, diffusion constant, density of states at the Fermi level, inelastic mean free path and relaxation time, estimated from this quantum correction analysis, are in excellent agreement with those from earlier experiments on binary systems. The thermoelectric power for all the alloys is positive at 300 K and its dependence on Al concentration is explained by the Mott s-d scattering model.

In chapter 7 we conclude the thesis by summarizing briefly the important results obtained from the present investigations. At the end the scope for future work has been spelt out.

Acknowledgements

It gives me a great pleasure to express my deep sense of gratitude to Prof. A. K. Majumdar, my supervisor who introduced me to the field of magnetism in disordered system. He has not only supervised my work but was also a constant source of inspiration and encouragement. I find him not only a good teacher but also approachable, communicative, open to ideas and suggestions, and very encouraging.

Dr. K. P. Rajeev was always available with his advice, help, and encouragement. I learnt from him a lot about low temperature techniques.

I acknowledge helpful discussions with Prof. D. Chowdhury at various stages. He was always ready to help whenever I was in doubt and clarified many of the basic concepts in condensed matter physics.

Amongst the faculty members at IIT Kanpur, I would also like to thank Profs. R. C. Budhani, R. Prasad, V. A. Singh, S. Kumar and K. Shahi for their valuable advice and suggestions at various stages. Drs. M. K. Verma, Ravi Shankar, R. N. Mukherjee, P. K. Bharadwaj, S. Sarkar, T. Chakraborty were there to boost up my morale.

My seniors, Drs. A. Banerjee, A. Das, and Rita Singhal extended their helping hand in the initial stages of this work. I extend my gratitude to them. It is a pleasant memory working with Dr. A. Das in the initial stage, especially during the installation of the liquid helium plant in the laboratory.

It is also my good fortune for the short but very productive interactions with Drs. T. R. Ravindran, Kapil Bajaj, M/s. Avik Ghosh, Mitrajit Dutta, Pinaki Sengupta, Abhinandan Majumdar and Ms. Shilpa Jain in the laboratory.

I am indebted to my colleagues in the laboratory for their excellent cooperation. I mention N. Sudhakar, Swapan Chakraborty, Gautam Sinha, and Ashutosh Tiwari in this connection.

I am grateful to Dr. S. V. Sharma for his excellent cooperation during the high temperature measurements and for his constant encouragement throughout my Ph.D. work. Words fail to thank him for his brotherly attitude and he was always a well wisher.

During this work I enjoyed prompt technical help from M/s. D. C. Banerjee, Ramprakash Pal and Ram Ashrey. I extend them my sincere thanks.

I would also like to thank Professor D.G. Naugle of Texas A & M University for providing some samples. I acknowledge the finacial assiatance provided by the institute (IIT Kanpur) and Department of Science and Technology, Government of India through Project No. SP/S2/M-24/93.

During the various stages of work I also received full support from the technical personnel in liquid nitrogen plant, physics workshop, central workshop, glass blowing workshop and different units of ACMS. H. K. Panda, L. S. Rathour, A. K. Srivastava and other members of Physics office extended their help and support whenever it was needed. I thank Mr. B. K. Jain for taking great care in drawing many of the figures in the thesis.

It would be unfair not to acknowledge the B-top gang. They were much more than friends – Samiran with his ebullience, Debnath with his down-to-earth attitude, Dinu whose Sunday night cooking were like the pie on the cream, Shanti with his innate sense of cracking the best jokes and Sujay with his stoicness. The association of Rajee, George, Diwakar, Malay, Sandeep, Prasen, Prabal, Gurjar, Amitda and Patnaik proved to be of immense value.

I gratefully acknowledge the cheerful company of my friends, Saji, Tamilarasu, Susanta, Neelu, Jethu, Tapa, Alok, Bera, Debotosh, Tapas, Gour, Bachcha, Babu, Nagrajan, Debolina, Bhaskar, GK, Abir, Kishore, Anirban, Satpati, Ranganda, Tapan Khan, Deba, Banga, Pratima, Sanju, Arpita, Manabendra, Panda, Chaitali and many others.

I acknowledge those friends, specially, Nagrajan, Vanu, Bera, Sujay, Shanti, Ranganda, Shyamal and Rajesh with whom I have shared my joys in victory and sorrows in defeat in several matches (soccer, volley, cricket, etc.) while participating as a member of the institute or

hall team. I enjoyed a lot participating in several cultural and religious programmes organised either by "Bodhi" or "Bengali Society" which made my stay in the campus lively.

It is a great pleasure to thank Mrs. S. Majumdar for extending warm hospitality (especially, in those painful days when I was down with Hepatitis) throughout my stay at IIT Kanpur.

It would be unfair not to acknowledge family members of Prof. R. N. Mukherjee, Mr. D. C. Banerjee, and Dr. S. V. Sharma for extending warm hospitality which made my stay very pleasant.

Finally, I must express my deep appreciation to my parents, brothers and sister for their enthusiastic support and encouragement. It was their love which kept me going and words would fail to express my feelings of indebtedness to them.

T. K. Nath

To my parents,
brothers and sister

Contents

Acknowledgements xi

1 Preamble **1**

1.1 **Frustrated spin system – spin glass** 2

1.1.1 **What is a spin glass ?** 3

1.2 Frustrated spin system – Reentrant spin glass (mix -ed phase) 9

1.3 Studies of 3d-transition metal alloys 13

1.3.1 Magnetism 13

1 3.2 Electrical transport - Resistivity : 16

1.3.3 Magneto-transport – Magnetoresistance : 22

1.4 Present Study and Motivation : 36

1.5 Organization of the Thesis : 42

2 Experimental Details **55**

2.1 Sample preparation and characterization 55

2.1.1 Fe-Ni-Cr alloys 55

2.1.2 Cu/Ni-Zr-Al metallic glass ribbons 59

2.2 Cryostat design and measurement techniques 60

2.2.1 Magnetoresistance measurement 60

2.2.2 dc-magnetization 62

2.2.3 Electrical resistivity 64

2.2.4 Thermoelectric power 73

3 **Electrical transport–resistivity [$\rho(T)$]** **76**

3.1 General features of the observed ρ(T) 78

3.1.1 Analysis of ρ(T) data in the temperature range T_{min} ($\approx$ 10K) $\leq$ T $\leq$ 70K ($\approx \Theta_D/5$) 82

3.1.2 Analysis of ρ(T) data in the temperature range 200 ($\approx \Theta_D/2$) $\leq$ T $\leq$ 600K 90

3.2 Conclusions 104

4 **Low-field magnetoresistance and magnetization and their correlations** **108**

4.1 General features and comparative study of low-field magnetoresistance and magnetization of Fe-Ni-Cr series 110

4.1.1 Magnetic field, temperature, and composition dependence of magnetoresistance of Fe-Ni-Cr series 128

4.2 Correlation between low-field magnetoresistance and magnetization 136

4.3 High-field (till 20 tesla) magnetoresistance study of Fe-Ni-Cr series 142

5 **High-field (till 20 tesla) magnetization study of γ-$Fe_{80-x}Ni_xCr_{20}$ (14 $\leq$ x $\leq$ 30) alloys** **153**

5.1 RESULTS and DISCUSSION 155

5.1.1 General features of the high–field M–H curves between 4.2 and 60 K and low–field M–T curves between 19 and 700 K 155

5.1.2 Spin–wave analysis of γ-$Fe_{50}Ni_{30}Cr_{20}$ alloy 176

5.1.3 x = 26 : Mixed-phase alloy 179

5.1.4 x = 19 and 21 : Spin-glass alloys 182

5.1.5 x = 14 : Antiferromagnetic alloy 182

5.2 Conclusion 188

6 Quantum corrections to Boltzmann conductivity in Cu-Zr-Al and Ni-Zr -Al amorphous alloys 193

6.1 Introduction 193

6.2 Results and Discussions 196

6.2.1 Superconducting Fluctuations 196

6.2.2 Quantum Correction Analysis 204

6.2.3 Thermoelectric Power 223

6.3 Conclusion 225

7 Conclusions 230

List of Tables

3.1 Ni concentration (x) dependence of magnetic transition temperatures (T_c, T_{SG}, T_N taken from ref.[1]), resistivities ρ at 10 and 300 K and TCR $[\rho^{-1}(\frac{d\rho}{dT})]$ at 300 and 500 K of γ-$Fe_{80-x}Ni_xCr_{20}$ ($14 \leq x \leq 30$) alloys. 79

3.2 Fitting parameters for the ρ(T) data to different fit functions, low-temperature ranges and the values of χ^2 (defined in text) for $\gamma - Fe_{80-x}Ni_xCr_{20}$ ($14 \leq x \leq 30$) alloys. 89

3.3 Ni concentration (x) dependence of the fitting parameters for the $\rho(T)$ data to Eq.(1.10) of the parallel-resistor model and the values of χ^2. The range of fit is taken between 200 and 600 K for the γ-$Fe_{80-x}Ni_xCr_{20}$ ($14 \leq x \leq 30$) alloys. . . 96

3.4 Fitting parameters for the $\rho(T)$ data to Eq.(1.14) of the ion–displacement model and the values of χ^2. The range of fit is taken between 200 and 600 K for the γ-$Fe_{80-x}Ni_xCr_{20}$ ($14 \leq x \leq 30$) alloys. 100

4.1 Values of the parameters n, and α (T) and also χ^2 for the fits to $\Delta\rho/\rho = -\alpha(T)H^n$ at various temperatures for $Fe_{80-x}Ni_xCr_{20}$ ($14 \leq x \leq 30$) alloys in the field range of 2 to 16.5 kOe. 130

4.2 Ni concentration dependence of α, M(0), and αM_0^2 as obtained from the fit to Eq.(4.5). 140

4.3 Temperature dependence of depth of minimum of MR, strength of field at which minimum observed (H_{min}), and the parameters obtained from the fit to Eq.(4.7) for Fe-Ni-Cr alloys. 145

5.1 Fit of the isothermal M–H curves of $Fe_{80-x}Ni_xCr_{20}$ alloys to several distinct fit functions till 20 T : compositions (x), fit functions, fit parameters (M_o, M_1 and n), field range, temperature and the values of χ^2. 161

5.2 Concentration dependence of different fit parameters (M_s, a and b) of the law of approach to saturation (Eq (5.2)), the values of χ^2, temperature and field ranges for several isothermal M–H curves of $Fe_{80-x}Ni_xCr_{20}$ alloys. 163

5.3 Composition (x), Curie constant (C), effective Bohr magneton number (P_{eff}), Paramagnetic Curie temperature (Θ), q_c, q_s, temperature for the onset of deviation from Curie–Weiss law (T_d), and effective number of electrons per atom outside the closed argon shell [n ($\approx$ <3d+4s>] of $Fe_{80-x}Ni_xCr_{20}$ alloys. 175

6.1 Values of density, resistivity (ρ_{300}), temperature coefficient of resistance (ρ^{-1} dρ/dT), crystallization temperature ($T_{crystal}$), susceptibility (χ), superconducting transition temperature (T_c), T_c(onset), electron-phonon coupling constant (Λ), Hall coefficient (R_H) and Debye temperature (Θ_D) for $(Cu_{0.36}Zr_{0.64})_{1-x}Al_x$ and $(Ni_{0.5}Zr_{0.5})_{1-x}Al_x$ alloys. 202

6.2 Fit to $\sigma(T) = \sigma_0 + m_\sigma \sqrt{T}$ in the temperature range ($T_c \leq T \leq 15$ K) : Al conc (x), parameters, χ^{2^b}, range of fit, diffusion constant(D), and density of states at the Fermi level [N(E_F)] for $(Cu_{0.36}Zr_{0.64})_{1-x}Al_x$ and $(Ni_{0.5}Zr_{0.5})_{1-x}Al_x$ alloys. 206

6.3 Fit in the temperature ranges $\Theta_D/10 \leq T \leq \Theta_D/3$ and $\Theta_D/3 \leq T \leq \Theta_D$: Al conc.(x), parameters, χ^2, range of fit, inelastic mean-free path (l_i), equations used, and inelastic relaxation time (τ_i) for $(Cu_{0.36}Zr_{0.64})_{1-x}Al_x$ and $(Ni_{0.5}Zr_{0.5})_{1-x}Al_x$ alloys. 211

6.4 Parameters A, B, and Δ, obtained from the fit to Eq.(6.8), χ^2, range of fit for $(Cu_{0.36}Zr_{0.64})_{1-x}Al_x$ and $(Ni_{0.5}Zr_{0.5})_{1-x}Al_x$ alloys. 220

List of Figures

1.1 (a) A triangular lattice and (b) a rectangular plaquette of magnetic ions having up- or down-spin illustrate "frustration" (where no arrangement can satisfy all the microscopic constraints). 3

1.2 A frozen spin glass with $J_1 > 0$ (ferromagnetic) and $J_2 < 0$ (antiferromagnetic). The zig-zag links indicate a broken bond; the spin at the heavy circle is frustrated. 4

1.3 The RKKY interaction J(r) between two magnetic impurities in a metal as a function of their separation r. 4

1.4 An amorphous spin glass for which the disordered lattice sites are 50% occupied by magnetic moments. 5

1.5 A random-bond spin glass where – implies FM coupling and – – implies AFM coupling. The number of FM bonds is equal to the number of AFM ones [ref.3]. 5

1.6 (a) Reversible and irreversible magnetization vs temperature for a spin glass. (b) Time-dependent magnetization of a spin glass (c) Frequency - dependent ac-susceptibility vs temperature of a spin glass. (d) Simplified illustration of magnetic spins at different times in various magnetic phases at T=0. 7

1.7 Gaussian distribution of exchange integrals according to the idea of Sherrington and Kirkpatrick [26]. 10

1.8 Magnetic phase diagram for vector spins interacting with infinite-range Gaussian distribution in the T - J_0 plane according to de Almeida and Thouless (AT) and Gabay and Toulouse (GT). M_1 and M_2 represent mixed magnetic phases of the re-entry transition. 12

1.9 Magnetoresistance data of Mg at various temperatures, fitted to Kohler's rule [ref.[79]]. 25

1.10 A schematic plot of the magnetoresistance for (a) $\tau_\imath \ll \tau_{so}$, (b)$\tau_\imath \sim \tau_{so}$, and (c) $\tau_\imath \gg \tau_{so}$ [102]. 26

1.11 Cooling curve for pure iron. 37

1.12 General spin structure of γ-Fe. 38

1.13 Magnetic phase diagram of $Fe_{80-x}Ni_xCr_{20}$ ($14 \leq x \leq 30$) alloys in the temperature - concentration (Ni) plane [157]. 40

2.1 Ternary diagram of FeNiCr system showing crystallographic and magnetic phases. The dot-dashed line separates the γ phase from α, δ and σ phases at room temperature. The solid line for T_c=0 separates the ferromagnetic (FM) phase from the paramagnetic (P) one (ref.[1,2]). 56

2.2 Metallurgical phase-diagram showing trend of reactions in steels alloyed with 18% chromium and 8% nickel. 57

2.3 Typical X-ray diffraction pattern for the alloys with x=19 and 21 (spin glass) using CuK$_\alpha$ ($\lambda = 1.5406 \mathring{A}$) radiation. 58

2.4 Schematic diagram of the magnetoresistance set-up. 61

2.5 Schematic diagram of the high temperature (300-600 K) resistivity set-up. . . 66

2.6 Schematic diagram of the heating arrangement for resistivity measurements in the temperature range 300-600 K. 67

2.7 Schematic diagram of the He^4 cryostat used for resistivity measurements in the temperature range 1.2–300 K. 69

2.8 Schematic diagram of the cold finger of the He^4 cryostat and the circuit diagram for the connection with the measuring instruments. 71

3.1 Experimental ρ(T) plot of $Fe_{80-x}Ni_xCr_{20}$ (x = 14,19,21,23,26, and 30) highly resistive austenitic stainless steel alloys in the temperature range between 10 and 600 K. The inset shows a typical dρ/dT vs T plot for x = 23. 80

3.2 Percentage change of resistivity ρ(500K) relative to ρ(10K) and ρ(200 K) of $Fe_{80-x}Ni_xCr_{20}$ ($14 \leq x \leq 30$) alloys as a function of Ni concentration(x). The inset shows the x - dependence of the residual resistivity (ρ(10 K)). The solid curve in the inset is just a guide to the eye. 81

3.3 Ni concentration (x) dependence of the temperature coefficient of resistivity (TCR = $\rho^{-1}\frac{d\rho}{dT}$) of $Fe_{80-x}Ni_xCr_{20}$ ($14 \leq x \leq 30$) alloys at 100 K, 300 K, and 500 K. 81

3.4 Resistivity (ρ which results from either thermal or compositional disorder) dependence of the TCR of $Fe_{80-x}Ni_xCr_{20}$ ($14 \leq x \leq 30$) alloys in the temperature range beyond 100 K. The solid line is the best-fitted curve. 83

3.5 Resistivity (ρ) vs T^2 plot of $Fe_{66}Ni_{14}Cr_{20}$ antiferromagnetic alloy in the temperature range of 10 - 60 K. The solid line is the best-fitted curve. The inset plots the percentage deviation of the fit from the experimental data. 84

3.6 Temperature dependence of resistivity of $Fe_{80-x}Ni_xCr_{20}$ (x = 19 and 21) spin-glass alloys in the low temperature range. The solid lines are the best-fitted curves for the function $a+bT^2+cT^3$. 86

3.7 ρ vs T^2 plots of $Fe_{50}Ni_{30}Cr_{20}$ ferromagnetic and $Fe_{80-x}Ni_xCr_{20}$ (x = 23 and 26) mixed-phase alloys in the low temperature range. The solid lines are the best-fitted curves. 87

3.8 Ni concentration (x) dependence of the fit parameters a and b of $Fe_{80-x}Ni_xCr_{20}$ ($14 \leq x \leq 30$) alloys in the low temperature range. The solid lines are just guides to the eye. 88

3.9 Experimental (dots) ρ vs T plots of $Fe_{80-x}Ni_xCr_{20}$ (x = 23,26, and 30) alloys in the temperature range between 150 and 600 K. The best-fitted curves (solid lines) for the alloys are plotted using Eq.(1.10) (parallel-resistor model). The inset shows the temperature dependence of a typical percentage deviation of fit for x = 23. 93

3.10 Experimental (dots) ρ vs T plots of $Fe_{80-x}Ni_xCr_{20}$ (x = 14,19, and 21) alloys in the temperature range between 150 and 600 K. The best-fitted curves (solid lines) for the alloys are plotted using Eq.(1.10) (parallel-resistor model). The inset shows a typical likelyhood distribution of the relative errors $[P(\frac{\Delta\rho}{\rho})]$ of the fit for x = 19. 94

3.11 Ni concentration (x) dependence of the fitting parameters ε and B of Eq.(1.10) (parallel-resistor model) of $Fe_{80-x}Ni_xCr_{20}$ ($14 \leq x \leq 30$) alloys. The solid lines are just guides to the eye. The inset shows the concentration (x) dependence of ρ_{sat}. 95

3.12 Experimental (dots) ρ vs T plots alongwith the best-fitted curves (solid lines) using Eq.(1.14) (ion-displacement model) in the temperature range between 200 and 600 K of $Fe_{80-x}Ni_xCr_{20}$ (x = 23, 26, and 30) alloys. The inset shows the temperature dependence of a typical percentage deviation of the fit for x = 23. 98

3 13 Experimental (dots) ρ vs T plots alongwith the best-fitted curves (solid lines) using Eq.(1.14) in the temperature range between 200 and 600 K of $Fe_{80-x}Ni_xCr_{20}$ (x = 14,19, and 21) alloys. The inset shows the temperature dependence of a typical percentage deviation of the fit for x = 21. 99

3 14 Plot of the variation of T_0 with ρ(10 K)(experimental) for $Fe_{80-x}Ni_xCr_{20}$ ($14 \leq x \leq 30$) alloys. T_0 is the characteristic temperature in Eq (1.14) of the ion-displacement model. The inset shows the comparative variation of ρ_m and ρ_{sat} (from Eqs.(1.14) and (1.10), respectively) with Ni concentration (x). The dashed lines are just guides to the eye. 101

4.1 Magnetic field (H) dependence of (a) longitudinal $((\frac{\Delta\rho}{\rho})_{\parallel})$ and (b) transverse $((\frac{\Delta\rho}{\rho})_{\perp})$ magnetoresistances at various temperatures for $Fe_{50}Ni_{30}Cr_{20}$ (FM) alloy. 111

4.2 (a) Comparative plot longitudinal (L) and transverse (T) Magnetoresistances showing the anisotropy of MR for x=30 alloy at various temperatures. (b) Same plot for the alloy with x=30 and 23 at 11 K. The inset clearly shows the anisotropy in the low field range (0 - 1000 Oe) for x = 30. 112

4.3 M-H isotherms of $Fe_{50}Ni_{30}Cr_{20}$ (FM) alloy at various temperatures in the field range of 0 to 16.5 kOe. 114

4.4 Arrott plots at various temperatures for $Fe_{50}Ni_{30}Cr_{20}$ (FM) alloy confirming the presence of large spontaneous moment. 115

4.5 Magnetic field (H) dependence of longitudinal $((\frac{\Delta\rho}{\rho})_{\parallel})$ magnetoresistance at various temperatures for $Fe_{54}Ni_{26}Cr_{20}$ (Mixed phase) alloy. 116

4.6 M-H isotherms of $Fe_{54}Ni_{26}Cr_{20}$ (Mixed phase) alloy at various temperatures in the field range of 0 to 16.5 kOe. 117

4.7 Magnetic field (H) dependence of (a) longitudinal $((\frac{\Delta\rho}{\rho})_{\parallel})$ and (b) transverse $((\frac{\Delta\rho}{\rho})_{\perp})$ magnetoresistance at various temperatures for $Fe_{57}Ni_{23}Cr_{20}$ (Mixed phase) alloy. 119

4.8 M-H isotherms of $Fe_{57}Ni_{23}Cr_{20}$ (Mixed phase) alloy at various temperatures in the field range of 0 to 16.5 kOe. 120

4.9 Arrott plots at various temperatures for $Fe_{57}Ni_{23}Cr_{20}$ (Mixed phase) alloys confirming the presence of ferromagnetic ordering below T_{SG}. 121

4.10 Magnetic field (H) dependence of (a) longitudinal $((\frac{\Delta\rho}{\rho})_{\parallel})$ and (b) transverse $((\frac{\Delta\rho}{\rho})_{\perp})$ magnetoresistances at various temperatures for $Fe_{59}Ni_{21}Cr_{20}$ (Spin glass) alloy. 123

4.11 M-H isotherms of $Fe_{59}Ni_{21}Cr_{20}$ (Spin glass) alloy at various temperatures in the field range of 0 to 16.5 kOe. 124

4.12 Magnetic field (H) dependence of longitudinal $((\frac{\Delta\rho}{\rho})_{\parallel})$ magnetoresistance at various temperatures for $Fe_{61}Ni_{19}Cr_{20}$ (Spin glass) alloy. 125

4.13 M-H isotherms of $Fe_{57}Ni_{19}Cr_{20}$ (Spin glass) alloy at various temperatures in the field range of 0 to 16.5 kOe. 126

4.14 Magnetic field (H) dependence of longitudinal (Long.) and transverse (Trans.) magnetoresistances at 4 2 K for $Fe_{66}Ni_{14}Cr_{20}$ (Antiferromagnetic) alloy. 127

4.15 M-H isotherms of $Fe_{66}Ni_{14}Cr_{20}$ (Antiferromagnetic) alloy at various temperatures in the field range of 0 to 16.5 kOe. 128

4 16 (a) Longitudinal MR vs H for $Fe_{80-x}Ni_xCr_{20}$ at 11 K. All the data (except for x=19 alloy) have been shifted vertically for clarity. (b) Ni concentration (x) dependence of α and n at T=4.2 K for $Fe_{80-x}Ni_xCr_{20}$ alloys. 133

4.17 Temperature dependence of longitudinal magnetoresistance of (a) $Fe_{50}Ni_{30}Cr_{20}$ (FM) and (b) $Fe_{57}Ni_{23}Cr_{20}$ (Mixed phase) alloys at magnetic fields of 5, 10 and 16.5 kOe. 134

4.18 (a)Temperature dependence of longitudinal MR of $Fe_{59}Ni_{21}Cr_{20}$ (SG) and (b) Ni concentration (x) dependence of longitudinal MR for $Fe_{80-x}Ni_xCr_{20}$ alloys at 11 K. The curves in both the plots are at magnetic fields of 5, 10 and 16.5 kOe. 135

4.19 Log-log plot of transeverse magnetoresistance and magnetization at different temperatures for $Fe_{59}Ni_{21}Cr_{20}$ (Spin glass) alloys. The slope of the plot gives $|\frac{\Delta\rho}{\rho})_{\|}| \sim M^{2\ 5}$. 137

4.20 Correlation between $(\frac{\Delta\rho}{\rho})_{iso}$ and M for $Fe_{80-x}Ni_xCr_{20}$ alloys at $T = 20$ K clearly showing a gradual evolution of MR as one goes from the long-range FM ordering towards the critical region ($x \approx x_c$) close to the SG regime. 138

4.21 Temperature dependence of dc susceptibility χ_{dc} (= dM/dH) $Fe_{80-x}Ni_xCr_{20}$ (x = 21, 23 and 30) alloys at a field of 6 kOe. 141

4.22 Magnetic field (H) dependence of longitudinal $((\frac{\Delta\rho}{\rho})_{\|})$ magnetoresistance at various temperatures for $Fe_{54}Ni_{26}Cr_{20}$ (Mixed phase) alloy in the field range of 0 - 20 tesla. 143

4.23 Magnetic field dependence of (a) normal and (b) anomalous contribution of MR for $Fe_{54}Ni_{26}Cr_{20}$ (Mixed phase) alloy at various temperatures in the field range of 0 - 20 tesla. 146

4.24 Magnetic field (H) dependence of longitudinal $((\frac{\Delta\rho}{\rho})_{\parallel})$ magnetoresistance at various temperatures for $Fe_{61}Ni_{19}Cr_{20}$ (Spin glass) alloy in the field range of 0 - 20 tesla. 147

4.25 Magnetic field dependence of (a) normal and (b) anomalous contribution of MR at various temperatures for $Fe_{61}Ni_{19}Cr_{20}$ (Spin glass) in the field range of 0 - 20 tesla. 148

5.1 Experimental M(H) plots of $Fe_{80-x}Ni_xCr_{20}$ (x = 14,19,26 and 30) austenitic stainless steel alloys in the magnetic field range of 0 to 20 tesla at 4.2 K. The topmost 3 curves are the M–H plots of $Fe_5Co_{50}Ni_{17}B_{16}Si_{12}$ amorphous ferromagnetic metallic glass at 4.2, 8.1 and 20.1 K. 157

5.2 M–H isotherms of the mixed phase alloy $Fe_{54}Ni_{26}Cr_{20}$ at 4.2, 8.1, 20.7 and 59.7 K in the field range of 0 - 20 tesla. The inset shows its hysteresis plot which is a measure of the field–induced anisotropy energy at 4.2 and 59.7 K in the low–field range of 0 - 1 tesla. 158

5.3 M–H and $\frac{dM}{dH}$ vs H plots of the AFM alloy $Fe_{66}Ni_{14}Cr_{20}$ at 4.2 K. The M–H plot shows a striking change of slope around 1 tesla (shown by an arrow) where $\frac{dM}{dH}$ shows a peak. This has been attributed to *spin–flop* transition at this field. . . 159

5.4 Ni concentration (x) dependence of fitting parameters M_s, a and b of the law of approach to saturation (Eq.(5.2)) for $Fe_{80-x}Ni_xCr_{20}$ alloys. The solid and the dashed lines are just guides to the eye. 165

5.5 M vs. H^{-1} plot of $Fe_{50}Ni_{30}Cr_{20}$ (FM) alloy. The solid line is the extrapolation of the fit to Eq.(5.2) in the very high-field range. The other two curves are the resolved contributions. 166

5.6 Arrott plots (M^2 vs H/M) for crystalline $Fe_{80-x}Ni_xCr_{20}$ (x = 14, 19, 26 and 30) alloys with wide varieties of magnetic phases at 4.2 K. The curvature changes (convex to concave) while passing through the critical concentration region. . . 167

5.7 Arrott–Belov–Kouvel (ABK) plots at various temperatures in the low–field range for the mixed phase alloy $Fe_{54}Ni_{26}Cr_{20}$ confirming the presence of the FM ordering. 169

5.8 Reciprocal susceptibility ($1/\chi$) vs temperature (T) for $Fe_{61}Ni_{19}Cr_{20}$ (SG) alloy at 0.2 tesla. The arrow shows the onset ($T_d \gg T_f$) of the deviation from the Curie–Weiss behaviour. The inset shows the same plot for $Fe_{50}Ni_{30}Cr_{20}$ (FM) alloy. The solid lines are the fits to Curie–Weiss law. 171

5.9 Reciprocal susceptibility ($1/\chi$) and magnetization (M) vs temperature (T) for $Fe_{66}Ni_{14}Cr_{20}$ alloy at 0.2 tesla Θ is small but negative and the Néel temperature is (26±1) K. 172

5.10 Ni conc. (x) dependence of the paramagnetic Curie temperature (Θ) and the effective Bohr magneton number (P_{eff}) (derived from Eq.(5.4)) for $Fe_{80-x}Ni_xCr_{20}$ alloys. The solid line is the best–fit straight line and the dashed one is a guide to the eye. 174

5.11 Change of reduced magnetization ($\frac{\Delta M}{M_o}$) as a function of reduced temperature (T/T_c) for $Fe_{50}Ni_{30}Cr_{20}$ (FM) alloy. The solid line is the non-linear least squares fit of the experimental data to the combination of *spin–wave* and Stoner *single-particle* excitations. The percentage deviation of the fit from the data, shown in the inset, indicates a very good quality of fit. 177

5.12 Temperature dependence of dc–susceptibility χ_{dc} ($= \frac{dM}{dH}$) for the mixed phase alloy $Fe_{54}Ni_{26}Cr_{20}$ at a field of 0.6 tesla. The solid line is a guide to the eye. The peaks appear at its two transition temperatures (T_c and T_f). 180

5.13 M–H plot of the alloy with x=21 is scaled on to that of x=19 implying the same kind of magnetization process at 4.2 K. The abbrebiations, VSM and FB stand for vibrating sample magnetometer and Faraday balance, respectively. 183

5.14 (a) First, (b) second, and (c) third kinds of antiferromagnetic orderings in f.c.c. lattice, after [9]. 186

5.15 (a) Magnetic-ordering phase diagram in the γ_1–γ_2 plane for the antiferromagnetic f.c c. lattice, after [9]. (b) Θ/T_N and Θ/T_C vs. ϱ ($=\gamma_2/\gamma_1$) for the f.c.c. lattice. The marked point is the position of the studied x=14 alloy. 187

6.1 Temperature dependence of the normalized electrical resistivity of $(Cu_{0.36}Zr_{0\ 64})_{1-x}Al_x$ ($0 \leq x \leq 0\ 2$) amorphous ribbons. The resistivity is normalized with respect to that at 300 K. The resistivity at 300 K is shown in the inset as a function of Al concentration. 197

6.2 Temperature dependence of the normalized electrical resistivity of $(Ni_{0\ 5}\ Zr_{0\ 5})_{1-x}\ Al_x$ ($0 \leq x \leq 0.2$) amorphous ribbons. The resistivity is normalized with respect to that at 300 K. The resistivity at 300 K is shown in the inset as a function of Al concentration. 198

6.3 Plot of normalized resistance $(\rho(T)/\rho(10K))$ versus T for $(Cu_{0.36}Zr_{0\ 64})_{1-x}Al_x$ ($0 \leq x \leq 0.2$) amorphous alloys each of which shows onset of superconducting transition. The inset shows $d\rho/dT$ versus T of x=0.0 alloy from which the T_c is estimated to be 1.7 K. 200

6.4 Plot of normalized resistance $(\rho(T)/\rho(10K))$ versus T for $(Ni_{0\ 5}Zr_{0\ 5})_{1-x}Al_x$ ($0 \leq x \leq 0.2$) amorphous alloys each of which shows onset of superconducting transition. The inset shows excellent fit with *EEI theory* (Eq.(6.3)) for x=0.05 alloy. A strong deviation from the fit is observed below 5 K because of the superconducting fluctuations. 201

6.5 Plot of $\Delta\sigma$ vs $\sqrt{T}$ for $(Ni_{0.5}Zr_{0\ 5})_{1-x}Al_x$ alloys and the best-fitted straight lines (Table 6.2) in the range of 1.2 to 15 K, showing linearity (Table 6.2) as predicted by the *EEI theory*. The inset shows the same for $(Cu_{0\ 36}Zr_{0\ 64})_{0\ 8}Al_{0\ 2}$ alloy. 207

6.6 (a) Diffusive paths of a conduction electron in a disordered system. The electron with two time reversal partial waves propagates in both directions (full and dashed lines). (b) The classical probability distribution of a diffusing electron (full curve) which starts at r=0 at time t=0. In quantum diffusion (dashed peak) it is twice whereas in the presence of large spin-orbit scattering (dot peak) it becomes half of the classical case 209

6.7 Linear dependence of $\Delta\sigma$ on T in the intermediate range (Table 6.3) for $(\mathrm{Cu}_{0.36}\mathrm{Zr}_{0.64})_{1-x}\mathrm{Al}_x$ amorphous alloys as predicted by the localization theory. 212

6.8 Linear dependence of $\Delta\sigma$ on T in the intermediate range (Table 6.3) for $(\mathrm{Ni}_{0.5}\mathrm{Zr}_{0.5})_{1-x}\mathrm{Al}_x$ amorphous alloys as predicted by the localization theory. 213

6.9 Linear dependence of $\Delta\sigma$ on $\sqrt{T}$ in the high-temperature range (Table 6.3) for $(Cu_{0.36}Zr_{0.64})_{1-x}Al_x$ amorphous alloys as predicted by the localization theory. 214

6.10 Linear dependence of $\Delta\sigma$ on $\sqrt{T}$ in the high-temperature range (Table 6.3) for $(Ni_{0.5}Zr_{0.5})_{1-x}Al_x$ amorphous alloys as predicted by the localization theory. . 215

6.11 Plot of ln($\Delta\sigma$) vs ln T for $(Cu_{0.36}Zr_{0.64})_{1-x}Al_x$ amorphous alloys depicting three distinct regions of $\sqrt{T}$, T and $\sqrt{T}$ dependence in agreement with QIE 217

6.12 Plot of ln($\Delta\sigma$) vs ln T for $(Ni_{0.5}Zr_{0.5})_{1-x}Al_x$ amorphous alloys depicting three distinct regions of $\sqrt{T}$, T and $\sqrt{T}$ dependence in agreement with QIE. Only raw data are shown in Figs. 6.7-6.12. 218

6.13 Plots of the normalized resistivity ($\rho(T)/\rho(300K)$) and the fit to Eq.(6.8) as a function of T for $(Cu_{0.36}Zr_{0.64})_{1-x}Al_x$ amorphous alloys. 221

6.14 Plots of the normalized resistivity ($\rho(T)/\rho(300K)$) and the fit to Eq.(6.8) as a function of T for $(Ni_{0.5}Zr_{0.5})_{1-x}Al_x$ amorphous alloys. 222

6.15 Al concentration dependence of thermopower divided by temeperature (S/T) near 300 K for (a) $(Cu_{0.36}Zr_{0.64})_{1-x}Al_x$ (b) $(Ni_{0.5}Zr_{0.5})_{1-x}Al_x$ (c) $(Ni_{0.67}Zr_{0.33})_{1-x}Al_x$ and (d) $(Ni_{0.64}Zr_{0.36})_{1-x}Al_x$ metallic glasses. 224

Chapter 1

Preamble

"Magnetism in Solids" is a subject which continues to draw attention because of its technological importance. It also challenges the ingenuity of both experimental and theoretical condensed matter physicists. Magnetism is a fascinating subject by itself and has some role to play in virtually every branch of *Science and Technology.*

Before a few decades, "Magnetism in Solids" was thought to be an orderly subject. In spite of having several disputes about the microscopic origin of different types of magnetic behaviour at that time, only five basic types of magnetic order were distinguished in the realm of magnetism. These are diamagnetism, paramagnetism, ferromagnetism (FM), antiferromagnetism (AFM) and ferrimagnetism. It had been established that, apart from closed shell diamagnetism and the diamagnetism and paramagnetism of conduction electrons, magnetic behaviour comes from permanent, microscopic magnetic moments, possessed by some or all the ions in a solid.

Later on an entirely new kind of theoretical and experimental activity involving (i) amorphous solids, in which no two atomic sites are equivalent and (ii) disordered alloys, in which different atoms occupy randomly the sites of a regular crystal lattice, created a lot of excitement in the *domain of "Magnetism in Solids"*. The subject has since then expanded from the original five types of magnetic behaviour to many more types, namely, mictomagnetic, asperomagnetic, sperimagnetic, metamagnetic, spin glass, cluster glass, superparamagnetic, etc..

Magnetic systems with competing interactions were first investigated four decades ago. Well known examples include the Ising model on the triangular lattice with AFM n.n. interactions studied by Wannier in 1950. Helical structure was discovered in the Heisenberg model with n.n. interactions independently by Yoshimori and Villain in 1959. However, extensive investigations in magnetic systems with competing interactions have really started with the concept of frustration introduced almost at the same time by Toulouse and Villain in 1977 in the context of spin glasses. Frustration was initially defined for Ising spin systems. It was later generalised to vector (Heisenberg) spin systems. Frustration is caused by competition of different kinds of interactions and / or by lattice geometry. In the case of frustrated vector spin systems, the ground state configuration is usually non-collinear. The ground state properties (degeneracy and symmetry) give rise to spectacular, and often unexpected behaviour at finite temperatures and are not yet well understood.

1.1 Frustrated spin system – spin glass

Most physical systems in condensed matter are *frustrated* in the sense that there usually exists several competing interactions, each favoring a different type of ordered state[1]. Such competition can often be revealed by changing a macroscopic parameter of the system (such as temperature, pressure, magnetic field, etc.) which serves to enhance the effect of a particular interaction and drives the system into a different ordered state. A number of examples can be cited for frustrating systems, namely, triangular lattice with AFM nearest neighbour interaction appearing to be the simplest example of *frustration caused by lattice-geometry*, spin glasses with frustrating bonds, etc. In frustrated systems, local minimization of energy is not compatible with global energy minimum (or minima).

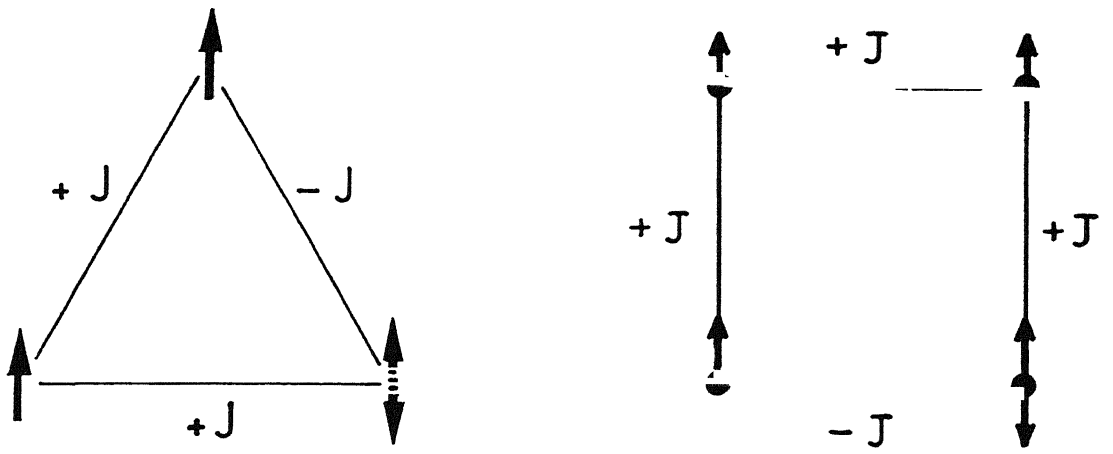

Figure 1.1: (a) A triangular lattice and (b) a rectangular plaquette of magnetic ions having up- or down-spin illustrate "frustration" (where no arrangement can satisfy all the microscopic constraints).

1.1.1 What is a spin glass ?

Generally speaking, spin glass is a new magnetic state of a system where the spins of the magnetic ions (impurities) become locked or "frozen" into random orientations below a characteristics temperature, T_{SG}, known as the spin - glass transition temperature.

To understand the frozen configuration let us imagine a triangular lattice or a rectangular plaquette (Figs.1.1 (a) and (b)), each vertices of which are occupied by a magnetic spin.

If the exchange parameter J between any two spins could be both positive and negative there is no arrangement that satisfies all the microscopic constraints. The system is thus frustrated. With such a simple picture one can visualize the ground or frozen state (T=0 K) of a spin glass. Its basic ingredients are *randomness (here it is the site occupancy), mixed interactions, and frustration (many possible ground state configurations).* So, we may define a spin glass as a random, mixed-interacting, magnetic system characterized by a random, yet co-operative freezing of spins at a well–defined temperature T_{SG} below which a highly irreversible, frozen state occurs without any long-range spatial magnetic order.

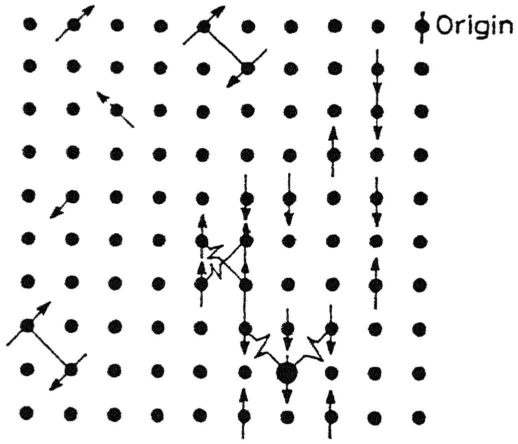

Figure 1.2: A frozen spin glass with $J_1 > 0$ (ferromagnetic) and $J_2 < 0$ (antiferromagnetic). The zig-zag links indicate a broken bond; the spin at the heavy circle is frustrated.

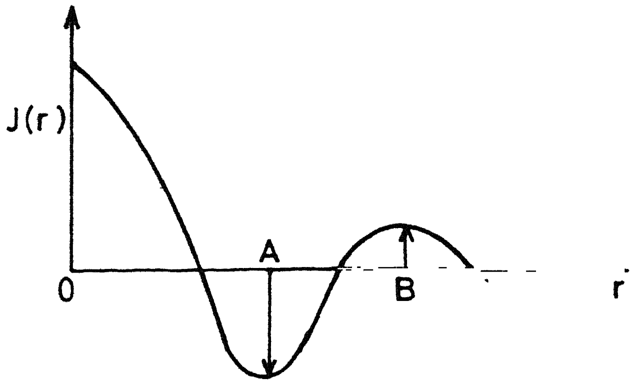

Figure 1.3: The RKKY interaction J(r) between two magnetic impurities in a metal as a function of their separation r.

Figure 1.2 depicts a frozen spin glass with $J_1 > 0$ (first nearest neighbour interaction is ferromagnetic) and $J_2 < 0$ (second nearest neighbour interaction is antiferromagnetic). The zig-zag links indicate a broken bond and the spin at the heavy circle is frustrated.

How to introduce randomness ?

Randomness in any system can be introduced mainly in two ways, namely, (i) site randomness and (ii) bond randomness.

(i) Site randomness :

In noble metal hosts like Au or Cu, when transition metals with 3d-electrons like Fe or Mn are substituted one encounters first the **Kondo** or non-interacting regime, where the 3d-electrons of the magnetic ions interact antiferromagnetically with the conduction electrons. At low temperatures, the extremely dilute (isolated) magnetic ions become non-magnetic and enhances the electron scattering cross section giving rise to resistivity minima. With the addition of more magnetic ions in the noble metal matrix, the magnetic ions, via the conduction electrons, start interacting through the **RKKY** indirect exchange $[J_{ij}(r_{ij}) \sim \frac{cos(2K_F r)}{r^3_{ij}}]$ whose magnitude and sign depend on the distance between the magnetic ions as shown in Fig.1.3.

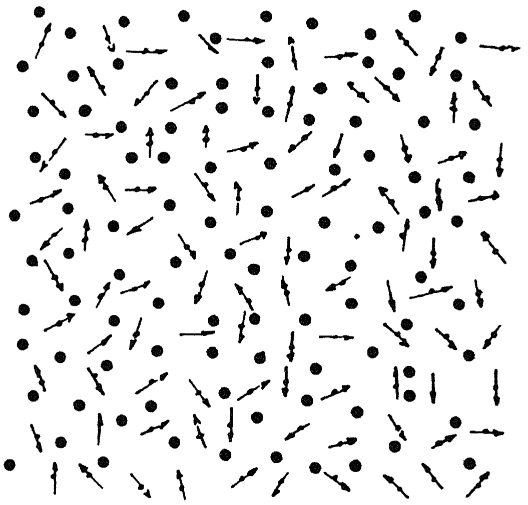

Figure 1.4: An amorphous spin glass for which the disordered lattice sites are 50% occupied by magnetic moments.

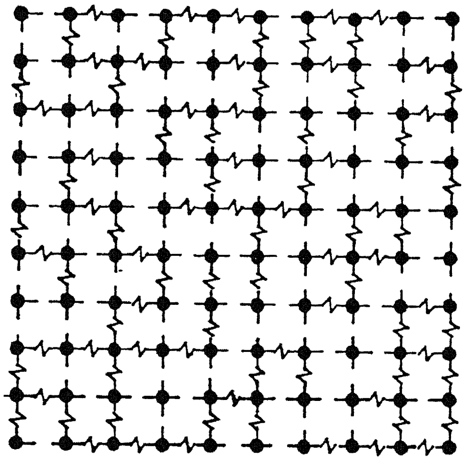

Figure 1.5: A random-bond spin glass where – implies FM coupling and – – implies AFM coupling. The number of FM bonds is equal to the number of AFM ones [ref.3].

Beyond a certain concentration of magnetic impurities, a good moment is stabilized and the canonical spin-glass (the name is due to B. R. Coles) phase is formed. Site substitution of magnetic solute for non-magnetic solvent occurs completely randomly (without any short-range order). Here the random-site occupancy introduces randomness in the alloy.

Figure 1.4 shows an amorphous spin glass, a typical example of site randomness. AuFe(1-10 at. % Fe), CuMn(1-10 at. % Mn), AuCr, AgMn, $Eu_xSr_{1-x}S$ (a semiconductor), $La_{1-x}Gd_xAl_2$ (a metal), etc., a plethora of systems have made spin glasses a general and a rather common type of magnetic ordering.

(ii) Bond randomnes :

Now let us assume that the magnetic interaction is only between nearest neighbours (short range) and imagine that this single coupling J alternates randomly in sign with $\pm J_{ij}$ values as we move through a lattice. Thus there are only parallel or anti-parallel bonds as illustrated by dash or zig-zag in Fig.1.5. This is a random-bond type of system and it was only recently unearthed in real materials (e.g., $Rb_2Cu_{1-x}Co_xF_4$ and $Fe_{1-x}Mn_xTiO_3$).

So, in a nutshell : there must be frozen disorder in the constitution of a spin glass, either site randomness or bond randomness and these together are called **quenched disorder.**

In the frozen state of a spin glass below T_{SG}, irreversible magnetic effects, non-exponential relaxation of time-dependent magnetic properties, broken ergodicity are some of the salient features. The frozen spin states are the consequence of the existence of multivalleys (a number of local minima) in the phase space - free energy domain. If the energy barrier between the free energy multivalley becomes infinite then

$$< quantity\ \psi\ measured\ by\ experiment >_{time} \neq < \psi >_{unrestricted\ ensemble}$$

The above inequality is a consequence of the fact that the measuring time scale (τ_{exp}) $\ll$ the maximum time for the frozen system to be in one of its local free energy minima (τ_{max}). Moreover, as N (number of spins) $\rightarrow \infty$, $\tau_{max} \rightarrow \infty$. Binder and Young[2] and Mydosh[3] have given complete reviews of spin glasses.

From literature survey it is clear that the experiments on spin glasses could be broadly divided into two classes, one of them exhibits sharp anomaly at T_{SG} while the other shows a smeared behaviour around T_{SG}. Figures 1.6 (a)-(c) show the various experimental results on spin glasses. These are the manifestations of the irreversible effects, time-dependent magnetic properties and the effect of measurement time on the spin freezing. Figure 1.6 (d) shows the simplified illustration of magnetic spins at different times in various magnetic phases at T=0.

Sharp Anomaly :

(1) Sharp cusp in low-field magnetic susceptibility (χ_{ac}) at T_{SG}[2], (2) Irreversible magnetic behaviour below T_{SG}, a large magnetic after-effect and an increase in the coercive force and remanent magnetization on cooling below T_{SG}[2], shift of magnetization curve along the H-axis with small hysteresis[4], (3) Splitting in Mössbauer spectra indicating the presence of static hyperfine fields below T_{SG}, (4) μSR depolarization, (5) Anomalous Hall effect, (6)

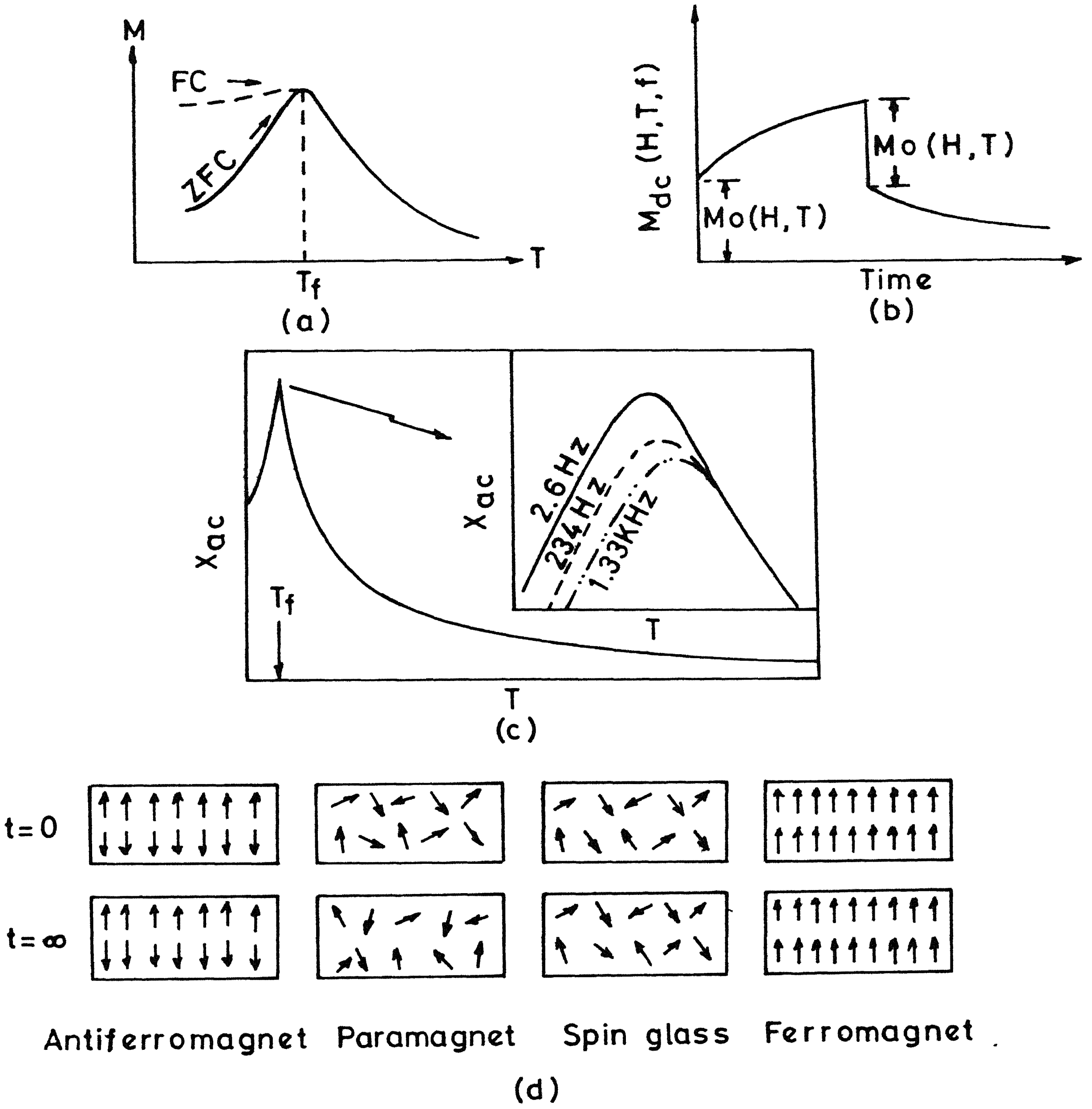

Figure 1.6: (a) Reversible and irreversible magnetization vs temperature for a spin glass. (b) Time-dependent magnetization of a spin glass. (c) Frequency - dependent ac-susceptibility vs temperature of a spin glass. (d) Simplified illustration of magnetic spins at different times in various magnetic phases at T=0.

Negative magnetoresistance ($\frac{\Delta\rho}{\rho} \propto -H^2$)[5], and (7) Logarithmic (slow) time dependence of magnetization (magnetic viscosity) given by $M = M_0 - S\ lnt$.

Smeared behaviour :

(1) Resistivity[3], (2) Specific heat[6], (3) Thermo power, (4) NMR, and (5) Ultrasonic velocity.

In 1975 Edwards and Anderson had proposed a model introducing an order parameter q, defined as

$$q = lim_{|t_2 - t_1| \to \infty} \overline{< S_i(t_1) S_i(t_2) >} \tag{1.1}$$

which shows a time-dependent correlation of individual spins at a particular site. The spin-glass phase is different from the PM and the FM phases in the following way :

PM	**SG**	**FM**
$q = 0$	$q \neq 0$	$q \neq 0$
$m =< S_i >= 0$	$m =< S_i >= 0$	$m =< S_i > \neq 0$

Edwards and Anderson proposed a Hamiltonian

$$\mathcal{H} = -\Sigma_{ij} J_{ij} S_i S_j - \Sigma_i H_i S_i \tag{1.2}$$

for the SG introducing disorder by suitable distribution

$$P(J_{ij}) = [2\pi(\Delta J_{ij})^2]^{-1/2} exp\left[\frac{-(J_{ij} - \overline{J_{ij}})^2}{2(\Delta J_{ij})^2}\right]. \tag{1.3}$$

The Sherrington-Kirkpatrick (SK) model is the infinite range version of the Edwards-Anderson model, assuming that the same distribution P(J_{ij}) holds for any pair of spins irrespective of their distance. Later on a lot of other theoretical treatments, namely, Thouless-Anderson-Palmer (TAP) approach[7], Parisi's replica symmetry-broken solution of the SK model[8], droplet model[9], fractal-cluster model[10], etc. have also attracted considerable attention.

In recent times the mathematics involved in the above models of spin glasses are being extensively used in models for biological evolution[11], neural-network computations[12], polymers, etc.

1.2 Frustrated spin system – Reentrant spin glass (mix -ed phase)

The introduction of random disorder in a magnetic system can generate frustration via a competition between FM and AFM exchange couplings. Theoretically it can be shown that in a FM with weak random frustration, the Curie temperature, T_c, decreases with increasing disorder up to a certain level where the random bond frustration is so strong that the system cannot accomodate a percolating FM ground state. However, such strongly disordered tuned system often exhibits a spin-glass transition : the spins freeze cooperatively in a non-trivial pattern that is random in space with no delta function magnetic Bragg peak[2, 13–15].

As mentioned in the earlier section, with the increase of magnetic impurity (Fe, Mn etc. (1-10%)) beyond the Kondo regime in a noble-metal host (Au, Cu, etc.) the system moves towards the canonical spin-glass regime with randomly frozen spins below T_{SG}. With further increase (10-15%) in the concentration of magnetic impurities there is a greater chance that any of them could become the 1st or the 2nd nearest neighbour of any other impurity. Consequently, there is a short-range RKKY like interaction which can strongly couple neighbouring impurities ferromagnetically or antiferromagnetically depending upon the particular magnetic element involved and their positions. Accordingly, magnetic clusters can form as a result of concentration fluctuations in a random alloy. This is called mictomagnetic or cluster-glass phase of the system where the magnetic behaviour is dominated by such clusters. As the concentration increases further, the size of such clusters increases and beyond a percolation threshold of infinite FM clusters, a long-range order generally sets in. However, very near to the percolation threshold for long-range FM ordering a strange situation is encountered. The spin-glass ordering does not simply disappear but continues to the FM phase. There have been

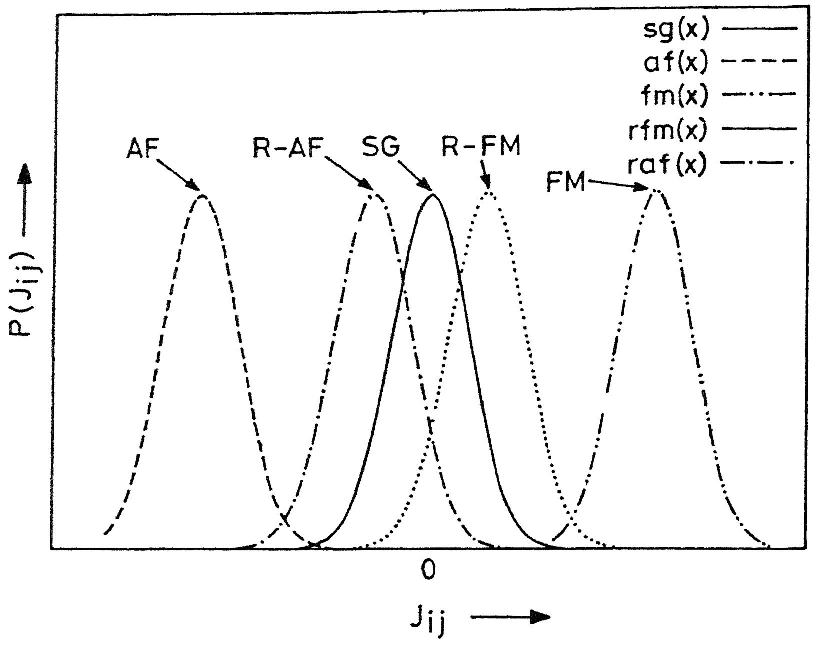

Figure 1.7: Gaussian distribution of exchange integrals according to the idea of Sherrington and Kirkpatrick [26].

a lot of experimental reviews[16–18, 20, 46] where it has been found that all these classes of systems show double magnetic transition [e.g., $Au_{82}Fe_{18}$, FeAl, PdMn, NiMn, FeNiMn, etc.].

At high temperatures such a system is in a PM phase and as the temperature is lowered to T_c or T_N (Neél temperature), the system enters a FM or an AFM phase where long-range order exists. As the temperature is lowered further the system, below a certain temperature, enters a new phase which is called the "re-entrant phase" or mixed phase.

The terminology "re-entrant spin glass" is somewhat misleading since the system does not re-enter a spin-glass phase at low temperatures. It was a paramagnet, and not an SG at higher temperatures. However, the system does re-enter a state which is magnetically less ordered at low temperatures, viz, the spin-glass phase. The above sequence of phase transitions implies that the SG phase has the lowest energy while the FM phase has more entropy which is rather counterintuitive. This is probably the main motivation behind the research efforts devoted to understand the problem of re-entrant spin glasses over the last decade.

A number of recent experimental investigations, namely, magnetization and χ_{ac}[21], neutron diffraction[22], neutron depolarization[23], Mössbauer spectroscopy[24], μSR experiments [25], etc. have thrown lot of light on this long-debated re-entrant SG phase.

Theoretically, the Sherrington-Kirkpatrick (SK) model, taking infinite range Ising interaction into account (in the concentrated range) and employing Edwards-Anderson mean-field Hamiltonian (H) and Gaussian probability distribution of random variables (J_{ij}), can successfully predict the double magnetic transition. In Fig.1.7, the Gaussian distribution of exchange integrals, according to the idea of Sherrington and Kirkpatrick[26], is shown.

However, the original SK solution of the model suffers from the following serious drawbacks:

1. The solution of it gives a negative entropy at sufficiently low temperatures.
2. The solution obtained does not correspond to a minimum of the free energy though it is an extremum.
3. In real systems there is no infinite range exchange interactions represented by the constant J_{ij} (as assumed in the SK model).

Gabay and Toulouse[27] (GT) have theoretically shown that the co-existence of SG and FM orderings is possible below the second transition within the framework of the SK model with m-component spins. They used the usual replica trick and found that for $m \neq 1$, there are two mixed phases M_1 and M_2 in the transition region from the SG to the FM order. The phase diagram obtained by Gabay and Toulouse is shown in Fig.1.8.

In the infinite range model the position of the ferromagnetic (FM) to the mixed phase (M_1) transition line $T_1(J_0)$, in the vicinity of the multicritical point, is given by

$$1 - T_1 \approx \frac{1}{2}\frac{m+4}{m+2}(J_0 - 1)^2, \; for \; J_0 \geq 1 \tag{1.4}$$

where J_0 is the mean value of the Gaussian probability distribution. For large J_0, T_1 vanishes asymptotically.

The mixed phase M_2 has the same co-existence of orderings as the phase M_1 and in addition has the spontaneous breaking of replica symmetry. For general m, the transition line between

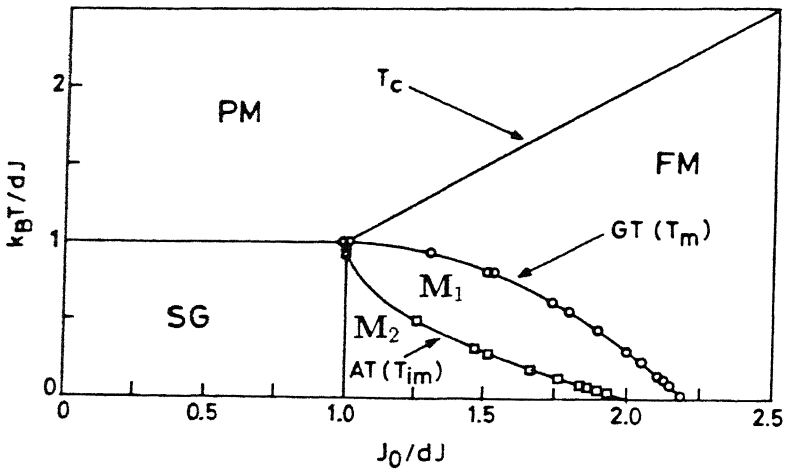

Figure 1.8: Magnetic phase diagram for vector spins interacting with infinite-range Gaussian distribution in the T - J_0 plane according to de Almeida and Thouless (AT) and Gabay and Toulouse (GT). M_1 and M_2 represent mixed magnetic phases of the re-entry transition.

the two mixed phases M_1 and M_2, defined by $T = T_2(J_0)$, behaves in the vicinity of the multicritical point according to

$$1 - T_2 \simeq \left(\frac{m+2}{2}\right)^{1/2} (J_0 - 1)^{1/2}, for\ J_0 \geq 1. \tag{1.5}$$

Later, Cragg, Sherrington and Gabay[28] contradicted the above result for vector spin glass in a magnetic field because replica symmetry breaking occured simultaneously with the transverse spin-glass-like ordering although the longitudinal irreversibility was weaker than the transverse irreversibility and a crossover to strong irreversibility took place at a lower temperature. Later on the demarkation line between the FM and M_1 phases was named the GT-line and that between M_1 and M_2 phases the AT-line (De Almeida–Thouless). At the 1st transition temperature T_{GT} (M_1), the transverse SG order parameter becomes non-zero but the phase remains replica symmetric. Below T_{AT} there is a cross over to strong irreversibility due to replica symmetry breaking. This transition is identical to the AT-line for the Ising case[29]. In the Ising limit, the GT-line disappears since there are no transverse degrees of freedom and the AT-line reduces to that for the SK model.

From the results of several experiments it is strongly suggested that a large number of FM's exhibiting RSG behaviour display a spin-freezing of the transverse spin component perpendicular to the direction of the intradomain magnetization established at T=T_c. Such a behaviour is compatible with the predictions of the mean-field-theory for 3d-Heisenberg spin glasses (GT-model).

However, further work on both theoretical and experimental fronts is needed to confirm the kind of magnetization that exists in the so-called re-entrant or mixed phase system. Suggestions of mixed phase were proposed even before Gabay and Toulouse[27] by Villian[30] who termed it as a *semi-spin glass* and Mookerjee[31] who named it as a canted random FM. A model proposed by Van enter and Van Hemmen suggests that the competition between the FM nearest neighbour interaction and the long-range AFM interaction leads to spin–canting at a temperature lower than the FM transition temperature.

1.3 Studies of 3d-transition metal alloys

1.3.1 Magnetism

Magnetism of 3d transition metal alloys is still of great interest because no unique theory has emerged which could explain by and large all experimental results. None of the two extreme models, namely, the Heisenberg theory of localized spins and the Stoner's itinerant electron model are successful in that sense. A lot of effort[32, 33] has been put in to find an unified theoretical model making a compromise between these two extreme ones.

In recent years, there have been a lot of theoretical effort to understand the nature of magnetism and the magnetic band structure of 3d transition metals and their binary alloys. A number of approaches and techniques have been employed, namely, local density approximation (LDA), coherent potential approximation (CPA) and cluster coherent potential approximation (CCPA) with Korringa, Kohn and Rostoker (KKR) formalism, local–spin–density calculation (LSD), linear muffin-tin orbital(LMTO), fixed-spin-moment (FSM), finite temperature theory of local environment effect (LEE) on Fe-Co binary alloys[34], density functional theory (DFT)[35], etc.. The local density calculation, taking into account all effects of electron exchange and correlation, correctly describes itinerant magnetism of 3d transition metals and alloys with non-integral values of spins. Electronic and magnetic band structure calculations for itinerant systems have become very promising.

No real system behaves exactly like either of the above two models. Magnetism in 3d transition metals and alloys is itinerant, but it does have some aspects of localization[36]. The orbital moment does not vanish completely in these systems. It has been found from different experiments[37] that not all 3d–3d alloys follow the Slater-Pauling curve (e.g., Ni-Cr, Ni-V, etc. alloys) which is mainly because of the formation of virtual bound states above the Fermi level as suggested by Friedel[38]. These are due to the presence of strong perturbations around the impurities (e.g., Cr or V in Ni host) resulting in splitting up of an impurity state above the Fermi level. Neutron scattering experiments in a series of Ni-based alloys[39] have demonstrated the correctness of Friedel's prediction of strong magnetic disturbances associated with impurities of transition metals. Low and Collins[39] first found that around Fe and Mn impurities in Ni matrix the moment disturbances are effectively confined to the solute atom site, whereas V or Cr impurities markedly reduce the magnetic moment on neighbouring Ni atoms.

In magnetic materials (either crystalline or amorphous), a random mixture of ferromagnetic (FM) and antiferromagnetic (AFM) bonds having strongly competing interactions between them (in Heisenberg picture), may lead to a diversity of magnetic structures at low temperatures. There could be a critical concentration range where FM and AFM exchange contributions to the free energy are equal. The ground state in this concentration range may be imagined as a spin-glass (SG) state with short-range FM and AFM orders. In recent years attempts have been made to go beyond the mean-field approximation and develop a theory of spin glass with a finite range of interaction[40]. Far away from critical concentration a long-range (FM and AFM) magnetic ordering generally sets in (e.g., Fe–Ni, Ni–Mn, Fe–Ni–Mn, Fe–Cr, Au–Cr, etc).

In the vicinity of a multicritical point, there is a subtle interplay between the long-range magnetic ordering and the randomness of the SG state. There could also be a particular regime near the critical concentration which may exhibit double magnetic transitions, one at a higher temperature T_c (PM→FM) and another (FM→Mixed FM and SG) at a lower temperature T_f. These are called mixed or re–entrant phase alloys (e.g., Au–Fe, Fe–Cr, Ni–Mn, Al–Fe, Fe–Ni–Mn, Cr–Fe, etc.). Re–entrant transition from an AFM state has been observed in $FeMgCl_2$ and Mn–rich CuMn binary alloys[41, 42]. The existence of sequential (double) magnetic phase transitions in FM's with substantial degree of exchange bond disorder continues to be a topic of considerable interest. During the last decade, re–entrant SG transitions have been investigated extensively both theoretically[2, 27, 30] and experimentally[43–48] by means of different techniques including not only the bulk magnetic measurements but also other methods probing the magnetic structure on a microscopic scale (e.g., small-angle neutron scattering and neutron depolarization studies[49, 50], Mössbauer studies[51, 52], electron spin resonance, μSR, etc.). However, the exact nature of the re–entrant transition is still unclear and highly controversial because of several debatable questions like :
What is the nature of magnetization in the so-called FM phase ($T_f \leq T \leq T_c$) for this kind of alloys ? What happens to it in the re–entrant or mixed phase ($T<T_f$)? Does the long-range FM ordering coexist with the SG ordering or is it a pure SG phase due to random freezing of spins at a temperature $T<T_f$? What are the physical origins of the field and temperature dependence of the bulk magnetization M(T,H) near and below T_f ?

In the light of the mean-field models of Heisenberg (3d vector spins) systems, Gabay and Toulouse[27] (GT) theoretically predicted the most plausible nature of magnetic transitions in mixed phase alloys. According to them, a sequence of three kinds of magnetic transitions are possible with decreasing temperature which are (i) PM→FM followed by (ii) a transition (crossing GT–line) to a mixed phase where FM state coexists with transverse SG ordering (say, in x-y plane) because of the random freezing of spins and a longitudinal long-range FM ordering with spontaneous magnetization in the direction of broken symmetry (say, z-axis) and (iii) a crossover from weak to strong irreversibility (crossing the AT-line). Magnetic phase diagrams of such systems ($(Pd_{1-y}Fe_y)_{1-x}Mn_x$[53], AuFe[43], Fe-Cr, Ni-Mn, $EuSr_{1-x}S_x$, Fe-Ni-Mn[44], etc) exhibit features which bear resemblance, atleast superficially, to the prediction of the vector-mean-field model proposed by Gabay and Toulouse.

However, no rigorous experimentally accessible criterion is currently available for assessing the genuine cooperative nature of the mixed phase transitions. Moreover, recently there are some reports on intermetallic compounds $CeFe_2$[54, 55], UCu_2Ge_2[56], etc. which reveal that all these systems undergo transitions from a long-range FM state at a higher temperature to an AFM state at a lower temperature via a canted phase. They show almost the same features as the so-called re-entrant or mixed phase systems. The interpretation of such types of magnetic phase transitions is sought within the model put forward by Morya and Usami[57] for itinerant system of electrons with strong correlation.

1.3.2 Electrical transport – Resistivity :

Transport properties, specially the variation of electrical resistivity with temperature in substitutionally highly disordered crystalline materials (with short electron mean free path) are still of interest because of the lack of complete understanding of the mechanisms involved despite intense theoretical efforts. In a disordered metallic alloy, the electrical transport mainly depends on $k_F l$, where l is the mean free path and k_F is the Fermi wave vector of the conduction electrons. The alloys in the dilute limit generally have $k_F l \gg 1$ and the electronic states still remain extended (long mean free path) throughout the sample[58]. It is assumed that in these alloys Mathiessen's rule holds, the various scattering frequencies are additive and the Boltzmann transport is still valid.

However, in the case of alloys in the weak-disorder limit with large values of electrical resistivities (with short electron mean free path and $k_F l \sim 1$ which is the *Ioffe - Regel*[59] criterion), the simple Boltzmann transport breaks down . The proposed universal *Mooij correlation*[60] has become almost a rule for these kinds of highly resistive crystalline or amorphous materials, though large discrepancies are found in some cases. According to Mooij, the correlation between the temperature coefficient of resistance (TCR) and the resistivity at room temperature (ρ_{rt}), the deviation from linearity (DFL) of resistivity at high temperatures and the resistivity minimum at low temperatures must have a common origin. At very low temperatures the quantum interference effects become important and as a consequence electron localization and electron - electron interaction (many-body effects) give quantum corrections to the conductivity of highly resistive materials[61]. At high temperatures, the deviation from linearity (DFL) of the resistivity leads to the so-called "resistivity saturation" and violates the simple Mathiessen's rule as well as the Bloch - Grüneisen theory. This happens in the case of many highly resistive (weak-disorder limit) materials[62, 63] as well as in intermediate T_c, d-band alloys (e.g., Nb_3Ge, Nb_3Sn, Nb_3Al, etc.) and rare earth superconductors[64, 65] (e.g., $Y_{5-x}Dy_xOs_4Ge_{10}$, $Sc_{5-x}Dy_xIr_4Si_{10}$, etc.). Over the years, despite lot of efforts been put to understand this phenomenon theoretically[66–72] and experimentally[62–65, 73–75], a quantitative , microscopic theory is still far from being developed.

In the case of disordered magnetic materials (specially the 3d transition metal alloys) the situation is much more difficult. Detailed quantitative study of concentrated magnetic systems is still not common. Electronic transport of magnetic alloys is very difficult to interpret because of the possibility of involvement of several scattering mechanisms compared to the case of simple metals. However, there are some extensive studies of electrical transport on noble metal - transition metal alloys, e.g., AuFe[76], CuMn[42], AuCr, AuMn, etc., in the spin-glass (SG), mictomagnetic or cluster - glass and in the long-range ferromagnetic (FM) or antiferromagnetic (AFM) phases beyond the Kondo or dilute non-interacting regime. Sufficient attempts had been made to find out the nature of impurity scattering due to magnetic ions in noble-metal host for the entire regime. Despite a number of studies of electrical transport in transition metal - transition metal alloys (e.g., CrFe, NiMn[77], NiMnPt[78], CrMn, CrMnV, etc.), a concrete picture of the magnetic contribution to the resistivity is yet to emerge.

Theory of electrical resistivity

It is very difficult to provide an exact theoretical description of the temperature dependence of resistivity of the alloys under investigation due to the following reasons. First of all, no theory has been developed so far which can describe the band structure as well as the spin structure of these kinds of 3d transition metal alloys. Moreover, a complete theory of disordered ternary alloys containing 3d transition metals is still awaited. In concentrated disordered magnetic alloys, the electron transport is much more difficult to understand because of the involvement of a large number of complicated scattering mechanisms and hence the validity of Matthiessen's rule as well as the theory of classical Boltzmann transport could be questioned. In the case of simple metals and alloys in the dilute limit where the Boltzmann transport is valid, generally in addition to the temperature – independent static disorder residual resistivity (ρ_0) contribution from impurity scattering, a major contribution to the temperature dependence of resistivity comes from the electron - phonon scattering. The well-known *Bloch - Grüneisen* formula[79] was developed to account for this electron - phonon interaction and is given by

$$\rho_{e-p}(T) = A \left(\frac{T}{\Theta_D}\right)^5 \int_0^{\frac{\Theta_D}{T}} \frac{z^5 dz}{(e^z - 1)(1 - e^{-z})}, \tag{1.6}$$

where A is a temperature - independent constant and Θ_D is the Debye temperature. At very low (T $\ll \Theta_D$) and high (T $\geq \Theta_D$) temperatures this electron - phonon scattering contribution [ρ_{e-p}] goes as T^5 and T, respectively which have been observed in many metals and alloys[80, 81].

In 3d transition metals and alloys the situation is not as simple. The scattering of the conduction s-electrons by phonons and the interaction with magnetic spin systems (spin-disorder resistivity) are the main sources of the temperature dependence of resistivity[79–81]. Generally, in both these cases the scattering may take place within a single band (s-s) or may involve s-d transitions. One of the earliest proposals to account for the resistivity variation with temperature of the transition metals due to electron - phonon scattering, in the presence of s-d interaction, was made by Wilson[82] and is given by

$$\rho_{sd}(T) = B\left(\frac{T}{\Theta_D}\right)^3 \int_0^{\frac{\Theta_D}{T}} \frac{z^3 dz}{(e^z - 1)(1 - e^{-z})}, \tag{1.7}$$

which goes as T^3 at low temperatures and as T above Θ_D. Thus, the temperature exponent at low temperatures can be expected to vary from 3 to 5 for the transition metals depending on the shapes and locations of the Fermi surface of the s and d bands. The exponent was found in various transition elements[83] to lie between 2.0 to 5.3.

Turov[84], Kasuya[85, 86], Mannari[87] and Goodings[88] had shown that the spin-wave treatment in the presence of s-s and s-d interactions can lead to a T^2 contribution to the spin-disorder resistivity (ρ_{mag}) at low temperatures for ferromagnetic metals. Based on the spin-wave dispersion relation $E_q = \mathcal{D}\, q^2$, Kasuya gave an expression for the spin-disorder resistivity

$$\rho_{mag}(T) = \frac{\pi^3 \mathcal{V} m \mathcal{G}_{s-d}^2}{8\mathcal{N} e^2 \hbar E_F}\,(g-1)^2\, j\left(\frac{kT}{k_F^2 \mathcal{D}}\right)^2, \tag{1.8}$$

where $\mathcal{G}_{s-d}$ is a parameter which describes the strength of the s-d interaction, g the Landé g factor, j the total quantum number of each magnetic atom, E_F the Fermi energy of the conduction electrons, $\mathcal{D}$ the spin-wave stiffness constant and $\mathcal{V}$ and $\mathcal{N}$ are the volume and the number of atoms in the crystal, respectively. Exactly the same kind of result was obtained using a slightly different method by Mannari[87]. He estimated ρ_{mag} for Ni and found excellent agreement with the experimental results obtained by White and Woods[83] for the case of Fe, Co, and Ni (where $\rho = (13 - 16) \times 10^{-6}\, T^2\, \mu\Omega$ cm) in the low – temperature range.

Besides these, another source of electrical resistance in transition metals and alloys arises from the collisions of the s-electrons with the charge fluctuations of the itinerant d-electrons. Here a T^2 dependent contribution, non-magnetic in origin, may appear in resistivity in the low temperature range as predicted by Baber[89, 90].

In any highly resistive alloys, the high temperature DFL of resistivity, which is the signature of resistivity saturation[91], is an interesting topic to focus on. Cote and Meisel[66] proposed a model which is referred to as the "phonon-ineffectiveness" model to interpret this downward DFL of resistivity in the case of highly resistive materials at high temperatures. This was based on the assumption that the electrons with very small mean free paths l effectively exclude long-wavelength phonons from contributing to the electron-phonon scattering at high temperatures The effects of such lower cut-off of the wavenumber were evaluated and considering only the phonons with wavenumber between $2\pi/l$ and q_D, they obtained a limiting resistivity when the electron mean free path l is of the order of the inter-atomic spacing. Taking the Debye-Waller factor to be 1, the electrical resistivity is given by

$$\rho(T) = \rho(0) + \left[1 - \frac{\rho(T)}{\rho_D}\right] C\,T\ , \tag{1.9}$$

where $\rho(0)$ is the measured residual resistivity and ρ_D is the saturation resistivity corresponding to $l = 2\pi/q_D$ and C is a constant. Here q_D is the lower cut off of the phonon wave number.

Fisk and Webb[62] observed experimentally this kind of DFL of resistivity in low T_c, A-15 superconductors (e.g., Nb_3Sn, Nb_3Sb, etc.). They, for the first time, used the term "resistivity saturation" in the case of highly resistive materials ($50 - 150$ $\mu\Omega$ cm) and interpreted this phenomenon qualitatively in terms of attainability of the electron mean free path l of its lowest possible value in the weak-disorder limit. This can be of the order of the interatomic spacing 'a' of the material ($l \sim$ a), according to the Mott[92] and *Ioffe - Regel criteria*[59] ($k_F l \sim 1$).

The most widely accepted model for the phenomenon of resistivity saturation in high-resistivity materials is the empirical "parallel-resistor" or "shunt-resistor" model first proposed by Wiesmann et al.[63]. They argued that in a disordered material, in addition to the usual Boltzmann conduction channel, there is an extra non-classical channel and these two act in parallel.

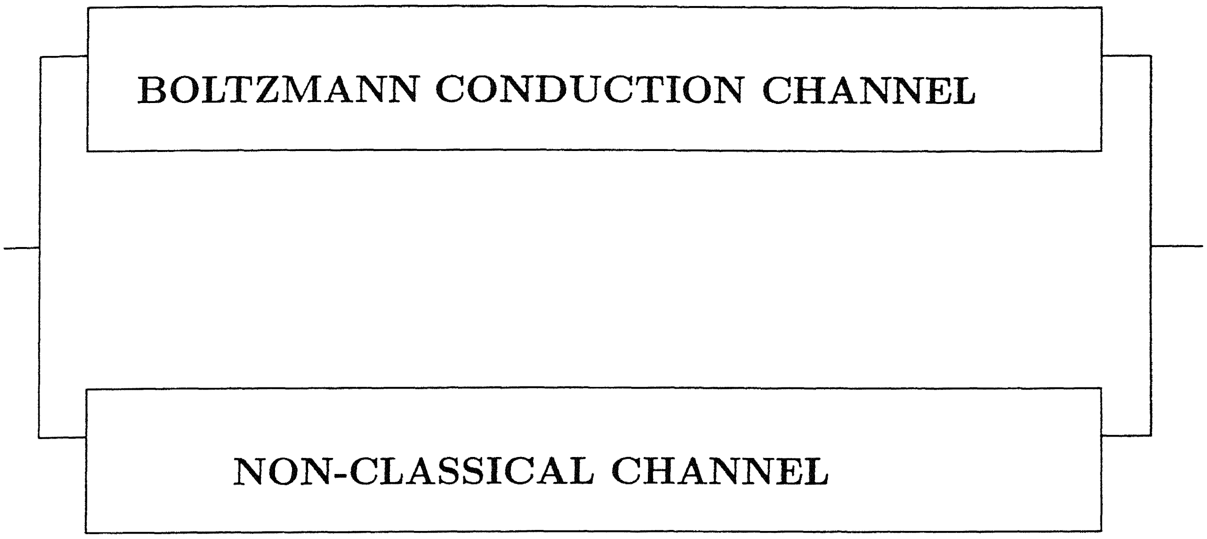

The total resistivity ρ (T) is given by

$$\frac{1}{\rho(T)} = \frac{1}{\rho_{ideal}(T)} + \frac{1}{\rho_{sat}} , \tag{1.10}$$

where

$$\rho_{ideal}(T) = \rho_{ideal}(0) + \rho_{ph}(T) \quad , \tag{1.11}$$

and

$$\rho_{ideal}(0) = \frac{\rho(0)\rho_{sat}}{\rho_{sat} - \rho(0)} \quad . \tag{1.12}$$

Here ρ_{sat} is the maximum limiting resistivity which is assumed to be independent of temperature and ρ (0) is the measured residual resistivity at T = 0 K. The ρ_{ph}(T) term is due to the electron-phonon interaction, the form of which can be assumed to be either the *Bloch-Grüneisen*[79] [Eq.(1.6)] or *Bloch-Wilson* [Eq.(1.7)] depending upon the behaviour of the system at low temperatures (T $\ll \Theta_{\mathrm{D}}$). Irrespective of the form chosen above, both of them vary linearly with temperature ($\approx$ T) at high temperatures (T$\geq \Theta_{\mathrm{D}}$). Several theories have thereafter appeared which tried to understand the physical origin of such a phenomenlogical shunt–resistor model. Among them the work by Allen et al.[67, 68], Gurvitch[70, 71], and Laughlin[69] can be cited. Gurvitch argued that the statistical distribution of relaxation times must have a lower cutoff (τ_o) and averaging over such a distribution had resulted in the parallel-resistor model (Eq.(1 10)) considering the *Ioffe–Regel*[59] criterion. Gurvitch[71] had shown that for different high resistivity metallic systems which show resistivity saturation, the *Ioffe–Regel* parameter ($k_F l$) lies between 3 and 6 instead of 1 if one assumes ($l \sim a$). In addition to that, the conductivities at saturation (σ_{sat}) of these alloys are much higher (10–30 times) as compared to the Mott's[92] *minimum metallic conductivity* ($\sigma_{min} = 0.026\ e^2 / \hbar\ a$) as seen in many metallic systems (e.g., metal-oxides) closer to the metal - insulator (M-I) transition and the relation is given by

$$\sigma_{sat} = (3\pi^2 n)^{2/3} a^2 \sigma_{min} \,, \tag{1.13}$$

where n is the density of electrons at the Fermi level and 'a' is the interatomic spacing.

Recently Ron[93] et al. have suggested an entirely different kind of model considering the effects of displaced ions on the conduction electrons to describe the DFL of resistivity at high temperatures. They have shown that the phenomenon of resistivity saturation can arise from the fact that the average ion displacement, at high enough temperatures, can exceed the wavelength of the electronic wavefunctions, while being still much smaller than the interatomic spacing. In this model, the electronic wavefunctions are extended, but may have short-length oscillations. Also, even in the dilute regime ($k_F l \gg 1$), saturation sets in long before the *Ioffe - Regel*[59] criterion comes into play. They obtained an expression for resistivity of the form

$$\rho(T) = \rho_m - D\ T_0\ exp\left[-\frac{T}{T_0}\right] \,, \tag{1.14}$$

where T_0 is a characteristic temperature, D a constant and ρ_m is the saturation resistivity. This model is especially suitable for the transition metals whose orbitals possess a large number of lobes, namely, the distance between the zeroes of the wavefunction is considerably smaller than the interatomic spacing.

1.3.3 Magneto-transport – Magnetoresistance :

The magnetoresistance (MR) of a metallic alloy is a very powerful tool for studying its electronic transport processes. The application of a magnetic field usually alters the electrical resistance of a metal. The magnetoresistance or the fractional change in resistance (ρ) of a material due to an applied field ($\vec{H}$) at any particular temperature (T) is defined as

$$\frac{\Delta\rho}{\rho_0} = \frac{\rho(H,T) - \rho(0,T)}{\rho(0,T)}. \tag{1.15}$$

Normal Magnetoresistance

The magnetoresistance is termed as "Longitudinal magnetoresistance" [LMR = $(\frac{\Delta\rho}{\rho})_{\parallel}$] when the applied magnetic field is in the direction of the current flow and "Transverse magnetoresistance" [TMR = $(\frac{\Delta\rho}{\rho})_{\perp}$], when it is perpendicular. At the same time, a potential gradient perpendicular to the applied electric field ($\vec{E}$) and the magnetic field ($\vec{H}$) builds up, giving rise to Hall voltage. For a single band which can be described as a spherical Fermi surface, as the applied field increases the Hall field compensates the Lorentz force and the transverse magnetoresistance vanishes identically keeping invariant the current stream lines. For a single band the longitudinal magnetorestance is also zero. In the simplest approximation one needs a two-band model for the transverse magnetoresistance to show up. This model consists of two overlapping bands, and is usually applied to transition metals and can also be used for some other metals[94]. This model gives non-vanishing transverse magnetoresistance given by[79].

$$\left(\frac{\Delta\rho}{\rho_0}\right)_{\perp} = \frac{\sigma_1\sigma_2(\beta_1 - \beta_2)^2 H^2}{(\sigma_1 + \sigma_2)^2 + H^2(\beta_1\sigma_1 + \beta_2\sigma_2)^2}, \tag{1.16}$$

where σ_1 and σ_2 are the conductivities associated with the two bands, $\beta = \frac{e\tau}{m^* c}$ where τ and m^* are relaxation time and effective mass, respectively. The magnetoresistance described above is a band effect. It essentially arises due to the motion of the electrons on the Fermi surface under the influence of a magnetic field. Making the simplest assumptions of putting $\sigma_1 = \sigma_2 = (1/2)\sigma_0$ and $\beta_1 = \beta_2 = \beta$, one obtains,

$$\left(\frac{\Delta\rho}{\rho_0}\right)_{\perp} = \left(\frac{\sigma_0}{2ne}\right)^2 H^2, \tag{1.17}$$

where $n_1 = n_2 =$ n are the carrier concentrations in the two bands. The above equation gives the correct order of magnitude of the effect. In high magnetic fields ($\omega_c\tau \gg 1$), this model leads to two distinct cases :

1. $n_1 \neq n_2$: the MR would tend to saturate.
2. $n_1 = n_2$ · the MR would increase quadratically.

Here $\omega_c \approx (eH/mc)$ is the cyclotron frequency and τ is the relaxation time.

In general, for low resistivity non-magnetic metals and alloys, longitudinal and transeverse magnetoresistances are positive. In low fields ($\omega_c\tau \ll 1$), $\Delta\rho \propto H^2$ and in high fields ($\omega_c\tau \gg 1$) and at low temperature, $\Delta\rho$ usually tends to saturate if electrons travel in closed orbits on the Fermi surface. For a non-magnetic metal in the low-field region ($\omega_c\tau \ll 1$) the time between electron collisions is short and the electrons traverse only a small fraction of the Fermi surface before scattering. In this regime the anisotropy of the scattering mechanisms dominates the magnetoresistance. On the other hand, in the high-field region ($\omega_c\tau \gg 1$) where electrons are able to complete many cyclotron orbits between collisions, magnetoresistance generally reveals the topology of the Fermi surface and not the details of scattering mechanisms that dominates the character of magnetoresistance for metals[94, 79].

For certain metals with open orbits $\frac{\Delta\rho}{\rho}$ continuously increases with H^2. Magnetoresistance of polycrystaline materials generally increases linearly with H. Ziman[79] suggested that this could be due to an averaging over seperate crystallites, for some of which $\frac{\Delta\rho}{\rho} \propto H^2$ while for others $\frac{\Delta\rho}{\rho}$ tends to a constant.

In materials with weak scattering the important parameters in magnetoresistance are the mean free path l of the electrons ($l = v_F\tau$, where v_F is the Fermi velocity) and the radius of curvature (r) of electron paths in a magnetic field, H ($r = \frac{mv}{eH}$). The ratio

$$\frac{l}{r} = \frac{e\tau H}{m} = \frac{H}{ne\rho_0} = \tau\omega_c$$

is closely related to the magnetoresistance in metals and alloys.

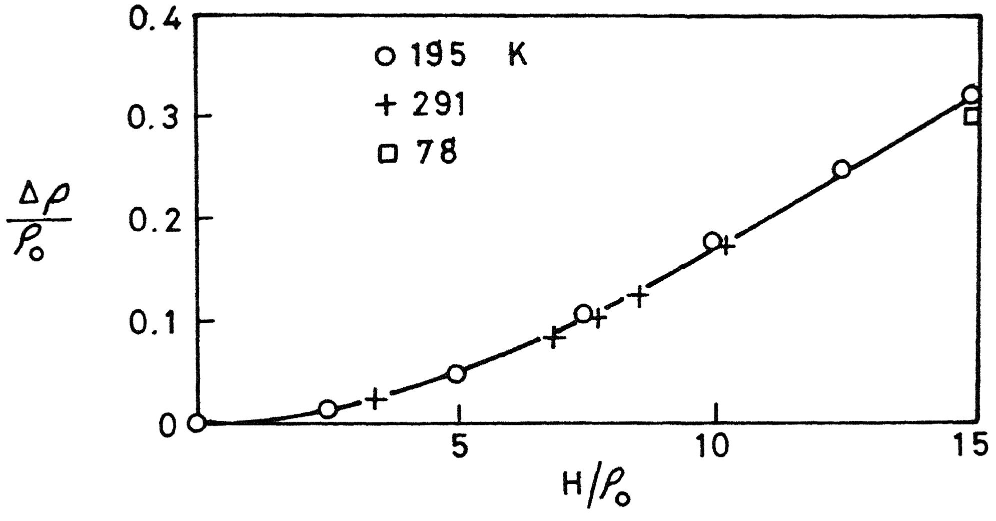

Figure 1.9: Magnetoresistance data of Mg at various temperatures, fitted to Kohler's rule [ref.[79]].

For normal (both longitudinal and transverse) magnetoresistance a generalized rule usually holds quite accurately which is called the **Kohler's rule**, commonly written as

$$\frac{\Delta\rho}{\rho_0} = f\left(\frac{H}{\rho_0}\right). \tag{1.18}$$

However, the nature of the function is different in the two cases (LMR and TMR).

By plotting $\frac{\Delta\rho}{\rho_0}$ as a function of H/ρ_0 for various temperatures and purities of samples, all the data can be made to lie on the same curve as shown in Fig.1.9 All the alkali metals (e.g., Na, K, Rb, Cs, etc.) having very low magnetoresistance appear lowest on the Kohler diagram whereas a semi-metal like bismuth lies in the upper part of the diagram[94].

Anomalous Magnetoresistance

Generally in a clean metal (in which Boltzmann transport theory is applicable) the magnetoresistance is essentially a band effect

$$\left[\frac{\Delta\rho}{\rho} \approx (\omega_c\tau)^2\right].$$

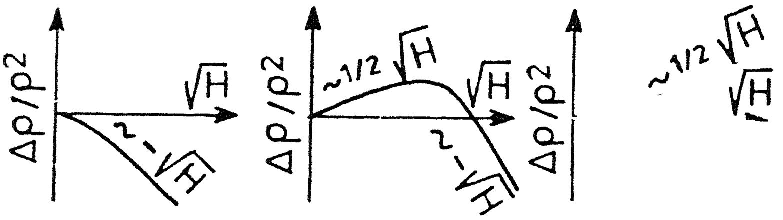

Figure 1.10: A schematic plot of the magnetoresistance for (a) $\tau_i \ll \tau_{so}$, (b)$\tau_i \sim \tau_{so}$, and (c) $\tau_i \gg \tau_{so}$ [102].

This effect is usually very small. Apart from this band effect there are a number of other sources from which an entirely different kind of magnetoresistance shows up in disordered systems (having small mean free path). These are :

(a) A dominant low-temperature contribution comes from the destruction of back scattering in *weak localization* and from *electron-electron interaction effects* with the application of an external magnetic field. The works of Abrahams[95], Altshuler and Aronov[96], Hickey *et al.*[97], Schulte *et al.*[98], Baxter *et al.*[99], Bieri *et al.*[100] and others have thrown some light on the understanding of the anomalous negative magnetoresistance using the ideas of the *quantum interference effects* (QIE). In a number of metallic glasses it has been found that $\frac{\Delta\rho}{\rho}$ is very large compared to the magnitude predicted by Kohler's rule[101, 102, 91]. In some metallic glasses, disordered alloys, doped semiconductors, metal films, inversion layer systems, etc.[102, 91, 103–106] the slope of $\frac{\Delta\rho}{\rho}$ curve at high fields is negative and even the value of the magnetoresistance could be negative.

Altshuler and Aronov[96], Fukuyama[107], Lee and Ramakrishnan[91] and others have independently developed theories regarding the effect of magnetic fields on *weak localization and electron-electron interaction.* Dugdale[101] has given a very simplified picture of the role of spin-orbit scattering in highly disordered alloys where QIE dominates. Generally, in addition to the inelastic (spin quantum number conserved) dephasing with lifetime, τ_i and dephasing due to magnetic fields, there are other mechanisms of scattering which change the spin state, e.g., spin-orbit scattering (having characteristic dephasing time τ_{so}) and *interaction of electron spin with localized magnetic moments* (having dephasing time τ_s). The behaviour of the **QIE** term can be put into three categories determined by the following conditions : (i) $\tau_i \ll \tau_{so}$ (ii) $\tau_i \approx \tau_{so}$ and (iii) $\tau_i \gg \tau_{so}$. The magnetoresistance for these three cases are shown (Fig.1.10) above schematically.

Weak localization :

When a magnetic field passes through the orbit of an electron on a closed path, the phase of its wavefunction is changed by $e\phi/\hbar$, where ϕ is the magnetic flux that threads the closed loop[101]. For the two time reversal paths of an electron wave, the relative phase is thus changed by $2e\phi/\hbar$. With the increase of external magnetic field the dephasing of the two partial wave reduces the probality of back scattering. As a consequence, because of the suppression of weak localization, resistivity of any disordered material diminishes and gives rise to a negative magnetoresistance (or a positive magnetoconductance).

The expression for positive magnetoconductance in the absence of any spin-orbit scattering in three-dimension, is given by Kawabata[108] as

$$[\Delta\sigma]_{\mathbf{WL}} = \frac{e^2}{2\pi^2\hbar}\left[\frac{eH}{\hbar}\right]^{1/2} f_3\left[\frac{4DeH}{\hbar}\tau_\phi\right], \tag{1.19}$$

where f_3 is defined as

$$f_3(x) = \sum_{n=0}^{\infty}\left[2\left(n+1+\frac{1}{x}\right)^{1/2} - 2\left(n+\frac{1}{x}\right)^{1/2} - \left(n+\frac{1}{2}+\frac{1}{x}\right)^{-1/2}\right] \tag{1.20}$$

and τ_ϕ is the dephasing time (also called the phase relaxation time).

In low fields (i.e.,$x = (4DeH/\hbar)\tau_\phi \ll 1$),

$$f_3(x) = \frac{x^{3/2}}{48}.$$

So, from Eq.(1.19), $[\Delta\sigma]_{\mathbf{WL}} \propto H^2$.

In high-field limit ($x \gg 1$),

$$f_3(x) = 0.605 \quad \text{and}$$

$[\Delta\sigma]_{\mathrm{WL}} \propto H^{1/2}$. $[\Delta\sigma]_{\mathrm{WL}}$ can be used to determine the dephasing time τ_{ϕ}[109]. In the presence of *spin-orbit interaction* the situation is more complex leading to a negative magnetoconductance at low fields (because in this case it is weak "anti-localization" which is destroyed by the field).

Electron-electron interaction effects :

When the electron-electron interaction effect is taken into account, an additional contribution comes to the MR due to spin-splitting and spin-orbit interaction. Both of them give rise to a positive magnetoresistance varying as H^2 at low fields and $\sqrt{H}$ at high fields[91]

(b) In magnetic systems, the magnetic exchange interaction modifies the electron scattering which leads to a negative magnetoresistance (except in antiferromagnets) which mask the normal magnetoresistance.

The magnetoresistance of a magnetic system is one such probe where the transport properties are coupled with the magnetic ones. It is a convenient tool to investigate local spin correlations which otherwise get averaged out in the bulk magnetic measurements such as susceptibility, magnetization, etc.. It is also to be noted that unlike the bulk magnetic measurements, *MR is less sensitive to domain effects if their size is greater than the mean free path.* In the magnetic materials studied here, the mean-free path is typically of the order of a few tens of Å implying a measurement time-scale, τ, of 10^{-12} to 10^{-15} s. which is comparable to that of neutron scattering measurements. It is observed that in most of the magnetic systems, the result of the MR measurements are on par with the more sophisticated measurements like neutron scattering.

Generally in a metal with magnetic spins, an additional quantum – mechanical scattering mechanism might be there. This is the "spin-flip" or "spin-exchange" scattering, where a conduction electron scatters by exchanging spin with a magnetic moment or a spin excitation. An external magnetic field increases the energy needed to flip a spin and thus decreases the amplitude for spin-flip scattering. In other words, with the application of an external magnetic field, the spin–flip scattering of conduction electrons from localized moments freezes out and yields a negative magnetoresistance ($\frac{\Delta\rho}{\rho} < 0$), i.e., suppression of fluctuation of localized spins by magnetic field.

The magnetoresistance in dilute NM-TM alloys were studied by Gerritsen *et al.*[111] and Röhrer[112] and the observed negative MR was explained on the basis of s-d scattering (in the second Born approximation) as proposed by Beal-Monod and Weiner[113]. According to this model, the variation of the magnetoresistivity is the product of (i) the field and temperature dependence of the conduction – electron scattering amplitudes, and (ii) the freezing out of the impurity spin degrees of freedom by the magnetic field. In the presence of external magnetic fields ($\frac{g\mu_B H}{k_B T} \leq 2$), the freezing out of the spins is mainly described by the square of the magnetization (M^2) and varies much more rapidly than the perturbation expansion of the scattering amplitudes (e.g., for CuMn, CuFe, AuFe, AuMn, etc.). For very high fields ($\frac{g\mu_B H}{k_B T} \geq 4$), the impurity spins are completely aligned with the field and the scattering amplitudes become the main source of variation of the magnetoresistivity (where normal magnetoresistance also might dominate).

A simple consideration of the weak-field spin-flip scattering amplitude between an electron and a single local magnetic moment is given by Abrikosov[114] who derived $\frac{\Delta\rho}{\rho(0)} = -\alpha\ (\mu H)^2$, where α is a positive constant and μ is the moment per magnetic scatterer. The spin-flip scattering from exchange between conduction electrons and spin excitations in an itinerant feromagnet was considered by Herring[115]. More sophisticated calculations of the field and temperature dependences of spin-flip scattering between conduction electron and various kinds of dynamic spin fluctuations were done by Mills and Leaderer[116] and are reviewed by Moriya[117]. The general conclusion is that the spin exchange leads to a MR of opposite sign to the orbital case. Another crucial difference between the orbital and the spin-flip mechanisms is that the spin-flip suppression is independent of the Lorentz force. It is present even if $\vec{J} \times \vec{H} = 0$, and so the spin-flip and the orbital effects can be cleanly separated by measurements of both the transverse ($\vec{J} \perp \vec{H}$) and the longitudinal ($\vec{J} \parallel \vec{H}$) magnetoresistances.

The typical magnetoresistance behaviours in the case of various magnetic phases are discussed below.

Ferromagnet :

Generally, in a conventional ferromagnet there are three types of changes of electrical resistance : (a) those associated with changes of magnetization at a fixed temperature (b) those associated with chages of magnetization as caused by temperature changes, and (c) those associated with the direction of magnetization relative to the current. The last effect is called an orientation effect or anisotropic effect by Smit[118]. At low fields, a large anisotropy of MR is found which is the result of spin–orbit coupling and s-d scattering[118]. The ferromagnetic anisotropy of resistivity (FAR) is defined[119] as

$$\frac{\Delta\rho}{\rho_0} = \frac{\rho_{\parallel} - \rho_{\perp}}{\frac{1}{3}\rho_{\parallel} + \frac{2}{3}\rho_{\perp}} \ , \tag{1.21}$$

where $\rho_{\parallel}$ and $\rho_{\perp}$ are the values of the resistivity when the $\frac{\Delta\rho}{\rho_0}$ vs H curve is extrapolated to $H_{internal} = 0$ for both field directions, parallel and perpendicular to the current density, respectively.

Smit[118] proposed a theory of magnetoresistance based on spin-orbit interaction and s-d scattering incorporating parallel current conduction. This theory has been used by Cambell, Fert, and Jaol[120] to derive a relation valid under the condition $\rho_{\downarrow}/\rho_{\uparrow} \gg 1$ and $\rho_{ss\downarrow} \ll \rho_{sd\downarrow}$ which hold for many crystalline Ni-based alloys. The relation is given by

$$\frac{\Delta\rho}{\rho_0} \simeq \gamma\left[\frac{\rho_{\downarrow}}{\rho_{\uparrow}} - 1\right]. \tag{1.22}$$

Here, $\rho_{\downarrow}$ and $\rho_{\uparrow}$ are the resistivities for spin-down and spin-up bands, and $\gamma \simeq 1 \times 10^{-2}$. Also, $\rho_{ss\downarrow}$ and $\rho_{sd\downarrow}$ are the contributions to $\rho_{\downarrow}$ from s-s and s-d scattering, respectively. A similar relation, where $\rho_{\downarrow}/\rho_{\uparrow}$ is replaced by $\rho_{\uparrow}/\rho_{\downarrow}$, holds for Fe-based alloys where $\rho_{\uparrow}/\rho_{\downarrow} \gg 1$ and $\rho_{ss\uparrow} \ll \rho_{sd\uparrow}$. Malozemoff[121] derived other forms of Eq.(1.22), which are more general. The traditional version of Smit theory[118] describes s-d scattering in the 1st Born approximation, appropriate for weak scattering potentials. The FAR is a measure of the anisotropy (direction dependent). It is large at low fields and it decreases with increasing temperature and finally vanishes at T = T_c.

The slope of the high field MR [$\approx \frac{1}{\rho}\frac{d\rho}{dH} = \frac{d}{dH}(\frac{\Delta\rho}{\rho})$] is negative, i.e., the resistance decreases with increasing field. At $T \ll T_c$, the magnitude of the slope is nearly zero (or positive due to normal MR). It progressively increases as T_c is approached. The suppression of scattering due to spin-waves in the presence of a field leads to a reduction in resistivity and consequently a negative MR above technical saturation. Both these features are common for crystalline and amorphous FM alloys. The negative MR of FM systems has been explained by Yamada and Takada[122] in the mean-field approximation for the spin system. Besides this Balberg *et al.*[123], Alexander *et al.*[124] have extended this approach to calculate MR for FM in a more rigorous way.

Spin Glass :

Magnetoresistance in canonical spin-glasses [Cu$\underline{\text{Mn}}$, Au$\underline{\text{Fe}}$, Au$\underline{\text{Cr}}$, and Ag$\underline{\text{Mn}}$ (with (0.5 - 10) at.% of 3d impurities) were measured by Nigam and Majumdar[5] and Senoussi[125]. The sailient features of the MR, as observed by them, are given below :

- $\frac{\Delta\rho}{\rho}$ is negative at all temperatures and fields.
- $\frac{\Delta\rho}{\rho} = -\alpha H^n$, where α is a constant and the value of the exponent $n = (1.9 \pm 0.1) \simeq 2$ at low fields below the SG freezing temperature.
- MR is isotropic, i.e., TMR and LMR are nearly identical.
- $\left|\frac{\Delta\rho}{\rho_0}\right| = \alpha M^2$ over a wide range of H and T.

Moreover, Senoussi observed hysteresis and relaxation effects of remanent magnetization in the resistivity of the field-cooled AuFe and CuMn[125] and jumps in their MR ($\frac{\Delta\rho}{\rho}$) below the SG freezing temperature. When the remanent magnetization m_r is saturated and parallel to the field H, $\frac{\Delta\rho}{\rho_0}$ varies linearly with H for low fields and exhibits jumps. When the field is perpendicular to the initial remanence m_r, $\frac{\Delta\rho}{\rho_0}$ is quadratic in H. The magnetoresistance depends on the macroscopic total magnetization (reversible and irreversible) which can be expressed according to Senoussi in the following form :

$$\begin{aligned}\frac{\Delta\rho}{\rho_0} &= -\alpha[(\chi_0\vec{H} + \vec{m_r})^2] \\ &\simeq -\alpha(\chi_0^2H^2 + 2\chi_0\vec{H}.\vec{m_r}) \ ,\end{aligned} \tag{1.23}$$

where χ_0, $\vec{H}$ and m_r are, respectively the reversible susceptibility, the applied magnetic field and remanent magnetization. α is a constant of proportionality.

In the zero-field-cooled state (no thermoremanent magnetization (TRM)), Eq.(1.23) reduces to

$$\frac{\Delta\rho}{\rho_0} = -\alpha\chi_0^2H^2.$$

This approach (Eq.1.23) accounts only for the RKKY couplings.

The MR of SG alloys, calculated by Mookerjee[126] within the frame-work of the Edwards-Anderson model, neglecting the complication of spin dynamics, is given by

$$\frac{\Delta\rho}{\rho_0} = -\left(\frac{J^2}{V^2}\right)\left[M\tanh\left(\frac{g\mu_BH}{2kT}\right) + 2\gamma M^2\right] . \tag{1.24}$$

Here V and J are the Coulomb and s-d exchange potentials, g the splitting factor, μ_B the Bohr magneton and γ is a constant. In spite of several approximations in the calculation, a reasonably good agreement was obtained with the data of Nigam and Majumdar[5]. Das *et al.*[127] have proposed a theory where they calculated MR within the mean-field approximation employing the method of the double time Green's function and the Kubo – Greenwood formula. Sherlekar *et al.*[128] computed the MR of ternary spin glasses by including higher order terms and obtained a better agreement with experiments as compared with Mookerjee's theory. Based on these results, they determined the value of the RKKY interaction strength J_{sd}.

These values are found to be in reasonable agreement with those determined from other magnetic measurements.

Mictomagnets, Cluster glass and Re-entrant Spin Glass (Mixed Phase) :

As the concentration of magnetic impurity (Fe, Mn, Cr) in a noble-metal host (e.g., Au, Cu, Ag, etc.) is increased, there is a greater statistical chance of any impurity becoming the 1st or 2nd nearest neighbour of another impurity. Generally, the wave functions for the 3d-electrons have a finite extent, there is an interaction overlap and a direct magnetic exchange may result. This adds short-range FM and AFM interactions and as a result magnetic clusters can form due to concentration fluctuations in randomly disordered alloys. AuFe (with Fe concentration of 10 - 18 at.%)[129], NiMn (21-28 at.% of Mn)[130], CuMn, AuMn (with very high Mn concentration)[42, 131], etc. show mictomagnetic or cluster-glass behaviour. So at the percolation boundary of all the above alloys (which have spin-glass freezing for lower concentrations), as the 3d impurity concentration is increased, they all subsequently develop long-range FM or AFM ordering. Near the percolation boundary the spin-glass phase does not simply dissapear but continues into the FM phase. This strange behaviour is related to the observation that a more disordered state appears from the more ordered one as the temperature is reduced. So the lowest temperature phase is a cluster glass created out of a percolating infinite FM clusters which have broken up into large but randomly frozen clusters. The word re-entrant, something of a misnomer here, means that the cluster - glass phase develops from a FM phase and thus reenters a frozen (disordered) phase which is different from a PM phase.

In a re-entrant SG system, the simple RKKY type of indirect interaction is not valid because of the effects of short - range direct interaction that comes into play at higher concentration. It is known that the magnetoresistance of a magnetic alloy is very sensitive to the change in the degree of magnetic disorder on the scale of the electron mean free path.

Therefore, a transition from a SG to a FM state is expected to be easily seen in the transport properties as it is necessarily accompanied by a sudden change in the degree of magnetic disorder, and therefore of the resistivity.

Generally the alloys around the percolation threshold have strong competing interactions and they are found to pass on to a phase where long - range order coexists with the spin-glass ordering, as predicted by Gabay and Toulouse[27]. The irreversible effects associated with the magnetization behaviour of spin glasses are also observed in this phase. MR studies reveal that the slope of MR ($\frac{1}{\rho}\frac{d\rho}{dH}$) increases as the system enters a mixed phase[132, 130] from a FM one. This increase is associated with the increase of random, uncorrelated components and the breakdown of FM order which results in an increase of high - field susceptibility. A number of reports on AuFe alloys with higher Fe concentration ($>$ 13 at.%)[5, 132–135] confirmed the coexistence of both the SG and the FM phases in the re-entrant phase through studies of MR, susceptibility, etc.. NiMn alloys[130, 136] also show the re-entrant behaviour below 25 at.% of Mn (percolation threshold). Magnetoresistance (TMR and LMR) studies of re-entrant spin glass alloys show[5, 130, 133–135, 137] the following common features :

- MR of all these alloys in the coexistence regime is strongly negative and isotropic with small FAR.
- $\frac{\Delta\rho}{\rho} = -\alpha H^n, n < 1(\approx 0.75)$, i.e., MR varies slower than linear (H) unlike a canonical SG ($n \approx 2$).
- Contribution of Lorentz force normal MR is negligibly small compared to magnetic contribution.
- $\left|\frac{1}{\rho}\frac{d\rho}{dH}\right|$ increases with temperature below T$_c$.
- Below the second transition to the frozen spin state, $\frac{\Delta\rho}{\rho} = -\alpha H^n, (n < 1)$, and $M \propto H^{n/2}$; as a consequence $\frac{\Delta\rho}{\rho} = \alpha M^2(H)$.
- There might be a possibility for the existence of a FM order on the scale of the electron–mean free path[133].

The magnetoresistance being a microscopic measurement, will have two contributions in these alloys; one due to the FM interaction among the spins inside a cluster and the other due to the SG type of interaction among these clusters. No direct magnetic interaction comes into play. Due to the additive nature of the two contributions, the negative $\frac{\Delta\rho}{\rho}$ is expected from either of the above two types of interactions[138].

Antiferromagnet :

There have been very few MR measurements in antiferromagnets, possibly because of their small values, which in some cases may be beyond the resolution of measuring instruments. Nagasawa[139] had observed that Nd, which has a complicated spin ordering with two antiferromagnetic phases at low temperatures, shows a positive magnetoresistance at sufficiently low temperature whereas as the temperature rises it becomes negative at the temperature where one of the antiferromagnetic phases disappears. This suggest that in such metals with oscillatory spin orderings the magnetic field does not simply suppress the fluctuations of spins, but may as well increase it leading to a positive magnetoresistance.

The high-field magnetoresistance studies[140] on antiferromagnetic monocrystalline $PrSn_3$ and $NdSn_3$ show positive MR. Initially the resistivity increases with increasing magnetic field and then it reaches a maximum at high magnetic fields. The observation of this maximum has been attributed to the *spin-flop* transition. Birss *et al.*[141] have reported that the antiferromagnetic HoCu and $HoCu_5$ exhibit a negative magnetoresistance above their Néel temperature (in the paramagnetic state). However, below their respective Néel temperatures (i.e., in the AFM state), the MR changes to a positive value. In the case of $(Fe_{1-x}Cr_x)_{84}B_{16}$, the high-field slope of the MR curve becomes increasingly positive with increasing Cr content[142]. This implies that with the increase of Cr the AFM coupling increases.

Yamada and Takada[143] have given a simple expression for the MR of AFM metals due to electron - spin scattering with localised spins through s-d interaction, using the molecular - field approximation. For AFM's the direction of external magnetic field is taken to be parallel or perpendicular to the *staggered magnetization*, and the latter (perpendicular) case includes the *spin-flop state*. The external magnetic field is assumed to be weak ($\omega_c \tau \ll 1$). They have shown that the MR is positive in the AFM state when the field is parallel to the sublattice magnetization in contrast to the negative MR in the FM and PM cases. In FM and PM cases the magnetic field increases the effective field acting on the localized spins and suppresses the fluctuation of spins which leads to a negative MR. On the other hand, in an AFM state with parallel field, the fluctuations of the spins of one sublattice may be suppressed whereas it might increase in the other. The MR is determined by the net spin-fluctuations in the two sublattices, and this may lead to a positive MR. For an AFM the MR is zero when the applied magnetic field is perpendicular to the sublattice magnetization. From these results it has been predicted that as the magnetic field is increaesd the MR of polycrystalline AFM metals changes from positive to zero and finally to negative values, the boundary of each region being rounded by the domain wall and polycrystalline effects. Such a behaviour of MR is consistent with the observation of Nd by Nagasawa[139].

1.4 Present Study and Motivation :

The study of soft magnetic materials having a random mixture of FM and AFM interactions continues to attract attention in the field of *Science and Technology* because of their variety of forms and the underlying mechanisms. One such kind of material is the binary alloy system Fe-Ni which is very interesting from the point of view of basic magnetism as well as industrial applications[144]. The iron - rich Fe-Ni alloys having 36 at.% Ni are known as *Invar alloy.* A great deal of efforts have been constantly put theoretically and experimentally to understand the *Invar anomalies*, such as the instability of the FM phase, lattice softening, and a vanishing thermal expansion coefficient at room temperature. The case of nickel-rich Fe-Ni alloys with high Ni-concentration of around 75 at.% Ni is well known as permalloy which are characterised by very high permeability and thus possess a wide range of applications in industry.

For practical applications a third alloying element (e.g., Mo, Si, Ge, Cr, B, etc.) is added to the Fe-Ni system so that the permeability can be increased while cost can be reduced

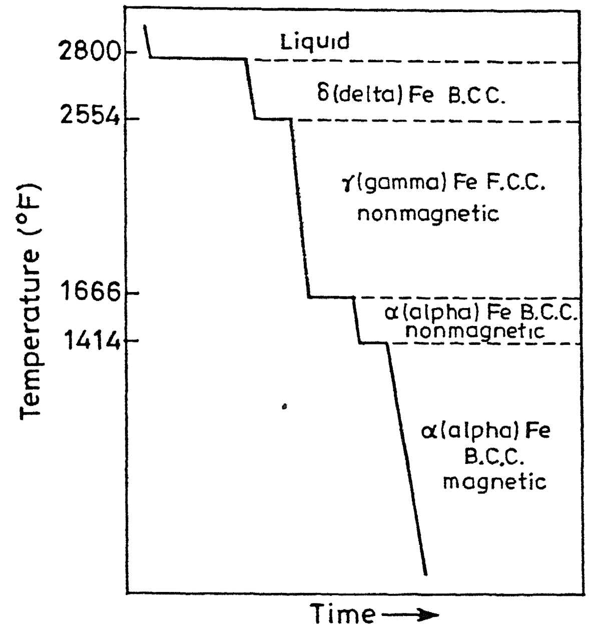
Liquid
δ(delta) Fe B.C.C.
γ(gamma) Fe F.C.C. nonmagnetic
α(alpha) Fe B.C.C. nonmagnetic
α(alpha) Fe B.C.C. magnetic
2800
2554
1666
1414
Temperature (°F)
Time ⟶

Figure 1.11: Cooling curve for pure iron.

by replacing the expensive nickel by a cheaper element. In particular, it has been found that the magnetic properties of Fe-Ni alloys can be very much improved by the addition of Cr. Nakamura[145] had shown that the initial permeability of Fe-Ni-Cr alloys increased with increasing Cr concentration and for 12 at.% Cr the permeability becomes almost ten times as large as that for the binary Fe-Ni alloys. To cite some typical industrial applications, $Fe_{38}Ni_8Cr_{54}$ alloys are used for manufacturing shield plates of floppy disc drives and video tape recorders, iron cores of watches, etc.

In the past decade there has been a revived interest in the properties of fcc γ-Fe, which when pure exists only at very high temperatures (between 1183 and 1667 K). In Fig.1.11 the cooling curve of pure Fe is shown. The existence of multiple magnetic phases, the relative stability of which depends critically on the lattice constant, has been demonstrated by band structure calculations[146, 147] and may be related to the properties of γ-Fe-based *Invar alloys*[148]. γ-Fe is of further technological interest since it forms the basis of austenite-type steels where it is stabilized at low temperatures by addition of interstitial carbon and other (transition metal) impurities. $\gamma - Fe$ can also be stabilised at low temperatures as small

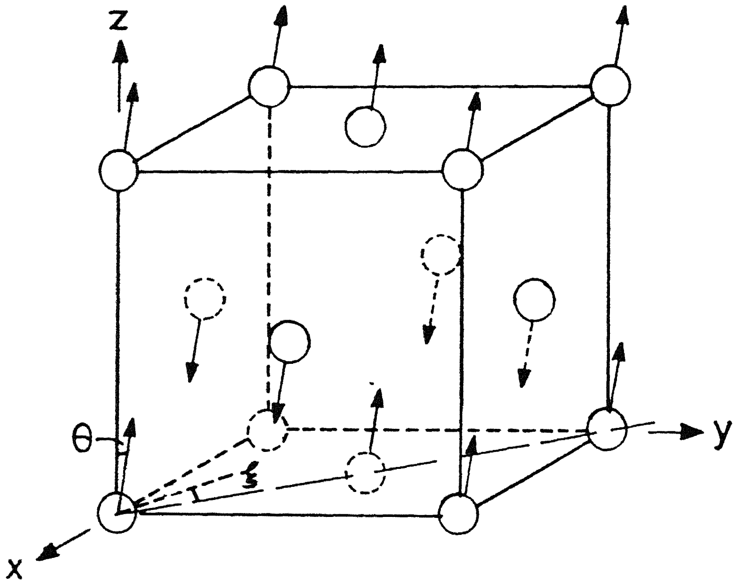

Figure 1.12: General spin structure of γ-Fe.

coherent precipitates in copper and copper alloy matrices[149] or as thin epitaxial films on Cu or Cu-based alloy substrates[150, 151].

There has been a long debate on the magnetic ground state of iron with f.c.c structure (γ-Fe). The AFM spin structure of γ-Fe was determined by Abrahams *et al.* through a neutron diffraction study of γ-Fe precipited in a single crystal of Cu. In Fig.1.12 the antiferromagnetic γ-Fe structure is shown as proposed by Abraham *et al.* and Ishikawa *et al.*[152, 153]. The AFM structure is of the 1st kind with spins inclined from the [001] axis at an angle θ in the plane which makes an angle ϕ with the (110) plane[153].

Although the f.c.c. γ-Fe (AFM) is unstable at room temperature, the fcc allotrope could be obtained by alloying with Ni and the resulting structure stabilized by the addition of Cr, Mn, V or Cu[37, 154]. These austenitic stainless steels have potential industrial applications. They are highly corrosion resistant because of the formation of a thin impervious layer of Cr_2O_3[154]. They are also non-toxic and non-magnetic and can be used as cryogenic materials. They are also used for sophisticated pharmaceutical euipment, and as creep–resistive and high-resistance materials[154].

In the present investigation we have chosen a particular series of γ–$Fe_{80-x}Ni_xCr_{20}$ ($14 \leq x \leq 30$) substitutionally disordered alloys of type–304,308,309 polycrystalline austenitic stainless steel. These isostructural (fcc structure) alloys are the closest realization of γ–Fe, the nature of the ground state of which was highly controversial but later on confirmed to be AFM[153, 155]. In γ–Fe two other issues[156] related to itinerant electron magnetism are also important . (i) the nature of magnetic interaction and (ii) the localizaton of magnetic moments.

These particular types (304,308,309) of austenitic stainless alloys are used for chemical and food processing equipment, recording wire, etc.. Higher Ni and Cr content increases corrosion and heat resistance and are principally used for welding filler metals to compensate for alloy loss in welding. Ni/Cr also increases corrosion and scaling resistance, as so are used in aircraft heaters, heat treating equipment, furnace parts,etc..

It is known that γ–FeNiCr alloys have competing exchange interactions[157, 158] because of which the local spin orientation is expected to depend on its environment. The effective exchange interaction can be positive, negative or nearly zero. In the Heisenberg local moment picture, the behaviour of the whole sample will be governed by the concentration, distribution and strength of the six different possible exchange interactions J_{ij} between the different magnetic atoms. As a result, a number of exotic magnetic phases are realized at low temperatures.

The antiferromagnetism of Fe in the f.c.c γ-phase of the Fe-Ni alloys arises out of the negative exchange integral of electrons of nearest neighbour Fe-atoms in the f.c.c. lattice. However, owing to the $\gamma - \alpha$ phase transition it is not possible to study the AFM phase of Fe below 1180 K. This difficulty can be circumvented by the addition of Cr or Mn or V so that the γ-phase is stablised and then the complete transformation region from AFM (Fe-rich) to FM (Ni-rich) within the same crystallographic fcc phase can be studied. In the alloy system Fe-Ni-Cr, nature has thus provided us with a convenient system whose ternary and magnetic phase diagrams are well studied[160, 157]. The magnetic phase diagram[157, 158] had been established in γ–$Fe_{80-x}Ni_xCr_{20}$ ($14 \leq x \leq 30$) through dc–magnetization[157], magnetic neutron scattering[159, 160] and ac–susceptibility measurements. Figure 1.13 shows the magnetic phase diagram of γ–$Fe_{80-x}Ni_xCr_{20}$ ($14 \leq x \leq 30$).

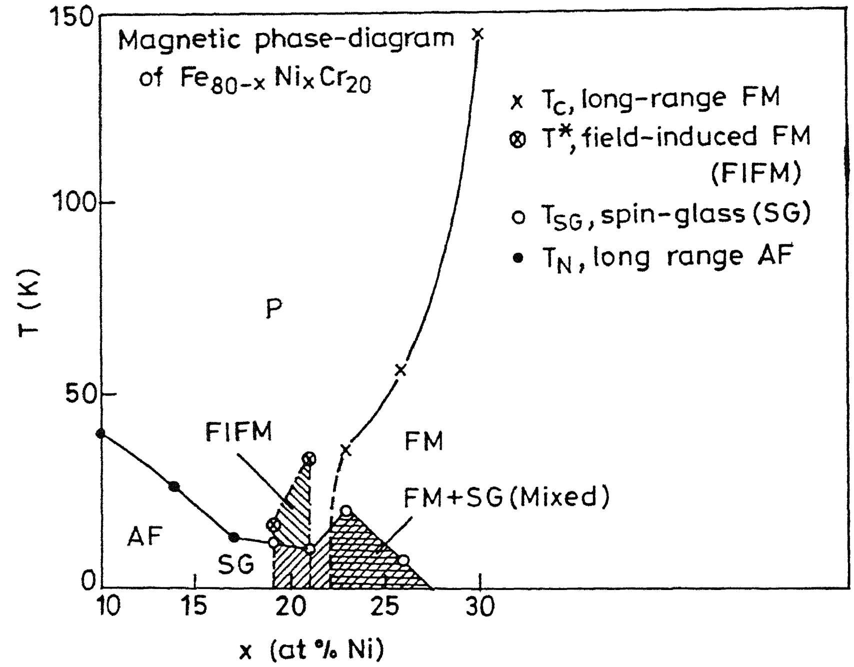

Figure 1.13: Magnetic phase diagram of $Fe_{80-x}Ni_xCr_{20}$ $(14 \leq x \leq 30)$ alloys in the temperature - concentration (Ni) plane [157].

Due to the strong competing exchange interaction between different kinds of magnetic atoms (nearest neighbour interaction is either FM or AFM with positive or negative values of exchange integral, J_{ij}), this system of alloys undergoes a compositional phase transition from long-range AFM (x = 10-14) to SG (17-21) to mixed FM and SG (23–26) or re–entrant phase and finally to long-range FM (30) order within the same crystallographic γ-phase. To our knowledge, so far there is no electronic or magnetic band structure calculation in this series of ternary magnetic alloys having such wide varieties of magnetic phases. The present investigation might lead to band structure calculations in this kind of magnetic systems.

It was found from low and intermediate–field magnetization[137] studies that the alloy with x=30, behaves like a distorted or a inhomogeneous FM unlike a conventional FM. Isothermal magnetization curves, in the PM state of each alloy, have strong curvatures even at temperatures much higher than their respective transition temperatures. Also their M–H curves did not show any tendency of saturation even till 6 tesla and down to 4.2 K[157].

The motivation behind the present investigation is to seek answers to many questions regarding these substitutionally disordered, highly resistive γ- Fe-Ni-Cr alloys near the critical concentration regime.

1. What distinct features does one observe in electronic transport properties if the crystallographic structure remains unchanged while the series undergoes a gradual change from one long-range ordered phase (FM) to another (AFM) with intermediate magnetically disordered phases (SG or re-entrant spin glass) by varying the composition?

2 How do the electronic transport properties (with moderate average mean free path l of conduction electrons) affected by short-range magnetic ordering, clustering or setting in of long-range FM or AFM clusters or frozen-in frustrated spins (arising out of strong competitive FM and AFM interactions) with no long-range order ? These can be revealed through powerful probes like the magnetoresistance. Will the dephasing effect of the *quantum interference* be sufficient to describe the MR of all these disordered materials ?

3. At sufficiently high temperatures (where the contribution to the resistivity from magnetic scattering can be neglected because of the complete disruption of magnetic ordering due to large values of thermal energy (k_BT)), the deviation from linearity (DFL) of the electrical resistivity which might lead to a saturation, gives one an opportunity to investigate thoroughly the long-debated phenomenon of resistivity saturation for highly resistive crystalline magnetic alloys. Several models or theories have been proposed on the DFL of resistivity which ultimately lead to a saturation. In the present work, we have considered some of them which are the most appropriate ones to explain this phenomenon and tested them rigorously with our ρ(T) data at high temperatures. The role of magnetic ordering in the electronic transport has also been examined since the alloys are near the percolation threshold or the critical regime.

4. What are the very high-field magnetic responses (χ_{HF}) of these wide varieties of magnetic phases (FM, mixed, SG and AFM) which are very close to the critical concentration and

the evaluation of an integral numerically using DO1AHF (1-D quadrature, adaptive, finite interval and strategy due to Patterson) NAG Routine, is given. This is suitable for any well-behaved function. In Appendix B(2) another software, developed for non-linear least squares fitting programme using the results of the above integral has been provided. A linear interpolation technique (software) used to find the temperature coefficient of resistivity (TCR) at any temperature and for any composition has also been given in Appendix C.

In Chapter 4 we have described the low-field magnetoresistance and magnetization studies and their correlations in the same Fe-Ni-Cr alloys. The measurements were done in the temperature range of 10 to 300 K up to a field of 16.5 kOe. High-field magnetoresistance studies of some of them have been made in the temperature range of 4.2 to 60 K and up to a field as high as 20 tesla.

In Chapter 5 very high-field magnetization M(H,T) studies for the Fe-Ni-Cr alloys up to fields of 19 tesla and down to 4.2 K are presented.

In Chapter 6 we describe the electrical and thermal transport studies of Pauli paramagnetic Cu/Ni-Zr-Al amorphous metallic glass ribbons. The electrical resistivities have been measured in the temperature range of 1.2 to 300 K at an interval of 50 mK. The data have been analysed in the light of *Quantum Interference Effects* which provide the quantum corrections to the Boltzmann conductivity.

In Chapter 7 we conclude the thesis by summarizing briefly the important results obtained in the present investigations. At the end of the chapter the scope for future work has been spelt out.

Bibliography

[1] G. Toulouse. Commun. Phys. **2**, 115 (1977).

[2] K. Binder and A. P. Young, Rev. Mod. Phys. **58**, 801 (1986).

[3] J. A. Mydosh, *Spin glasses : an experimental introduction* (Taylor and Francis, London, Washington DC, 1993).

[4] P. A. Beck, Prog. Mater. Sci. **23**, 1 (1978).

[5] A. K. Nigam and A. K. Majumdar, Phys. Rev B **27**, 495 (1983).

[6] G. E. Brodale, R. A. Fisher, W. E. Fogle, N. E. Philips, and J. Van Curen, J. Magn. Magn. Mater. **31-34**, 1331 (1983).

[7] D. J. Thouless, P. W. Anderson, and R. G. Palmer, Philos. Mag. **35**, 593 (1977).

[8] G. Parisi, Phys. Rev. Lett. **43**, 1754 (1979); J. Phys. **A13**, 1101 (1980); ibid **13**, 1887 (1980).

[9] D. S. Fisher and D. A. Huse. Phys. Rev. Lett. **56**, 1601 (1986); Phys. Rev. **B38**, 386 (1988).

[10] A. P. Malozemoff and B. Barbara, J. Appl. Phys. **57**, 3410 (1985).

[11] David W. Tank and John J. Hopfield, Scientific American, December, 1987.

[12] Daniel L. Stein, Scientific American, July, 1989.

[13] Michel J. P. Gingras, *Magnetic systems with competing interactions* edited by H. T. Diep (World Scientific, Singapore, 1994).

[14] M. Mźard, G. Parisi, and M. A. Virasoro, *Spin glass theory and beyond* (World Scientific, Singapore, 1987).

[15] K. H. Fisher and J. A. Hertz, *Spin glasses* (World Scientific, Singapore, 1987).

[16] B. R. Coles, Phil. Mag. B **49**, L21 (1984).

[17] D. H. Ryan ,*Recent progress in random magnets*, edited by D. H. Ryan (World Scientific, Singapore, 1992), p.1.

[18] I. Mirebeau, M. Hennion, S. Mitsuda, and Y. Endoh, ibid., p.41.

[19] I. A. Campbell and S. Senoussi, Phil. Mag. B **65**, 1267 (1992).

[20] B. R. Coles and S. B. Roy, *Selected topics in magnetism*, edited by L. C. Gupta and M. S. Multani (World Scientific, Singapore, 1993), p.363.

[21] A P. Murani, S. Roth, P. Radhakrishnan, B. D. Rainford, B. R. Coles, K. Ibel, G. Goetz, and F. Mezei, J. Phys. F **6**, 425 (1976); B. R. Coles, B. V. B. Sarkissian, and R. H. Taylor, Phil. Mag. B **37**, 489 (1978).

[22] G. Aeppli, S. M. Shapiro, R. J. Birgeneau and H. S. Chen, Phys. Rev. B, **28**, 5160 (1983); ibid.,**29**, 2589 (1984).

[23] I. Mirebeau, S. Itoh, S. Mitsuda, T. Watanabe, Y. Endoh, M. Hennion, and R. Papoular, Phys. Rev. B, 41 (1990) 11405.

[24] A. Keren, Hyp. Int. **97**, 369 (1994).

[25] S. G. Barsov, Hyp. Inter. **64**, 415 (1990); C. Boekema, Hyp. Int., **31**, 369 (1986).

[26] D. Sherrington and S. Kirkpatrick, Phys. Rev. Lett. **35**, 1792 (1975); Phys. Rev. B17, 4384 (1978).

[27] M. Gabay and G. Toulouse, Phys. Rev. Lett. **47**, 201 (1981).

[28] D M. Cragg, D Sherrington, and M. Gabay, Phys. Rev. Lett. **49**, 158 (1982).

[29] J. R. L. de Almeida, and D. J. Thouless, J. Phys. A **11**, 983 (1978).

[30] J. Villian, Z. Phys. B **33**, 31 (1979).

[31] A. Mookerjee, Pramana **14**, 11 (1979).

[32] V. Korenman, J. Murray, and R. E. Prange, Phys. Rev. B **16**, 4032 (1977).

[33] T. Moriya and Y. Takahashi, J. Phys. Soc. Japan **45**, 397 (1978); J. de Phys. **39**, C6-1466 (1978).

[34] Yoshiro Kakehashi, J. Magn. Magn. Mater. **37**, 189 (1983); Y. Kakehashi and O. Hosohata, Phys. Rev. B **40**, 9080 (1989) and references therein.

[35] R. Dreizler and E. Gross, *Density functional theory*, Springer-Verlag, New York (1990); S. Peng and H. Jansen, Phys. Rev. B **43**, 3518 (1991); P. Ordejon, D. Drabold, M. Grambach, and R. Martin, Phys. Rev. B **51**, 1456 (1995).

[36] Henri J. F. Jansen, Physics Today, 50, April (1995).

[37] R. Bozorth, *Ferromagnetism*, Van Nostrand-Reihold, Princeton, New Jersey (1951), p.441.

[38] J. Friedel, Can. Journ. Phys. **34**, 1190 (1956); J. Fridel, Nuovo Cimento Suppl. **7**, 287 (1958).

[39] G. G. Low and M. F. Collins, J. Appl. Phys. **34**, 1195 (1963); G. G. Low, J. Appl. Phys. **39**, 1174 (1968); M. F. Collins and G. G. Low, Proc. Phys. Soc., London **86**, 535 (1965).

[40] H. Bouchiat, J. Phys. C **16**, L145 (1983); **30**, 3963 (1984); A. P. Malozemoff, S. E. Barnes, and B. Barbara, Phys. Rev. Lett. **51**, 1704 (1983).

[41] J. Gelard, F. Bensamka, D. Bertand, A. R. Fert, J. P. Redoules, and S. Legrand, J. Phys. C **16**, L939 (1983).

[42] A. Banerjee and A. K. Majumdar, Phys. Rev. B, **46**, 8958 (1992).

[43] B R. Coles, B.Sarkissian, and R. H. Taylor, Phil. Mag. B **37**, 489 (1978); B. V. B. Sarkissian, J. Phys. F **11**, 2191 (1981).

[44] J Hesse, Ch. Böttger, A Wulfes, J. Sievert, and H. Ahlers, Phys. Stat. Sol. (A) **135**, 343 (1993).

[45] H. Kunkel, R. M. Roshko, W. Ruan, and G. Williams, Phil. Mag. B **64**, 153 (1991).

[46] I. A. Campbell, H. Hurdequint, and F. Hippert, Phys. Rev. B **33**, 3540 (1986); I. A. Cambell, S. Senoussi, F. Varret, J. Teillet, and A. Hamzic, Phys. Rev. Lett. **50**, 1615 (1983).

[47] S. Senoussi, S. Hadjoudj, and R Fourmeaux, Phys. Rev. Lett. **61**, 1013 (1988); S. Hadjoudj, S. Senoussi, and I. Mirebeau, J. Magn. Magn. Mater. **93**, 136 (1991).

[48] W. Abdul-Razzaq and J. S. Kouvel, Phys. Rev. B **35**, 1764 (1987); J. S. Kouvel and W. Abdul-Razzaq, J. Magn. Magn. Mater. **53**, 139 (1985).

[49] I. Mirebeau, S. Itoh, S. Mitsuda, F. Watanabe, Y. Endoh, M. Hennion, and P. Calmettes, J. Appl. Phys. **67**, 5232 (1990).

[50] T. Sato, T. Ando, T. Watanabe, S. Itoh, Y. Endoh, and M. Furusaka, Phys. Rev. B **48**, 6074 (1993).

[51] B. Huck and J. Hesse, J. Magn. Magn. Mater. **78**, 247 (1989).

[52] Jürgen Hesse, Hyperfine Interactions **47**, 357 (1989).

[53] B. H. Verbeek, G. J. Nieuwenhuys, H. Stocker, J. A. Mydosh, Phys. Rev. Lett. **40**, 586 (1978).

[54] S. B Roy and B. R. Coles, J. Phys. : Cond. Mat. **1**, 419 (1989).

[55] S. J. Kennedy and B. R. Coles, J. Phys. : Cond. Mat. **2**, 1213 (1989).

[56] S. B. Roy and B. R. Coles, Phil. Mag. B **54**, 741 (1991).

[57] T. Moriya and K. Usami, Solid State Commun. **23**, 935 (1977).

[58] P. A. Lee and T. V. Ramakrishnan, Rev. Mod. Phys.**57**, 287 (1985).

[59] A. F. Ioffe and A. R. Regel, Prog. Semiconductors **4**, 237 (1960).

[60] J. H. Mooij, Phys. Stat. Sol.(a), **17**, 521 (1973).

[61] B. L. Altshuler and A. G. Aronov in *Electron-electron interactions in disordered systems*, edited by A. L. Efros and M. Pollak (Amsterdam : North - Holland, 1985).

[62] Z. Fisk and G. W. Webb, Phys. Rev. Lett., **36**, 1084 (1976).

[63] H. Wiessmann, M. Gurvitch, H. Lutz, A. K. Ghosh, B. Schwarz, M. Strongin, P. B. Allen, and J. W. Halley, Phys. Rev. Lett., **38**, 782 (1977).

[64] K. Ghosh, S. Ramakrishnan, and Girish Chandra, Phys. Rev. B **48**, 10440 (1993).

[65] S. Ramakrishnan, K. Ghosh, and Girish Chandra, Phys. Rev. B **46**, 2958 (1992).

[66] P. J. Cote and K. V. Meisel, Phys. Rev. Lett., **40**, 1586 (1978).

[67] P. B. Allen, W. E. Pickett, K. M. Ho, and M. L. Cohen, Phys. Rev. Lett., **40**, 1532 (1978).

[68] B. Chakraborty and P. B. Allen, Phys. Rev. Lett., **42**, 736 (1979).

[69] R. B. Laughin, Phys. Rev. B **26**, 3479 (1982).

[70] M. Gurvitch, Phys. Rev. B **24**, 7404 (1981).

[71] M. Gurvitch, Phys. Rev. B **28**, 544 (1983).

[72] A. Ron, B Shapiro, and M. Weger, Phil. Mag. B **54**, 553 (1986).

[73] M. Gurvitch, A. K. Ghosh, B. L. Gyorffy, H. Lutz, O. F. Kammerer, J. S. Rosner, and M. Strongin, Phys. Rev. Lett., **41**, 1616 (1978).

[74] J. A. Wollam and S. A. Alterovitz, Phys. Rev. B **19**, 749 (1979).

[75] J. J Lin, C. Yu, and Y. D. Yao, Phys. Rev. B **48**, 4864 (1993).

[76] J. A Mydosh, P. J. Ford, M. P. Kawatra, and T. E. Whall, Phys. Rev. B **10**, 2845 (1974).

[77] S. Senoussi and Y. Öner, Phys. Rev. B **28**, 455 (1983).

[78] H. Z. Durusoy and Y. Öner, Phys. Rev. B **42**, 6831 (1990).

[79] J. M. Ziman in *Electrons and phonons* (Oxford University Press, London, 1963).

[80] G. T. Meaden in *Electrical resistance of metals* (Plenum Press, New York, 1965).

[81] J. S. Dugdale in *The Electrical properties of metals and alloys* (The structures and properties of solids, Vol.5, 1976).

[82] A. H. Wilson, Proc. Roy. Soc. (London), Ser.A **167**, 580 (1938).

[83] G. K. White and S. B. Woods, Phil. Trans. Roy. Soc. (London), Ser.A, **251**, 273 (1959).

[84] E. A. Turov, Izv. Akad. Nauk SSSR, Ser. Fiz., **19**, 426 (1955).

[85] T. Kasuya, Prog. Theoret. Phys. (Kyota), **16**, 58 (1956).

[86] T. Kasuya, ibid., **22**, 227 (1959).

[87] I. Mannari, ibid., **22**, 335 (1959).

[88] D. A. Goodings, Phys. Rev. B **132**, 542 (1963).

[89] W. G. Baber, Proc. Roy. Soc. (London) A **158**, 383 (1937).

[90] J. Appel, Phys. Rev., **125**, 1815 (1962); Phil. Mag., **8** (8), 1071 (1963).

[91] Patrick A. Lee and T. V. Ramakrishnan, Rev. Mod. Phys. **57**, 287 (1985).

[92] N. F. Mott in *Metal-insulator transition* (Taylor and Francis, London, 1974); N. F. Mott, Phil. Mag. B **44**, 265 (1981).

[93] A. Ron, B. Shapiro, and M. Weger, Phil. Mag. B **54**, 553 (1986).

[94] J. P. Jan, *Galvanomagnetic and thermomagnetic effects in metals*, Solid State Physics **5**, 1 (1957).

[95] E. Abrahams, P. W. Anderson, D. C. Licciardello and T. V. Ramakrishnan, Phys. Rev. Lett. **42**, 673 (1979).

[96] B. L. Altshuler and A. G. Aronov, *Electron-electron interactions in disordered systems*, edited by A. L. Efros and M. Pollak (Amsterdam : North-Hollannd), p. 4-153 (1985).

[97] B. J. Hickey, D. Grieg, and M. A. Howson, J. Phys. F · Met. Phys. **16**, L13 ( ); Phys. Rev. Lett. **42**, 673 (1979).

[98] A. Schulte, G. Fritsch, and E. Lüscher, Z. Phys. B - Condens. Matter **78**, 457 (1990); A. Schulte and G. Fritsch, J. Phys. F : Met. Phys. **16**, L55 (1986); A. Schulte, Solid State Commun. **60**, 99 (1986).

[99] David V. Baxter, R. Richter, M. L. Trudeau, R. W. Cochrane, and J. O. Strom - Olsen, J. Phys. France **50**, 1673 (1989).

[100] J. B. Bieri, A. Fert, G. Cruezet, and A. Schulte, J. Phys. F : Met. Phys. **16**, 2099 (1986); J. B. Bieri, A. Fert, G. Creuzet and J. C. Outsset, Solid State Commun. **49**, 849 (1984).

[101] J. S. Dugdale, Contemp. Phys. **28**, 547 (1987).

[102] M. A. Howson and B. L. Gallagher, Physics Reports **170**, 265 (1988).

[103] T. F. Rosenbaum, K. Andres, G. A. Thomas, and P. A. Lee, Phys. Rev. Lett. **46**, 568 (1981).

[104] G. Bergman, Phys. Rev. Lett.**48**, 1046 (1982).

[105] M. A. Howson and D. Greig, J. Phys. F **13**, L155 (1983).

[106] D. J. Bishop, R. C. Dynes, and D. C. Tsui, Phys. Rev. **B26**, 773 (1982).

[107] H. Fukuyama and K. Hosino, J. Phys. Soc. Japan **50**, 2131 (1981).

[108] A. Kawabata, J. Phys. Soc. Japan **49**, 628 (1980).

[109] G. Bergman, Phys. Rep. **107**, 1 (1984).

[110] B. L. Altshuler, A. G. Aronov, A. I. Larkin, and D. E Khemel'nitskii, Sov. Phys. - JETP **54**, 411 (1981).

[111] A. N. Gerritsen and J. O. Linde, Physica (Utrecht) **17**, 584 (1951); A. N. Gerritsen, ibid. **19**, 61 (1953).

[112] H. Rohrer, Phys. Rev. **174**, 583 (1968).

[113] M. T. Béal Monod and R. A. Weiner, Phys. Rev. **170**, 552 (1968).

[114] A. A. Abrikosov, *Fundamentals of the theory of metals* (North-Holland, New York, 1988).

[115] C. Herring in *Magnetism* edited by G. Rado and H. Suhl (Academic, New York, 1966), vol. IV.

[116] D. L. Mills and P. Leaderer, J. Phys. Chem Solids **27**, 1805 (1966).

[117] T. Moriya *Spin fluctuations in itinerant electron magnetism* (Springer - Verlag, New York, 1985).

[118] J. Smit, Physica **17**, 612 (1951).

CENTRAL LIBRARY
I. I. T. KANPUR
Acc. No. A 125662

[119] T. R. McGuire and R. I. Potter, IEEE Trans. Magn. MAG-11, 1018 (1975).

[120] O. Jaol, I. A. Campbell, and A. Fert, J. Magn. Magn. Mater. **5**, 23 (1977).

[121] A. P. Malozemoff, Phys. Rev. **B22**, 6080 (1985).

[122] Hiroshi Yamada and Satoshi Takada, Prog. Theor. Phys. **48**, 1828 (1972).

[123] L. Balberg, Physica **91B**, 71 (1977).

[124] S. Alexander, J. S. Helman, and I. Balberg, Phys. Rev. B **13** 304 (1976).

[125] S. Senoussi, J. Phys. F **10**, 2491 (1980); J. de Phys. Lett. **42**, L35 (1981).

[126] A. Mookherjee, J. Phys. F : Met. Phys. **10**, 1559 (1980).

[127] S. K. Das, R. S. Tripathi, and S. K. Joshi, Phys. Rev. B, **25**, 1921 (1982).

[128] G. Sherlekar, C. M. Srivastava, A. K. Nigam, and G. Chandra, Phys. Rev. **B34**, 498 (1986).

[129] S. Crane, D. W. Carnegie Jr., and H. Claus, J. Appl. Phys. **53**, 2179 (1982).

[130] S. Senoussi and Y. Öner, J. Appl. Phys. **55**, 1472 (1984); Phys. Rev. **B28**, 455 (1983); J. Magn. Magn. Mater. **40**, 12 (1983).

[131] S. P. McAlister, L. R. Lupton, and C. M. Hurd, Solid State Commun. **25**, 903 (1978).

[132] A. Hamzic and I. A. Campbell, J. de. Physique-Letters **42**, L309 (1981).

[133] H. Rokoto, J. C. Ousset, S. Senoussi, and I. A. Campbell, J. Magn. Magn. Mater. **46**, 212 (1984).

[134] A. K. Nigam, S. Radha, and Girish Chandra, J. Phys. Condens. Matter. **5**, 9197 (1993).

[135] A. K. Nigam, Girish Chandra, and S. Ramakrishnan, J. Phys. F : Met. Phys. **16**, 1255 (1986).

[136] J. Scaf and P. Pureur, J. Magn. Magn. Mater. **68**, 358 (1987).

[137] T. K. Nath and A. K. Majumdar, J. Appl. Phys. **70**, 5828 (1991).

[138] K. A. Mirza and J. W. Loram, J. Phys. F : Met. Phys. **15**, 439 (1985).

[139] H. Nagasawa, Phys. Letters. **41A**, 39 (1972).

[140] Z. Kletowski, B. Stalinski, and C. Bazan, J. de Physique, Supplement **40**, C5-145 (1979).

[141] R. R. Birss, R. V. Houldsworth, and D. G. Lord, J. Magn. Magn. Mater. **15-18**, 917 (1980).

[142] Yang Fu-Min, Wu Yong-Sheng, Wang Yi-Zhong, Zhao Xi-chao, Shen Bao-Gen, Liu Zui-Yi, and Pan Shio-Thur, *High Field Magnetism* edited by M. Date, (North-Holland Publishing Company, Amsterdam, 1982), p.121.

[143] Hiroshi Yamada and Satoshi Takada, J. Phys. Soc. Japan **34**, 51 (1973).

[144] Y. Ishikawa and N. Miura, *Physics and engineering applications of magnetism* edited by Y. Ishikawa and N. Miura (Springer-Verlag, Berlin, 1991).

[145] Y. Nakamura, Hyperfine Interaction **83**, 55 (1994).

[146] J. Kübler, Phys. Lett. **81A**, 81 (1981).

[147] C. S. Wang, B. M. Klein, and H. Krakauer, Phys. Rev. Lett. **54**, 1852 (1985).

[148] E. F. Wasserman, Phys. Scr. **T25**, 209 (1989).

[149] S. A. Abrahams, L. Guttman, and J. S. Kasper, Phys. Rev. **127**, 2052 (1962); G. J. Johanson, M. B. McGire, and D. A. Wheeler, Phys. Rev. B **1**, 3208 (1970); A. Onodera, Y. Tsunoda, N. Kunitomi, O. A. Pringle, R. M. Nicklow, and R. M. Moon, Phys. Rev. B **50**, 3532 (1994).

[150] W. A. A. Macedo and W. Keune, Phys. Rev. Lett. **61**, 475 (1988).

[151] W. Keune, T. Ezawa, W. A. A. Macedo, U. Glos, K. P. Schletz, and U. Kirschbaum, Physica B **161**, 269 (1989).

[152] S. C. Abrahams, L. Guttman, and J. S. Kasper, Phys. Rev. **127**, 2052 (1962).

[153] Y. Ishikawa, M. Kohgi, and Y. Noda, J. Phys. Soc. Japan **39**, 675 (1975).

[154] Sidney H. Avnar, *Introduction to physical metallurgy* (Mcgraw-Hill, 1987).

[155] Y. Ishikawa, Y. Endoh, and T. Takimoto, J. Phys. Chem. Solids **31**, 1225 (1970).

[156] F. Gautier in *Magnetism of metals and alloys*, edited by M. Cyrot (North-Holland, New York, 1982), p.1.

[157] A. K. Majumdar and P. v. Blanckenhagen, Phys. Rev. B **29**, 4079 (1984).

[158] A. Z. Men'shikov and A. Ye. Teplykh, Fiz. Metal. Metalloved. **44**, 1215 (1977).

[159] A. K. Majumdar and P. v. Blanckenhagen, J. Magn. Magn. Mater. **40**, 227 (1983).

[160] A. Z. Men'shikov, N. N. Kuz'min, V. A. Kazantsev, S. K. Sidorov, and V. N. Kalinin, Phys. Metal. Metalloved. **40**, 174 (1975).

[161] T. K. Nath and A. K. Majumdar, Phys. Rev. B **53**, 12148 (1996).

Chapter 2

Experimental Details

In this chapter the various aspects involved in the experiments are described. These are (1) sample preparation and characterization, (2) cryostat design and (3) measurement techniques. All these are common to both the systems, namely, (a) the highly resistive polycrystalline $Fe_{80-x}Ni_xCr_{20}$ (10 $\leq$ x $\leq$ 30) austenitic stainless steel alloys, and (b) the highly resistive non-magnetic Cu/Ni-Zr-Al amorphous metallic glass ribbons.

Different softwares, developed for acquisition (data acquisition through IEEE-488 interfaced devices with an IBM compatible PC/AT (80386)) and analysis of the data, are given in the Appendix (A,B and C) of this thesis. The techniques described here are developed during the course of this thesis work. To keep the thesis to a managable size, only the main features will be discussed.

2.1 Sample preparation and characterization

2.1.1 Fe-Ni-Cr alloys

The alloys $Fe_{80-x}Ni_xCr_{20}$ with x = 14, 19, 21, 23, 26 and 30 were prepared[1] by induction melting in an argon atmosphere from metals of atleast 99.99% purity. As mentioned in

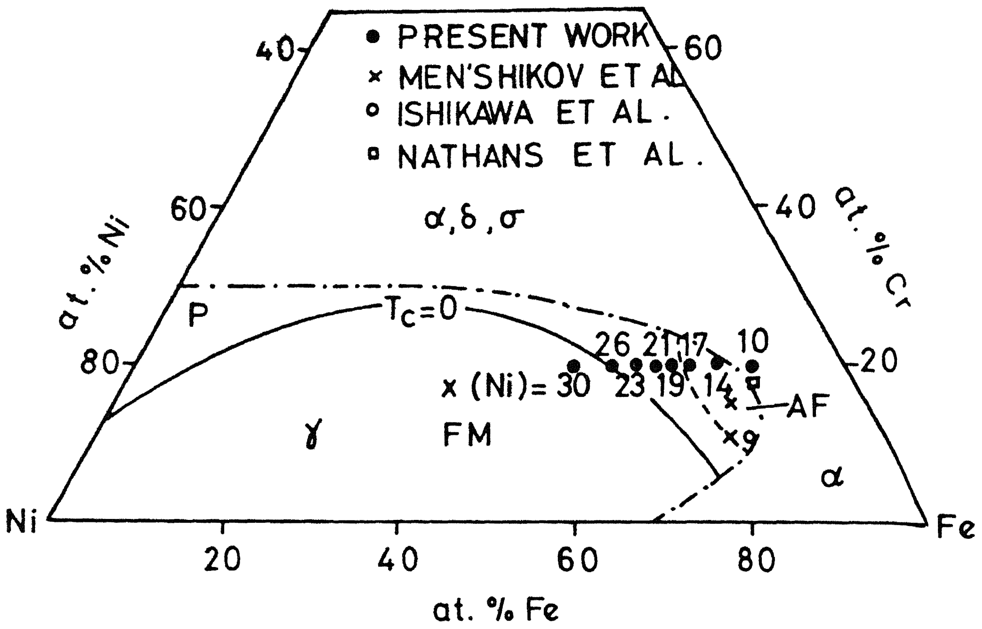

Figure 2.1: Ternary diagram of FeNiCr system showing crystallographic and magnetic phases. The dot-dashed line separates the γ phase from α, δ and σ phases at room temperature. The solid line for $T_c=0$ separates the ferromagnetic (FM) phase from the paramagnetic (P) one (ref.[1,2]).

Chapter 1, it is not possible to study the AFM $\gamma - phase$ of Fe below 1180 K due to $\gamma \rightarrow \alpha$ transformation. Introduction of Cr stabilizes the $\gamma - phase$ and allows one to study in Fe-Ni alloys a complete transition region from AFM (Fe-rich) to FM (Ni-rich) within the same crystallographic fcc phase. The magnetic phase diagram[1] of $Fe_{80-x}Ni_xCr_{20}$ (10 $\leq$ x $\leq$ 30) has already been shown in Fig.1.13. of Chapter 1. The ternary phase diagram[1] with the dot - dashed line separating the γ from the α and other crystallographic phases of Fe-Ni-Cr alloys is shown in Fig.2.1. The so-called "critical scattering" appears at those compositions for which the Curie temperature T_c is close to zero. The solid line for T_c = 0 is the critical concentration line and it separates the FM phase from the paramagnetic (P) one.

In Fig.2.2, a typical trend in the changes (of reactions) of steel with 18% Cr, 8% Ni, and varying carbon content[3] have been shown. The austenitic $\gamma - phase$ formed at the elevated temperature is a particularly stable phase reluctant to transform and it retains its character after annealing. The 0 % carbon-content line (y-axis) is applicable to all our alloys

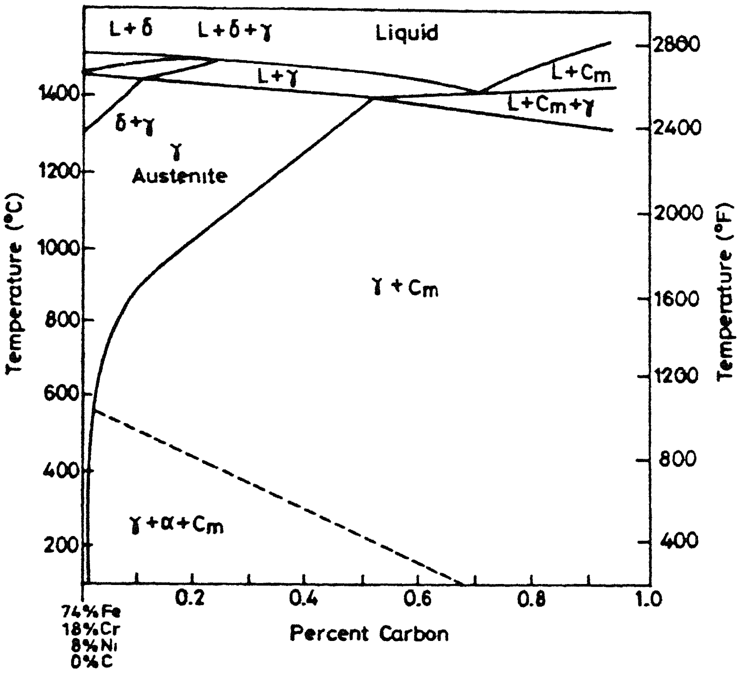

Figure 2.2: Metallurgical phase-diagram showing trend of reactions in steels alloyed with 18% chromium and 8% nickel.

of $Fe_{80-x}Ni_xCr_{20}$ with x = 14, 19, 21, 23, 26 and 30 (with negligibly small carbon content). So it shows that even at room temperature the $\gamma - phase$ (austenite) is stable.

Alloys of each composition are sealed in quartz tubes in an argon atmosphere and homogenized at 1100^0C for 100 hours. This thermal treatment is very important in these substitutionally disordered polycrystalline samples in preventing any possible chemical clustering. Moreover, at 1100^0C Fe is in the $\gamma - phase$ (AFM, fcc structure) as already shown in the cooling curve (Fig.1.11 of Chapter 1) and in Fig.2.2 of this chapter. So this heat treatment also preserves the high-temperature crystallographic (γ–Fe) phase.

All the homogenized alloys in bulk form are then cold rolled (30% cold work) in the form of a sheet and cut into thin rectangular strips as well as in needle forms for various transport and magnetic measurements. All the pieces (needle and rectangular strip shaped) are then finally annealed in argon atmosphere in a sealed quartz tube for 30 hours at 1050^0C to reduce strain in each specimen introduced due to the cold work. All these annealed samples are

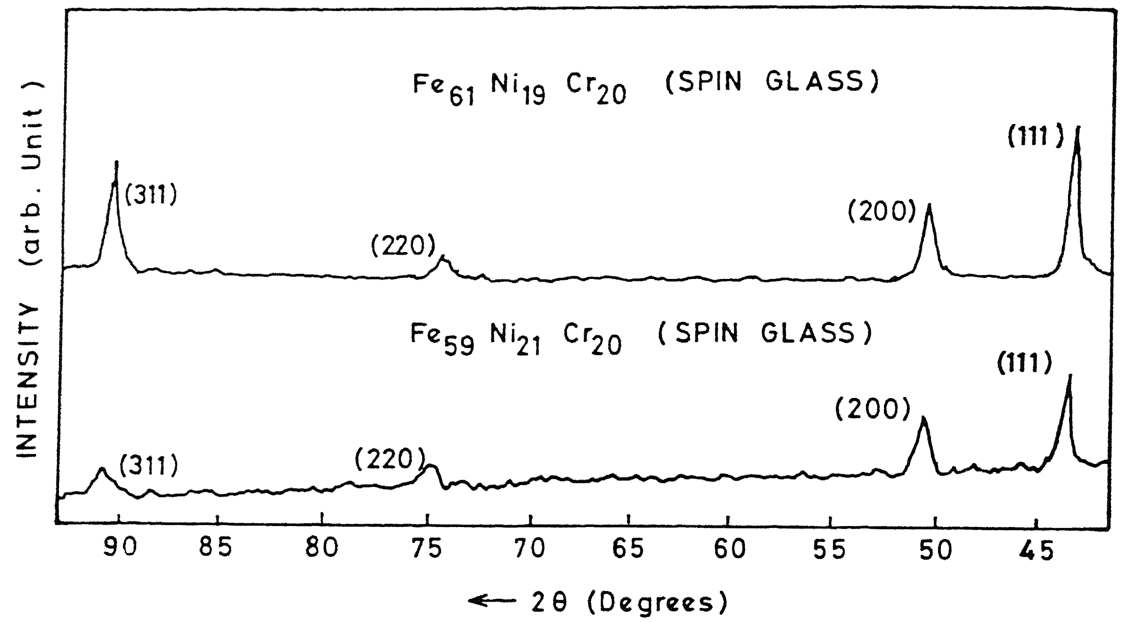

Figure 2.3: Typical X-ray diffraction pattern for the alloys with x=19 and 21 (spin glass) using CuK$_\alpha$ ($\lambda = 1.5406 \mathring{A}$) radiation.

then quenched fast to room temperature in brine. The quenching process has to be as fast as possible for retaining the disordered $\gamma - Fe$ phase at room temperature. A slow quenching does introduce a bit of the $\alpha - phase$ (FM, bcc structure).

X-Ray diffraction, SEM and EDAX study

The powder X-ray diffraction (XRD) pattern are recorded for the characterization of all the samples employing a Rich Seifert Isodebyeflex 2002 diffractometer using CuK$_\alpha$ ($\lambda = 1.5406 \mathring{A}$) radiation. In Fig.2.3, we have shown a typical XRD pattern for the alloys with x=19 and 21 (spin glass). The scanning has been done for all the samples from $2\theta = 15$ to 160^0 with 1.2^0/min. speed (slow-scan mode). The X-ray unit is operated at 20mA/30kV power with a proper cooling arrangement. The reason for taking the scan with low speed is to investigate the possible presence of any second phase (say, of bcc $\alpha-Fe$ structure) apart from the fcc $\gamma-phase$.

The diffraction patterns reveal that all the alloys have single phase fcc structure similar to that of γ-Fe in austenite state, with lattice parameter a = (3.58 ± 0.01) Å. There is a very small change in the lattice constant with concentration. The nominal chemical composition of the alloys was checked through scanning electron microscope (SEM) and energy dispersive X-ray analysis (EDAX). The analysed compositions are found to be within 0.5% of the nominal ones for Ni and Cr.

2.1.2 Cu/Ni-Zr-Al metallic glass ribbons

Master alloys of $(Cu_{0\ 36}Zr_{0\ 64})_{1-x}Al_x$ with x = 0, 0.1, 0.15, and 0.2 and $(Ni_{0\ 5}Zr_{0\ 5})_{1-x}Al_x$ with x = 0, 0.05, 0.1, 0.15, and 0.2 were prepared by melting each element (ingredient) of 99.9% purity in an argon atmosphere using an arc furnace[4]. Each alloy was melted several times to ensure a homogeneous mixing of the constituent elements. Metallic glass ribbons of all these alloys were prepared in an argon atmosphere by induction melting the alloy ingot in a quartz crucible and ejecting it into a single-roller melt spinner. The surface speed of the wheel was approximately 27 m/s. The amorphous nature and composition of all the melt-spun metallic glass samples $(Cu_{0\ 36}Zr_{0\ 64})_{1-x}Al_x$ with x = 0, 0.1, 0.15, and 0.2 and $(Ni_{0\ 5}Zr_{0\ 5})_{1-x}Al_x$ with x = 0, 0.05, 0.1, 0.15, and 0.2 have been confirmed through XRD, SEM and EDAX techniques. All these samples are in the form of ribbons having (20–30) μm thickness and (1–1.5) mm width The X-ray diffractometer with a Cu target (K_α = 1.5406 Å) as well as a chromium target (K_α = 2.2909 Å) has been used to record the XRD pattern. The scanning speed was again kept at $2\theta = 1.2^0$/min. and it was done from $2\Theta = 10^0$ to 160^0. All the XRD patterns show a broad peak at low angles. This is observed, in general, in all metallic glasses and is ascribed to the short-range order. The pattern did not show any other observable peak, confirming the absence of any crystalline phase(s).

2.2 Cryostat design and measurement techniques

2.2.1 Magnetoresistance measurement

The magnetoresistance measurement between 11 and 300 K have been carried out in fields up to 16.5 kOe, provided by an electromagnet (V-3800, Varian) with 15 inch pole pieces and with a proper cooling arrangement. A closed-cycle helium refrigerator (Cryosystems Inc. and RMC, USA) is used to achieve the minimum temperature of 11 K. A schematic diagram of the cryostat used for the closed-cycle helium refrigerator and the experimental arrangement using the electromagnet and IEEE-488 interfaceble equipment with PC/AT (80386) are shown in Fig.2.4.

An extra attachment on the cold head has been made in such a way that any sample when placed on the sample holder (top platform of the cryotip), in both transeverse and longitudinal orientations, is exposed to a uniform magnetic field. At the same time it kept the cold head sufficiently away from the magnetic field for it to function smoothly at fields as high as 16.5 kOe. This extra attachment consisted of a 2 inch OFHC (oxygen free high conductivity) copper tube soldered at both ends to 1 inch diameter copper discs of thickness 2 mm[6] This is fixed rigidily to the original platform by nuts and bolts. Indium foils are placed in the intervening space This resulted in an increase in the lowest attainable temperature from 8 to 11 K. The magnetic field is always in the plane of the sample.

A dc–current of 100 mA from a constant current source (Hewlett Packard, Model 6177C) is passed through the sample. The voltage is measured by a 7 and 1/2 digit digital mulitimeter (Datron, Model 1071). A precalibrated Si-diode and a carbon glass resistance thermometer (CGR-1-1000, LakeShore) are used to monitor and control the temperature along with a temperature controller (LakeShore, Model DRC-93C) adapted with a multipurpose card (CGR and diode cards are used here). The CGR thermometer is used because of its low magnetoresistance (-0.2% at 10 K and 2.5 tesla). At a given temperature the field is fixed at every 1/2 kOe and the data are recorded. The temperature could be held constant within 0.2 K during

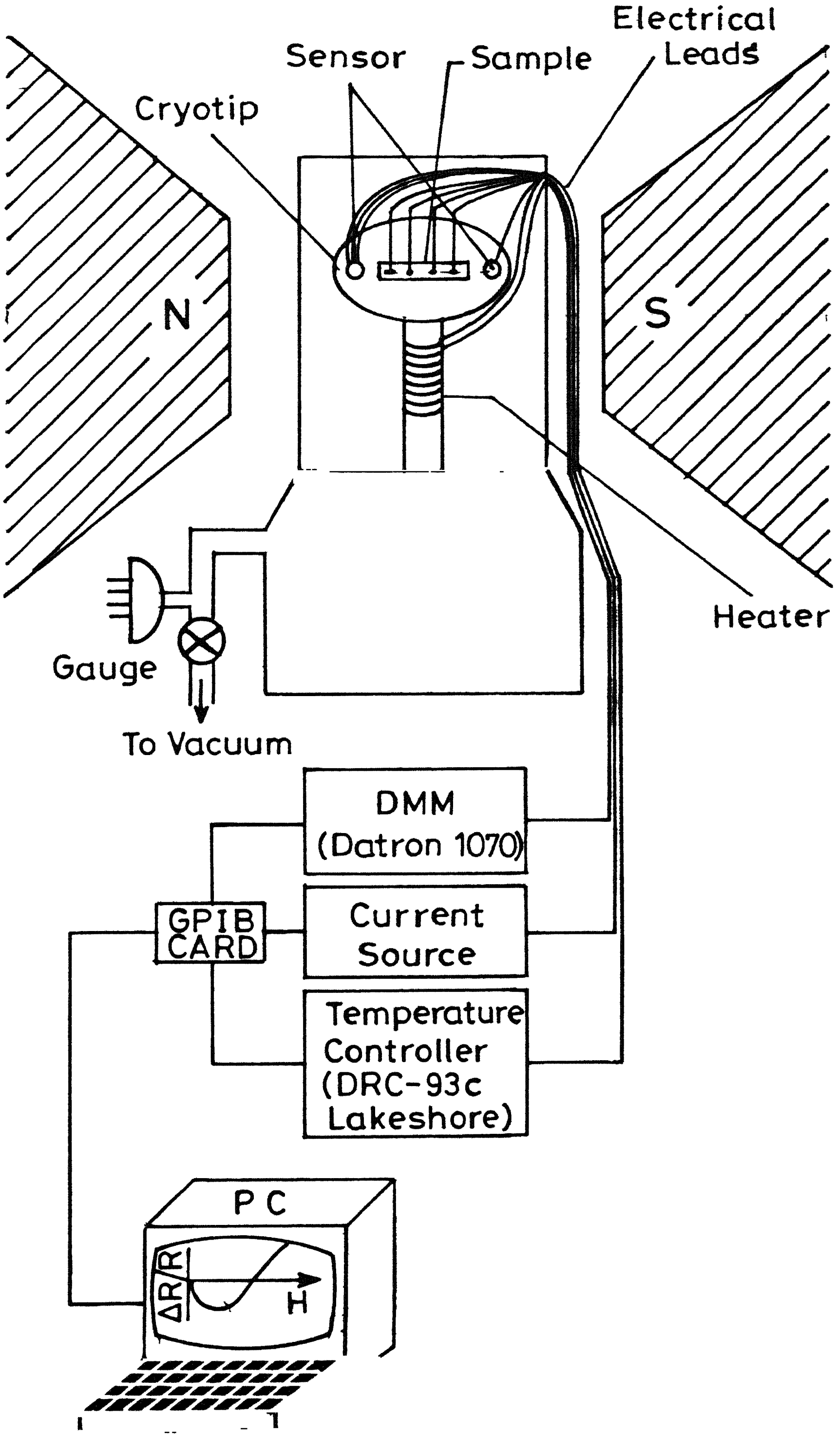

Figure 2.4. Schematic diagram of the magnetoresistance set-up.

the period of measurements (0 to 16.5 kOe) which is about 30 minutes. Using this set-up we are able to detect changes in resistance of a few parts in 10^6.

The magnetic field is monitored and sensed using a combination of a magnet power supply (Varian, Fieldial), a Gaussmeter (RFL, USA, Model 912) and a Hall probe.

2.2.2 dc-magnetization

The dc-magnetization measurements [M(H) and M(T)] are carried out between 19 and 300 K in magnetic fields up to 16.5 kOe. For this purpose, a closed-cycle helium refrigerator (CTI,RMC, USA), suitably modified by the manufacturer to fit with the vibrating sample magnetometer (Princeton Applied Research, Model 155) assembly, alongwith the electromagnet (Varian 15") is used. The use of the cryotip in conjunction with the VSM, however, created two major difficulties.

(1) In this system there is either a OFHC Cu or a Cu-Be tube inside which the sample vibrates, driven by a transducer assembly (which converts ac signal of frequency 82 Hz from an internal oscillator to mechanical vibration). Low pressure He exchange gas is used in the sample zone. As the temperature is lowered, the electrical conductivity of Cu rises and there is a lot of unwanted shielding of the signal due to eddy currents. To overcome this a modification to the existing set up has been incorporated[5, 6]. This reduced the shielding significantly but did not remove it completely.

(2) When the cryotip of the closed-cycle He refrigerator is switched on, due to its vibration the accuracy of the data is reduced by atleast an order of magnitude because of the noise introduced. To examine contributions from the various kinds of excitations to the temperature–dependent demagnetization process (where the magnetization is very small), we have tactfully carried out very careful dc-magnetization M(T) measurements (accuracy of 1 part in 10^4) at 100 mK temperature interval in a field of 1 tesla. This is done in the following way. After cooling the sample in zero field (ZFC), a magnetic field of 1 tesla is switched on. Then the cryotip is switched off at the lowest temperature and M(T) data were taken as the temperature gradually increased. In this way we have eliminated the effect of the extra noise

added to the signal of the VSM coming from the to and fro movement of the piston of the closed-cycle helium refrigerator.

A 100 Ω precalibrated platinum resistance thermometer, mounted very close to the sample, is used to monitor the temperature, employing a PID temperature controller (Lakeshore, DRC-93C) adapted with a multipurpose card (Pt card is used here). This ensures high accuracy in the measurement of temperature. A 50 Ω twisted Nichrome wire, wound on the OFHC copper tube very near to the sample, is used as a heater wire. An external constant current source (Hewlett Packard, Model 6226B) is used for supplying the heater current.

A high–temperature oven assembly in conjunction with the VSM is used for the dc - magnetization measurements in the temperature range of 300–700 K. A special high–temperature vibrating rod attachment, consisting of fused quartz extension with high purity boron–nitride guides and sample holder cup, is used for this purpose. Inert helium gas is used at the sample zone because its high thermal conductivity provided a good thermal contact between the sample and the hot wall surrounding it. All the measurements are done at a constant magnetic field of 2 - 5 kOe. A chromel-alumel thermocouple is used to measure the temperature with an accuracy of ±0.5 K.

The very high-field dc–magnetization (M–H) and magnetoresistance $[\frac{\Delta\rho}{\rho}(H)]$ measurements are carried out using a computer contolled Vibrating Sample Magnetometer (Princeton Applied Research, Model FM-1) adapted with a water–cooled Bitter coil magnet (2–T type) of 52.5 mm bore at the Francis Bitter National Magnet Laboratory, Massachussets Institute of Technology, USA. All the M–H measurements are done between 4.2 and 60 K and up to magnetic fields as high as 20 tesla using a 10 MW power supply[7]. The data acquisition is done through a PC / AT in both continuous scanning increasing and decreasing field modes. The temperature of the sample is measured by a calibrated carbon resistor glued to the vibrating rod somewhere between the heater and the sample. However, the temperature is controlled by a similarly mounted glass–ceramic capacitance sensor and matching electronics.

Both the VSM's are calibrated with standard Ni samples as well as low magnetic moment (paramagnetic Er_2O_3, Gd_2O_3) compounds after the usual saddle point adjustments. The absolute accuracy in dc–magnetization measurements is better than 1 part in 2500. The stability of temperature during the measurements is within ± 100 mK below 60 K.

2.2.3 Electrical resistivity

At the beginning of this thesis work there was no liquid helium plant in the laboratory. Because of the non-availability of liquid He^4 at that time, all the measurements were restricted at the most down to 8 K obtained from closed - cycle helium refrigerators. However, during the later part of the work, a liquid helium plant (KOCH–1400, USA) was acquired. I took an active part in the installation process. Only since the last three years that the He^4 plant has become operational after rectification of different kinds of problems (e.g., problems in cryogenic parts, leaks in the recovery gas line, electrical faults, problems associated with the chilling unit which is supposed to cool the compressor of the liquid He^4 plant, problems associated with the liquefier itself (expansion engine) failing to work in the automatic mode, etc.).

Electrical resistivity measurements $[\rho(T)]$ of the two series (crystalline and amorphous) of alloys are carried out using three different set-ups in various temperature ranges. All these set-ups were developed during the course of this work.

10–370 K Resistivity set-up

Before liquid He^4 was available, the resistivity $[\rho(T)]$ measurements of all the samples under the present study have been carried out in the temperature range of 10–370 K using a combination of a closed-cycle helium refrigerator (Cryosystem Inc.,RMC, USA), a LakeShore Cryotonics temperature controller (Model DRC-93C), a 7 and 1/2 digit Datron (Model 1071) digital multimeter, an IBM compatible PC/AT (80386) and a GPIB card. A typical cryostat and a measuring unit used with closed-cycle helium refrigerator have already been shown earlier (Fig.2.4) where the magnetoresistance set-up was discussed.

All the resistivity measurements are carried out using a standard four probe dc technique. The typical length of the samples used is $\sim$ 2 cm. The electrical contacts to the sample are made by soldering thin phosphor–bronze wires with Zn-Cd non-superconducting solder using $ZnCl_2$ flux. A low wattage soldering iron is used for soldering purpose. The sample is mounted on the cold head of the closed-cycle helium refrigerator with GE (General Electric) varnish which gives both good thermal contact and electrical insulation between the sample and the cold head. Precautions are also taken to thermally anchor all the wires leading to the sample. The current and voltage leads are connected to a digital multimeter (Datron, Model 1071) which measures the four wire resistance directly with 7 and 1/2 place resolution at 10 Ω full scale. The measuring current is kept at 10mA. Two calibrated silicon diodes (LakeShore, Model DT-470) are placed very near to the sample to monitor the temperature. Both these sensors are attached to the cold head with indium foils for contact between them. A heater is wound with non-inductive winding just below the cold head. The stability of temperature during the measurements is within ± 10 mK. The absoulute value of resistivities are accurate to within 5% due to uncertainty in the measurements of the dimensions of the samples. However, the relative accuracy of the resistivity data is better than (1–5) parts in 10^5 in the low temperature range.

300–600 K resistivity set-up

As very accurate $\rho(T)$ data are essential even at temperatures beyond 300 K in the disordered Fe-Ni-Cr alloys, a special set-up is designed for measurements up to 700 K. In Figs. 2.5 and 2.6 we have shown the high-temperature resistivity set-up which has been developed during the course of this study.

Figure 2.5 shows a schematic diagram of the set-up along with the measuring equipment. The measurements are carried out in a big cylindrical quartz tube properly placed inside a furnace. Highly resistive nichrome wires are used to wind the heater coil of the furnace. In Fig.2.6, the complete heating assembly along with the temperature sensing and monitoring unit have been shown. A combination of a furnace heater coil (100 Ω), a variac (0-250 volt ac), an ac-ammeter (0-5 amp.) and a highly sensitive digital programmable PID temperature controller (Yamatake–Honeywell, Japan, Model DIGITRONIK–DCP 200) adapted with a solid state relay (Yamatake–Honeywell, Japan, Model PGM152AO) have been used. The current

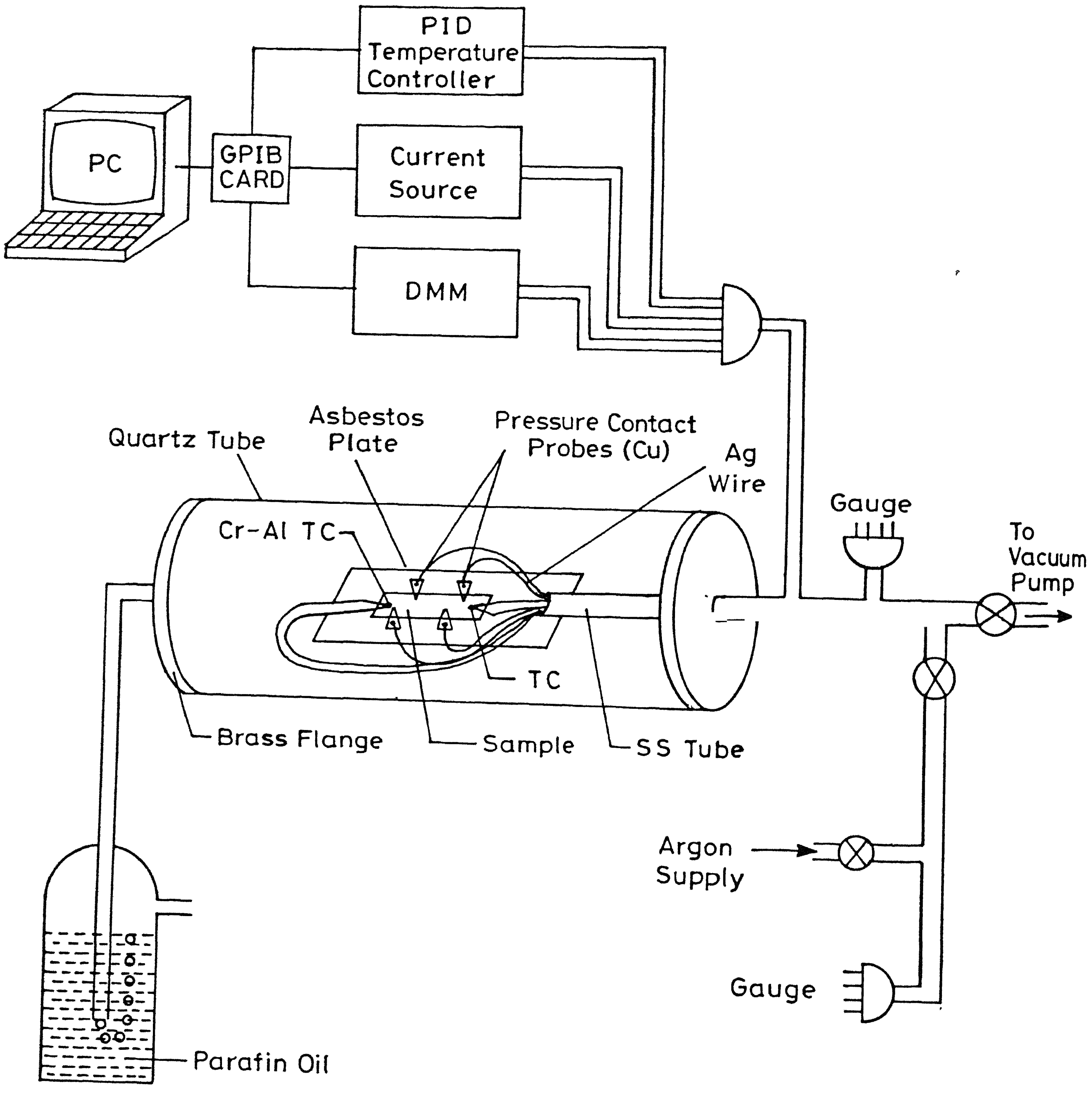

Figure 2.5: Schematic diagram of the high temperature (300-600 K) resistivity set-up.

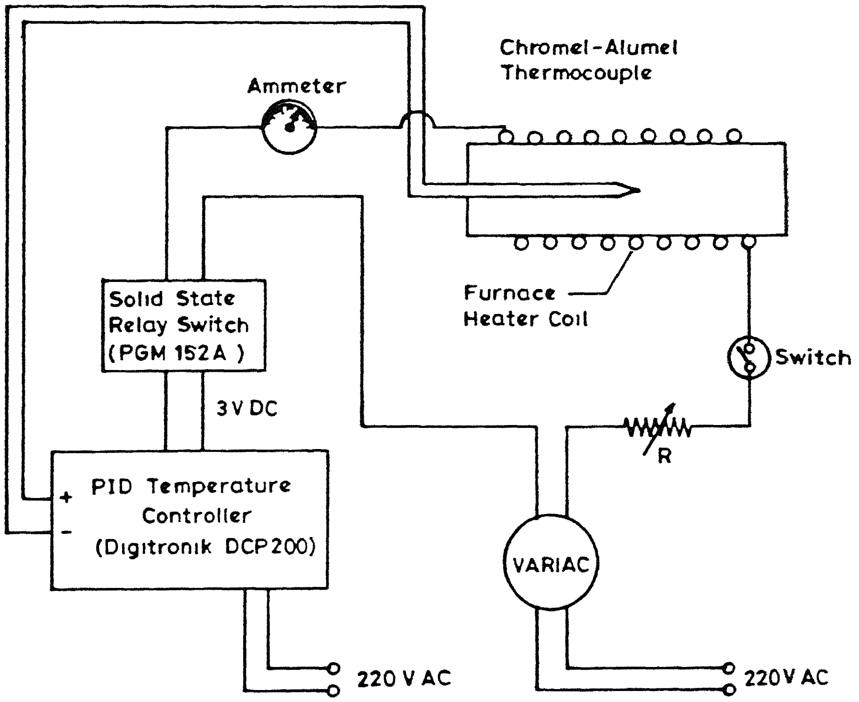
Chromel-Alumel Thermocouple
Ammeter
Solid State Relay Switch (PGM 152A)
Furnace Heater Coil
Switch
3 V DC
R
+
-
PID Temperature Controller (Digitronik DCP200)
VARIAC
220 V AC
220V AC

Figure 2.6: Schematic diagram of the heating arrangement for resistivity measurements in the temperature range 300-600 K.

in the furnace coil was always kept at less than 4 ampere with a proper setting of the variac, a resistance (R), the PID temperature controller and the 3 volt dc driven solid-state relay.

The sample holder used is an asbestos sheet of 9 cm length and 3 cm breadth, on top of which a plane mica sheet is attached. The electrical connections are made by pressure contacts employing 4 sharply edged copper block tightened by springs and screws. Four high purity Ag wires (Oxford Instruments) are used as current and voltage leads to the sample. This avoids formation of even a trace of any insulating oxide at high temperatures thus providing a better electrical contact. Two chromel-alumel thermocouples are used very near to the two extreme ends of the sample and the temperature recorded is the average of these two thermocouple readings. The difference between the two readings never exceeds 0.5 K. The inner zone of the quartz tube is first evacuated to 10^{-3} torr and a continuous flow of 1.5 psi argon gas is set from a gas cylinder adapted with a high-precision pressure regulator. Argon gas from the other end of the quartz tube is allowed to vent slowly through a capillury tube, one end of which is immersed in oil. Argon comes out through it in the form of bubbles, the rate of which is set at 7-10 bubbles/minute. This facilitates taking near-equilibrium data during slow heating and cooling. A constant current source (Hewlett Packard, Model 6177C), a 7 and 1/2 digit display digital multimeter (Datron, Model 1071) and a double pole double throw (DPDT) switch are used for taking data for both direct and reverse currents. The sample current used is 100 mA.

During each measurement the stability of temperature is better than ± 0.5 K in the high temperature range. The time taken for a typical run from 300 K to 600 K in this high-temperature set-up is typically 5-6 hours.

1.2–300 K resistivity set-up using liquid He^4

Figures 2.7 and 2.8 schematically show the cryostat and the measuring unit used for resistivity measurement for some melt-spun metallic glass samples $(Cu_{0\ 36}\ Zr_{0\ 64})_{1-x}Al_x$ with x = 0, 0.1, 0.15, and 0.2 and $(Ni_{0.5}Zr_{0.5})_{1-x}Al_x$ with x = 0, 0 05, 0.1, 0.15, and 0.2 in the temperature range of 1.2 to 310 K using liquid He^4 as a coolant.

The cryostat is made to fit inside a glass dewar system. The cold finger of the cryostat consists of high conductivity OFHC copper block. The same is used as a base plate for the sample holder and for anchoring heater wires (Figs.2.7 and 2.8). This base plate (block) is supported by three stainless steel rods which are brazed to the top flange (made of brass) of the cryostat (Fig.2 7). Stainless steel being a poor thermal conductor minimizes the heat leak to the surrounding. A small brass plate is used as a radiation shield (Fig.2.7). A 50 Ω manganin heater, wound around the base block and attached by low temperature GE-varnish (General Electric, UK), is used for temperature variation. 35 SWG high purity coaxial copper wires are used as leads for current, voltage, heater wire and sensors. All the current and voltage pairs are twisted together to reduce the flux noise in the measurements. All the leads are thermally anchored to a copper screw attached with the top flange. A calibrated Si-diode (LakeShore, Model DT-470), attached to the base block (Fig.2.8) near the samples is used for monitoring the temperature. The top and bottom faces of the copper block (Fig.2.8) are shorted by a

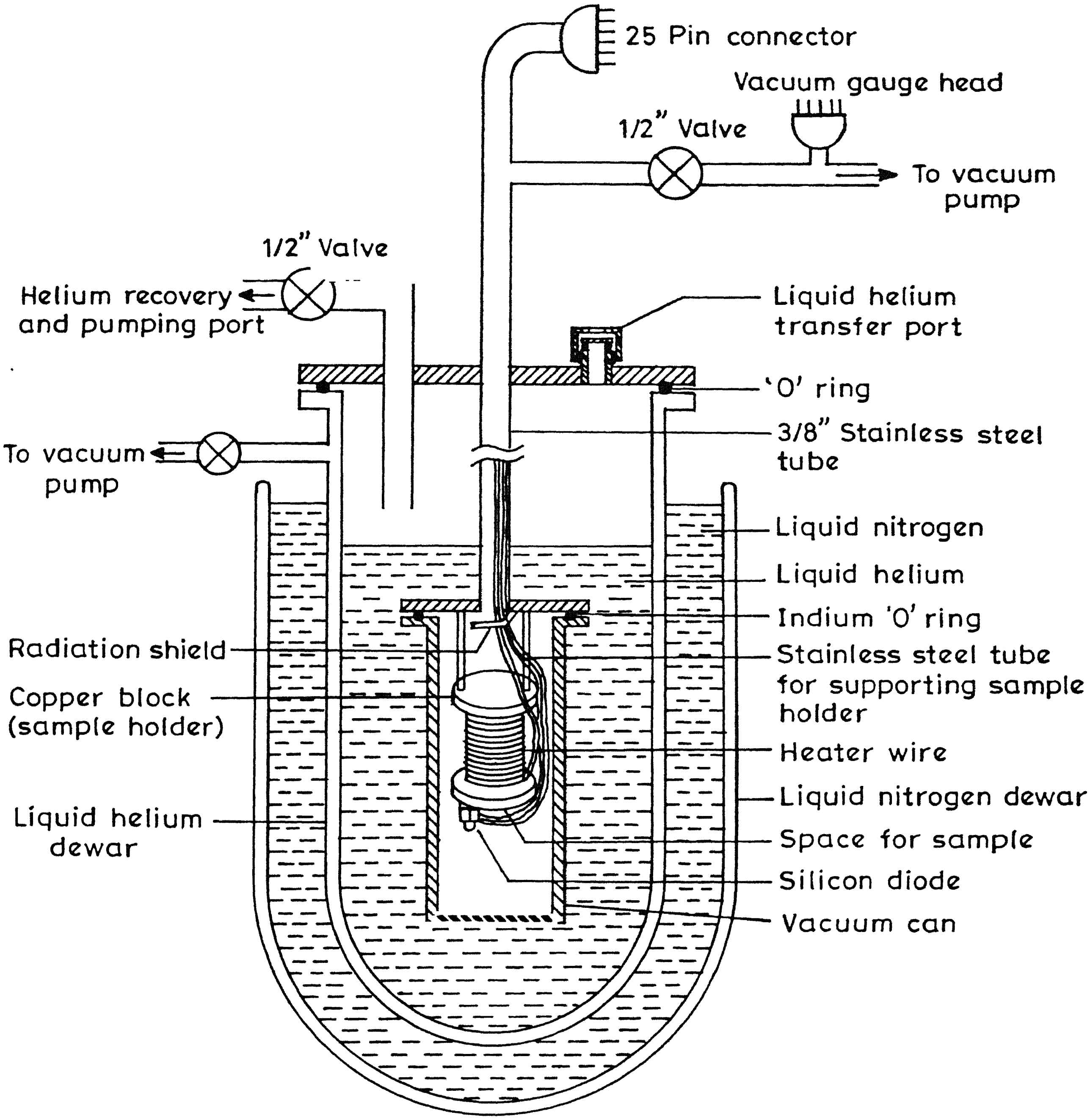

Figure 2.7: Schematic diagram of the He^4 cryostat used for resistivity measurements in the temperature range 1.2–300 K.

thick copper wire for better thermal stability. An indium 'O'-ring is used between the top flange and the vacuum can.

A conventional four-probe dc technique has been employed to measure the electrical resistance ($\rho(T)$) of nine metallic glass ribbons. The current and voltage contacts with the sample are made with non-superconducting Zn-Cd solder and Zn-Cl_2 flux. A very low wattage (15 W) soldering iron is employed to make each contact within a very short time to prevent, as far as possible, any crystallization at the point of contact. Samples are placed at the bottom of the copper block very near the Si-diode using GE-varnish (diluted) which provides good electrical insulation as well as good thermal contact between the samples and the copper block. Moreover, a very small amount of helium exchange gas is used in the sample zone for good thermal contact between the wall of the metal can and the samples mounted on the copper block.

A combination of a PID temperature controller (LakeShore, Model DRC-93C), a current source (Keithley, Model 220) and a digital multimeter (Prema, Model 6001) adapted with a 20 channel scanner is employed. Data acquisition is done for $\rho(T)$ measurements through PC/AT (80386) and IEEE-488-interfaced measuring instruments employing a GPIB I/O card. The software developed for data acquisition for simultaneous measurements of two samples have been provided in the APPENDIX–A of the thesis. Only two channels have been used in the present set up. The same software with small modifications can be used for simultaneous measurements of 20 samples exploiting all the 20 channels of the scanner.

The cryostat is first evacuated to 10^{-3} torr and then the outermost dewar is filled with liquid N_2. After transferring liquid helium to the inner dewar from a 16 litre helium container with the help of a transfer siphon, sufficient time has to be given to the sample zone to attain 4.2 K. Then the lowest temperature of 1.2 K is attained by pumping on the He^4 bath by a very high speed Kinney pump (Model KDH–130, pumping speed 130 ft^3/min.). A typical measuring current of 15-30 mA has been used to minimize any heating effect in these highly resistive metallic glasses even at 1.2 K. We found that larger measuring currents (> 50 mA) disturb the thermal stability considerably at the lowest temperature of 1.2 K. $\rho(T)$ data are

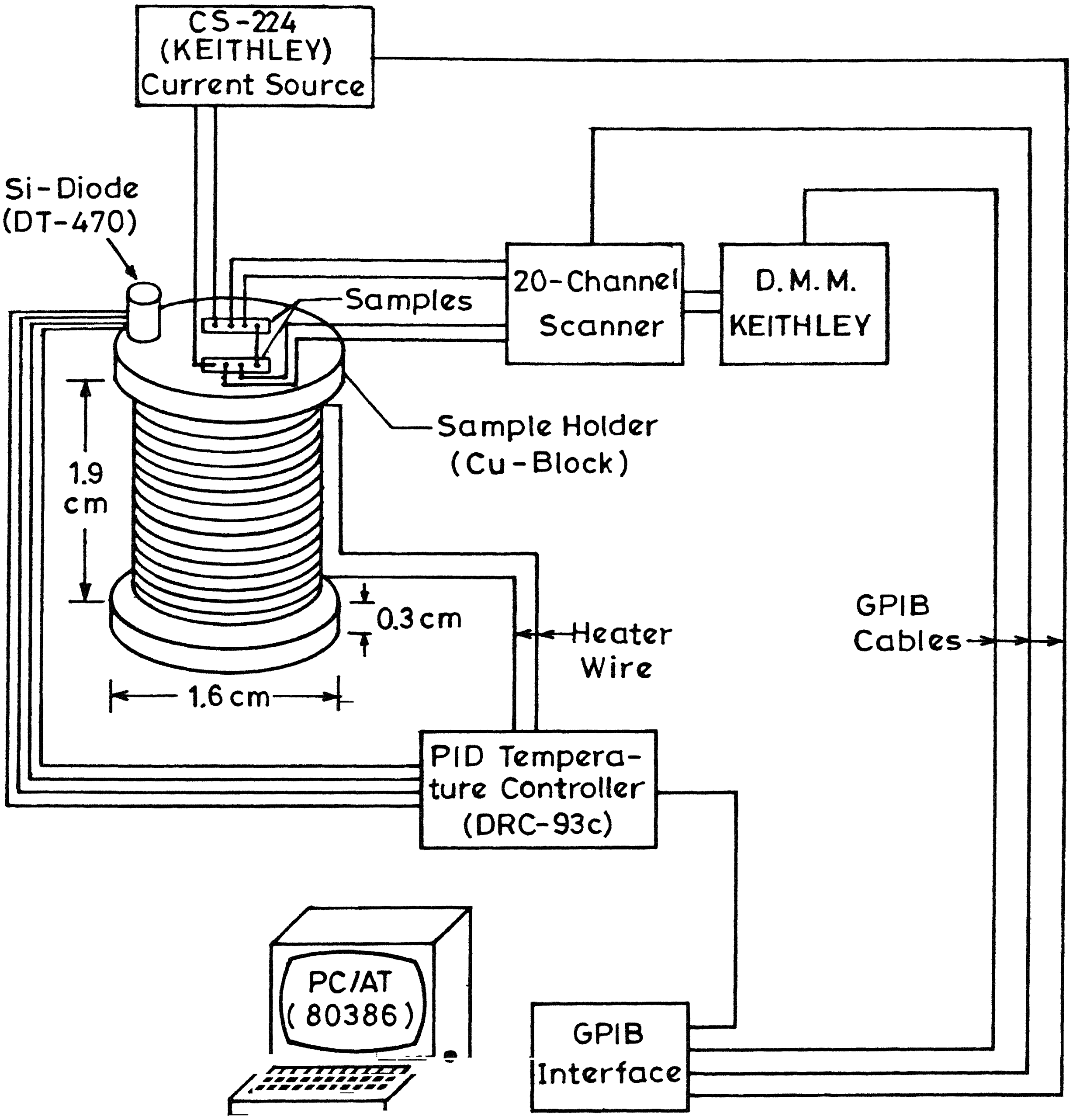

Figure 2.8: Schematic diagram of the cold finger of the He^4 cryostat and the circuit diagram for the connection with the measuring instruments.

taken at intervals of 50 mK in the range of 1.2 - 50 K and then 100 mK till 310 K. The temperature stability during each measurement is ±10 mK. The time taken for a typical run from 1.2 K to 310 K in this cryostat is 13-14 hours for simultaneous measurements of two samples. The geometrical factors for converting resistance to resistivity are determined from mass, density, length and width of these metallic glass ribbons. The absolute accuracy of the resistivity is only within 5% due to the uncertainties in the measurements of the geometrical factors. The relative accuracy ($\Delta R/R$), however, is better than 1-5 parts in 10^6.

Methodology for temperature stability and resistivity measurements (1.2 to 310 K) used in the software (Appendix-A)

The automation is done by attaching a GPIB I/O card to an IBM compatible PC/AT (80386) and IEEE-488 interfacing attached to the respective instruments. The low level software support is provided by a device driver, GPIB.COM, supplied by the manufacturer of the GPIB card. The next level of the software is written in *Turbo Pascal* to make a link between the device driver and the high level language. While writing the software for data acquisition in *Turbo Pascal*, some important steps are taken. These are mentioned below.

The temperature of the copper block and hence the sample is controlled by sensing the temperature through the Si-diode and giving the required current to the heater. The heater current is controlled by the proportional–integral–derivative (PID) control parameters of the temperature controller (LakeShore, Model DRC-93C). By a proper choice of the PID values of the controller the temperature of the sample can be controlled within 10 mK in the temperature range of 1.2 - 310 K.

After the stabilization of temperature, the current source is set to send a forward current (I+, which is between 15 and 30 mA depending upon the resistance of the sample) through the current leads of the sample. Then after a delay of 5 s, the digital multimeter (DMM) is set to measure the volatage developed across the voltage leads of the sample. The DMM is set to take 20 sampling voltage data (v+) for the forward current and store into its buffer memory.

The acquisition of each data takes about a 10^{-3} s. Then the current source is set to send the same current in the reverse direction (I-). After a 5 s delay the DMM takes 20 sampling voltage data (V-) for the reverse current and stores again into its buffer memory. Then all the data are sent to the PC/AT through IEEE-488 bus. Finally it calculates the mean value of the resistances and the standard deviation for that particular stabilized temperature.

Taking one set of data as mentioned above at any temperature for one sample, the built-in scanner with the DMM is set in such a way as to connect the next channel for the measurement of resistance of the second sample. In principle, one can measure 20 samples simultaneously using this 20 channel built-in scanner of the DMM. At present two channels have been used. After setting the second channel it does the same exercise of measuring the mean resistance and the standard deviation of the second sample at that particular temperature. Reversing the current is essential to eliminate the effect of any thermo-emf. Then the copper block along with the samples are taken to some other temperature (with a small increment ~ 50 mK) by giving the required current to the heater controlled by the PID temperature controller.

The criterion for the temperature to be considered as steady has been implemented in this software in the following way :

- While taking 20 sampling voltage data (v+) for forward current (I+), 20 sampling temperature data (T_{FS}) are also taken simultaneously. The absolute value of the standard deviation of these 20 samplings $T_{FS} \leq$ a preassigned tolerance limit.
- For the reverse current (I-) also, the absolute value of the standard deviation of the 20 sampling temperatures $T_{RS} \leq$ a preassigned tolerance limit.
- $\left|\overline{T_{FS}} - \overline{T_{RS}}\right| \leq$ a preassigned tolerance limit where $\overline{T_{FS}}$ and $\overline{T_{RS}}$ are the mean values of 20 sampling temperatures during forward and reverse currents, respectively.

2.2.4 Thermoelectric power

The thermoelectric power (TEP) measurements of all the nine amorphous Cu/Ni-Zr-Al metallic glass ribbons are carried out using the standard differtial technique in which a thermocouple grade copper wire is used as a reference material. The sample whose TEP is to be measured is tightly held between two polished copper blocks (supported by stainless steel rods) using GE-varnish and copper screws. The inner surface of the copper block is electrically insulated but thermally connected by Ge-varnish. A small carbon resistor is used as a heater attached to the top of the copper block. A differential Cu-constantan thermocouple, attached to the copper disc, is used to measure the temperature difference between the hot and cold ends of the sample. A Si-diode (LakeShore, Model DT-470) is attached to one of the blocks to measure the sample temperature (after taking into account all corrections). A 50 Ω twisted manganin wire is used as a heater wire for changing the sample temperature. The voltage ΔV and the temperature difference ΔT across the two ends of the sample are measured using a nanovoltmeter (Keithley, Model 182) in combination with a scanner (Keithley, Model 705) and a source measuring unit (Keithley, Model 238) used as a current source. Then $\Delta V/\Delta T$ gives the thermopower of the sample with respect to copper. The absolute TEP is obtained by adding to this quantity the thermopower of copper which is obtained from reported data[8]. The calibration of the set-up is done with a high purity Pt. The estimated absolute error in the measurement of TEP is less than 10 %. Data acquisition is done through PC/AT (80386) and IEEE-488-interfaced measuring instruments employing a GPIB I/O card.

Bibliography

[1] A. K. Majumdar and P. v. Blanckenhagen, Phys. Rev. B **29**, 4079 (1984).

[2] A. Z. Men'shikov, S. K. Sidorov, and A. Ye. Teplykh, Phys. Met. Metallogr. (USSR) **45**, 42 (1979).

[3] Sidney H. Avnar, *Introduction to Physical Metallurgy* (Mcgraw-Hill, 1987).

[4] A. K. Bhatnagar, R. Pan, and D. G. Naugle, Phys. Rev. B **39**, 12460 (1989).

[5] A. Banerjee, Ph.D. thesis, Indian Institute of Technology, Kanpur, India, 1990.

[6] A. Das, Ph.D. thesis, Indian Institute of Technology, Kanpur, India, 1993.

[7] Lawrence G. Rubin and Peter A. Wolf, Physics Today 24, August (1984).

[8] D. S. Dugdale, *Electrical properties of metals and alloys*, Edward Arnold, London (1977).

Chapter 3

Electrical transport–resistivity $[\rho(T)]$

In this particular study we have performed systematic measurements of the electrical resistivity (ρ(T)) of γ-$Fe_{80-x}Ni_xCr_{20}$ ($14 \leq x \leq 30$) highly resistive austenitic stainless steel alloys in the fcc γ-phase in the temperature range between 10 and 600 K. The magnetic phase diagram[1, 2] had been established in this alloy system through dc-magnetization, magnetic neutron scattering and ac-susceptibility measurements. The ingredient of these alloys are the 3d-transition metals Fe, Ni and Cr where every atom is magnetic in nature. Due to the competing exchange interaction (in the model of Heisenberg exchange) between the different kinds of magnetic atoms (nearest neighbour interaction is either FM or AFM with positive or negative values of exchange integral, J_{ij}), this system of alloys undergoes a compositional phase transition from long-range AFM (x = 10-14) to SG (17-21), to mixed FM and SG (23-26), to long-range FM ($x \geq 30$) state within the same crystallographic γ-phase. In the mixed phase alloys (x = 23–26), the coexistence of long-range FM and SG orderings was confirmed through M–H[1, 3] and magnetoresistance[3] measurements. This is understood on the basis of the Gabay - Toulouse[4] model of mixed phase where the transverse spin freezing (say, in x-y plane) takes place alongwith long-range FM ordering (in z direction) below the second transition.

We have reported earlier[3] (also to be discussed in details in Chapter 4) the magnetoresistance (MR) measurements on these alloys where we found that the MR are negative till

---

[1] This chapter is mainly based on the published work by T. K. Nath and A.K. Majumdar, *Phys. Rev. B* **53**, 12148 (1996).

a temperature $\approx 50K$ in the field range of 0-1.7 tesla. A correlation between magnetization and magnetoresistance was observed only in the SG alloys (x =19,21) with $\Delta\rho/\rho \propto M^{2\,5}$. ρ(T) measurements on this system of alloys at low temperatures were recently reported by Banerjee and Raychaudhuri[5, 6]. They found a resistivity minimum in each alloy[5] around 8-10 K. The low-temperature rise in ρ(T) below T_{min} in each alloy had $\sqrt{T}$- like functional dependence which has been ascribed to the electron - electron interaction in the presence of weak localization. This becomes dominant at low temperatures and provides a quantum correction to the Boltzmann conductivity They concluded that the magnetic state does not play any significant role in the $\sqrt{T}$ behaviour which is due to quantum interference effects. In the temperature range between T_{min} and 80 K[6], they have found contributions to ρ(T) from T^2 and T^3 – dependent terms, their relative proportion being dependent on the Ni concentration.

The motivation behind the present work is to study the electrical transport properties over a wider range of temperature (10 to 600 K) of γ-$Fe_{80-x}Ni_xCr_{20}$ ($14 \leq x \leq 30$) alloys with varying magnetic phases. At very high temperatures (where the contribution to the resistivity from magnetic scattering can be neglected because of the complete disruption of magnetic ordering due to large values of thermal energy (k_BT)), the deviation from linearity (DFL) of resistivity which might lead to a saturation, gives one an opportunity to investigate thoroughly this long-debated phenomenon for highly resistive crystalline magnetic alloys. Several models or theories have been proposed on the DFL of resistivity (already discussed in Sec.1.3.2) which ultimately leads to a saturation value. In the present work, we have considered some of them which are the most appropriate ones to explain this phenomenon and tested them rigorously with our experimental ρ(T) data at high temperatures. The role of magnetic ordering in the electronic transport has also to be examined since the alloys are near the percolation threshold or the critical regime.

3.1 General features of the observed ρ(T)

In Fig. 3.1 we have shown the resistivity ρ(T) data in the temperature range of 10 – 600 K for the six disordered magnetic alloys of γ-$Fe_{80-x}Ni_xCr_{20}$ ($14 \leq x \leq 30$), all of which are around the stainless steel composition in the austenite state. The inset of Fig.3 1 shows a typical behaviour (x = 23) of the temperature dependence of dρ/dT of these alloys. From these ρ(T) curves the following observations can be made :

(i) There is no distinct signature of any magnetic transition in the ρ(T) plots at the respective transition temperatures (T_c , T_{SG} or T_N given in Table 3.1).

(ii) There is a peak in dρ /dT for each alloy at around 100K as shown in the inset of Fig.3.1.

(iii) ρ(T) of each alloy varies faster than T ($\sim T^2$) till 50 to 60 K.

(iv) The ρ(T) curve for each alloy starts deviating from linearity in the downward direction roughly beyond 200 K ($\approx \Theta_D/2$).

This behaviour is manifested in dρ/dT curve as well, where it starts to fall significantly from the maximum value. However, in sharp contrast to these results, Banerjee and Raychaudhuri[6] have observed that above 100 K, the ρ(T) plot for each alloy is linear till 300 K (their highest temperature of measurements). There is no indication of any saturation effect even at 300 K.

In Table 3.1 we have shown the different magnetic transition temperatures (T_c, T_{SG} and T_N) taken from reference 23, and ρ(10K), ρ(300K) and the temperature coefficient of resistance (TCR = ρ^{-1} dρ /dT) at 300 and 500 K from the data of Fig.3.1 for the alloys under investigation. From Table 3.1 one observes that all these disordered concentrated magnetic alloys possess very high values of residual resistivity (ρ(10K)). The TCR of each alloy is very small at 300 K and becomes still smaller at 500 K. It is also noticed that the magnitude of the TCR at room temperature decreases with ρ(300K) for varying alloy composition, thus obeying Mooij criterion[7]. Figure 3.2 shows the variation of the percentage change of ρ(500K) with respect to ρ(10K) and ρ(200K) with an increase of Ni concentration (x). It shows a roughly

Table 3.1: Ni concentration (x) dependence of magnetic transition temperatures (T_c, T_{SG}, T_N taken from ref.[1]), resistivities ρ at 10 and 300 K and TCR $[\rho^{-1}(\frac{d\rho}{dT})]$ at 300 and 500 K of γ-$Fe_{80-x}Ni_xC$ r_{20} (14 $\leq$ x $\leq$ 30) alloys.

Ni x (at.%)	T_c (K)	T_{SG} (K)	T_N (K)	ρ_{10K} $\mu\Omega$ cm	ρ_{300K} $\mu\Omega$ cm	$[\rho^{-1}(\frac{d\rho}{dT})]_{300K}$ ($\times 10^{-4}$ /K)	$[\rho^{-1}(\frac{d\rho}{dT})]_{500K}$ ($\times 10^{-4}$ /K)
14			26	58.4	91.0	11.5	7.5
19		12		67.8	96.6	9.3	6.5
21		10		72.1	105.1	9.3	6.0
23	35	20		83.0	109.0	7.8	5.5
26	56	7		90.6	118.3	7.6	5.2
30	135			87.9	109.0	6.5	4.1

linear dependence. The percentage change of ρ(500K) becomes smaller on the high Ni concentration side with large values of residual resistivity. The inset of Fig.3.2 shows an increase of the residual resistivity ρ(10K) with Ni concentration (x) till x $\approx$ 27.

Figure 3.3 is a plot of TCR vs x at three temperatures (100, 300 and 500 K). At each temperature the best-fitted curve shows a linear dependence of TCR on x. The slopes of the best-fitted straight lines as well as the TCR gradually decrease with temperature and both have a tendency to become zero beyond a certain temperature when the best-fitted line coincides with the x-axis. This implies saturation of the resistivity beyond a certain temperature.

Figure 3.4 shows a very striking correlation in these highly resistive alloys. It reveals that the thermal and compositional disorders have similar effects on the resistivity saturation. This is a plot of TCR with ρ for all the alloys as well as for the whole range of temperature beyond 100 K Here the increase of ρ at a fixed temperature implies increase in the compositional or chemical disorder. At the same time, the increase of temperature for a particular alloy

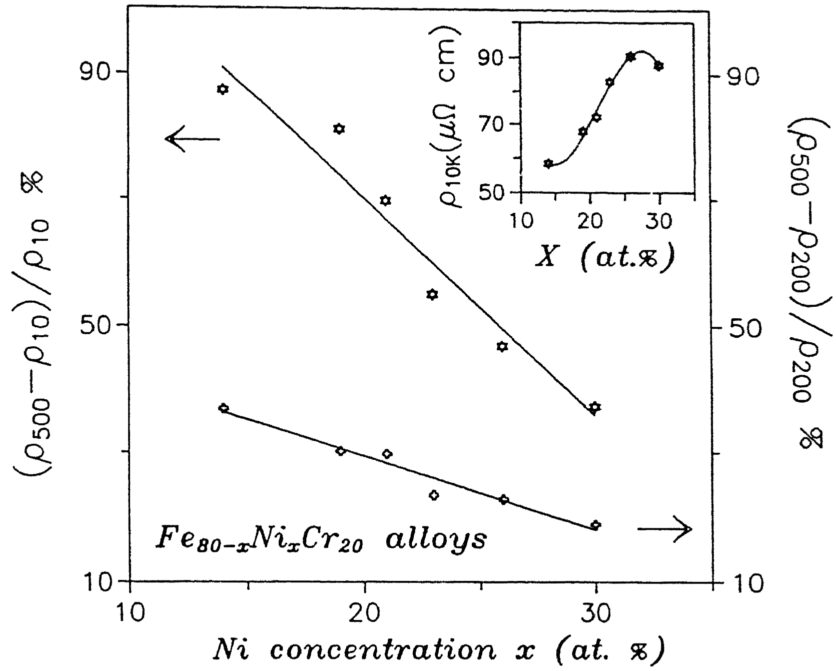

Figure 3.2: Percentage change of resistivity ρ(500K) relative to ρ(10K) and ρ(200 K) of $Fe_{80-x}Ni_xCr_{20}$ ($14 \leq x \leq 30$) alloys as a function of Ni concentration(x). The inset shows the x - dependence of the residual resistivity (ρ(10 K)). The solid curve in the inset is just a guide to the eye.

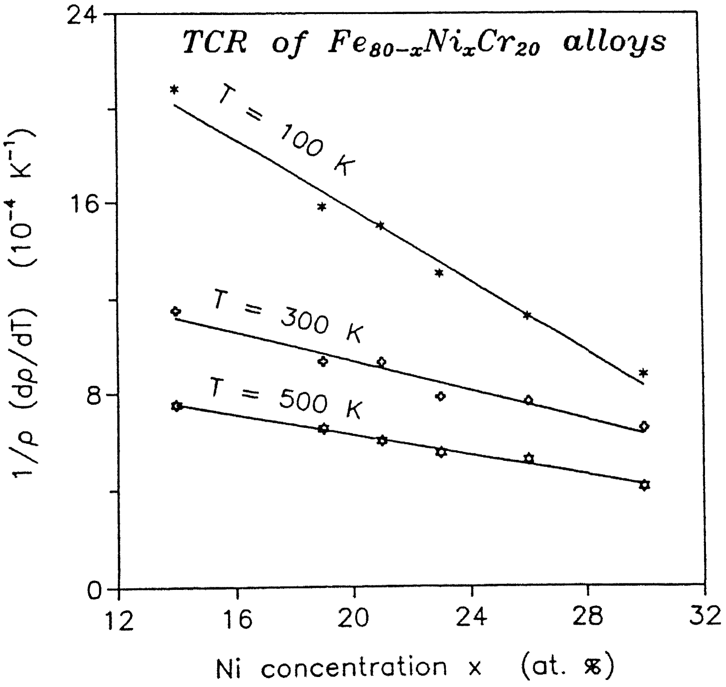

Figure 3.3: Ni concentration (x) dependence of the temperature coefficient of resistivity (TCR $= \rho^{-1}\frac{d\rho}{dT}$) of $Fe_{80-x}Ni_xCr_{20}$ ($14 \leq x \leq 30$) alloys at 100 K, 300 K, and 500 K.

corresponds to an increase in the thermal disorder. Surprisingly, for all the six alloys in the temperature range beyond 100 K, the data points fall on a common curve, no matter what causes the change of resistivity, compositional disorder or thermal disorder. As the disorder is increased (compositional or thermal), the TCR (α) decreases gradually. We have fitted this curve to an empirical relation α = -(γ/ρ) + δ , where γ and δ are constants ($\chi^2 \approx 10^{-7}$). By extrapolation of this best-fitted curve to TCR (α) = 0 where it cuts the ρ-axis, we have estimated the value of the saturation resistivity as $\rho_{\mathrm{sat}} \approx 180$ $\mu\Omega$ cm. This kind of correlation has also been found recently in crystalline TiAl alloys[8].

3.1.1 Analysis of ρ(T) data in the temperature range T_{min} ($\approx$ 10K) $\leq$ T $\leq$ 70K ($\approx \Theta_D/5$)

We have tried to fit the observed ρ(T) data of each alloy to a single temperature dependent term bT^n along with a constant term 'a' in the temperature range of 10 - 60 K. The fit functions, the values of the fitting parameters, the ranges of temperature and the values of χ^2, which give the goodness of fit, for all the six alloys are listed in Table 3.2. χ^2 is defined as

$$\chi^2 = \frac{1}{N}\sum_{i=1}^{i=N}\left(\frac{\rho^i_{expt.} - \rho^i_{fit}}{\rho^i_{expt}}\right)^2$$

where N is the number of data points. From Table 3.2 the following observations can be made:

(1) For the alloy with x = 14 which has a single PM - AFM transition[1] with $T_N = 26$ K, the data fit very well with the function a + bT^2 in the low-temperature range of 10 - 60 K beyond which the fit becomes poor. Between 10 and 60 K, $\chi^2 \approx 10^{-8}$ and is consistent with the experimental accuracy. We have shown the experimental data and the best-fitted curve in Fig.3.5 which is a plot of ρ vs T^2 for the alloy with x=14. The figure shows a clear linear dependence in the low temperature range. The inset of Fig.3.5 shows the percentage deviation of the experimental data from the best-fitted values as a function of temperature.

(2) For the alloys with x = 19 and 21, which have PM–SG transitions[1] at around 12 and 10 K, respectively, an additional T^3 term is necessary along with the T^2 term between

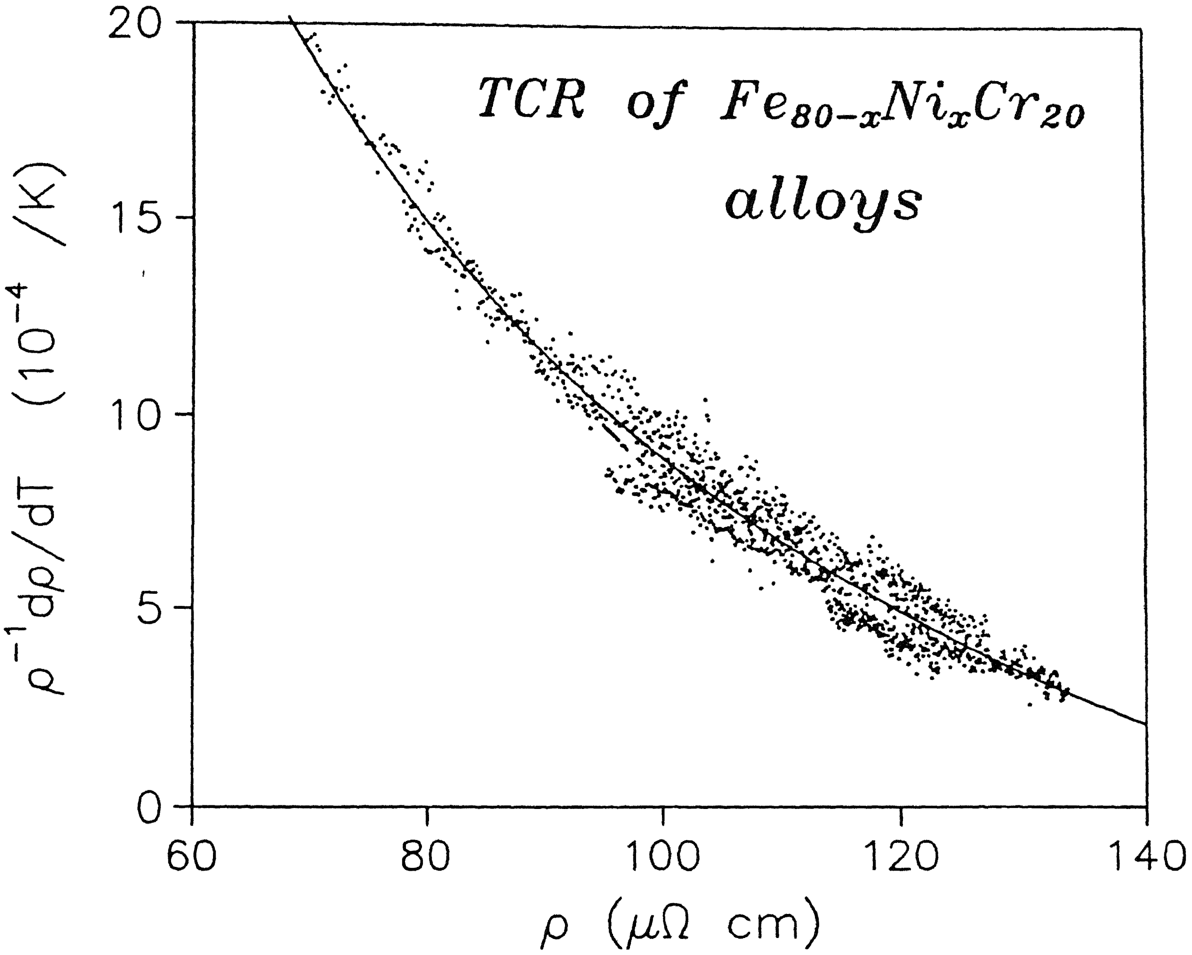

Figure 3.4: Resistivity (ρ which results from either thermal or compositional disorder) dependence of the TCR of $Fe_{80-x}Ni_xCr_{20}$ ($14 \leq x \leq 30$) alloys in the temperature range beyond 100 K. The solid line is the best-fitted curve.

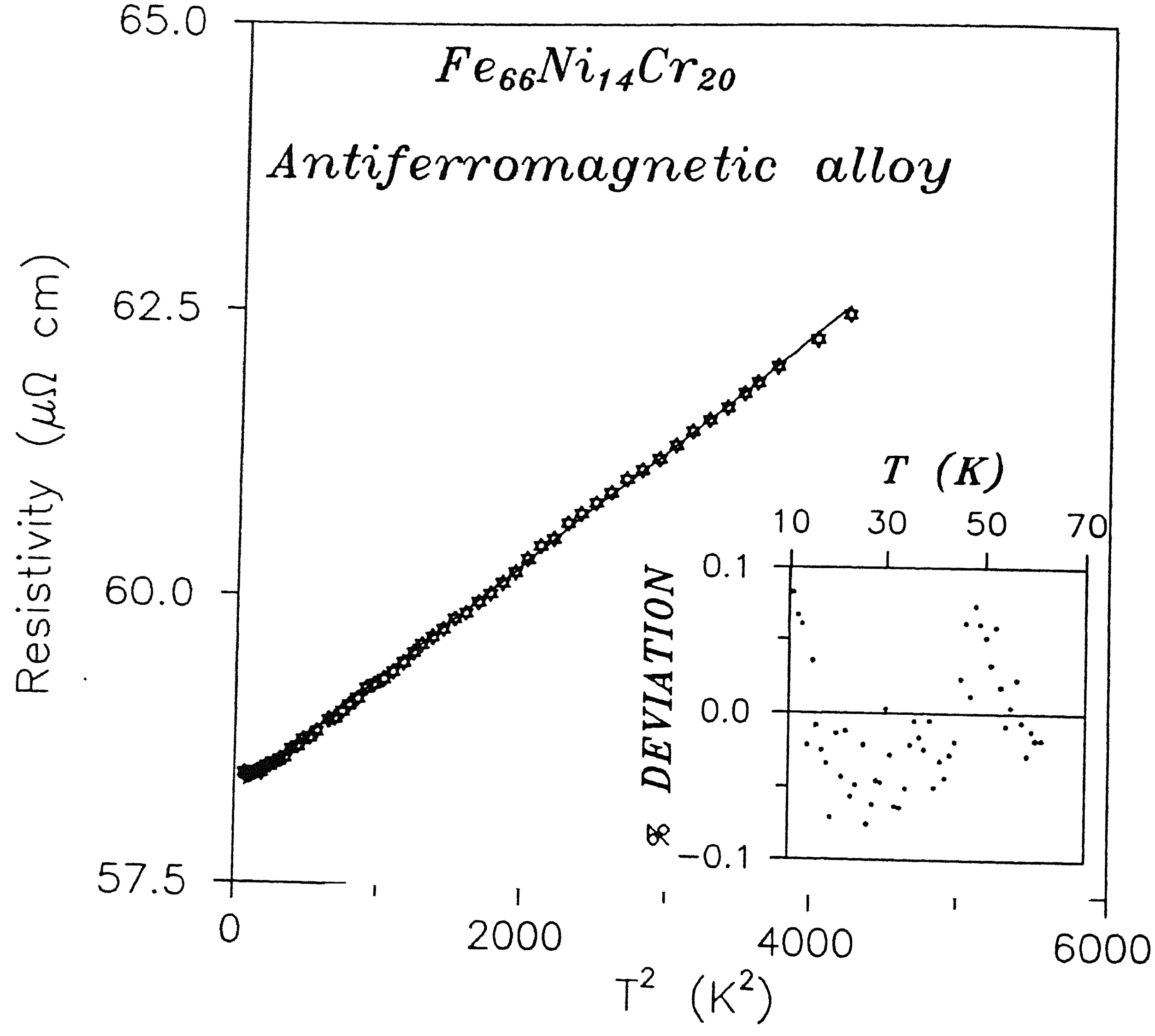

Figure 3.5: Resistivity (ρ) vs T^2 plot of $Fe_{66}Ni_{14}Cr_{20}$ antiferromagnetic alloy in the temperature range of 10 - 60 K. The solid line is the best-fitted curve. The inset plots the percentage deviation of the fit from the experimental data.

10 and 50 K to make the χ^2 ($\approx 10^{-8}$) consistent with the experimental accuracy. A single temperature-dependent term as for the antiferromagnetic (x = 14) alloy gives a poor fit with χ^2 larger by atleast 2 orders of magnitude With the addition of a cT^3 term, the χ^2 improves significantly so as to become consistent with the experimental accuracy in the temperature range of 10 – 50 K. The experimental data and the best-fitted curves are shown in Fig.3.6 for the spin-glass alloys (x=19 and 21).

(3) For the alloys with x = 23 and 26 which are in the mixed phase having T_c and T_{SG} at 35, 20 and 56, 7 K, respectively, the function a $+bT^2$ again, in the low-temperature region, fits very well. This fit is as good as in the earlier alloys.

(4) For the alloy with x = 30, which has only a PM–FM transition[1] at 135 K, the fit function a + bT^2 seems to be the correct choice giving a $\chi^2 \approx 10^{-8}$ between 10 and 50 K. The experimental data alongwith the best-fitted curves for x=23, 26, and 30 are shown in Fig.3.7 where ρ is plotted against T^2. These curves show a clear linear dependence in the low-temperature region.

Figure 3.8 shows how the fitting parameters, namely the constant term 'a' and the coefficient of the T^2 term 'b', vary with the increase of Ni concentration (x). The constant 'a', which can be attributed to the residual resistivity of these alloys, increases with 'x' and has a peak at around x = 27 (percolation threshold ≈ 20 at.% of Ni). Thus its behaviour is very similar to that of ρ(10K) as shown earlier in the inset of Fig.3.2. The coefficient 'b' has a large value for x = 14. It has got a minimum near x = 19 and then it regains its large value around x = 23 – 30 at.% of Ni. From these observations , it appears that the T^2 contribution dominates for the alloys which are away from the spin-glass region (x = 17 - 21) and in which long-range (FM or AFM) magnetic ordering sets in. Here the value of 'b' is more or less constant ($\approx 1 \times 10^{-3} \mu\Omega$ cm K^{-2}).

The T^3 contribution appears only in alloys with x = 19 and 21 which are in the spin-glass phase at the lowest temperature. In these alloys the T^2 contribution is somewhat small as compared to those of the others.

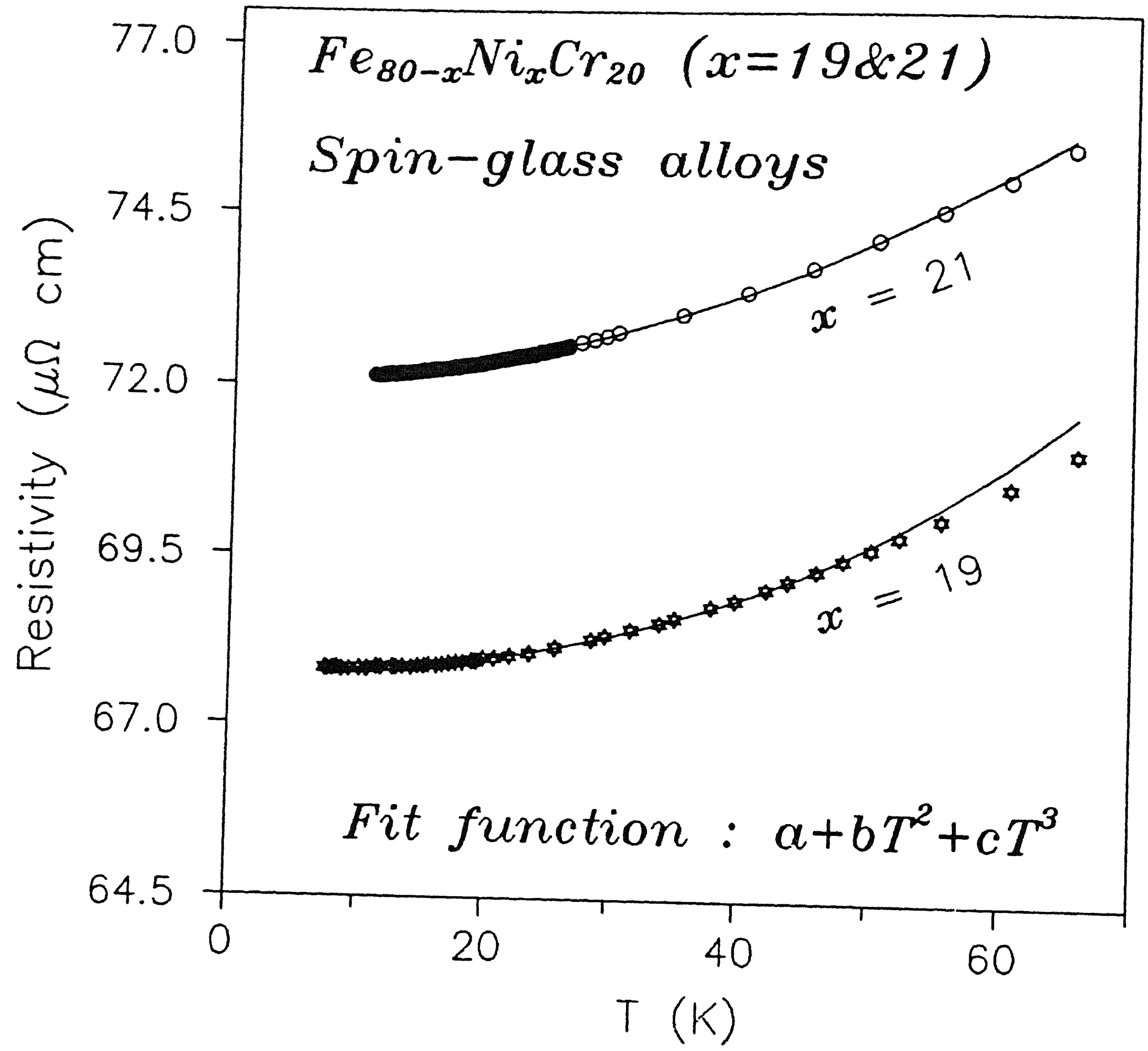

Figure 3.6: Temperature dependence of resistivity of $Fe_{80-x}Ni_xCr_{20}$ (x = 19 and 21) spin-glass alloys in the low temperature range. The solid lines are the best-fitted curves for the function $a+bT^2+cT^3$.

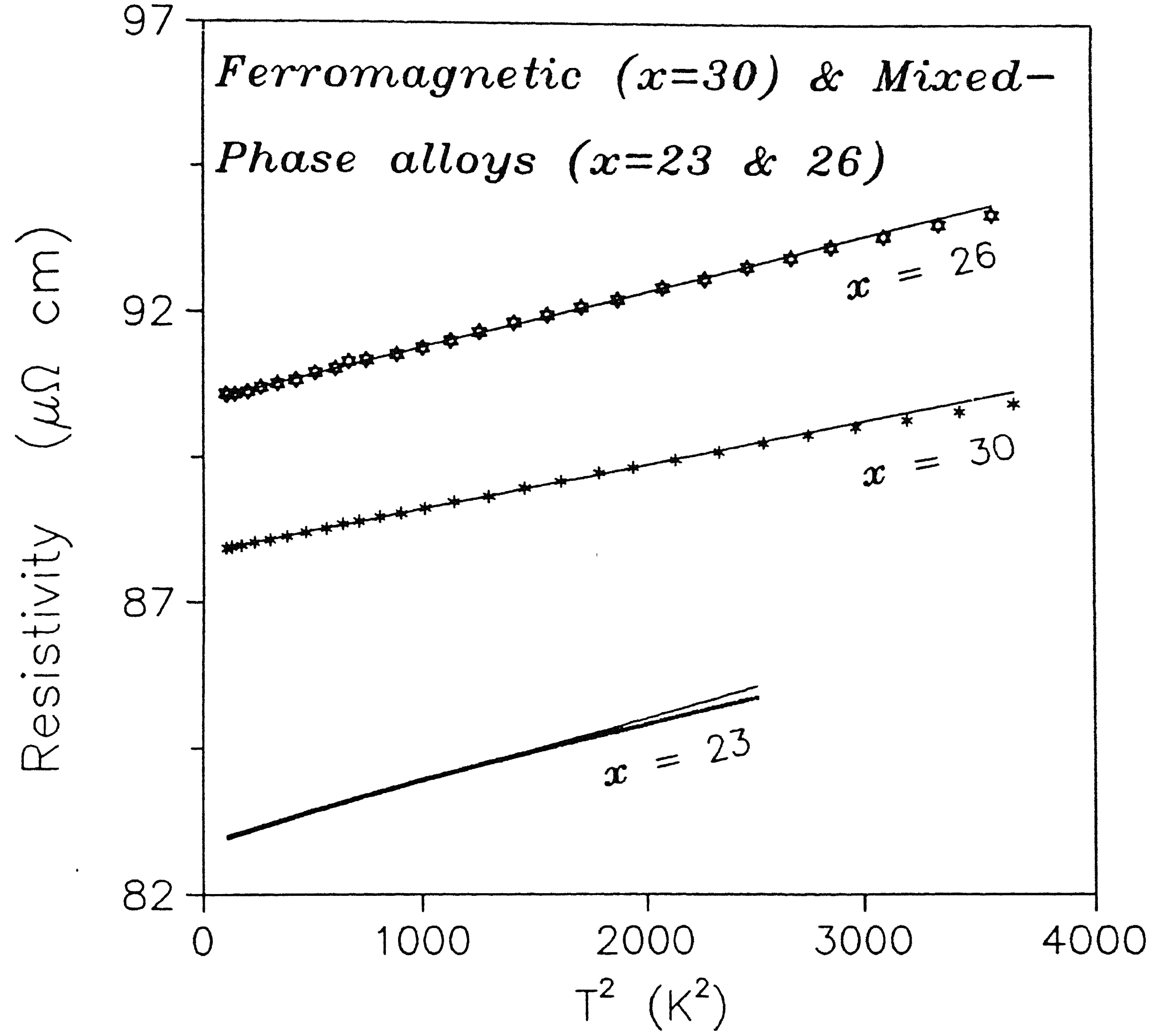

Figure 3.7: ρ vs T^2 plots of $Fe_{50}Ni_{30}Cr_{20}$ ferromagnetic and $Fe_{80-x}Ni_xCr_{20}$ (x = 23 and 26) mixed-phase alloys in the low temperature range. The solid lines are the best-fitted curves.

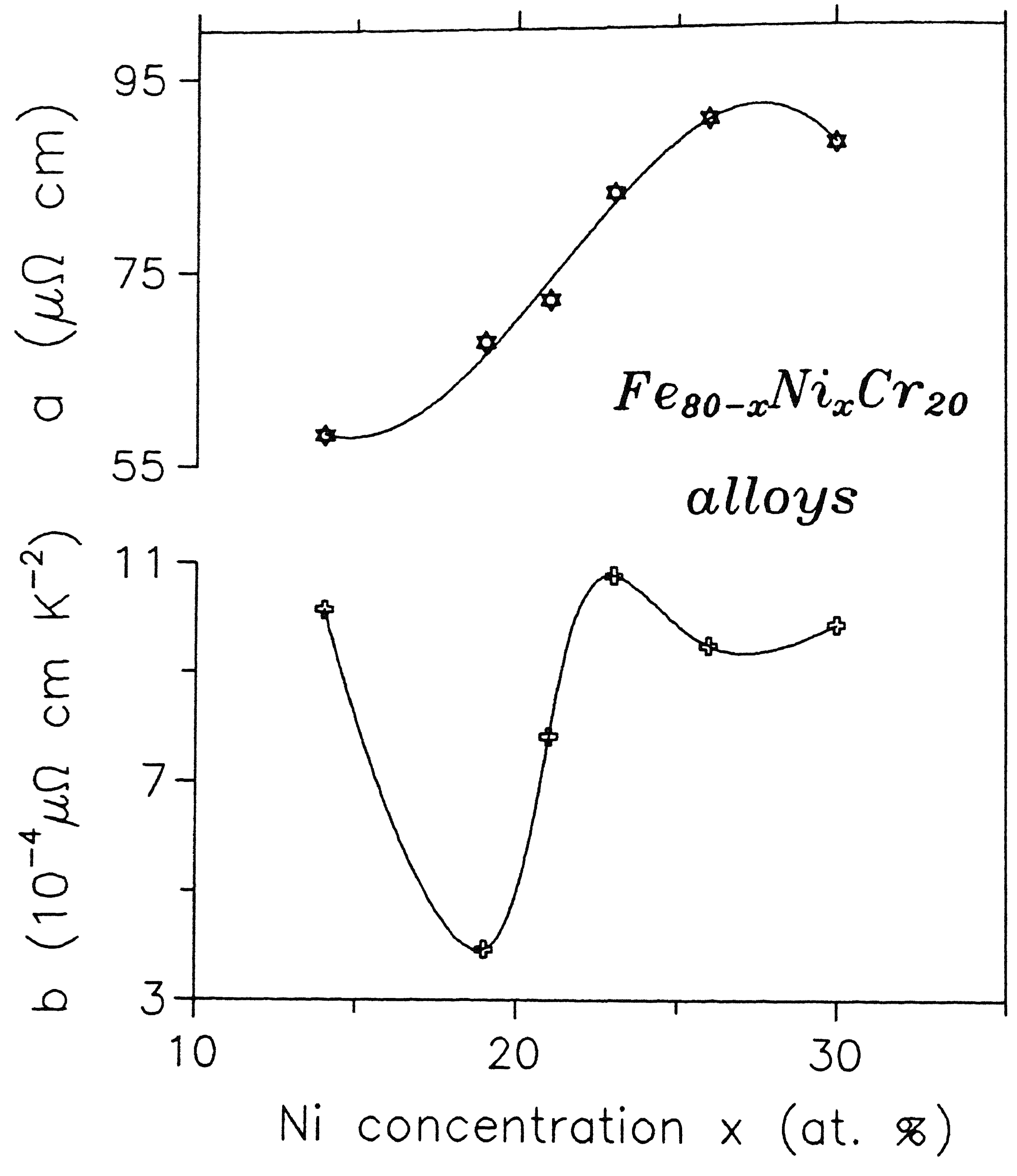

Figure 3.8: Ni concentration (x) dependence of the fit parameters a and b of $Fe_{80-x}Ni_xCr_{20}$ ($14 \leq x \leq 30$) alloys in the low temperature range. The solid lines are just guides to the eye.

Table 3.2: Fitting parameters for the ρ(T) data to different fit functions, low-temperature ranges and the values of χ^2 (defined in text) for $\gamma - Fe_{80-x}Ni_xCr_{20}$ ($14 \leq x \leq 30$) alloys.

Ni x (at.%)	Fit function	Fit range (K)	a ($\mu\Omega$ cm)	b 10^{-3} $\mu\Omega$ cm K^{-2})	c 10^{-6} $\mu\Omega$ cm K^{-3})	χ^2 (10^{-8})
14	$a+bT^2$	10-60	58.3	1.01		2.9
19	$a+bT^2+cT^3$	10-50	67.8	0.39	7.5	6.1
21	$a+bT^2+cT^3$	10-50	72.0	0.74	2.1	0.4
23	$a+bT^2$	10-40	82.9	1.07		3.9
26	$a+bT^2$	10-50	90.5	0.94		3.7
30	$a+bT^2$	10-50	87.8	0.99		1.6

In these γ-$Fe_{80-x}Ni_xCr_{20}$ ($14 \leq x \leq 30$) concentrated magnetic alloys, the appearance of a T^2 contribution to ρ at low temperatures cannot be attributed directly to a single mechanism. As mentioned earlier in Sec.3.1, a number of mechanisms could be involved in these magnetic alloys in the low-temperature range Nevertheless, we can atleast examine them with some logical arguments. If we compare the T^2 contribution to ρ of these alloys with those in pure Fe, Ni, and Co, as investigated by White and Woods[9], we find that b $\approx$ (0.4 - 1.1) $\times 10^{-3} \mu\Omega$ cm K^{-2} in the present case which is one to two orders of magnitude higher than those in pure Fe, Ni, or Co ($\approx$ (1.3 - 1.6) $\times 10^{-5} \mu\Omega$ cm K^{-2}) and the one calculated by Baber[10, 11]. Thus the T^2 contribution due to Baber mechanism is too small to explain our results.

Next we attempt to explain this T^2 dependence of ρ in the light of the electron - magnon (spin wave) scattering mechanism which seems to be the most plausible one. It also provides a rather consistent picture. It is clear that for the alloys in the long-range FM (x = 30) or AFM (x = 14) regimes as well as those in the mixed-phase (x = 23 and 26) regime where the long-range magnetic ordering starts appearing, the T^2 contribution could be very large. So it is rather natural to associate the T^2 term with the electron - magnon (spin wave) scattering. In the case of the alloys (x = 19 and 21) in the SG regime, the T^2 contribution drops down and the appearance of the extra T^3 term can be linked with the electron - phonon scattering in the presence of s-d interaction (Eq.(1.7)) in the transition metals.

We can, in principle, estimate the spin-disorder resistivity (ρ_{mag}) in these alloys theoretically in the light of the spin-wave theory using Eq.(1.8). Unfortunately, there is no information on the spin-wave stiffness constant ($\mathcal{D}$) and the strength of s-d interaction ($\mathcal{G}_{\mathrm{s-d}}$) for these magnetic alloys as no band theory calculation has been developed so far for this system of alloys. Thus it is not possible at this stage to estimate ρ_{mag} quantitatively.

When we compare our findings with those of Banerjee and Raychaudhuri[6] we find that there is an excellent qualitative agreement at low temperatures. However, some minor differences exist, e.g., for the long-range or mixed-phase ordering (x = 14, 23, 26, and 30) the contribution of the T^3 term is about 1% of that of the T^2 term in their work whereas it is smaller than 0.1% in the present case. Although the experimental resolution is about the same, the fact that the values of χ^2 are much less in our studies in comparision to theirs ($\chi^2 \approx 10^{-8}$ and 10^{-6}, respectively) implies that the fit of our ρ(T) data to various functions is better.

3.1.2 Analysis of ρ(T) data in the temperature range 200 ($\approx \Theta_D/2$) $\leq T \leq$ 600K

From Fig.3.1, which shows ρ(T) of all the alloys under investigation, it is obvious that each curve shows a strong downward deviation from linearity (DFL) at high temperatures and also a tendency towards saturation at still higher temperatures. Since each of these alloys are magnetic[1] having low T_c , T_{SG} or T_N, it is very unlikely that at those high temperatures (T

$\gg T_c$, T_{SG} or T_N) when the alloys are in a paramagnetic state, the randomly oriented d-spins of these transition metal alloys will contribute to any correlated magnetic spin scattering. Moreover, despite having wide varieties of magnetic phases (FM, FM and SG, SG or AFM) at different temperatures and compositions of these alloys, all of them show very similar kind of behavior of DFL of ρ(T) at very high temperatures. As a consequence one can simply conclude that this DFL of resistivity which leads to a saturation limit at high temperatures is not of magnetic origin. We have attempted to explain this behaviour of ρ(T) in the light of the various models mentioned in Sec.1.3.2.

Obviously ρ(T) at high temperatures is not consistent with that predicted by a simple electron - phonon scattering theory, viz, $\rho(T) \sim T$ as in *Bloch–Grüneissen*[12] formula and Eq.(1.7) (Wilson). Therefore, we have fitted our data to the "phonon-ineffectiveness" model predicted by Cote and Meisel[13] (Eq.(1.9)) in the temperature range 200–600 K. However, it is found that the fits in all the alloys are very poor ($\chi^2 \approx 10^{-4}$) in comparison with the experimental accuracy. As a consequence, we rule out the validity of this model in this system of alloys.

We have also fitted the high-temperature ρ(T) data to Eq.(1.10) which is obtained from the widely accepted "parallel – resistor" model. The form of ρ_{ph}(T) that we have chosen is contained in Eq.(1.7). This arises due to the phonon assisted s-d scattering as proposed by Wilson[14] for transition metals. Since the exponents of T of the observed ρ(T) in the low-temperature range are small (2 to 3) for this system of magnetic 3d – transition metal alloys, the use of Eq.(1.7) (Wilson) instead of *Bloch – Grüneisen* formula is justified although both are of the same form at high temperatures ($\rho \propto T$, $T \geq \Theta_D$). We have abbreviated $\rho_{ideal}(0) = \varepsilon$ which is a temperature - independent constant.

The value of the Debye temperature (Θ_D) used in Eq.(1.7) is $\approx$ 400 K, as obtained from the specific heat measurements reported by Pecherskaya et al.[15], falling in the range of 370 to 400 K. No appreciable change in the quality of fit (χ^2) is observed as we vary Θ_D between 370 and 400 K. Recently, from a thorough investigation of the resistivity saturation of $Ti_{1-x}Al_x$ ($x \leq 0.135$) disordered alloys by Lin et al.[8, 16], it was concluded that a single value of

$\rho_{\rm sat}$ cannot describe the resistivity saturation for the entire range of x . Also a proper choice of the range of fit made the quality of fit much better as well as the fitting parameters more meaningful in their case.

Along the same lines, here we have kept $\rho_{\rm sat}$, a free adjustable fitting parameter along with ε ($\approx \rho_{\rm ideal}(0)$) and B (in Eqs.(1.10), (1.11) and (1.7)). The range of fit is selected within 200 ($\approx \Theta_{\rm D}/2$) - 600 K for all the alloys. Despite the fact that the integrand of Eq.(1.7) is a well-behaved function having no singularity for all z, the integration can not be carried out analytically. We have evaluated the integral of Eq.(1.7) numerically using DO1AHF (1-D quadrature, adaptive, finite interval and strategy due to Patterson) NAG Routine which is suitable for any well-behaved function. A non-linear least-squares method is employed for fitting the experimental ρ(T) data to Eq.(1.10) (parallel-resistor model). In Table 3.3 we have listed all the fitting parameters, namely, ε, B and $\rho_{\rm sat}$ and the values of χ^2 for the six γ-$\rm Fe_{80-x}Ni_xCr_{20}$, ($14 \leq x \leq 30$) alloys.

Figure 3.9 plots the experimental ρ(T) data (dots) alongwith the best-fitted curves (continuous line) using Eq.(1.10) for the alloys with x = 23, 26, and 30 in the temperature range of 200 to 600 K. The excellent quality of fit is obvious from the indistinguishability between the data and the best-fitted curves. The inset of Fig.3.9 shows the temperature dependence of a typical percentage deviation of the data (x = 23) from the best-fitted values. Figure 3.10 is the same as Fig.3.9 except that it is for the samples with x = 14, 19, and 21. In the inset of Fig.3.10 we have shown a typical likelyhood distribution of the relative errors P($\frac{\Delta\rho}{\rho}$) for these kinds of fits for x = 19. Generally, for a perfect fit and negligible experimental error (ideal condition), one gets a very narrow peak, centered around $\frac{\Delta\rho}{\rho} = 0$. This follows a Gaussian - like (normal) distribution. However, in our case, the plot has some spread with secondary maxima which appear at both the positive and negative sides of $\frac{\Delta\rho}{\rho} = 0$. We have drawn a smooth curve which follows a Gaussian - like distribution with a peak at $\frac{\Delta\rho}{\rho} = 0$ and a full width at half maximum (FWHM) $\approx 4 \times 10^{-4}$. We have mentioned in Chapter 2 that the accuracy of our experimental data at the higher temperatures is about 5 parts in 10^4. So the FWHM resulting from this kind of fitting procedure and the order of χ^2 ($\approx 10^{-7}$) given

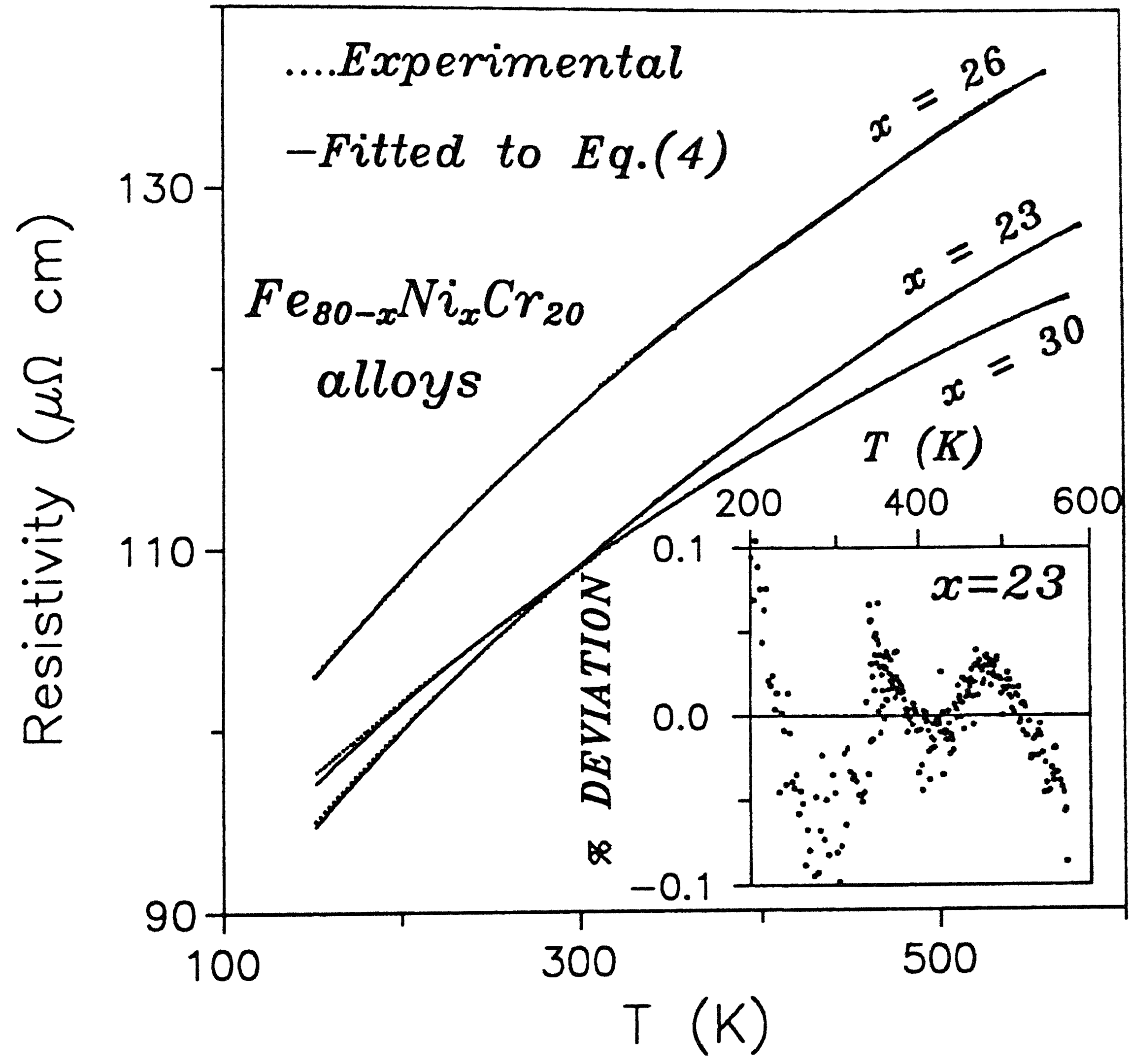

Figure 3.9: Experimental (dots) ρ vs T plots of $Fe_{80-x}Ni_xCr_{20}$ (x = 23,26, and 30) alloys in the temperature range between 150 and 600 K. The best-fitted curves (solid lines) for the alloys are plotted using Eq.(1.10) (parallel-resistor model). The inset shows the temperature dependence of a typical percentage deviation of fit for x = 23.

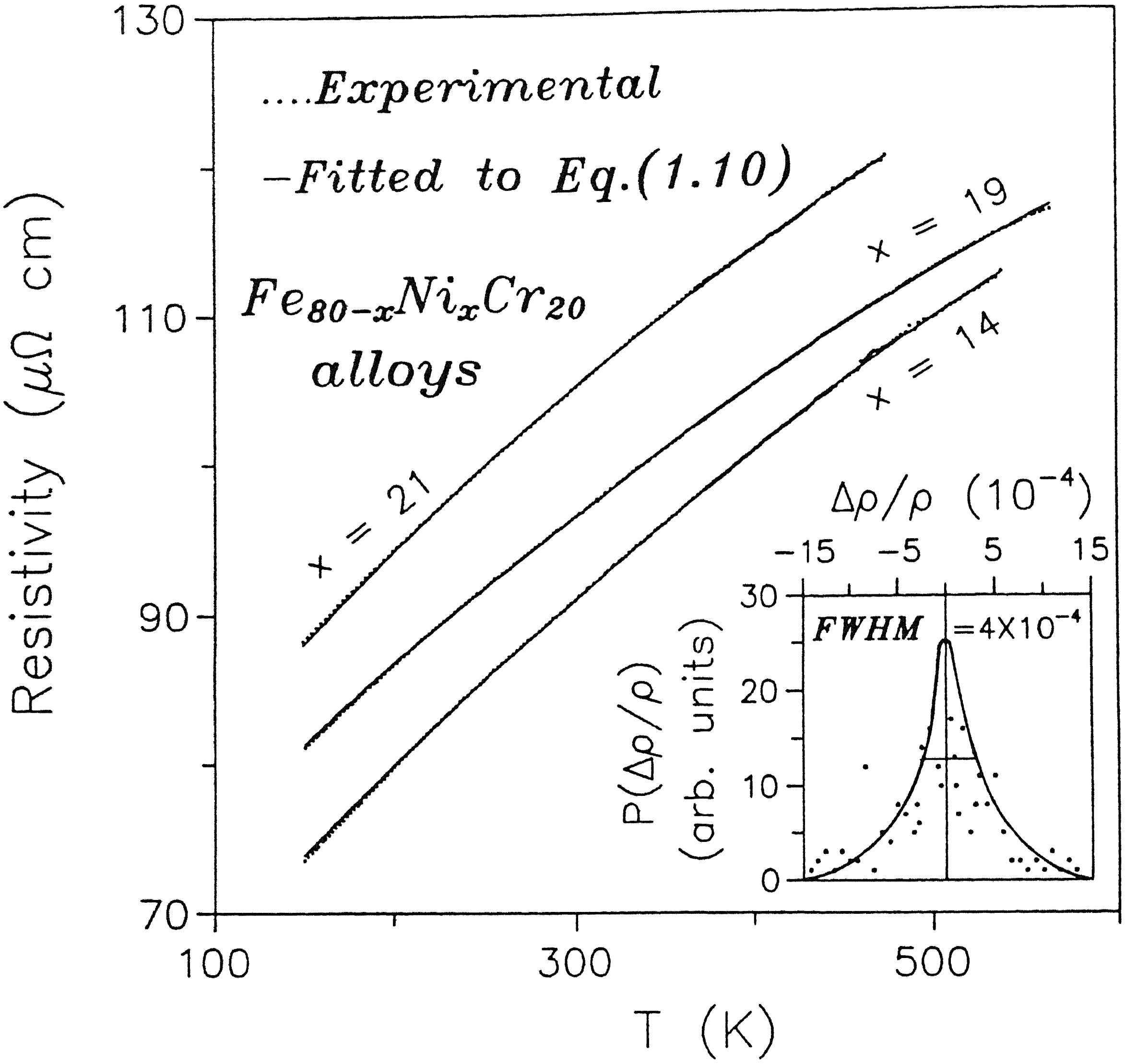

Figure 3.10: Experimental (dots) ρ vs T plots of $Fe_{80-x}Ni_xCr_{20}$ (x = 14,19, and 21) alloys in the temperature range between 150 and 600 K. The best-fitted curves (solid lines) for the alloys are plotted using Eq.(1.10) (parallel-resistor model). The inset shows a typical likelyhood distribution of the relative errors $[P(\frac{\Delta\rho}{\rho})]$ of the fit for x = 19.

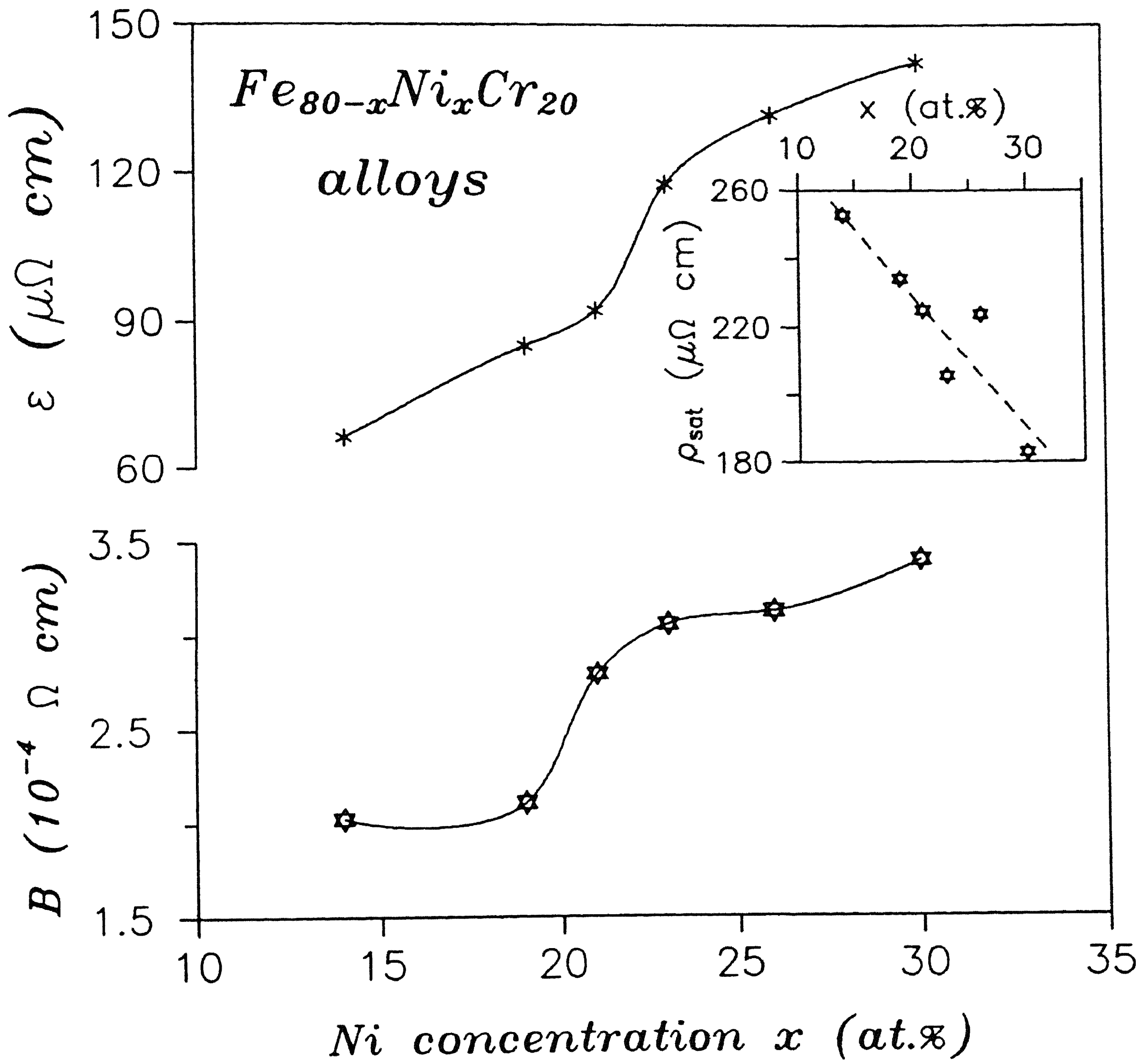

Figure 3.11. Ni concentration (x) dependence of the fitting parameters ε and B of Eq.(1.10) (parallel-resistor model) of $Fe_{80-x}Ni_xCr_{20}$ ($14 \leq x \leq 30$) alloys. The solid lines are just guides to the eye. The inset shows the concentration (x) dependence of ρ_{sat}.

Table 3.3: Ni concentration (x) dependence of the fitting parameters for the $\rho(T)$ data to Eq.(1.10) of the parallel-resistor model and the values of χ^2. The range of fit is taken between 200 and 600 K for the γ-Fe$_{80-x}$Ni$_x$Cr$_{20}$ ($14 \leq x \leq 30$) alloys.

Ni x(at.%)	$\varepsilon[=\rho_{ideal}(0)]$ ($\mu\Omega$ cm)	B ($10^{-4}\Omega$ cm)	ρ_{sat} ($\mu\Omega$ cm)	χ^2 (10^{-7})
14	66.2	2.0	252.7	5.9
19	85.0	2.1	234.1	3.4
21	92.1	2.8	225.0	2.8
23	117.6	3.1	205.8	1.4
26	131.8	3.1	223.7	5.1
30	142.5	3.4	183.0	3.0

in Table 3.3 are clearly of the same order as the experimental accuracy. The high quality of this fit indicates that the parallel-resistor model can reproduce reasonably well the saturation behaviour of ρ in our γ-Fe$_{80-x}$Ni$_x$Cr$_{20}$ alloys at high temperatures.

From Table 3.3 we observe that (i) the values of the parameter ε ($\rho_{\text{ideal}}(0)$ of Eq.(1.11)) increase with Ni the concentration (x) (shown in Fig.3.11), (ii) the parameter B, which is the strength of the Bloch- Wilson's electron - phonon interaction in the presence of s-d scattering term, increases ((2.0 – 3.4) × $10^{-4}\Omega$ cm) with the Ni concentration (x) (shown in Fig.3.11), and (iii) the saturation values of the resistivity, ρ_{sat}, differ ((183 – 253) $\mu\Omega$ cm) from each other for various alloys. The inset of Fig.3.11 shows the concentration (x) dependence of ρ_{sat}.

Whether the values of these fitting parameters are physically meaningful has to be seen. Using Eq.(1.12) and the best-fitted parameters ϵ $[=\rho_{\text{ideal}}(0)]$ and ρ_{sat}, we have obtained the value of $\rho(0)$ which are within 10% of our measured $\rho(10K)$ for all the alloys. Also, the strength of the Bloch – Wilson interaction term, B, is enhanced with the increase of Ni concentration (x) at the cost of Fe. This may be attributed to the enhancement of the electron – phonon scattering due to possible changes in the density of the d-states at the Fermi level. The values of ρ_{sat} decrease roughly linearly with the Ni concentration . If we assume a single value of ρ_{sat} with some fluctuations, then on averaging the best-fitted values for all the alloys we get $\rho_{sat} \approx (220 \pm 30)$ $\mu\Omega$ cm. However, the validity of having a single value of ρ_{sat} for the entire concentration (x) is not very clear. Some of the experimental results[8, 16] support mulitple values of ρ_{sat} for a range of concentrations.

We have also examined our experimental data in the light of the ion – displacement model of Ron et al.[17] through non-linear least-squares fits to Eq.(1.14). We have kept ρ_m, D and T_o as adjustable parameters in the range of 200 - 600 K. Figure 3.12 plots the experimental data (dots) and the best-fitted curves (continuous lines) for alloys with x = 23, 26, and 30. The typical percentage deviation is shown in the inset of Fig.3.12 for x = 23. Figure 3 13 and its inset are the same as Fig.3.12 except that they are for x = 14, 19, and 21 alloys and the inset is for x = 21. We have summarized in Table 3.4 the values of the fitting parameters ρ_m, D and T_o as well as the values of χ^2 obtained from fitting the data to Eq.(1.14).

The following features can be observed from the table :

(i) No unique value of the saturation resistivity (ρ_m) is found, very much like the earlier case of the parallel - resistor model. ρ_m varies from (148 - 176) $\mu\Omega$ cm in these alloys. The range of this ρ_m is smaller than that of ρ_{sat} ((183 - 253) $\mu\Omega$ cm) as found from the parallel-resistor model. In the inset of Fig.3.14 we have shown the comparative plots of ρ_m and ρ_{sat} as a function of $\rho(10K)$ for all the alloys. The nature of both the plots is more or less similar though their absolute values differ.

(ii) The values of the electron – phonon scattering coefficient D lie between (0.12 - 0.16) $\mu\Omega$ cm K^{-1} .

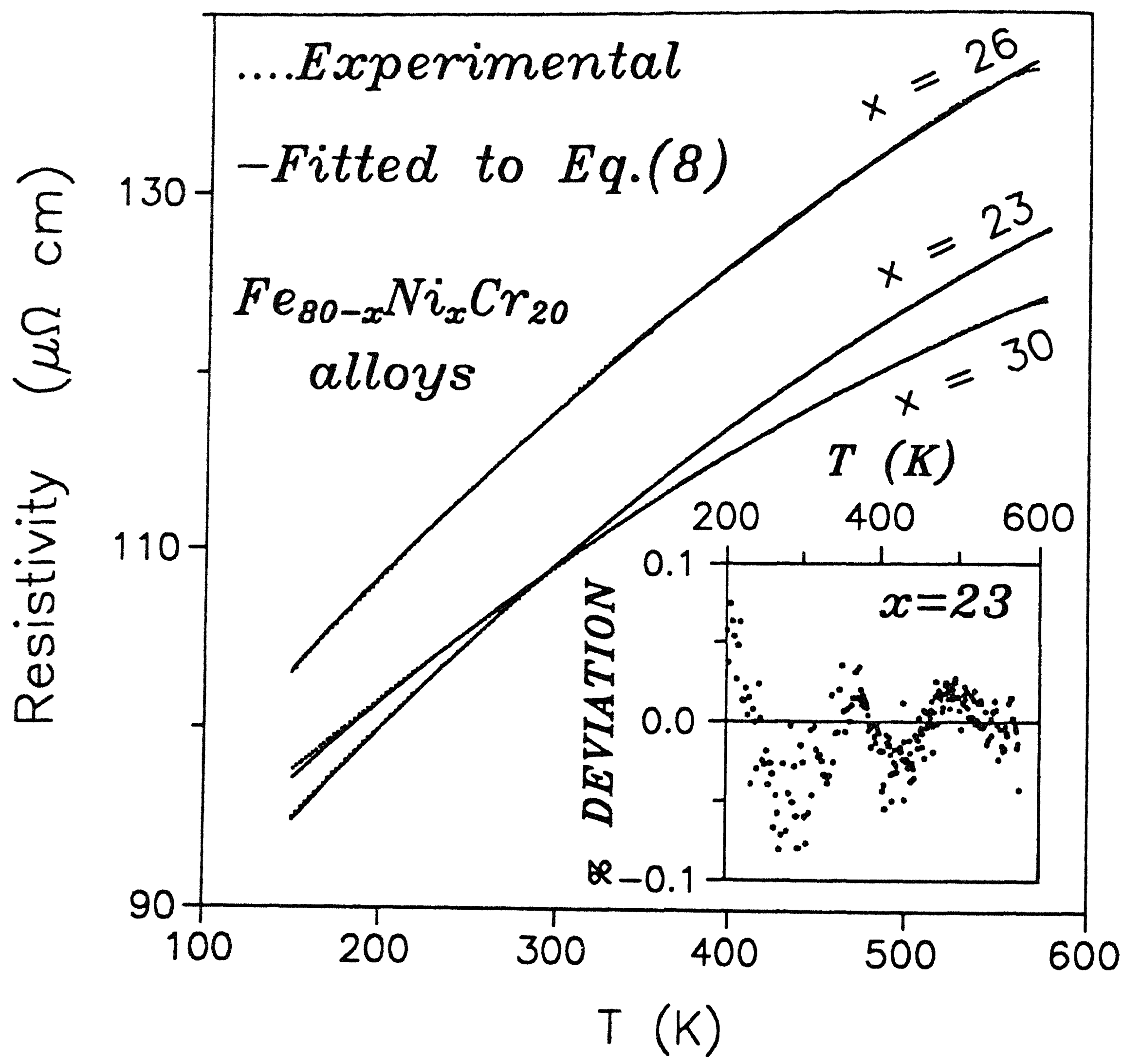

Figure 3.12: Experimental (dots) ρ vs T plots alongwith the best-fitted curves (solid lines) using Eq.(1.14) (ion-displacement model) in the temperature range between 200 and 600 K of $Fe_{80-x}Ni_xCr_{20}$ (x = 23, 26, and 30) alloys. The inset shows the temperature dependence of a typical percentage deviation of the fit for x = 23.

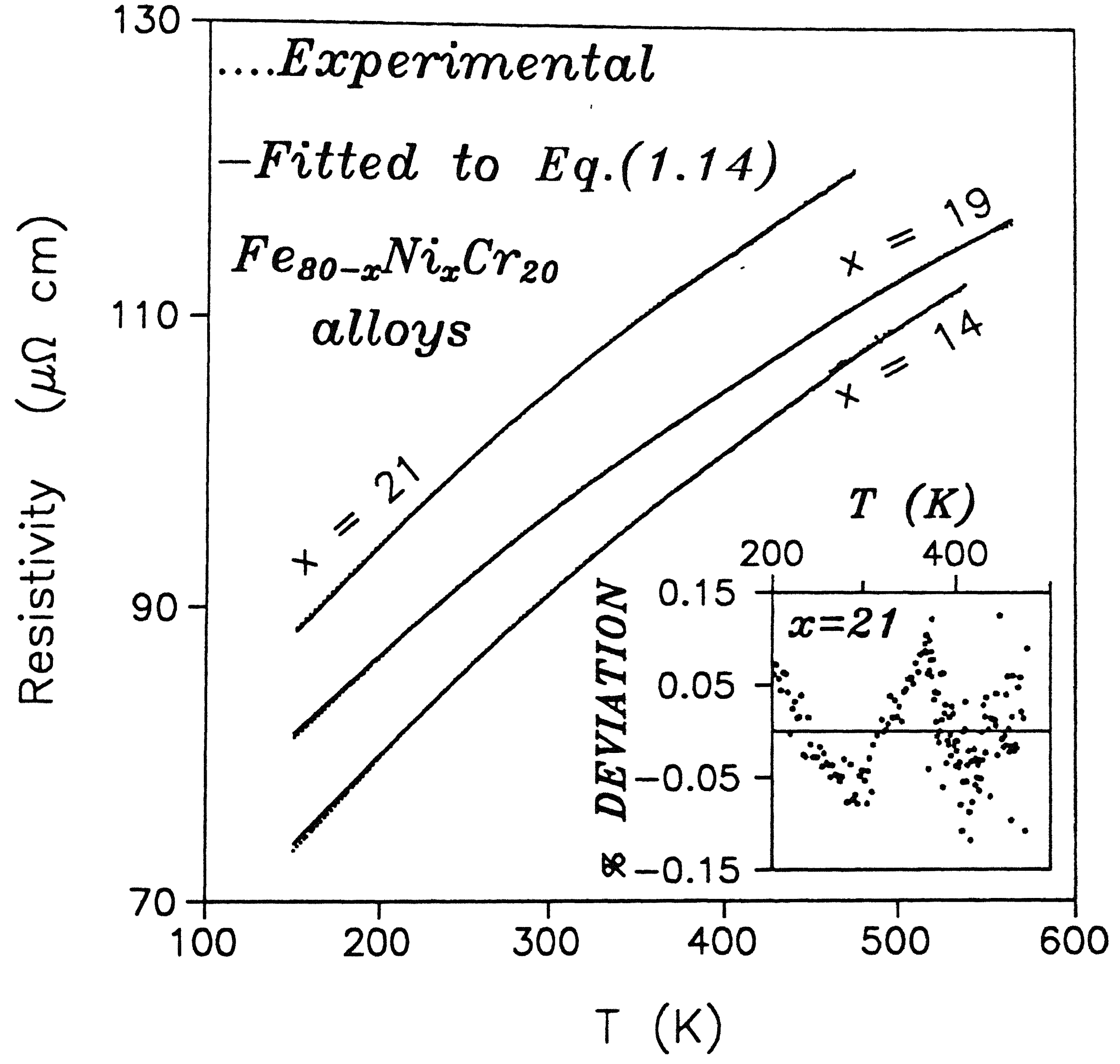

Figure 3.13: Experimental (dots) ρ vs T plots alongwith the best-fitted curves (solid lines) using Eq.(1.14) in the temperature range between 200 and 600 K of $Fe_{80-x}Ni_xCr_{20}$ (x = 14,19, and 21) alloys. The inset shows the temperature dependence of a typical percentage deviation of the fit for x = 21.

Table 3.4: Fitting parameters for the $\rho(T)$ data to Eq.(1.14) of the ion–displacement model and the values of χ^2. The range of fit is taken between 200 and 600 K for the γ-Fe$_{80-x}$Ni$_x$C r$_{20}$ ($14 \leq x \leq 30$) alloys.

Ni x(at.%)	ρ_m ($\mu\Omega$ cm)	D (($\mu\Omega$ cm K^{-1})	T$_o$ (K)	χ^2 (10^{-7})
14	176.3	0.149	823.0	7.9
19	168.4	0.133	786 9	3.6
21	165.8	0.163	608 7	2.5
23	160.3	0.139	603.8	8.3
26	174.7	0 139	648.6	6.1
30	147.9	0.119	557.7	1.9

(iii) The fitted values of the characteristic temperature T$_o$ decrease monotonically from $\approx$ 825 to 600 K as the Ni concentration (x) and ρ(10K) increase. This is shown in Fig.3.14. Equation (1.14) of the ion-displacement model can be written as

$$\rho_{\rm m} = \rho(0K) + D\ T_o\ , \tag{3.1}$$

putting T = 0. T$_o$ is the characteristic temperature at which the average ion-displacement first becomes comparable with the distance between the zeroes of the electronic wavefunction.

The form of Eq.(3.1) tells us that the static and thermal disorders play equally important roles in determining the resistivity saturation.

(iv) The values of χ^2 ranges from (1.9 - 8.3) × 10^{-7} in these fits to the ion-displacement model (Eq.(1.14)) and are consistent with the experimental accuracy. The order of χ^2 as well

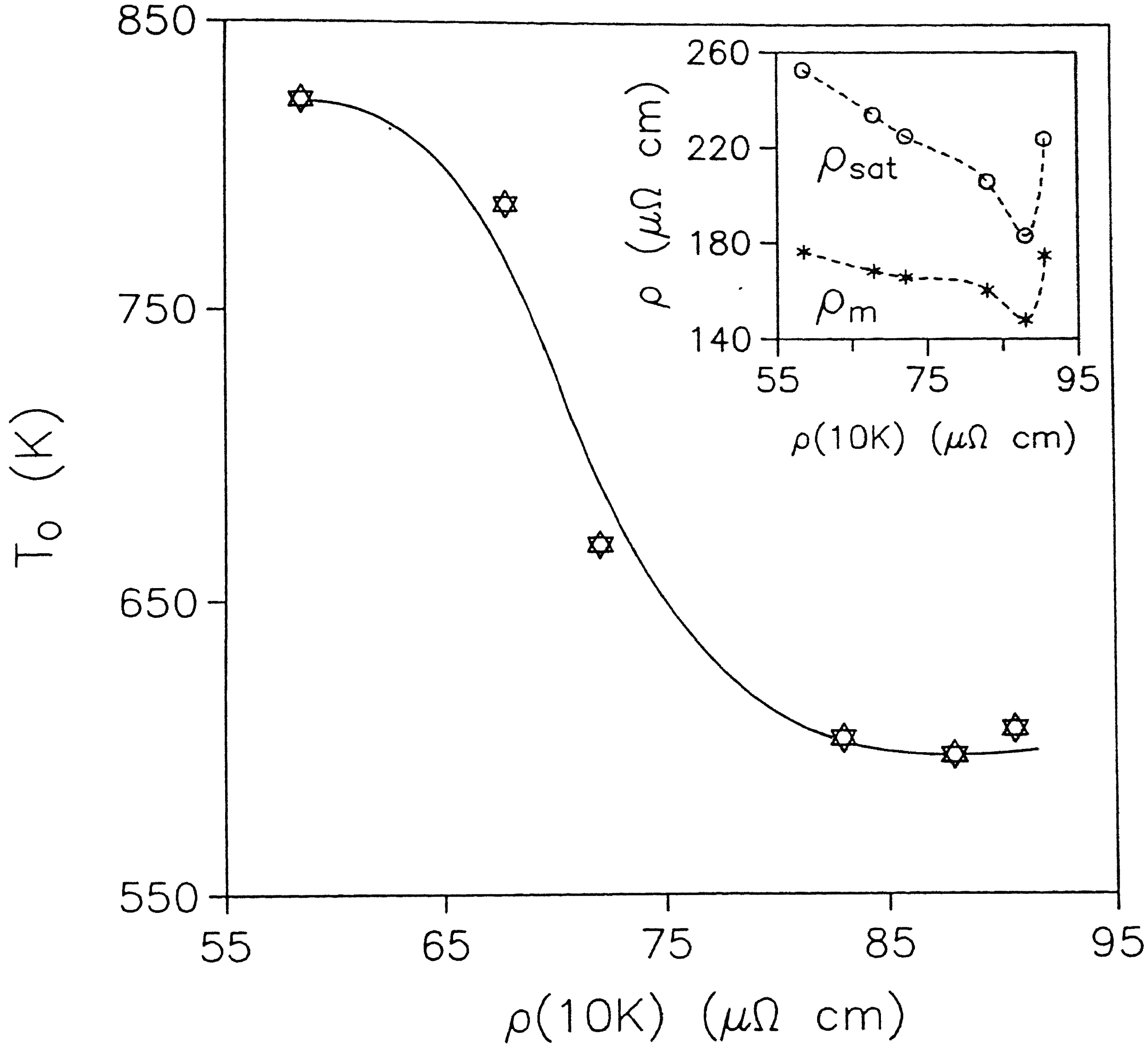

Figure 3.14: Plot of the variation of T_0 with $\rho(10\ K)$(experimental) for $Fe_{80-x}Ni_xCr_{20}$ (14 $\leq$ x $\leq$ 30) alloys. T_0 is the characteristic temperature in Eq.(1.14) of the ion-displacement model. The inset shows the comparative variation of ρ_m and ρ_{sat} (from Eqs.(1.14) and (1.10), respectively) with Ni concentration (x). The dashed lines are just guides to the eye.

as the percentage deviation indicate that the ion-displacement model is also a strong candidate which can explain our experimental high-temperature ρ(T) data reasonably well

Mott and others[18] calculated the saturation value of resistivity ρ_{sat} using the Kubo - Greenwood formula with the condition that the electron mean free path is as small as the lattice spacing ($l \sim$ a) in the strong-disorder limit and found that

$$\sigma_{\text{sat}} = \rho_{\text{sat}}^{-1} = (0.33e^2/\hbar a) \ . \tag{3.2}$$

Mott also claimed that a similar result like that of Eq.(3.2) can be found from the Boltzmann formula assuming spherical Fermi surface (free electron model). Gurvitch[19] had generalized the form of Eq.(3.2) considering α free electrons per cubic cell a^3 and wrote a modified relation

$$\sigma_{\text{sat}} = 0.33\alpha^{2/3}e^2/\hbar a \ , \tag{3.3}$$

or,

$$\rho_{\text{sat}} = 1.29 \times 10^{18}/(n^{2/3}a) \ , \tag{3.4}$$

where the electron concentration n is in cm^{-3} and the lattice spacing a is in Å. We have estimated ρ_{sat} in our alloys using the value of n = (6–7) × 10^{22} /cm^3, as found from the recent Hall effect measurements[20] at room temperature and the lattice spacing 'a' of 3.58 Å obtained from our XRD measurements. Substituting these values in Eq.(3.2) we obtain $\rho_{\text{sat}} \approx$ 215 $\mu\Omega$ cm. This is in excellent agreement with our average value of ρ_{sat} ($\approx$ 220 $\mu\Omega$ cm) using the parallel - resistor model. However, this value is a bit higher than the average ρ_{sat} ($\approx$ 165 $\mu\Omega$ cm) obtained from the ion – displacement model. It was mentioned earlier at the end of Sec.3.1 how ρ_{sat} was estimated from the extrapolation of the plot of TCR vs ρ (Fig.3.4) to TCR = 0 giving the value of $\rho_{\text{sat}} \approx$ 180 $\mu\Omega$ cm. This agreement is very satisfying since the value of ρ_{sat} is found here by mere extrapolation of the experimental data independent of any model. Thus the values of ρ_{sat}, derived from our experiments using the parallel-resistor and the ion-displacement models, are more or less in good agreement with the theoretical value obtained from Eq.(3.4) in this system of disordered alloys.

The values of the electron - phonon scattering term D in the ion-displacement model are found in the range (0.12 - 0.16) $\mu\Omega$ cm K^{-1} as given in Table 3.4. In the high-temperature limit, the form of $\rho_{\rm ph}(T)$ in Eq.(1.11) of the parallel-resistor model reduces to βT where β = B / (2 Θ_D) in Eq.(1.7) of Wilson model[14] for transition metals. Substituting Θ_D = 400K and the values of B from Table 3.3, we get β in the range of (0.25 - 0.40) $\mu\Omega$ cm K^{-1}. With alloying the density of states [N(E_F)] at the Fermi level (E_F), the Fermi velocity (v_F) and the electron - phonon coupling constant ($\lambda_{\rm tr}$) are not expected to vary significantly. Therefore, it is possible to estimate β, atleast roughly, in our alloys employing the theoretical[21, 22] relation

$$\beta = \left[\frac{6\pi k_B\lambda_{tr}}{\hbar N(E_F) < v_F >^2 e^2}\right], \tag{3.5}$$

where k_B is the Boltzmann constant and $\hbar$ the Planck's constant. As we have mentioned earlier, to the best of our knowledge there is no band theory calculation available for these systems of ternary 3d-transition metal alloys. It is therefore difficult to estimate β from Eq.(3.3). Nevertheless, we have attempted to estimate β using N(E_F) $\approx$ 14 states / ev / unit cell as found from the low-temperature specific heat measurements in the temperature range of 4.2 to 45 K on similar FeNiCr alloys (concentrations are not exactly alike) by Pecherskaya et al.[15]. We have used the value of the transport electron - phonon coupling constant $\lambda_{\rm tr}$ = 0.6 obtained from a different work of the same authors[23]. Substituting all these values in Eq.(3.5) one obtains $\beta \approx$ 0.02 $\mu\Omega$ cm K^{-1} . This value is roughly 10 times smaller than those obtained from the parallel-resistor (B / 2 Θ_D) and the ion-displacement (D) models. Although this theoretical estimate of β is very crude due to the lack of knowledge of the band structure, its value is not too far from those derived from our electrical transport measurements.

We have also compared the values of $\rho_{\rm sat}$ ($\approx$ 200 $\mu\Omega$ cm) obtained from our experiments with the theoretical value when these metallic systems approach Mott's minimum metallic conductivity[18] regime (near to the metal-insulator transition). Mott has always made a distinction between the two situations , namely, conductivity 'σ' when the electron mean free path approaches the lattice spacing ($l \sim$ a) and the minimum metallic conductivity (as seen in different metal-oxides). As mentioned earlier, Gurvitch[19] has shown that σ_{sat} ($\approx \rho_{\mathrm{sat}}^{-1}$) is always larger than σ_{min} ($\approx 0.026e^2/\hbar a$, the minimum metallic conductivity) and has given a relationship between them [Eq.(1.13)]. We have estimated σ_{min} using a = 3.58 Å (e and $\hbar$ being constants) and find that our $\sigma_{\mathrm{sat}} \approx 25\ \sigma_{\mathrm{min}}$. We have also evaluated the same factor from Eq.(1.13) using $n = 6 \times 10^{22}$ / cm^3 (Ref. 45) and a = 3.58 Å and find that it is 20 and not 25. Thus for the alloys under investigation, in the saturation regime ($l \sim$ a), the conductivity is still much higher and is not at all close to Mott's minimum metallic conductivity (σ_{min}) regime. This observation supports Gurvitch's argument[19].

3.2 Conclusions

We have performed systematic electrical resistivity measurements on γ-$Fe_{80-x}Ni_xCr_{20}$ ($14 \leq x \leq 30$) substitutionally disordered, crystalline, magnetic alloys. In the high-temperature region (T > 200 K) we observe a noticeable downward deviation of ρ from a linear temperature dependence. This is an indication of resistivity saturation in all these alloys independent of their low-temperature magnetic states in sharp contrast to the linearity of ρ(T) continuing even up to 300 K, as reported by Banerjee and Raychaudhuri[6]. Our study provides a rigorous test of all the theoretical models. In conclusion, we argue that the particular way in which the alloys approach saturation can be understood quite well on the basis of the parallel – resistor model. The phonon – ineffectiveness model has failed to explain this strong downward DFL of ρ at high temperatures, atleast in our alloys. The ion – displacement model also provides a consistent explanation of the DFL of ρ at high temperatures. However, every model has its own limitations. None of them provide a single constant saturation resistivity derived from the experimental data. One also does not know whether a unique saturation resistivity or a number of them is desirable for the entire range of concentration (x) of this particular alloy system because of insufficient theoretical inputs. Further, we conclude that the σ_{sat} in these alloys are much higher than those expected if this system approached the minimum metallic conductivity region (σ_{min}). Thus the two situations, namely, the conductivity 'σ' when the electron mean free path approaches the lattice spacing ($l \approx$ a) and the minimum metallic conductivity, are not alike. Greater attention should be paid in the direction of the band - theory calculations in ternary 3d-transition metal alloys which ultimately will help in understanding the transport properties of these systems in a more quantitative manner. At low temperatures, we conclude that the T^2 dependence of ρ of these magnetic alloys in the long-range (FM or AFM) regime mainly arises from the electron - magnon (spin wave) scattering. The latter also provides a more consistent picture for the entire range of x. We also find that the Baber mechanism is too small to explain this low - temperature T^2 behaviour. We further conclude that for the alloys (x = 19 and 21) in the SG regime, the T^2 contribution becomes somewhat smaller (as it should be) and an additional T^3 contribution, which arises from the electron - phonon scattering in the presence of s-d interaction, plays an important role in the behaviour of the low-temperature ρ(T).

Bibliography

[1] A. K. Majumdar and P. v. Blanckenhagen, Phys. Rev. B **29**, 4079 (1984).

[2] A. K. Majumdar and P. v. Blanckenhagen, J. Magn. Magn. Mater., **40**, 227 (1983).

[3] T. K. Nath and A. K. Majumdar, J. Appl. Phys., **70** (10), 5828 (1991).

[4] M. Gabay and G. Toulouse, Phys. Rev. Lett., **47**, 201 (1981).

[5] S. Banerjee and A. K. Raychaudhuri, Solid State Commun., **83**, 1047 (1992).

[6] S. Banerjee and A. K. Raychaudhuri, Phys. Rev. B **50**, 8195 (1994).

[7] J. H. Mooij, Phys. Status Solidi A **17**, 521 (1973).

[8] J. J. Lin, C. Yu, and Y. D. Yao, Phys. Rev. B **48**, 4864 (1993).

[9] G. K. White and S. B. Woods, Phil. Trans. Roy. Soc. (London), Ser.A, **251**, 273 (1959).

[10] W. G. Baber, Proc. Roy. Soc. (London) A **158**, 383 (1937).

[11] J. Appel, Phys. Rev., **125**, 1815 (1962); Phil. Mag., **8** (8), 1071 (1963).

[12] J. M. Ziman in *Electrons and Phonons* (Oxford University Press, London, 1963).

[13] P. J. Cote and K. V. Meisel, Phys. Rev. Lett., **40**, 1586 (1978).

[14] A. H. Wilson, Proc. Roy. Soc. (London), Ser.A **167**, 580 (1938).

[15] V. I. Pecherskaya, D. N. Bolshutkin, A. V. Butenko, V. N. Beilinson, V. I. Ovcharenko, V. A. Pervakov, and N. Yu. Tyutryumova, Sov. J. Low Temp. Phys., **14**(9), 505 (1988).

[16] C. Y. Wu and J. J. Lin, Z. Phys. B **93**, 269 (1994).

[17] A. Ron, B. Shapiro, and M. Weger, Philos. Mag. B **54**, 553 (1986).

[18] N. F. Mott in *Metal-Insulator Transition* (Taylor and Francis, London, 1974); N. F. Mott, Philos. Mag. B **44**, 265 (1981).

[19] M. Gurvitch, Phys. Rev. B **24**, 7404 (1981).

[20] S. Banerjee, Ph.D. Thesis, Indian Institute of Science, Bangalore, India, 1993.

[21] P. B. Allen, W. E. Pickett, K. M. Ho, and M. L. Cohen, Phys. Rev. Lett., **40**, 1532 (1978).

[22] B. Chakraborty and P. B. Allen, Phys. Rev. Lett., **42**, 736 (1979).

[23] V. I. Pecherskaya, A. V. Butenko, and D. N. Bolshutkin, Fiz. Nizk. Temp., **13**, 1146 (1987) [Sov. J. Low Temp. Phys., **13**, 648 (1987)].

Chapter 4

Low-field magnetoresistance and magnetization and their correlations

As mentioned in Chapter 1, the magnetic phase diagram[1] had been established in $Fe_{80-x}Ni_x$ Cr_{20} ($10 \leq x \leq 30$) alloys through *dc*-magnetization, magnetic neutron scattering and *ac*-susceptibility measurements. As x is increased the system undergoes a compositional phase transition from long-range antiferrromagnetism ($x = 10 - 14$) to spin-glass (17-21) to mixed ferromagnetic and spin-glass (23-26) to long-range ferromagnetic phase (30) within the same crystallographic f.c.c. γ-phase. The cusp-like peak in *ac*-susceptibility and the thermomagnetic history dependence of *dc*-magnetization (M) are evidences for the spin-glass (SG) phase below the transition temperature of $T_{SG} \simeq 16K$ in $x = 17 - 21$. The ferromagnetic interaction is already significant in $x = 21$. The alloys with $x = 23$ and 26, besides showing all the above characteristics of a SG below $T_{SG} = 20$ and $7K$, respectively, are also found to have long-range ferromagnetic (FM) order down to the lowest temperature ($4.2K$) as evidenced from the $M - H$ measurements with spherical samples with known demagnetization factor. The latter experiment provides the only proof for a possible co-existence of a transverse spin-freezing and a longitudinal long-range ferromagnetic order below T_{SG}. This is very similar to the Gabay-Toulouse[2] mixed phase rather than the re-entrant SG phase below the second transition. For $T > T_{SG}$, these alloys are purely FM till their respective Curie temperatures of $T_C = 35$ and 56K, respectively.

---

[1] This chapter is mainly based on the published work by T. K. Nath and A.K. Majumdar, *J Appl. Phys.* **70** (10), 5828 (1991), T. K. Nath, N. Sudhakar, A. K. Majumdar and E. J McNiff, *Annual Report of MIT National Magnet Laboratory*, page 78, 1992.

Magnetoresistance (MR) measurements are supposed to throw new light on or confirm the proposed magnetic phase diagram in the sense that each of the above phases has characteristic field, temperature and orientation dependence of MR. Conversely, the present system of concentrated alloys form an interesting set where one could study the MR behaviour of almost continuously varying magnetic phases originating from competing interactions within the same chemical constituents and crystal structure. With the above motivation in mind we have taken up MR $[\Delta\rho/\rho = \{\rho(H) - \rho(0)\}/\rho(0)]$ and *dc*-magnetization studies in the alloys with x=21, 23 and 30 to start with. For canonical[3] SG's (AuMn, CuMn, AgMn, etc.) the MR is isotropic and negative and varies as $\alpha(T)H^2$ at low fields. α is roughly independent of temperature below T_{SG} and then falls off with temperature. Over a wide range of temperature and magnetic fields $\Delta\rho/\rho$ is found to be roughly proportional to M^2, rather than to H^2. Due to the spin-orbit interaction present in a FM, the MR should be anisotropic at low fields. At high fields it becomes negative. The magnitude of the slope $[(1/\rho)\partial\rho/\partial H]$ decreases with decreasing temperature since there is less electron-magnon scattering for $T \ll T_C$. We have measured $\Delta\rho/\rho$ and M *vs* H at several temperatures on the same piece for each composition for more meaningful possible correlations between them. Arrott plots (M^2 vs H/M) at the lowest temperature in each sample would indicate the presence of long-range FM order, if any. This will be of vital importance in confirming the FM order (non-zero value of spontaneous magnetization in the absence of any magnetic field) in the possible mixed-phase alloys with $x = 23$ and 26 and the FM alloy (x=30) close to the critical concentration region for long-range order.

$\underline{Au}Fe$ binary alloys[4] in the Au-rich region is a similar system which shows SG behaviour below the percolation concentration ($\simeq$ 15 at.%Fe). Above 15 at.%Fe, it goes from a paramagnetic to a ferromagnetic to a mixed ferro-spin-glass phase as the temperature is lowered. In the latter state the MR is found to be negative and isotropic and varies slower than H below T_C.

Here we have presented a comprehensive study of magnetoresistance (MR) of the crystalline Fe-rich γ-phase Fe alloy series $Fe_{80-x}Ni_xCr_{20}$ $14 \leq x \leq 30$. As mentioned in Chapter 1, the dominant contribution to the MR is a band contribution (as predicted by Kohler's rule). However, in this particular magnetic alloy system having high concentration of 3d atoms with competing exchange interactions, the contribution from magnetic effects will be dominant. Suppression of spin-flip scattering with the application of a magnetic field along with magnetic domains effects and spontaneous magnetization complicate the MR of this particular class of alloys in the vicinity of the critical composition for the long-range magnetic ordering

4.1 General features and comparative study of low-field magnetoresistance and magnetization of Fe-Ni-Cr series

(a) In Figs.4.1(a) and 4.1(b) we have shown the longitudinal $\left[(\frac{\Delta\rho}{\rho})_{\parallel}\right]$ and transeverse $\left[(\frac{\Delta\rho}{\rho})_{\perp}\right]$ magnetoresistances of the alloy with x=30 (FM) in the temperature range of 11 - 150 K and up to a field of 16.5 kOe. The MR in both the orientations is negative and varies slower than H below 50 K. $(\Delta\rho/\rho)_{\perp}$ at 11 K and a field at 16.5 kOe is only $\approx$ 0.17%. Above 50 K the MR becomes positive and shows a normal ($\frac{\Delta\rho}{\rho} \sim H^2$) magnetoresistance behaviour (Kohler type) till 300 K. Figure 4.2 (a) shows the comparative plots of both the orientations at several temperatures ranging from 11 K to 50 K. It can be clearly seen that $\left|(\frac{\Delta\rho}{\rho})_{\perp}\right|$ is always greater than $\left|(\frac{\Delta\rho}{\rho})_{\parallel}\right|$, i.e., a small but finite anisotropy is indeed present till T = 50 K. The typical value of the anisotropy of the MR here (= $[\left|(\frac{\Delta\rho}{\rho})_{\parallel}\right|$ - $\left|(\frac{\Delta\rho}{\rho})_{\perp}\right|]$) is 0.04% at T = 11 K and at magnetic field of 16.5 kOe. This value of anisotropy of MR in x = 30 (FM) is very small in contrast to the much larger values for a homogeneous FM. In the inset of Fig. 4.2(b) we have shown the behaviour of both the LMR and the TMR of x = 30 in a very small field range of

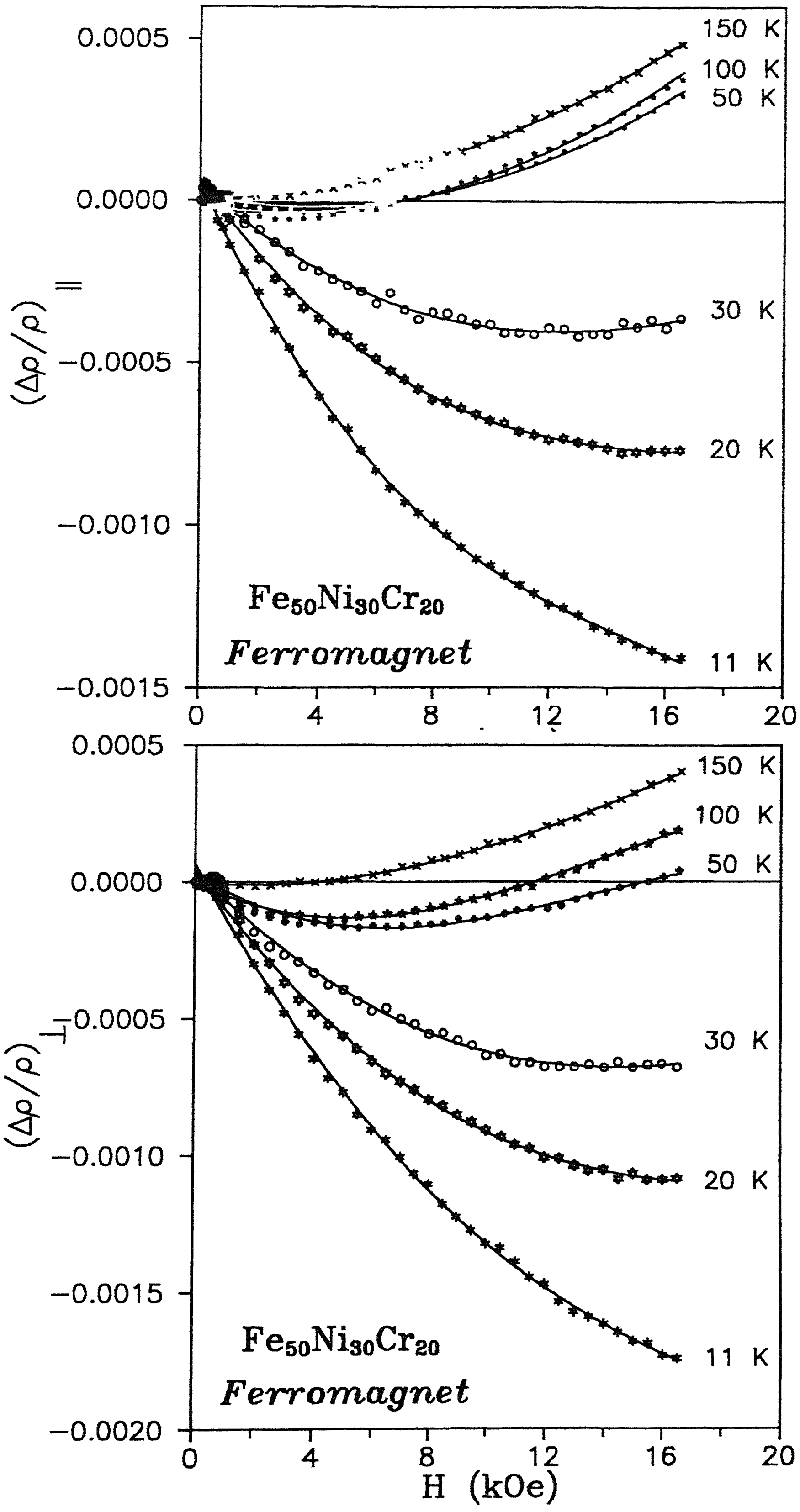

Figure 4.1: Magnetic field (H) dependence of (a) longitudinal ($(\frac{\Delta\rho}{\rho})_{\parallel}$) and (b) transverse ($(\frac{\Delta\rho}{\rho})_{\perp}$) magnetoresistances at various temperatures for Fe$_{50}$Ni$_{30}$Cr$_{20}$ (FM) alloy.

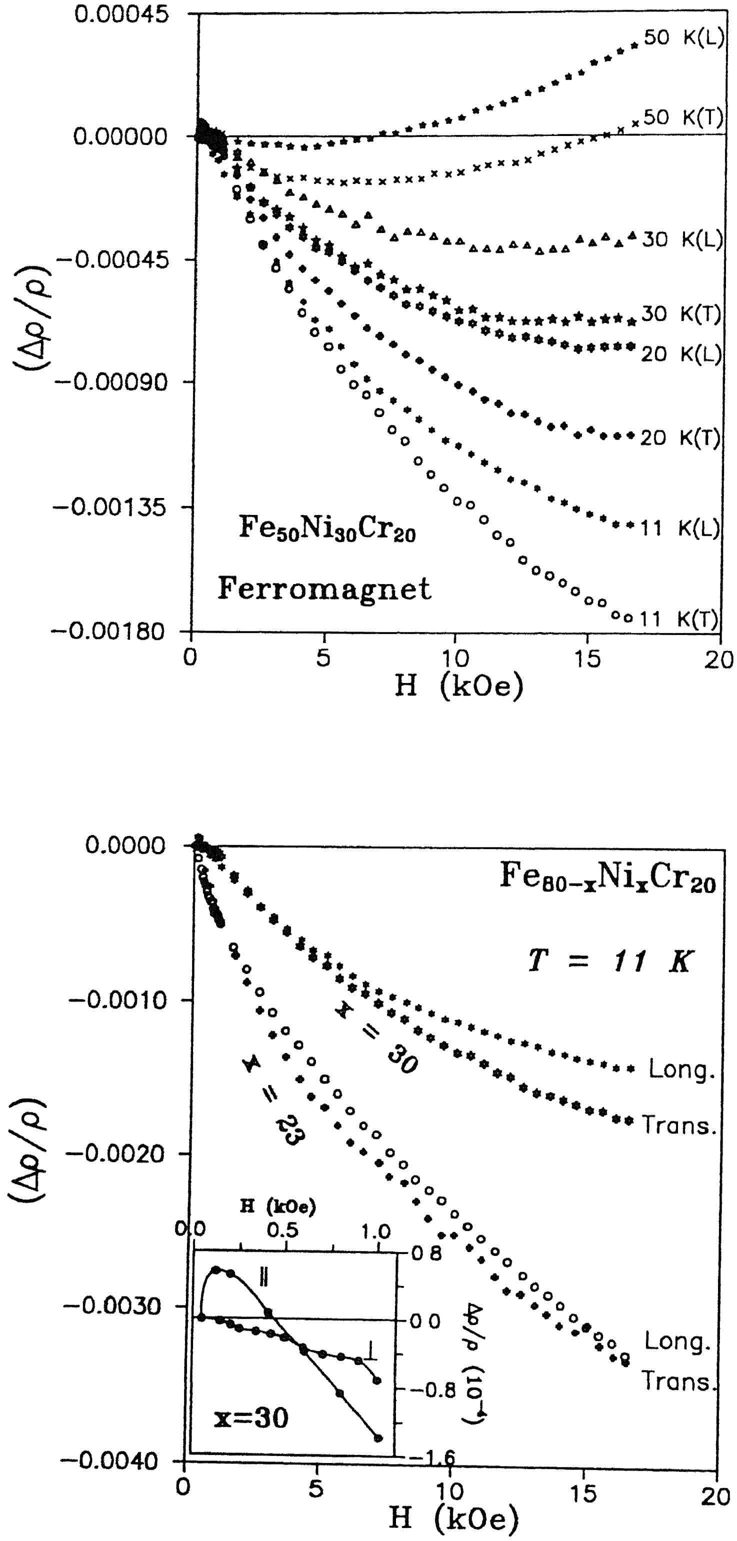

Figure 4.2: (a) Comparative plot longitudinal (L) and transverse (T) Magnetoresistances showing the anisotropy of MR for x=30 alloy at various temperatures. (b) Same plot for the alloy with x=30 and 23 at 11 K. The inset clearly shows the anisotropy in the low field range (0 - 1000 Oe) for x = 30.

0 to 1 kOe at 11 K. The LMR is positive ($\frac{1}{\rho}\frac{\partial\rho}{\partial H}$ and $\frac{\Delta\rho}{\rho}$) at low fields with a maximum at H = 130 Oe, followed by a sharp decrease ($\frac{1}{\rho}\frac{\partial\rho}{\partial H} < 0$) eventually going to a large negative value ($\frac{\Delta\rho}{\rho} < 0$) at higher fields. The TMR shows a continuous decrease ($\frac{1}{\rho}\frac{\partial\rho}{\partial H}$ and $\frac{\Delta\rho}{\rho} < 0$) till the highest measuring field of 16.5 kOe. The reproducibility of these observations at very low fields showing small anisotropy has been confirmed through several measurements. The origin of such an anisotropy term $(\Delta\rho_{\|} - \Delta\rho_{\perp})/\rho_0$ at the lowest fields and temperatures can be associated with the domain orientation in ordinary FM's like Ni and also in NiMn (21 at.% Mn) alloy near the percolation threshold[5].

The field dependence of magnetization at several temperatures (isotherms) for x = 30 has been presented in Fig.4.3 up to a field of 16.5 kOe. We observe a clear tendency towards saturation but true saturation is not achieved even at the highest field (16.5 kOe) at the lowest temperature (19 K). The field dependence of magnetization at 19 K is found to be given by $M \propto H^{0.05}$ in the field range of 2 - 16.5 kOe. With the increase of temperature, this alloy eventually evolves towards a PM phase ($M \propto H$) beyond 200 K as clearly seen from Fig.4.3. Arrott plots ($M^{1/\beta}$ vs $(H/M)^{1/\gamma}$, keeping $\beta = 0.5$, and $\gamma = 1$ (the mean-field values of the critical exponents) for x = 30 is shown in Fig. 4.4. We find a set of parallel lines having both positive and negative intercepts on the M^2-axis from which T_c can be estimated to be 135 K. The large positive intercepts in Arrott plots at lower temperatures confirm its FM state (large spontaneous moment at $H_{int} = 0$).

(b) Figure 4.5 is a plot of the LMR $[(\frac{\Delta\rho}{\rho})_{\|}]$ as a function of H at several constant temperatures (isothermal) for x = 26 (mixed phase or re-entrant phase) in the temperature range of 11 K to 75 K and up to a field of 16.5 kOe. In this alloy also the MR is negative till 75 K and varies slower than H. $(\frac{\Delta\rho}{\rho})_{\|}$ at 11 K and a field of 16.5 kOe is $\approx$ 0.18%. In Fig. 4.6, we have shown several isothermal M–H plots in the temperature range of 19 - 250 K. The plot at 19 K and fields up to even 16.5 kOe has a lot of curvature indicating lack of saturation of the magnetization. The functional dependence of this plot was obtained from the fit to $M \propto H^{0\,1}$ in the field range of 2 – 16.5 kOe. The Arrott plots (not shown here) show large positive intercepts on the M^2 –axis which confirms the FM ordering below 60 K.

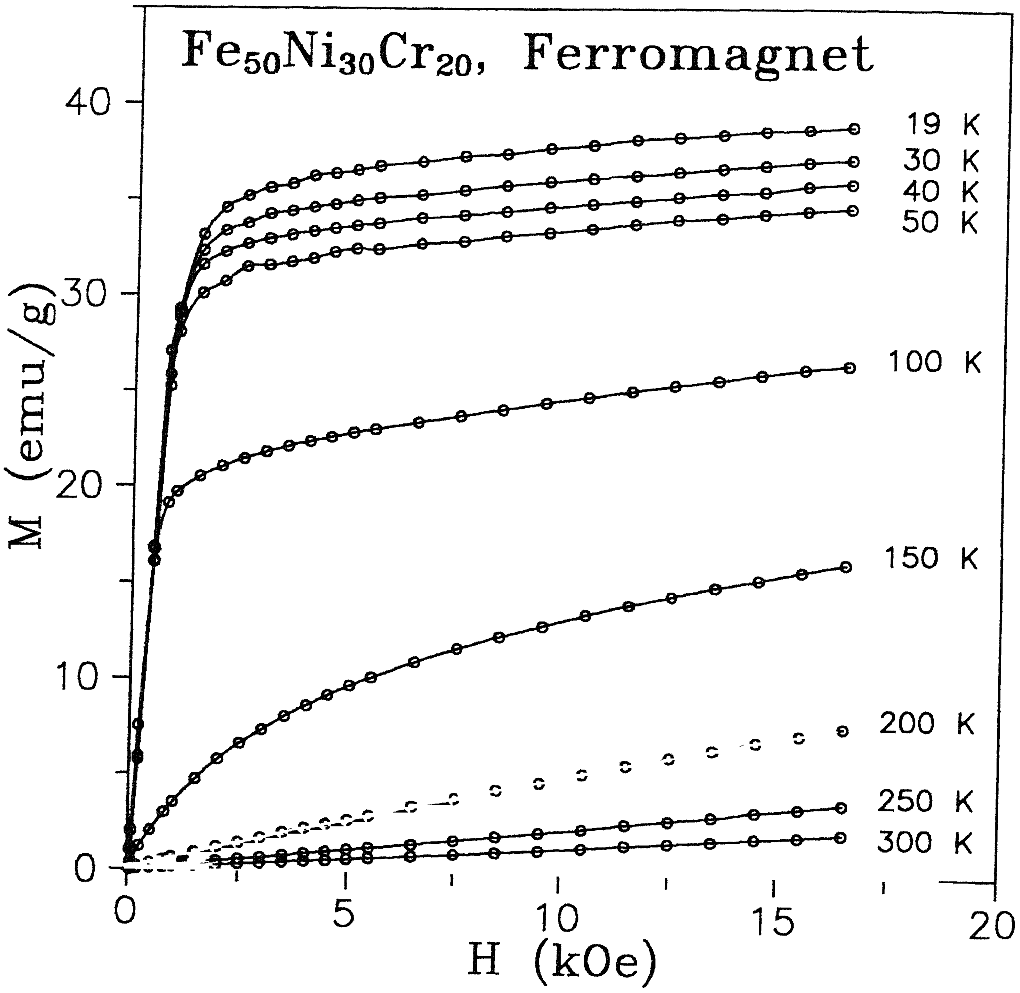

Figure 4.3: M-H isotherms of $Fe_{50}Ni_{30}Cr_{20}$ (FM) alloy at various temperatures in the field range of 0 to 16.5 kOe.

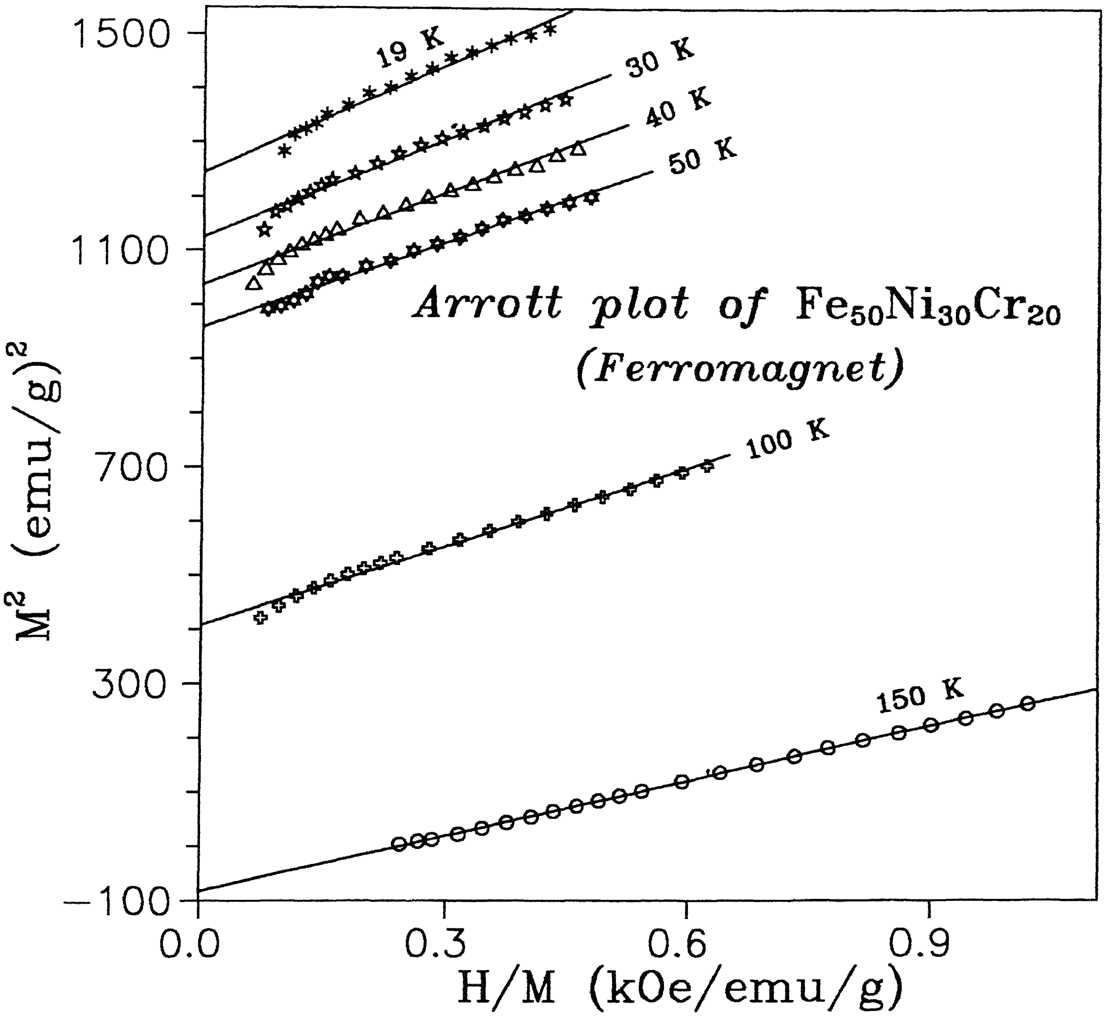

Figure 4.4: Arrott plots at various temperatures for $Fe_{50}Ni_{30}Cr_{20}$ (FM) alloy confirming the presence of large spontaneous moment.

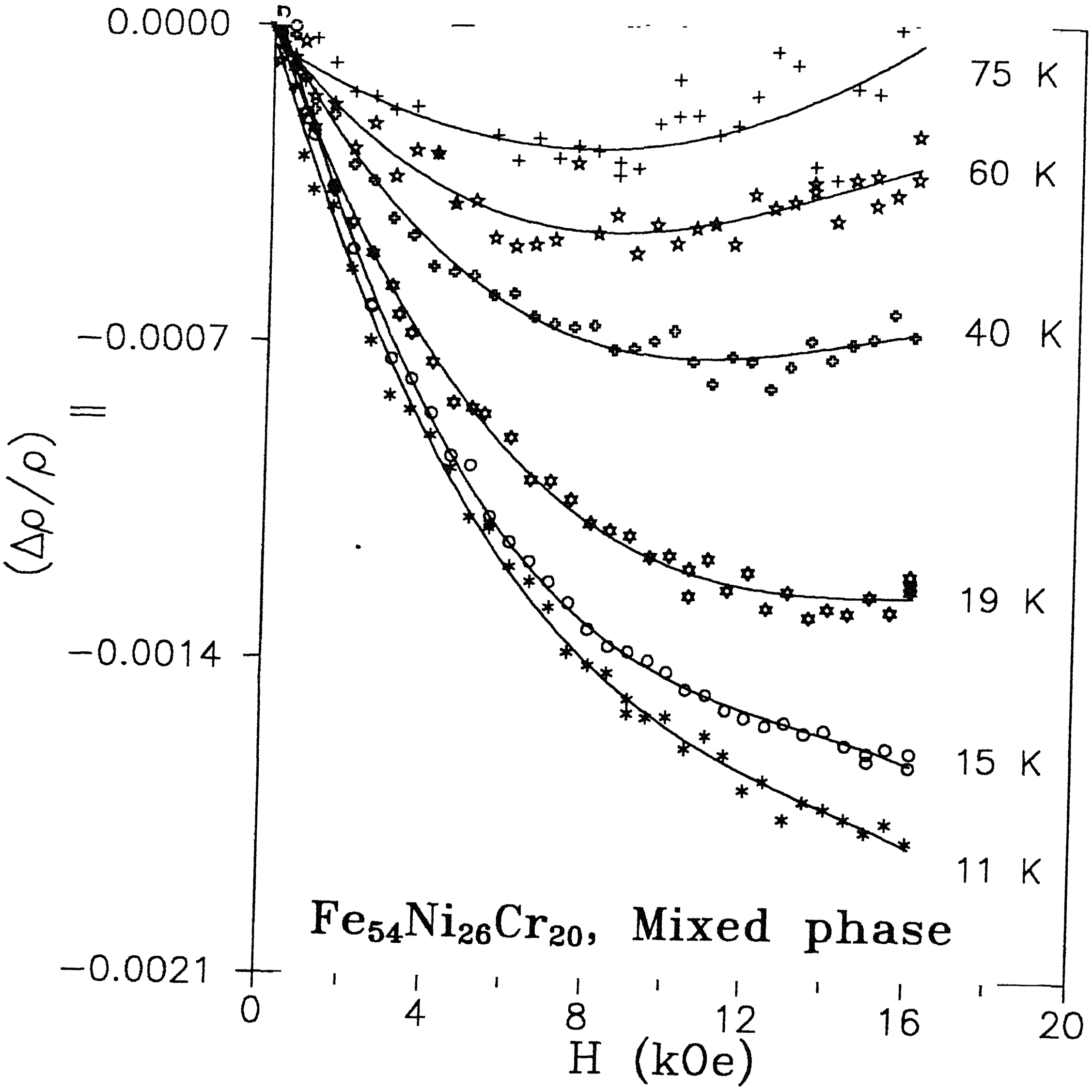

Figure 4.5: Magnetic field (H) dependence of longitudinal $((\frac{\Delta\rho}{\rho})_{\parallel})$ magnetoresistance at various temperatures for Fe$_{54}$Ni$_{26}$Cr$_{20}$ (Mixed phase) alloy.

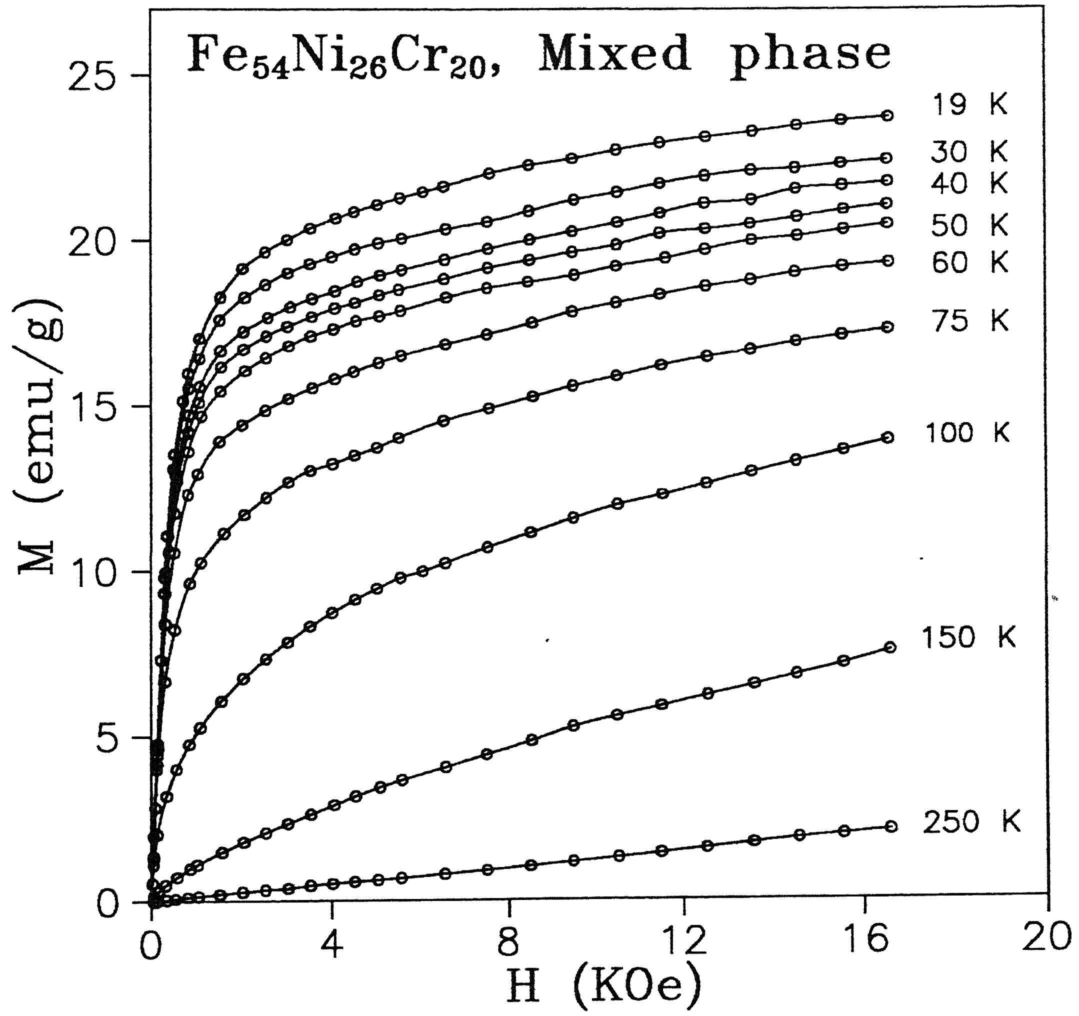

Figure 4.6: M-H isotherms of $Fe_{54}Ni_{26}Cr_{20}$ (Mixed phase) alloy at various temperatures in the field range of 0 to 16.5 kOe.

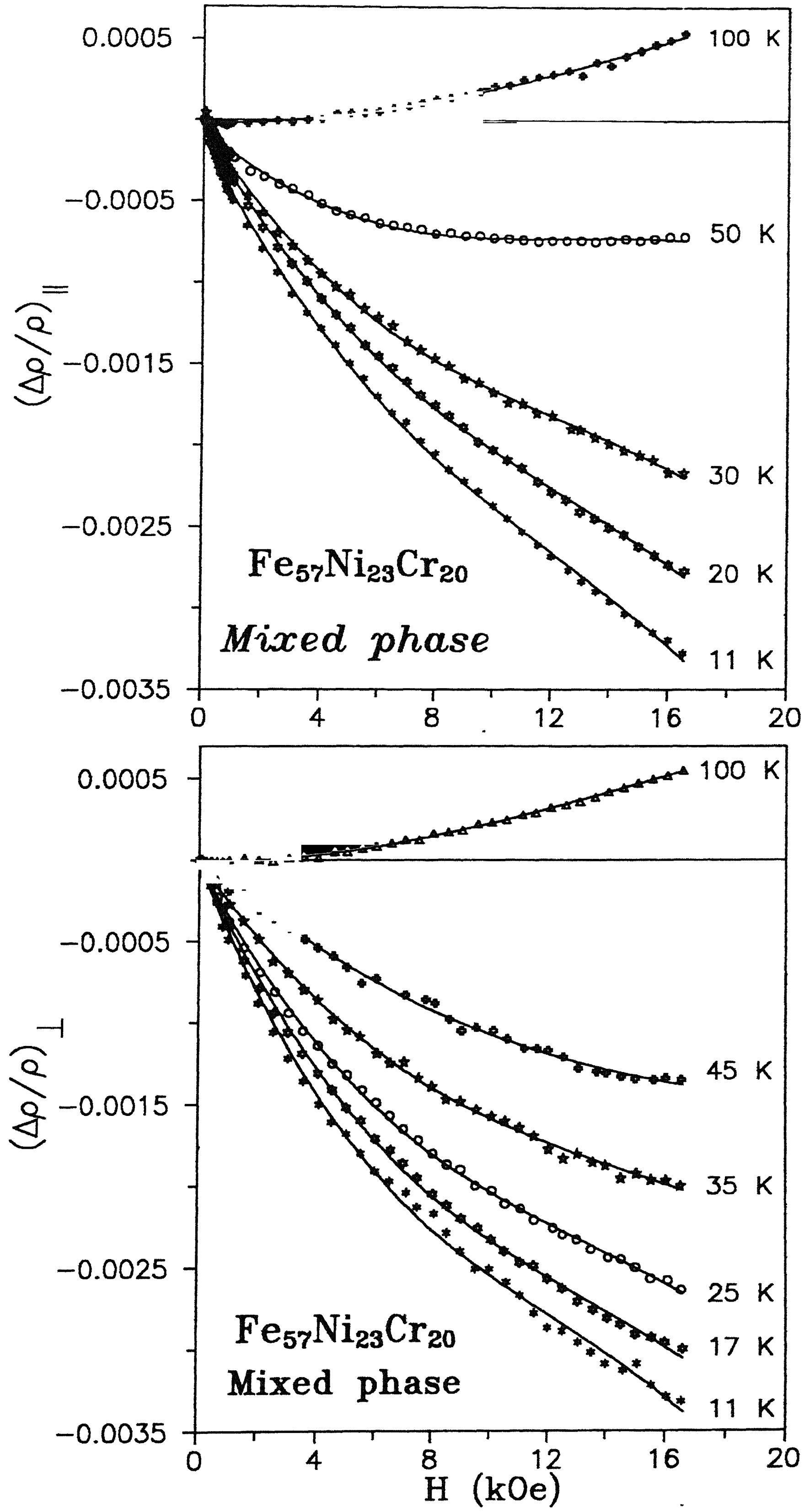

Figure 4.7: Magnetic field (H) dependence of (a) longitudinal ($(\frac{\Delta\rho}{\rho})_{\parallel}$) and (b) transverse ($(\frac{\Delta\rho}{\rho})_{\perp}$) magnetoresistance at various temperatures for Fe$_{57}$Ni$_{23}$Cr$_{20}$ (Mixed phase) alloy.

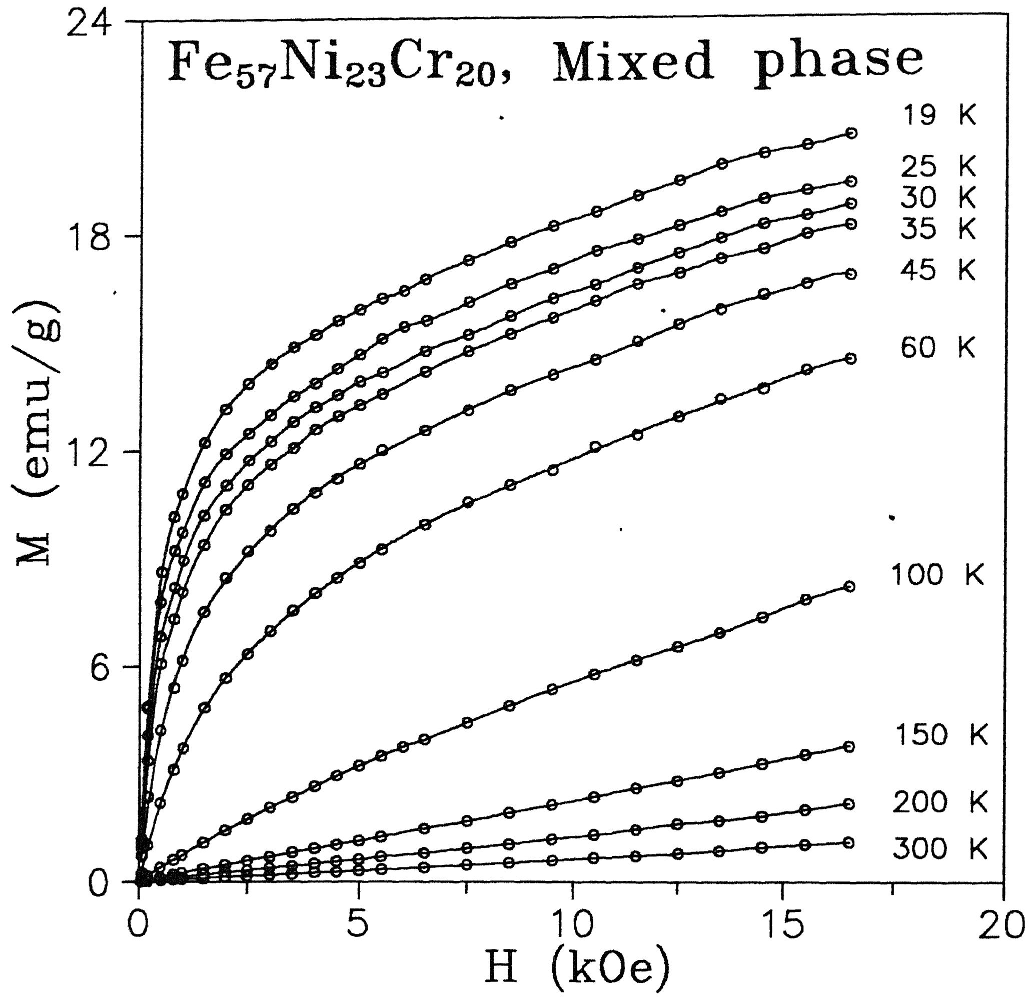

Figure 4.8: M-H isotherms of $Fe_{57}Ni_{23}Cr_{20}$ (Mixed phase) alloy at various temperatures in the field range of 0 to 16.5 kOe.

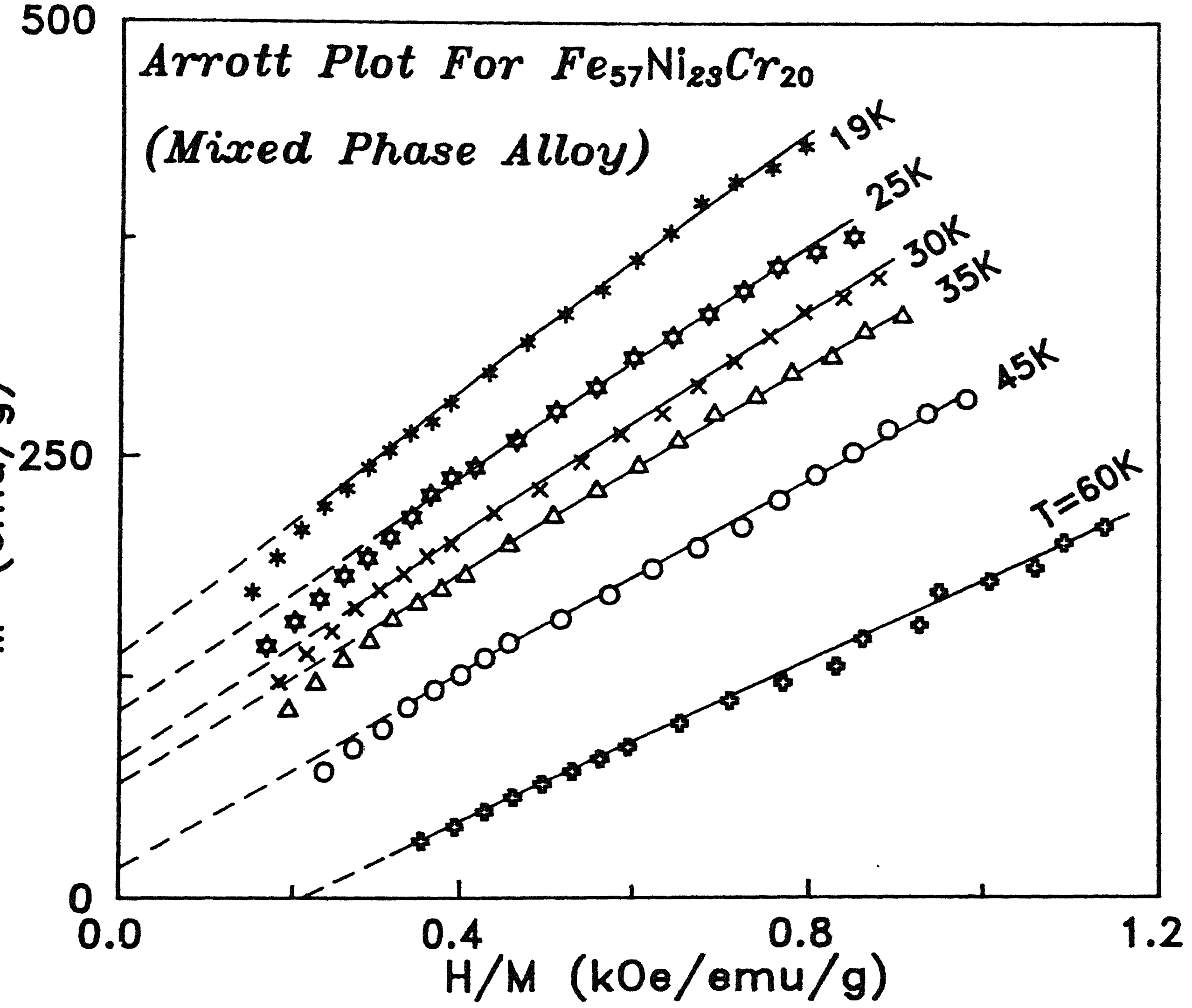

Figure 4.9: Arrott plots at various temperatures for $Fe_{57}Ni_{23}Cr_{20}$ (Mixed phase) alloys confirming the presence of ferromagnetic ordering below T_{SG}.

(d) Figures 4.10(a) and 4.10(b) show the field dependence of the LMR and TMR at several temperatures for the alloy with x = 21 (SG). It is important to note that at each temperature the curves in both the orientations are indeed identical (completely isotropic, FAR ≈ 0) within the resolution of our experiment. The curves at 100 K and above show positive normal magnetoresistance. Below 50 K, the MR varies slower than H. The value of the TMR is $\approx$ 0.4% at 11 K and at 16.5 kOe and is rather large in comparison with those of the other alloys (x) Figure 4.11 shows the field dependence of the magnetization of x=21. At the lowest temperature (19 K), the M–H plot does not show any tendency of saturation due to the strong competing interactions between FM and AFM exchange couplings (also seen in, say, AuFe with 4–8 at.% Fe impurity)[9]. At 19 K, $M \propto H^{0.4}$ till 15 kOe. The Arrott plot of this alloy at 19 K does not show any spontaneous FM ordering (no positive intercept on the M^2 –axis) and rules out any FM ordering at this temperature.

(e) In Fig. 4.12, the low-field LMR $[(\frac{\Delta\rho}{\rho})_{\parallel}]$ at several temperatures are shown. Its value at 11 K is $\approx$ 0.26 %. At the lowest temperature $\frac{\Delta\rho}{\rho}$ varies slower than H. However, at higher temperatures it varies faster than H. This kind of behaviour has also been found in AuFe alloy (8 - 13 at.% of Fe)[10]. The MR above 100 K becomes positive (normal MR).

The M–H plots (Fig. 4.13) of this alloy (x=19) resembles those of x =21. At the lowest temperature (19 K) $M \propto H^{0.45}$. The Arrott plots of this alloy do not have any positive intercept on the M^2-axis even at the lowest temperature which confirms the absence of any FM ordering (no spontaneous moment).

(f) In Fig. 4.14 we have shown the field dependence of both the LMR and TMR $[(\frac{\Delta\rho}{\rho})$ vs H] for the alloy with x =14 (AFM) at 4.2 K. Initially the LMR increases with field followed by a maximum and ultimately it becomes negative. In contrast, the TMR is negative for all fields from 0 to 14 kOe. As mentioned in Chapter 1, as the magnetic field is increased, the LMR of polycrystaline AFM metals should change from positive to zero and finally to negative values where at boundaries between the regions the curve is rounded by the domain wall and polycrystalline effects. In this AFM (x = 14) the field dependence of the LMR exhibits a similar behaviour and is consistent with studies on other AFM alloys, viz, Nd by Nagasawa[11].

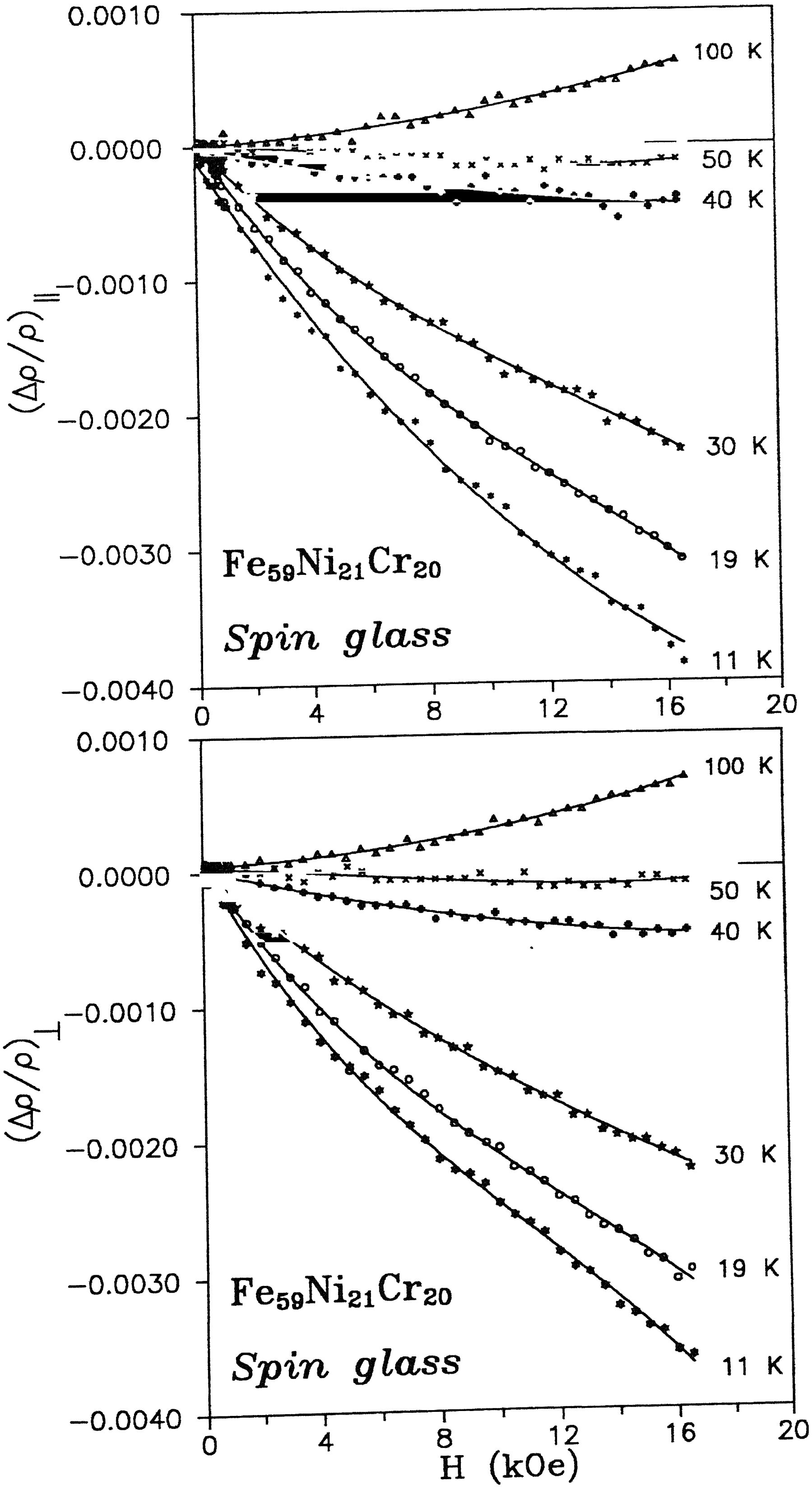

Figure 4.10: Magnetic field (H) dependence of (a) longitudinal $((\frac{\Delta\rho}{\rho})_{\parallel})$ and (b) transverse $((\frac{\Delta\rho}{\rho})_{\perp})$ magnetoresistances at various temperatures for $Fe_{59}Ni_{21}Cr_{20}$ (Spin glass) alloy.

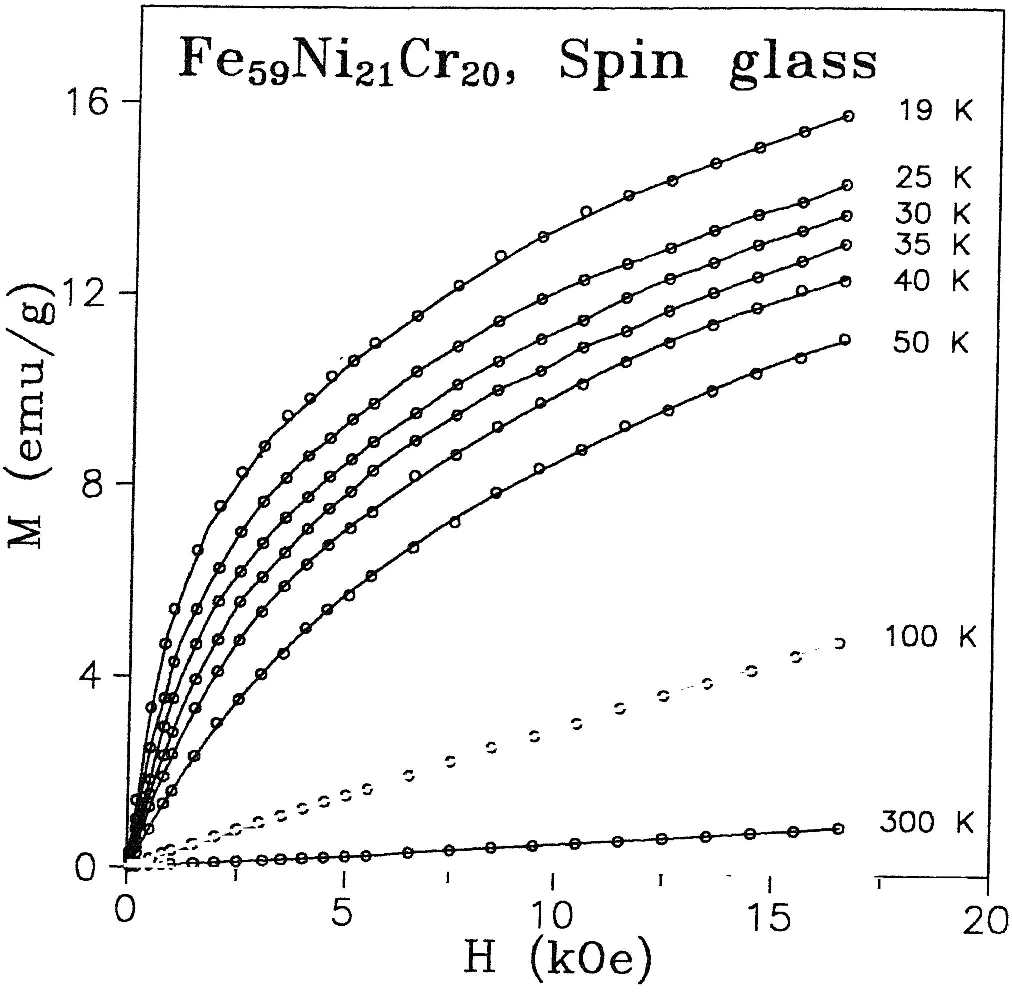

Figure 4 11: M-H isotherms of $Fe_{59}Ni_{21}Cr_{20}$ (Spin glass) alloy at various temperatures in the field range of 0 to 16.5 kOe.

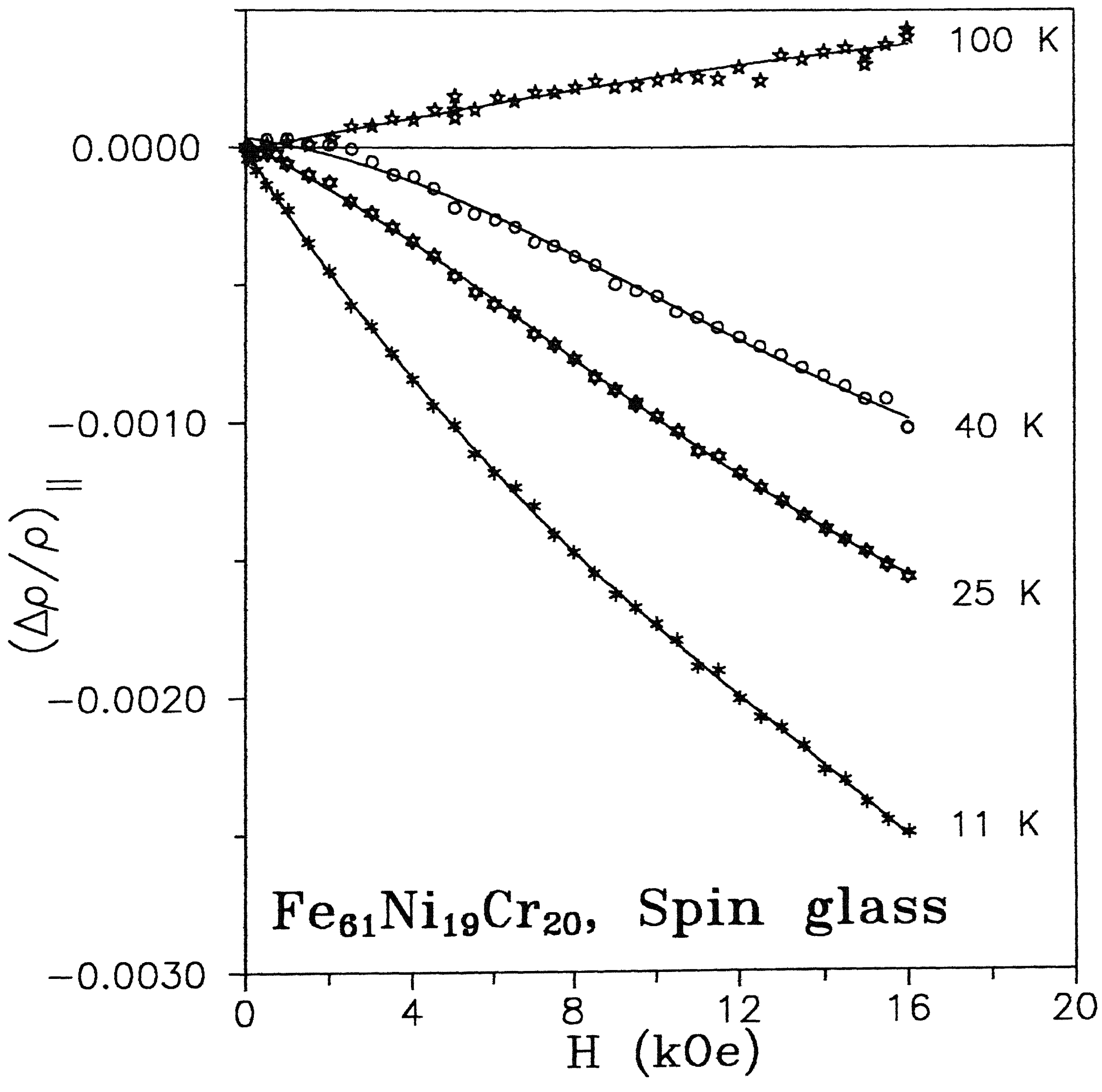

Figure 4.12: Magnetic field (H) dependence of longitudinal ($(\frac{\Delta\rho}{\rho})_{\|}$) magnetoresistance at various temperatures for $Fe_{61}Ni_{19}Cr_{20}$ (Spin glass) alloy.

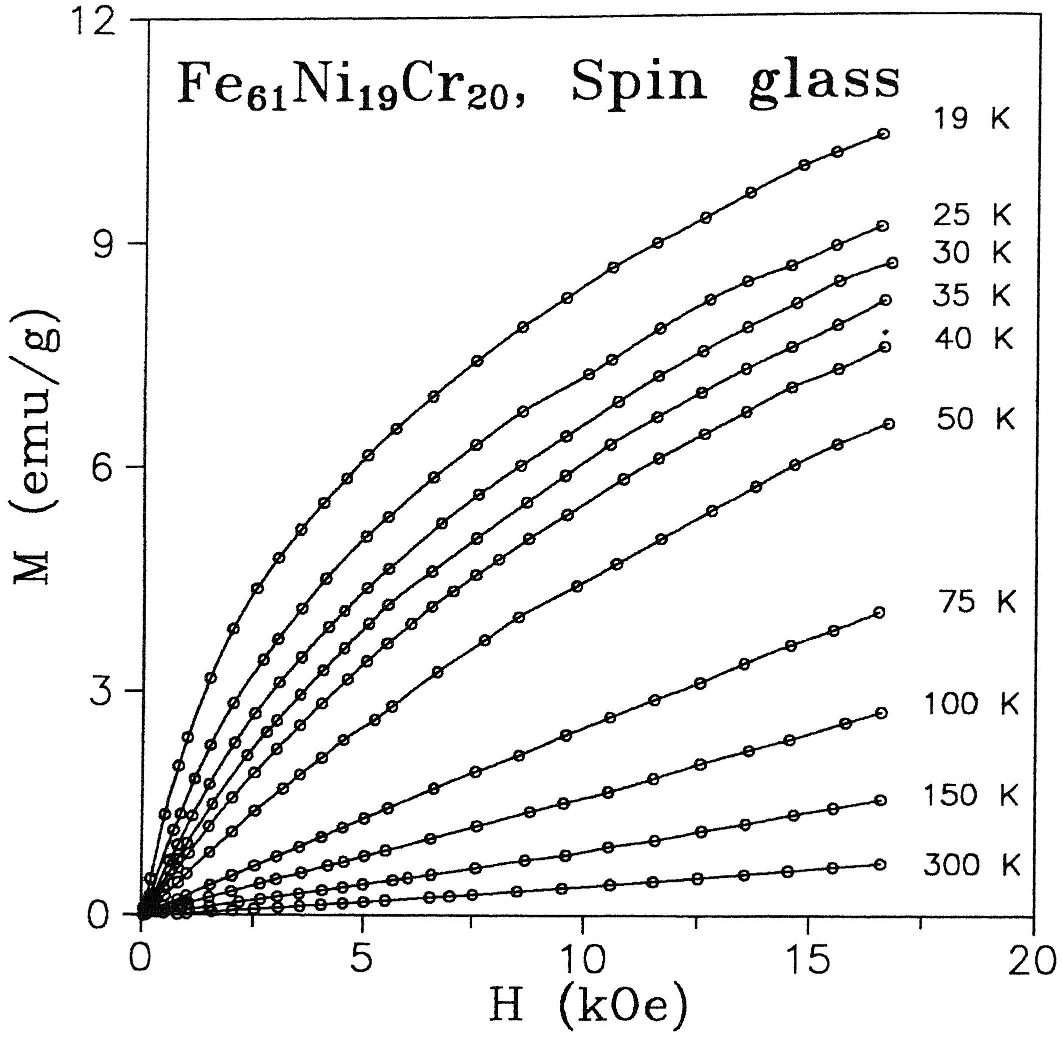

Figure 4.13: M-H isotherms of Fe$_{57}$Ni$_{19}$Cr$_{20}$ (Spin glass) alloy at various temperatures in the field range of 0 to 16.5 kOe.

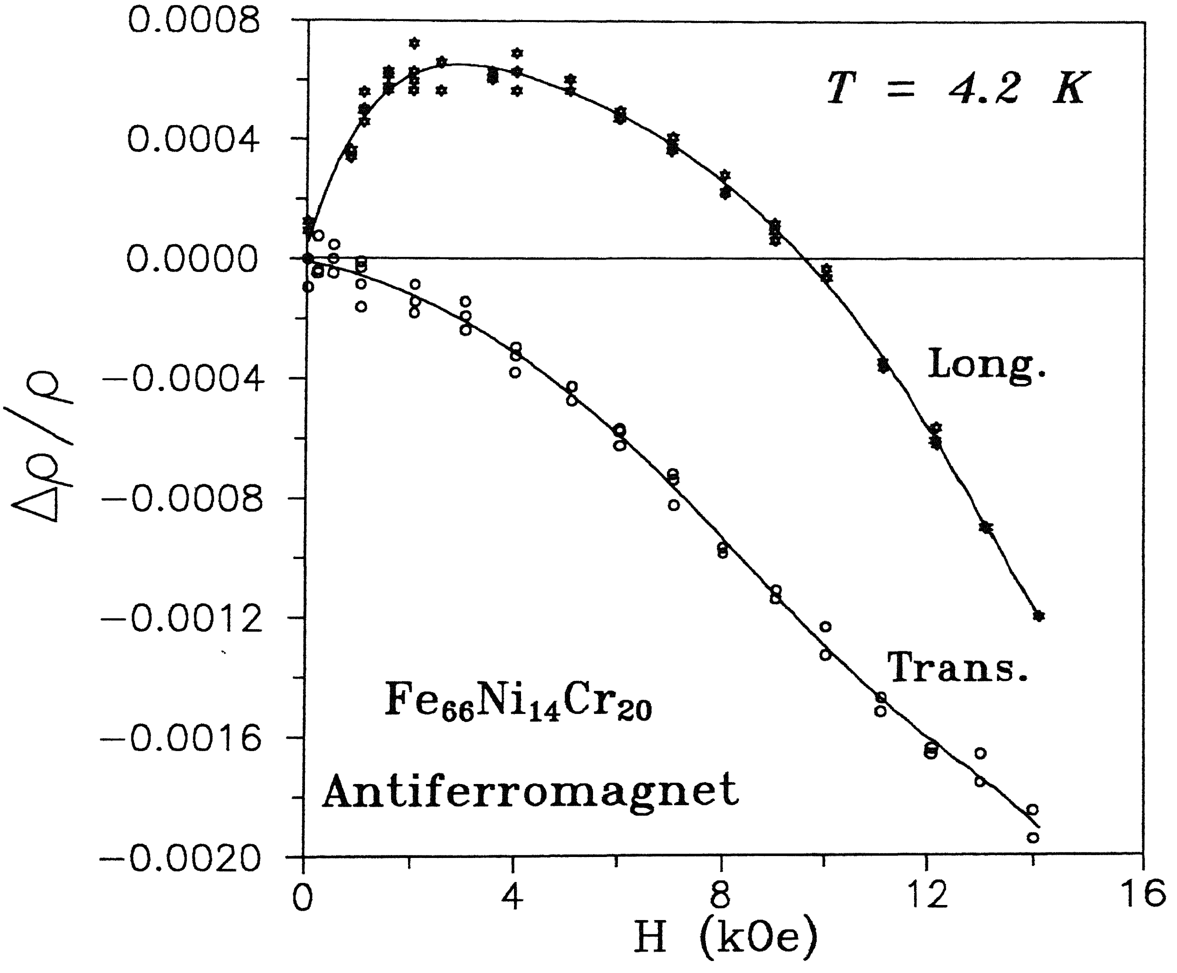

Figure 4.14: Magnetic field (H) dependence of longitudinal (Long.) and transverse (Trans.) magnetoresistances at 4.2 K for $Fe_{66}Ni_{14}Cr_{20}$ (Antiferromagnetic) alloy.

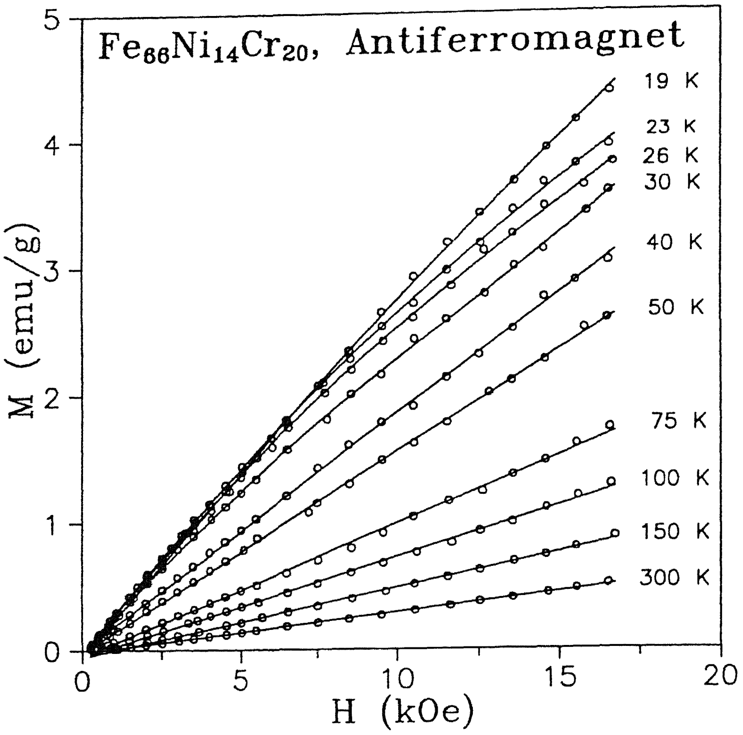

Figure 4.15: M-H isotherms of $Fe_{66}Ni_{14}Cr_{20}$ (Antiferromagnetic) alloy at various temperatures in the field range of 0 to 16.5 kOe.

Figure 4.15 shows the field dependence of magnetization of x=14 (AFM). At the lowest temperature (T=19 K), $M \propto H^{1.01}$ up to about 10 kOe above which it starts deviating from linearity. This may be associated with the *spin-flop transition* in this AFM alloy (x = 14) above 10 kOe. M–H plots of AFM alloys are much more linear as compared to those of SG, RSG and FM alloys.

4.1.1 Magnetic field, temperature, and composition dependence of magnetoresistance of Fe-Ni-Cr series

The magnetic field dependence of $\frac{\Delta\rho}{\rho}$ of all the alloys under investigation heve been fitted to the relation

$$\frac{\Delta\rho}{\rho} = -\alpha(T)H^n$$

using a non-linear least-squares fit programme. We have also estimated the contribution to the MR from Lorentz force normal MR and find that it is negligible compared to the magnetic term for all the concentrations in the field range of 1 - 16.5 kOe and temperature range of 11 - 50 K Above 100 K the MR of all the alloys are positive where the normal MR dominates. In Table 4.1 we have summarized the values of n, α(T), and χ^2 till 50 K for all the alloys in the magnetic field range of 2 - 16 kOe. The values of χ^2 ($\approx 10^{-6}$) are consistent with our experimantal accuracy. From this table we observe that :

(1) For the alloy with x = 19 (SG phase), the exponent of H, n = 0.8 at 11 K. The value of n increases with temperature. Above the ordering temperature (T_{SG}), n increases continuously to values between 1 and 2. This indicates the existence of short-range correlations, since in a completely paramagnetic state, n is 2[4, 12]. In canonical SG's[3] where spin freezing takes place because of random bond frustration (magnetic impurities are indirectly ferro- or antiferromagnetically coupled to each other via RKKY exchange interactions), the exponent (n) was found to be 2 with almost temperature-independent coefficient α below its freezing temperature. In this alloy (x=19) where the SG phase arises not due to RKKY exchange interaction mediated by conduction electrons but due to direct competiting FM and AFM exchange interactions (concentrated) SG), the value of n < 1. This kind of observation was also made in NiMn alloys[5] (only qualitative study) in the SG phase near the critical composition for ferromagnetism ($25 \leq x \leq 28$).

(2) In the case of x = 21 (spin-glass or cluster-glass phase), we find that n $\simeq$ 3/4 and is temperature independent as well. Here also we find n different from 2 unlike the canonical SG's[3]. There are some recent reports on $Au_{87}Fe_{13}$[7], $Au_{85}Fe_{15}$[10, 13] and $Au_{82}(Fe_{1-x}Cr_x)_{18}$[13] alloys with $15 \leq x \leq 25$ which find the same value of the exponent, n ($\approx 0.75 \pm 0.04$) below the $T_{SG/CG}$ phase. Moreover, they have referred our value[14] as the only available one for comparing their data for the concentrated alloys in the SG/CG regime.

Since this alloy (x=21) is very near the mixed-phase or re-entrant SG-phase regime (x=23-26), it must have cluster-glass-like ordering below $T_{SG/CG}$. Hence the MR will have contributions from both inter-cluster interaction which is of spin-glass-type and intra-cluster interaction which is ferromagnetic. The unique value of the exponent of H (n $\approx \frac{3}{4}$) results from the above combined effects for all the alloys in the SG/CG regime.

Table 4.1: Values of the parameters n, and α (T) and also χ^2 for the fits to $\Delta\rho/\rho = -\alpha(T)H^n$ at various temperatures for $Fe_{80-x}Ni_xCr_{20}$ (14 $\leq$ x $\leq$ 30) alloys in the field range of 2 to 16.5 kOe.

Alloy (x)	T (K)	n	$\alpha(T)$ (10^{-4} kOe^{-n})	χ^2 (10^{-6})
19 (SG)	11	0.80	2.8	5.0
	25	1.07	0.8	3.9
	40	1.40	0.2	6.0
21 (SG)	11	0.74	4.9	15
	15	0.77	4.0	31
	19	0.76	3.7	9
	30	0.78	2.6	18
	40	0.73	0.6	82
23 (Mixed phase)	11	0.66	6.0	6.4
	17	0.66	5.5	7.0
	20	0.66	4.6	2.4
	25	0.65	4 7	9.8
	30	0.64	3.9	1.8
	35	0.65	4.6	8.7
	45	0.65	3.7	12
26 (Mixed phase)	11	0.54	4.3	6.0
	15	0.53	4.0	9.0
	19	0.48	3.6	8.5
	40	0.52	2.2	8.8
	60	0.27	2.1	12
	75	0.19	1.4	21
30 (FM)	11	0.74	2.4	25
	20	0.67	6.7	19
	30	0.60	1.4	50
	50	0.10	1.3	11

(3) For the alloy with x = 23 (mixed or re-entrant phase), the exponent of H is 2/3 and is independent of T up to 50 K which is above both T_{SG} and T_c. This value of n is different from the value of $\frac{6}{7}$ found for AuFe (18 at.% Fe)[4] for T < T_{SG}. There it depends strongly on temperature for T > T_{SG}. However, a recent study on $Au_{82}(Fe_{1-x}Cr_x)_{18}$ alloys for 0.05 $\leq$ x $\leq$ 1[10] which show RSG behaviour, the value of n is found to be 0.67 ($\pm$ 0.02) or $\simeq \frac{2}{3}$ in the temperature range of 4.2 to 200 K (i.e., above both T_c and T_{SG}) and in the field range of 2 - 45 kOe. It is interesting to note that in all these alloys the range of fit of $H^{2/3}$ - dependence of $\Delta\rho/\rho$ extends beyond the Curie temperature. Moreover, in the same study[13], they have rechecked the data for $Au_{82}Fe_{18}$ (RSG) alloy and found that the value of n $\approx \frac{2}{3}$ only between 140 to 160 K which is close to its T_c (150.7 K). Below T_{SG}, n $\approx$ 0.8 $\pm$ 0.2. They have also referred our value[14] as the only available one for comparing their data[13] in the case of concentrated alloys in the mixed-phase (or RSG) regime.

According to Balberg, the field dependence of MR of a weak ferromagnet at high fields is given by[12]

$$\Delta\rho \propto -H^{(1-\alpha)/\beta\delta} ,$$

provided $(\mu H/kT) \gg \left|1 - \frac{T}{T_c}\right|$, where μ is the magnetic moment of the ion, α the specific heat exponent, β and δ are the critical exponents for spontaneous magenetization and critical isotherm, respectively. In the case of AuFe (RSG) alloys, magnetization[15] and non-linear susceptibility[16] measurements near the critical temperature show that the critical exponents are very close to those of 3d-Heisenberg systems[17]. Putting the values of the critical exponents for 3d-Heisenberg system, n ($\approx \frac{1-\alpha}{\beta\delta}$) is found to be 0.64 which is very close to the value found for our RSG alloys ($\approx \frac{2}{3}$).

So our present study along with the studies mentioned above reveal that $\frac{\Delta\rho}{\rho} \propto -H^{2/3}$ could be claimed as a characteristic feature of re-entrant spin glasses or mixed-phase alloys in the field range above their technical saturation.

(4) For the alloy with x = 26 (RSG, very close to FM ordering), the value of n is found to be $\frac{1}{2}$ in the temperature range of 11 -50 K and is temperature independent. This particular alloy is very close to the critical concentration for long-range FM ordering. The different value

of the exponent n compared to that in the RSG regime (n $\approx$ 2/3) can be attributed to the fluctuations due to the formation of large clusters along with the spin-glass freezing.

(5) In the case of the alloy with x = 30 (FM phase), n varies strongly with temperature. α (T), the coefficient of H^n, is the strength of the MR. It decreases with temperature in all the samples. As mentioned in the earlier section, a small but finite anisotorpy (FAR)is found in the very low-field region (0 – 200 Oe) and at high fields (16.5 kOe) as well, the former FAR is about 0.01 %.

In Fig. 4.16 (a) we have shown $(\frac{\Delta\rho}{\rho})_{\parallel}$ vs. H plot for all the alloys at 11 K for comparison. Each curve except for x = 19 has been shifted vertically by some amount for clarity. From this figure it is clear that with the decrease of Ni concentration (x), the curve become steeper. The value of $(\frac{\Delta\rho}{\rho})_{\parallel}$ is found to be maximum for x = 21 (SG phase, close to the critical concentration region x $\approx$ x$_c$).

In Fig.4.16(b) we have shown the composition (x) dependence of the coefficient α (Table 4.1) and the exponent, n at 11 K. The value of α increases with x, reaches a maximum at x = 23 and then decreases as the alloys approach long-range FM. The value of n decreases with x, reaches a minimum at x = 26 and then increases with x.

Figure 4.17 (a) shows the temperature dependence of $(\frac{\Delta\rho}{\rho})_{\parallel}$ for x = 30 (FM) at fields of 5, 10 and 16.5 kOe. Above 50 K the sign of $(\frac{\Delta\rho}{\rho})_{\parallel}$ changes from negative to positive. The decrease of the $\left|(\frac{\Delta\rho}{\rho})_{\parallel}\right|$ with the increase of temperature indicates an enhancement of the amplitude for spin-flip scattering of conduction electrons from localized moments of the magnetic ions. Figures 4.17 (b) and 4.18 (a) show the same plot for x = 23 (mixed phase) and x = 21 (SG) alloys, respectively. In Fig. 4.18 (b) the composition dependence of $(\frac{\Delta\rho}{\rho})_{\parallel}$ has been shown at 11 K for fields of 5, 10 and 16.5 kOe. It can be clearly seen from the figure that the magnitude of the MR is maximum in the SG regime (critical concentration x $\approx$ x$_c$).

So we observe a definite trend of MR, α and n with composition as the Fe-Ni-Cr system evolves from long-range AFM ordering to long-range FM ordering through the critical concentration region ($x \approx x_c$) where the maximum change of all the three quantities occurs.

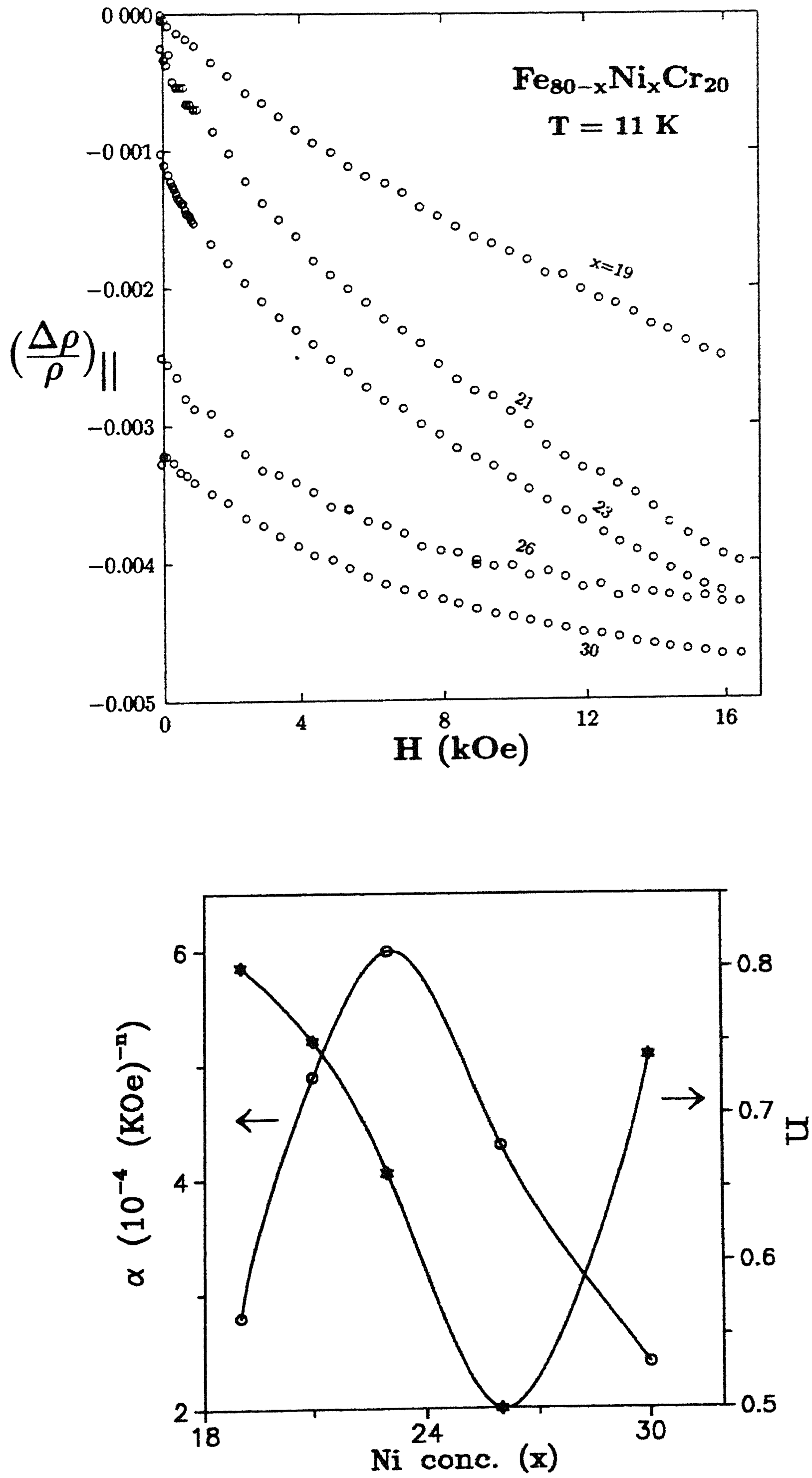

Figure 4.16: (a) Longitudinal MR vs H for $Fe_{80-x}Ni_xCr_{20}$ at 11 K. All the data (except for x=19 alloy) have been shifted vertically for clarity. (b) Ni concentration (x) dependence of α and n at T=4.2 K for $Fe_{80-x}Ni_xCr_{20}$ alloys.

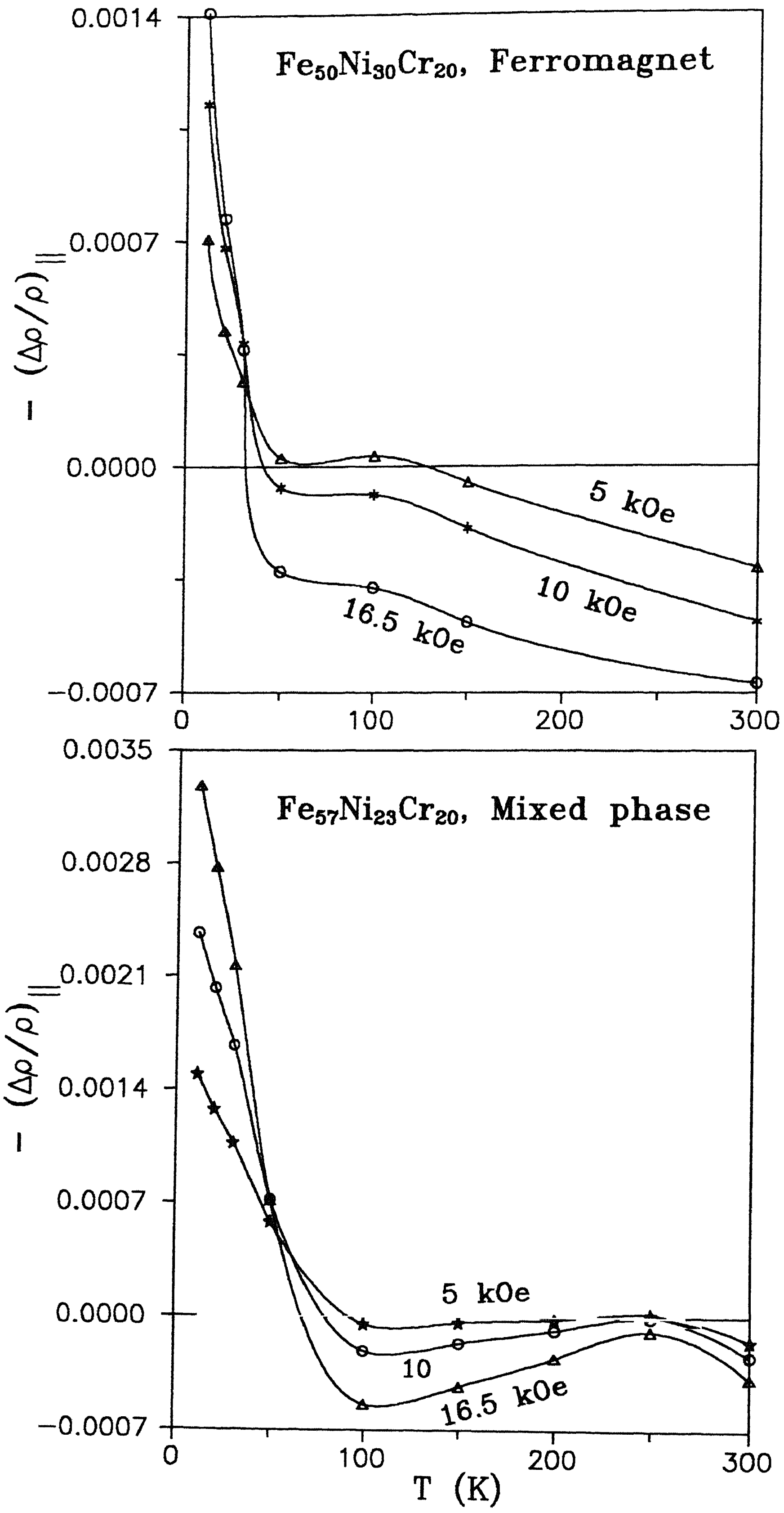

Figure 4.17: Temperature dependence of longitudinal magnetoresistance of (a) $Fe_{50}Ni_{30}Cr_{20}$ (FM) and (b) $Fe_{57}Ni_{23}Cr_{20}$ (Mixed phase) alloys at magnetic fields of 5, 10 and 16.5 kOe.

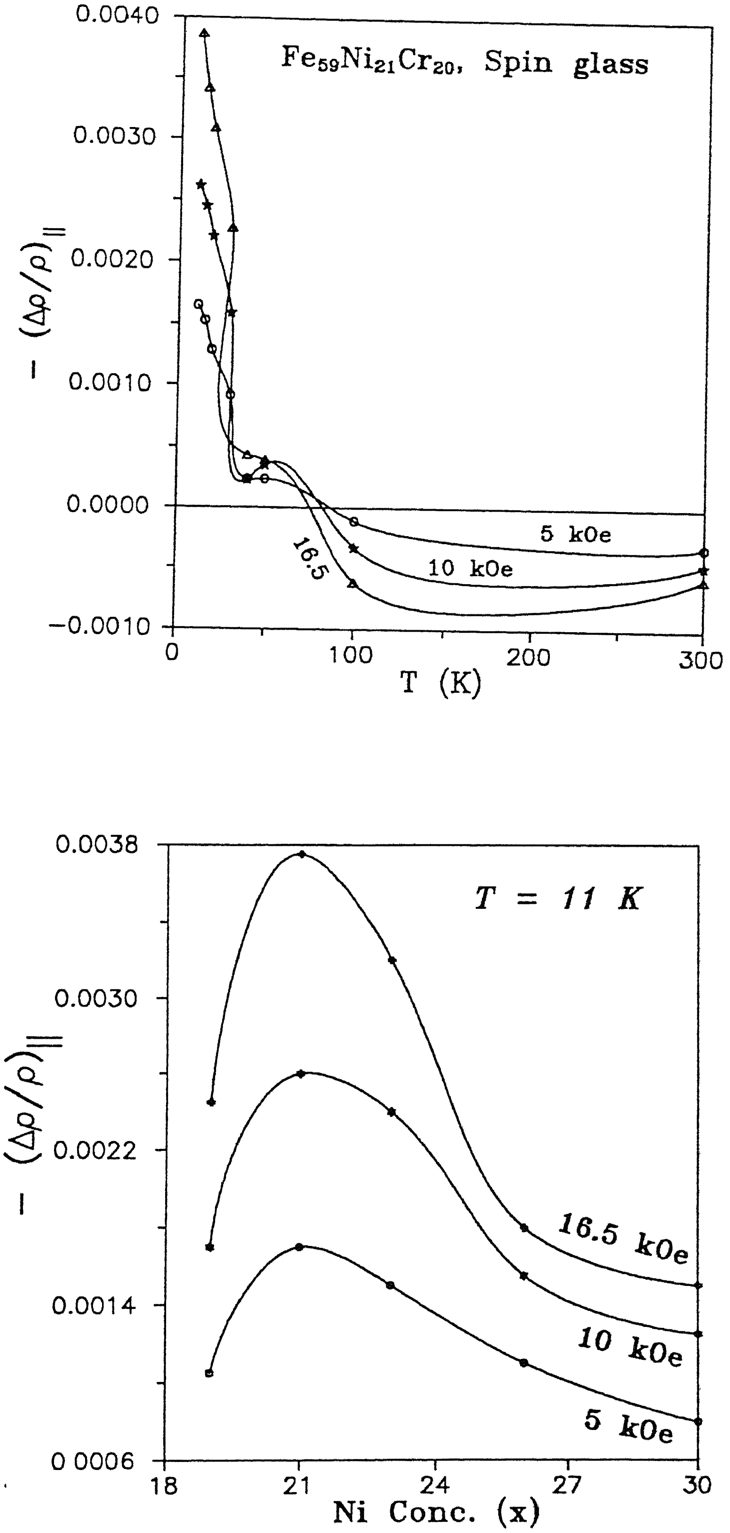

Figure 4.18: (a)Temperature dependence of longitudinal MR of $Fe_{59}Ni_{21}Cr_{20}$ (SG) and (b) Ni concentration (x) dependence of longitudinal MR for $Fe_{80-x}Ni_xCr_{20}$ alloys at 11 K. The curves in both the plots are at magnetic fields of 5, 10 and 16.5 kOe.

There are reports on MR of NiMn alloys[5, 8] with about 21–30 at % Mn (which are very near the critical concentration regime for FM ordering) in SG, RSG, and FM phases. In all these phases they have also found the field dependence of $\frac{\Delta\rho}{\rho}$ to be slower than linear. However, no quantitative study has been made on those alloys.

4.2 Correlation between low-field magnetoresistance and magnetization

In this section we have studied the magnetization dependence of magnetoresistance of the Fe-Ni-Cr series. The diversity of magnetic states at low temperature manifests itself in the magneto-transport studies since in any magnetic system the MR probes the electron transport which is coupled to its magnetic state. If the alloy system is magnetically homogeneous, atleast on the scale of the electron mean – free path, a definite correlation between the magnetic property and its magneto-transport property is expected.

To find out any meaningful correlation between $\frac{\Delta\rho}{\rho}$ and M, we have carried out $\frac{\Delta\rho}{\rho}$(H,T) and M(H,T) measurements under identical conditions (at same H and T) on the same piece for each compositions in this Fe-rich Fe-Ni-Cr series. Eliminating H between the two sets, namely,

$$\left|\frac{\Delta\rho}{\rho}\right| \propto H^n, \quad \text{and} \quad M \propto H^m ,$$

one gets

$$\left|\frac{\Delta\rho}{\rho}\right| \propto M^{n/m}, \quad \text{at any temperature T.} \tag{4.1}$$

Thus we can find $\frac{\Delta\rho}{\rho}$ vs M at any temperature T without using any theoretical model. Figure 4.19 shows log $\left|\frac{\Delta\rho}{\rho}\right|$ vs log $|M|$ plot for x = 21 at various temperatures from 11 – 30 K. Fitting the data to a straight line ($\chi^2 \approx 10^{-6}$) yields $\frac{\Delta\rho}{\rho} \propto M^{2.5}$ over a wide range of temperature and field. However, the data above 30 K do not fall on this curve. In the case of x =23 (mixed phase) such plots yield the values of the exponent of M varying from 3.1 to 2.0 as T changes from 19 to 45 K, thus showing no correlation between $\frac{\Delta\rho}{\rho}$ and M. For x =

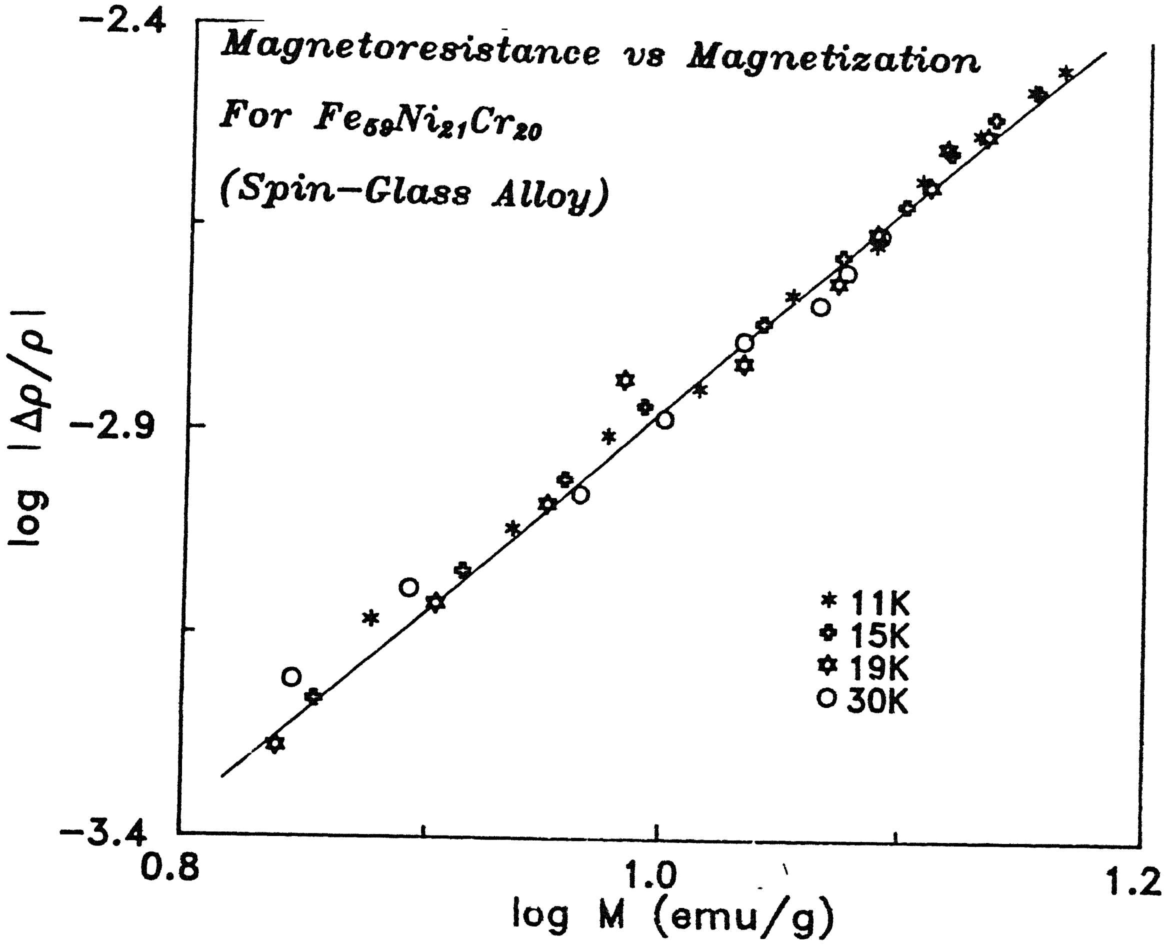

Figure 4.19: Log-log plot of transeverse magnetoresistance and magnetization at different temperatures for $Fe_{59}Ni_{21}Cr_{20}$ (Spin glass) alloys. The slope of the plot gives $|\frac{\Delta\rho}{\rho})_{\|}| \sim M^{2.5}$.

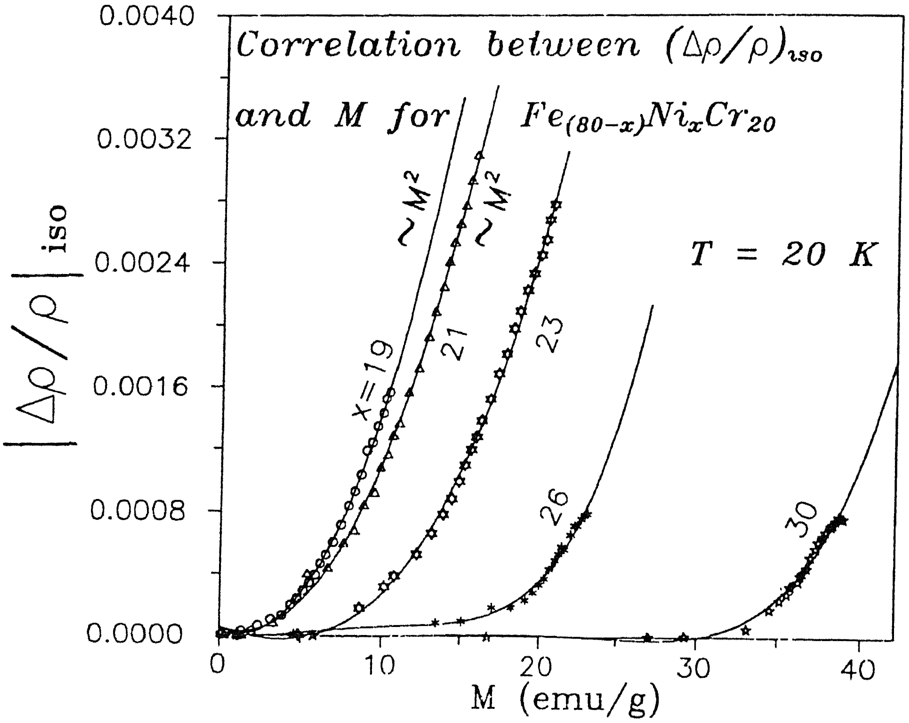

Figure 4.20· Correlation between $(\frac{\Delta\rho}{\rho})_{iso}$ and M for $Fe_{80-x}Ni_xCr_{20}$ alloys at T = 20 K clearly showing a gradual evolution of MR as one goes from the long-range FM ordering towards the critical region ($x \approx x_c$) close to the SG regime.

30 (FM), $\frac{\Delta\rho}{\rho}$ (H) is strongly dependent on temperature while M(H) has a weak temperature dependence for T $\ll$ T_c making the attempt of correlation meaningless. So for the FM alloy and also for the alloys in the RSG phase such dependence of $\frac{\Delta\rho}{\rho}$ on M is not observed. This is a very important observation because it shows that the MR of the RSG is more like that of a FM than that of a SG.

For canonical spin glasses (e.g., AuFe, CuMn, etc.) where indirect RKKY interaction (J_{RKKY}) between magnetic impurities dominates, it is known that

$$\frac{\Delta\rho}{\rho} \propto M^2 \propto \chi^2 H^2 \qquad \text{for ZFC} \tag{4.2}$$

and

$$\frac{\Delta\rho}{\rho} \propto (m_r + \chi H)^2 \qquad \text{for FC states,} \tag{4.3}$$

where χ, H, and m_r are, respectively, the reversible susceptibility, the applied field and the remanent magnetization (m_r, irreversible part).

Eq.(4.2) can be rewritten as

$$\frac{\Delta\rho}{\rho}(H) = -\alpha[M(H)]^2 \qquad \text{for homogeneous SG alloys.} \tag{4.4}$$

In a similar way, for homogeneous randomly canted FM's with non-zero spontaneous magnetic moment, Senoussi[8, 7] suggested that

$$\frac{\Delta\rho}{\rho}(H) = -\alpha[M^2(H) - M^2(0)], \tag{4.5}$$

where M(0) is the spontaneous magnetization in μ_B/ion (estimated by extrapolation from measurements in strong enough fields to align the domains).

The situation can be more complex, in particular, we can have a system with no spontaneous magnetization but with FM short-range order (SRO) at low temperatures. If the ferromagnetic correlation length is of the order of the electron mean-free path, we can not expect any simple relationship between $\Delta\rho$ and M(H). This will be the case near the critical concentration where the FM correlation length is expected to vary very rapidly as a function of the composition.

As we have seen in earlier sections, that in all our alloys (FM, RSG, SG, etc.) in the vicinity of the critical composition (x ≈ x_c), the anisotropy $[|(\frac{\Delta\rho}{\rho})_{\|}| - |(\frac{\Delta\rho}{\rho})_{\perp}|]$ is weak and there is a comparatively large isotropic contribution to the MR. We have made an attempt to correlate the isotropic part of the MR of each alloy with their magnetization. In any polycrystalline magnetic material with random initial domain orientations, the isotropic MR is defined by

$$\left[\frac{\Delta\rho}{\rho}\right]_{\mathrm{iso}} = \frac{(\frac{\Delta\rho}{\rho})_{\|} + 2(\frac{\Delta\rho}{\rho})_{\perp}}{3}\ . \tag{4.6}$$

In Fig.4.20 we have plotted $[\frac{\Delta\rho}{\rho}]_{iso}(H)$ vs. M(H), eliminating H from both, for all the alloys under investigation at T = 20 K. For the lower concentrations corresponding to the SG alloys (x = 19, 21), $[\frac{\Delta\rho}{\rho}]_{iso}$ is exactly proportional to M^2(H) showing that the alloys behave more or less as homogeneous spin glasses confirming the results of Senoussi[18]. However, for x = 23 (mixed phase or RSG), there is a weak departure from the M^2 behaviour. This becomes more severe for x = 26 (RSG). This change of behaviour is a precursor to the FM ordering. Finally,

Table 4.2: Ni concentration dependence of α, M(0), and αM_0^2 as obtained from the fit to Eq.(4.5).

Ni concentrtion (x)	α 10^5 (emu/gm)$^{-2}$	M(0) (emu/gm)	αM_0^2 (10^{-4})
19	1.40	0	0
21	1.19	0	0
23	0.84	10.1	8.5
26	0.36	18.2	11.1
30	0.23	34.0	26.1

in the case of x = 30 (FM) one observes a behaviour which is almost the characteristic of a homogeneous canted FM state (Eq. 4.5) or atleast the state has started to set in. Fitting the data to Eq.(4.5), one obtains a value of M(0) which is very close to the value of M where one observes technical saturation in the M-H curve (Fig.4.3).

At low fields alignment of domains produces a rapid increase in M without affecting the resistivity as the domain size is much greater than the electron mean-free path. At higher fields (beyond technical saturation) once a single domain structure is established, the progressive alignment of individual moments of canted spins (which is manifested in the high-field slope of the M-H curve (Fig.4.3) beyond the technical saturation) dominates the MR behaviour and the M^2 dependence (Eq.(4.5)).

We have fitted the data to Eq.(4 5), viz, $\frac{\Delta\rho}{\rho}(H) = -\alpha[M^2(H) - M^2(0)]$ for all the samples at T = 20 K (shown in Fig.4.20) and the best fitted parameters are summarized in Table 4.2. We find that for x = 19 and 21 (SG), the values of M(0) $\approx$ 0 as expected. For x = 23 and 26 (mixed phase or RSG) and 30 (FM), the M(0) values are very close to their values at technical saturation (Figs. 4.8,4.6 and 4.3, respectively). The values of α decrease with the increase of Ni concentration as the system approaches long-range FM ordering through the critical concentration region (x $\approx$ x_c).

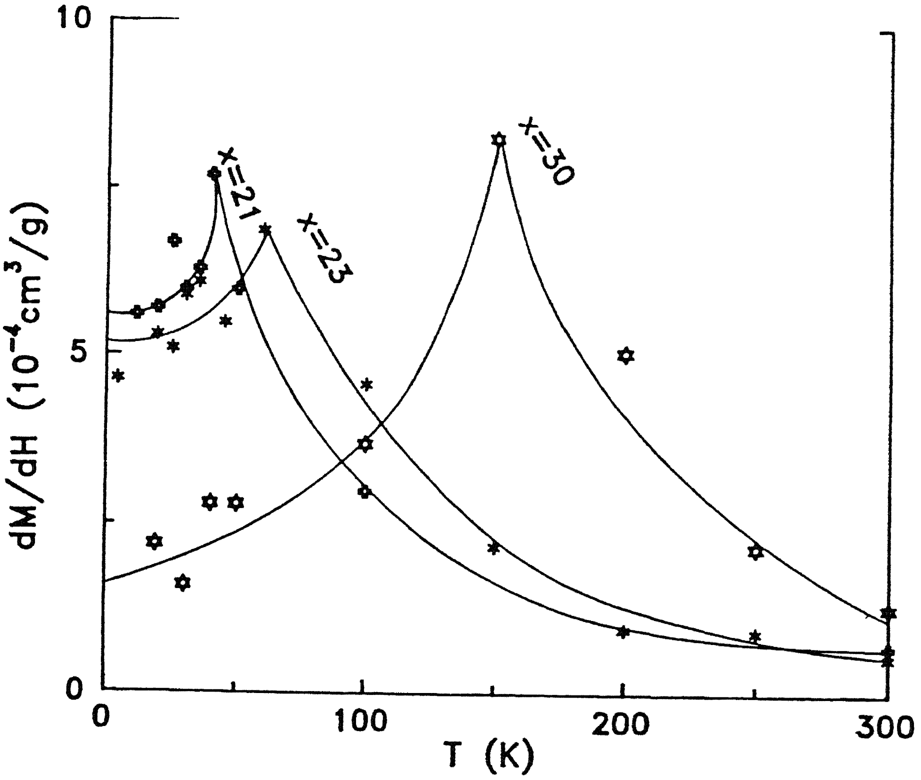

Figure 4.21: Temperature dependence of dc susceptibility χ_{dc} (= dM/dH) $Fe_{80-x}Ni_xCr_{20}$ (x = 21, 23 and 30) alloys at a field of 6 kOe.

We thus conclude that the RSG's (x = 23 and 26) are the precursor to the FM ordering. In the SG (x=19 and 21) alloys, $\frac{\Delta\rho}{\rho}$ varies as M^2 as expected. For x = 30, the homogeneous canted FM phase sets in. For the RSG alloys there is a short-range FM ordering on the scale of electron mean-free path (~ 10 - 20 Å).

Figure 4.20 clearly shows a gradual evolution of MR as one goes from the long-range FM ordering towards the critical region ($x \approx x_c$) close to the SG regime.

In Fig. 4.21 the temperature dependence of *dc*–susceptibility, χ_{dc} (= $\frac{dM}{dH}$) is shown at a field of 6 kOe which is above the technical saturation for all the three alloys. Each curve has got a sharp peak around their respective T_C or T_{SG}, indicating a phase transition from paramagnetic to some other phase. As the temperature drops below T_C or T_{SG}, χ_{dc} decreases. In the case of x = 30 the decrease is very rapid and χ_{dc} goes to a significantly low value at low temperatures. This type of behaviour is similar to that of a conventional FM where χ_{dc} drops to zero as $T \to 0$. In contrast, for $x = 23$, although χ_{dc} drops below T_C, even at fairly low temperatures it remains high. So, just below T_C the system behaves as a FM, although all the spins are not fully aligned and as temperature goes down it looks like a *'semi-spin-glass'* as found by Hamzic and Campbell[19] in concentrated AuFe (19 at.%Fe). For the alloy with $x = 23$, there is an overall long-range order in a certain direction (say, z-direction) and a simultaneous freezing of spins in the transverse direction (xy-plane). These two phases, however, coexist over the entire volume of the sample as envisaged in the Gabay-Toulouse model[2]. In the case of the $x = 21$, the finite and large susceptibility below T_{SG} indicates SG-type of ordering.

4.3 High-field (till 20 tesla) magnetoresistance study of Fe-Ni-Cr series

We have also carried out longitudinal magnetoresistance $[(\frac{\Delta\rho}{\rho})_{||})(H)]$ up to fields as high as 20 tesla in the temperature range of 4.2 - 60 K for $Fe_{80-x}Ni_xCr_{20}$ (x = 14, 19, 26 and 30) alloys. The experiments were performed at the NML of MIT using a Bitter magnet (type 2Y, 52.5mm bore, 41 k A maximum current for 20 tesla field) using liquid He^4 as a coolant. The experimental details are already given in Chapter 2.

However, the data except for the alloys with x = 26 and 19, suffer from lot of scatter. The typical accuracy for x = 26 is slightly better than 1 part in 1000 and for x = 19 it is better than 1 part in 750. The resolution of the data for the alloy with x = 14 and 30, being worse than 1 part in 50, forced us to discard them.

In Fig.4.22 we have shown $[(\frac{\Delta\rho}{\rho})_{||})]$ vs. H for x = 26 (mixed phase) in the temperature range of 4.2 - 60 K up to a field of 20 tesla. In the earlier section, Fig.4.5 was the MR plot for the same alloy till 16.5 kOe where $[(\frac{\Delta\rho}{\rho})_{||})]$ was found to be negative having a typical value of 0.18 % at 16.5 kOe at 11 K. Figure 4.22, where the same plot has been extended till 20 tesla,

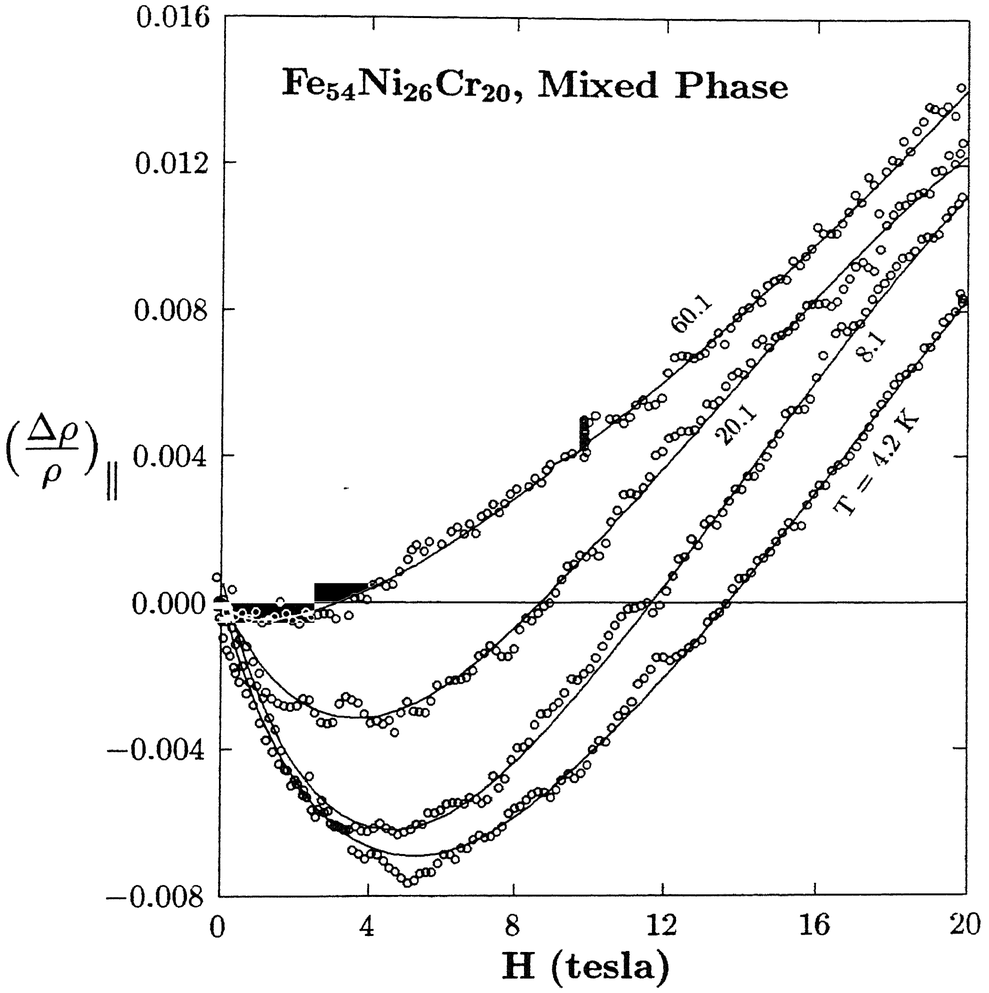

Figure 4.22: Magnetic field (H) dependence of longitudinal ($(\frac{\Delta\rho}{\rho})_{\|}$) magnetoresistance at various temperatures for $Fe_{54}Ni_{26}Cr_{20}$ (Mixed phase) alloy in the field range of 0 - 20 tesla.

shows that $[(\frac{\Delta\rho}{\rho})_{||})]$ is negative at low fields, passes through a minimum at H$_{min}$ and becomes positive at higher fields. At higher temperatures the depth of the minimum reduces, the value of H$_{min}$ shifts towards lower fields and the MR $[(\frac{\Delta\rho}{\rho})_{||})]$ becomes more and more positive. It should be noted that above 75 K, $[(\frac{\Delta\rho}{\rho})_{||})]$ becomes completely positive (as shown in Fig.4.5) at all fields. This observation is also consistent with the current high-field study at higher temperatures. In Table 4.3, we have given the values of the depth of minima and H$_{min}$.

To the best of our knowledge no theory has been developed for any magnetic system so far which could explain these observations where an unknown positive (an additional excess spin-flip scattering) contribution appears or dominate at higher fields. Generally, with the application of a magnetic field, the amplitude of the spin-flip scattering (s-d interaction) of the conduction electrons with the magnetic ions gets suppressed because of the alignment of the magnetic spins. As a result all magnetic systems (except AFM) show negative $\frac{\Delta\rho}{\rho}$ (H). Higher the field, more of the canted spins will be aligned. But beyond a certain field this anomalous (negative) contribution will be smaller compared to the normal (Kohler) MR which originates from band effects, $\left[\left(\frac{\Delta\rho}{\rho}\right)_{normal} \sim (\omega_c\tau)^2\right]$, where $\omega_c = \frac{eB}{mc}$ and τ is the relaxation time. Higher the B, ω_c and hence $(\frac{\Delta\rho}{\rho})_{normal}$ will be higher and ultimately the latter dominates at the highest field. At the moment, we think that this might be a plausible reason which could explain the above observation.

So the MR can be thought of as composed of one positive and one negative term which can be expressed as

$$\begin{aligned}\left[\frac{\Delta\rho}{\rho}\right](H) &= \left[\frac{\Delta\rho}{\rho}\right]_n + \left[\frac{\Delta\rho}{\rho}\right]_a \\ &= aH^2 - bH^n \end{aligned} \tag{4.7}$$

The first term is due to the normal (Kohler) MR and the second term is the anomalous one (as discussed in section 4.1.1). a, b, and n are temperature-dependent adjustable parameters. In the low-field studies (till 16.5 kOe) (section 4.1) we have already observed the dominating H^2-dependence of the normal MR for all the alloys above 100 K. In this high-field investigation

Table 4.3: Temperature dependence of depth of minimum of MR, strength of field at which minimum observed (H_{min}), and the parameters obtained from the fit to Eq.(4.7) for Fe-Ni-Cr alloys.

Sample	Depth of minimum $[\frac{\Delta\rho}{\rho}(\%)]$	H_{min} (tesla)	T (K)	a (10^{-4}) $(\text{tesla})^{-2}$	b (10^{-2}) $(\text{tesla})^{-n}$	n	$^b\chi^2$ (10^{-4})	Range of field (tesla)
$Fe_{54}Ni_{26}Cr_{20}$ (mixed phase)	0.702	5.0	4.1	0.585	0.375	0.433	5.1	0–20
	0.620	4.5	8.1	0.605	0.358	0.375	9.7	0–20
	0.315	3.5	20.1	0.448	0.229	0.173	7.0	0–20
	0.046	1.3	60.1	0.380	0.002	0.100	7.5	0–20
$Fe_{61}Ni_{19}Cr_{20}$ (spin glass)	0.50	6.0	8.1	0.279	0.294	0.386	8.7	0–19
	0.21	4.5	20.1	0.312	0.138	0.458	1.7	0–19

$^b\chi^2 = 1/N\sum_{i=1}^{i=N}[Y_i(data) - Y_i(fit)]^2/[Y_i(data)]^2$

it is found that the positive contribution (H^2-dependent) dominates only at higher fields (> 5 tesla at 4.2 K) at low temperatures.

In Table 4.3, we have listed the values of the fitting parameters (a,b,n), χ^2, and the field range of fit. Figures 4.23(a) and 4.23(b) show the field dependence of the individual contributions from the normal and anomalous magnetoresistance, respectively at various temperatures.

In Fig.4.24, the high-field $[(\frac{\Delta\rho}{\rho})_{\parallel})]$ plot has been shown for the alloy with x = 19 (SG) at 8.1 and 20.1 K. These are the best fitted curves to Eq.(4.7). The field dependence of individual contributions (normal and anomalous) are shown in Figs. 4.25 (a) and 4.25 (b), respectively. The fitting parameters are given in Table 4.3.

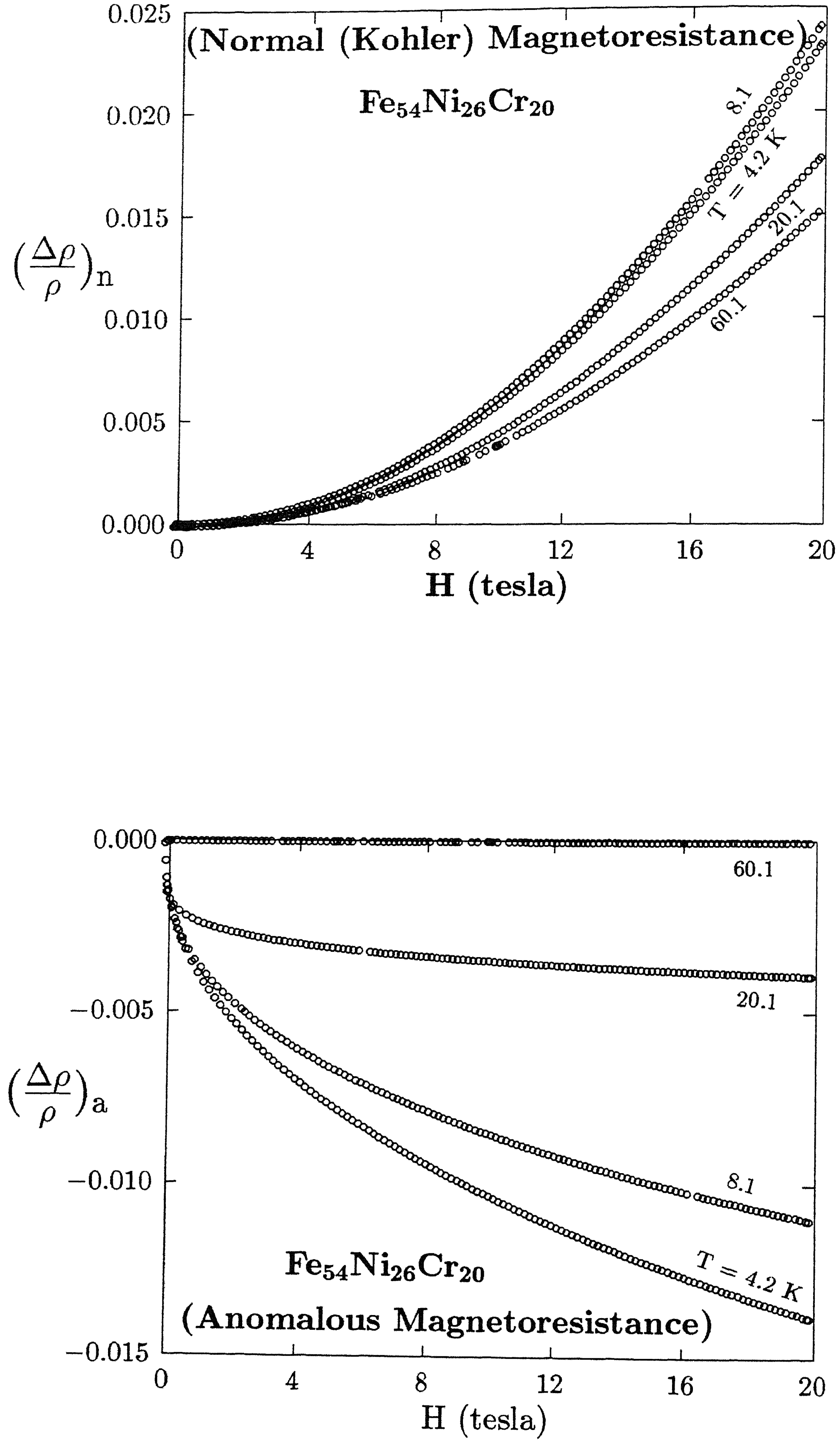

Figure 4.23: Magnetic field dependence of (a) normal and (b) anomalous contribution of MR for $Fe_{54}Ni_{26}Cr_{20}$ (Mixed phase) alloy at various temperatures in the field range of 0 - 20 tesla.

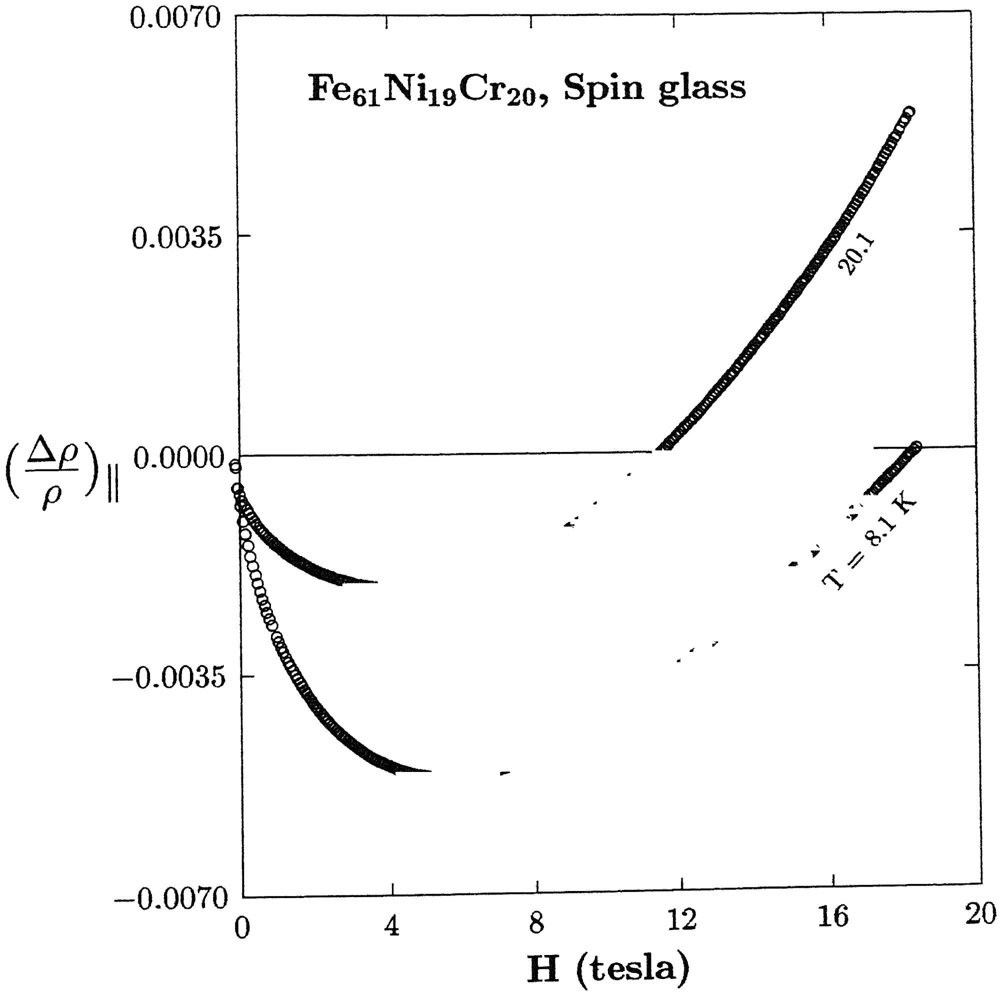

Figure 4.24: Magnetic field (H) dependence of longitudinal $((\frac{\Delta\rho}{\rho})_{\|})$ magnetoresistance at various temperatures for $Fe_{61}Ni_{19}Cr_{20}$ (Spin glass) alloy in the field range of 0 - 20 tesla.

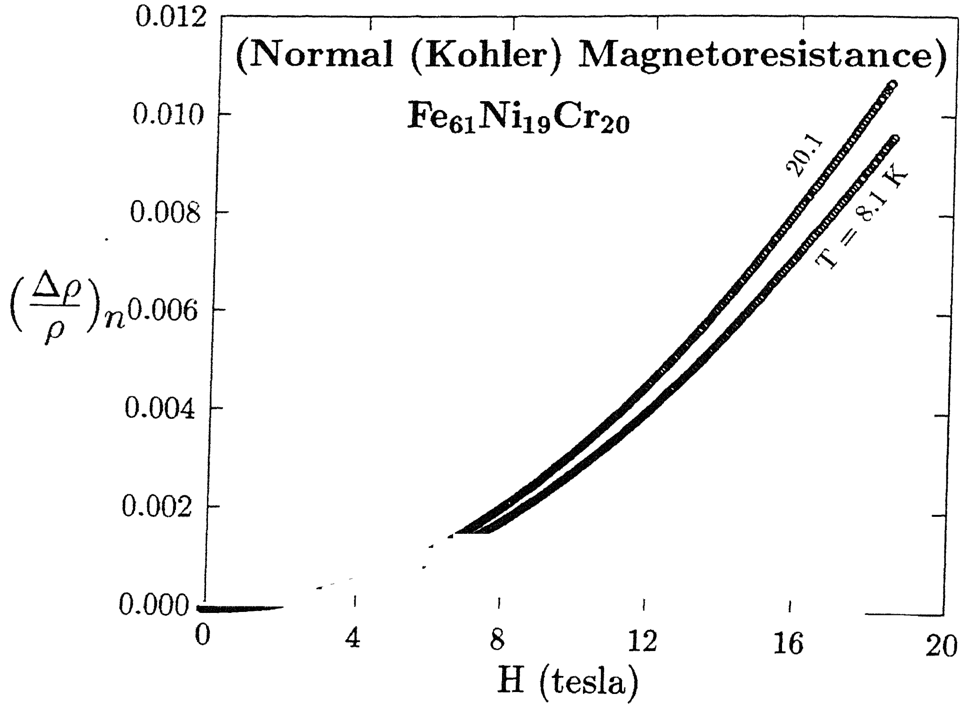

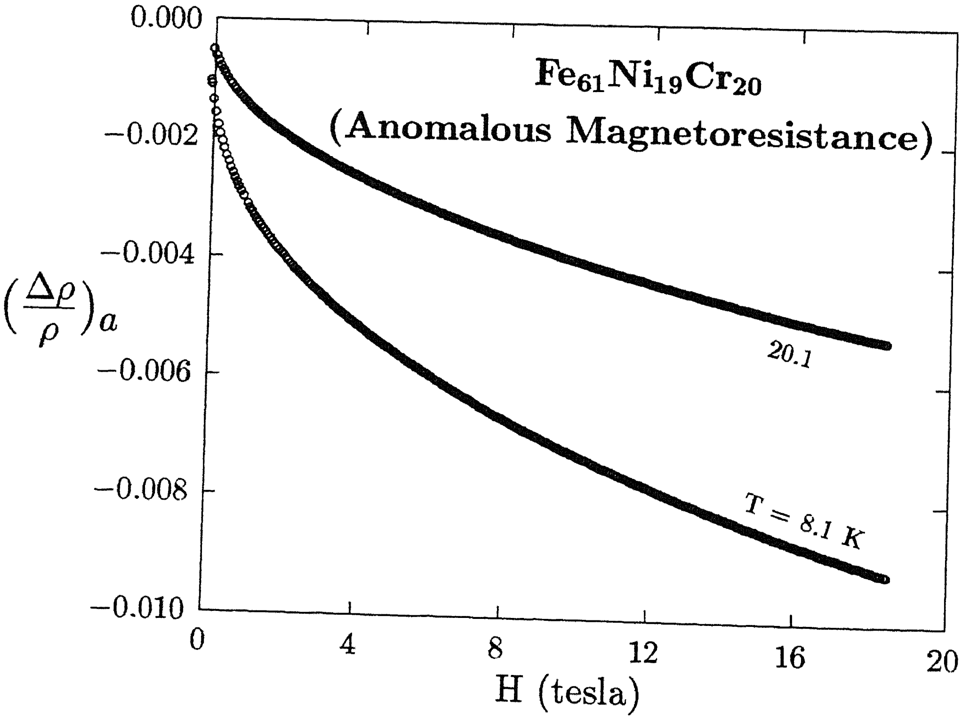

Figure 4.25: Magnetic field dependence of (a) normal and (b) anomalous contribution of MR at various temperatures for $Fe_{61}Ni_{19}Cr_{20}$ (Spin glass) in the field range of 0 - 20 tesla.

So we find that the high-field MR data for $x = 26$ and 19 can be well described by Eq.(4.7) within the experimental resolution. As it stands we can assign the negative contribution essentially to some magnetic origin.

As mentioned in Chapter 1, a part of the negative MR contribution can come from *quantum interference effects* (QIE) at low temperaures as observed in many highly disordered metallic glasses. So one might argue that the negative MR in these disordered alloys ($\rho_{300K} \sim$ (100–130) $\mu\Omega$-cm)[20] might arise from QIE. The magnetoresistance due to electron–electron interaction effects (EEI) is positive[21] and so our observation of a negative magnetoresistance can not be explained through EEI effects.

The MR due to weak localization is generally negative (in the absence of any spin-orbit interaction). In the presence of a magnetic field the time reversal symmetry between the two time reversed paths (weak localization picture) breaks down. The electron waves traversing the two otherwise equivalent paths acquire a phase difference proportional to the enclosed area and the strength of the field. This destroys the constructive interference between the two counter propagating waves giving rise to a negative MR just as inelastic scattering produces a negative TCR at finite temperatures.

The magnetocondutance due to weak localization effect can be estimated using Eqs. (1.19) and (1.20) and is given by

$$[\Delta\sigma]_{\mathbf{WL}} = \frac{e^2}{2\pi^2\hbar}\left[\frac{e}{\hbar}\right]^{1/2}\sqrt{\mathbf{H}} \tag{4.8}$$

$$\approx 0.9\,\sqrt{H} \quad S/cm, \qquad\qquad (H \text{ in } k\ Oe). \tag{4.9}$$

We estimate the contribution to the magnetoconductance due to QIE at 5 tesla using the above relation and get $\Delta\sigma_{WL} \approx 6.3$ S/cm. At 5 tesla and T = 4.2 K, the typical observed change in conductivity $\Delta\sigma$ for x = 26 is 70 S/cm. Thus the contribution from the quantum correction term to the MR is very small (if present at all) compared to the magnetic contribution. Moreover, a very important point should be mentioned here that the presence of any small ferromagnetic impurity can destroy weak localization. In all these random magnetic alloys Ni is ferromagnetic and there are also strong FM interactions among some other pairs.

It is very unlikely that weak localization can persist in these magnetic alloys. So one has to be very careful in invoking QIE in these Fe-Ni-Cr alloys.

Bibliography

[1] A K. Majumdar and P. v. Blanckenhagen, Phys. Rev. B **29**, 4079 (1984).

[2] M. Gabay and G. Toulouse, Phys. Rev. Lett. **47**, 201 (1981).

[3] A. K. Nigam and A. K Majumdar, Phys. Rev. B **27**, 495 (1983); A. K. Majumdar, ibid. **28**, 2750 (1983).

[4] A. K. Nigam, G. Chandra, and S. Ramakrishnan, J. Phys. F **16**, 1255 (1986).

[5] S. Senoussi and Y. Öner, J. Appl. Phys. **55**, 1472 (1984).

[6] T. Sakakibara, T. Goto, and Y. Miyako, Solid State Commun. **58**, 563 (1986).

[7] H. Rokoto, J. C. Ousset, S. Senoussi, and I. A. Campbell, J. Magn. Magn. Mater. **46**, 2112 (1984).

[8] S. Senoussi and Y. Öner, J. Magn. Magn. Mater. **12-16** (1983).

[9] J. J. Smit, G. J. Nienwenhuys, and L. J. de Jough, Solid State Commun. **32**, 233 (1979).

[10] A. K. Nigam, S. Radha, and Girish Chandra, J. Phys. Condens. Matter. **5**, 9197 (1993).

[11] Nagawasa, Phys. Letters. **41A**, 39 (1972).

[12] I. Balberg, Physica **91B**, 71 (1977).

[13] S. Radha, Ph.D. Thesis, Tata Institute of Fundamental Research, Bombay, India, 1995.

[14] T. K. Nath and A. K. Majumdar, J. Appl. Phys. **70**, 5828 (1991).

[15] A. K. Gangopadhyay, S. B. Roy, and A. K. Majumdar, Phys. Rev. B **33**, 5010 (1986).

[16] T. Bitoh, T. Shirane, and S. Chikazawa, J. Phys. Soc. Japan, **62**, 2837 (1993).

[17] J. C. Guillon and J. Zinn Justin, Phys. Rev. B, **48**, 9504 (1983).

[18] S. Senoussi J. Phys. **F10**, 2491 (1980); J. de Phys. Lett. **42**, L-35 (1981). Solid State Commun. **45**, 407 (1983).

[19] A. Hamzic and I. A. Campbell, J. de Physique - Letters **42**, L-309 (1981).

[20] T. K. Nath and A. K. Majumdar, Phys. Rev. B **53**, 12148 (1996).

[21] B. L. Altshuler, A. G. Aronov, A. I. Larkin, and D. E. Khemel'nitskii, Sov. Phys. - JETP, **54**, 411 (1981).

[22] B. L. Altshuler and A. G. Aronov, *in Electron-electron interaction in disordered systems*, edited by A. L. Efros and M. Pollak (Elsevier, New York, 1985), p. 1.

[23] Patrick A. Lee and T. V. Ramakrishnan, Rev. Mod. Phys. **57**, 287 (1985).

[24] E. Abrahams, P. W. Anderson, D. C. Licciardello, and T. V. Ramakrishnan, Phys. Rev. Lett. **42**, 673 (1979).

[25] A. Kawabata, J. Phys. Soc. Japan **49**, 628 (1980).

Chapter 5

High-field (till 20 tesla) magnetization study of γ-Fe$_{80-x}$Ni$_x$Cr$_{20}$ $(14 \leq x \leq 30)$ alloys

We had reported earlier[1] that the magnetoresistance (MR) of γ–Fe$_{80-x}$Ni$_x$Cr$_{20}$ $(14 \leq x \leq 30)$ alloys is negative till as high as 50 K in the field range of 0 - 2 tesla. A striking correlation between the magnetization and the MR was observed only in the SG alloys (x = 19,21) with $\frac{\Delta\rho}{\rho} \propto M^2$ [5]. The isotropic nature of the MR as well as the thermomagnetic history effect of the field–cooled (FC) magnetization[1, 2] confirmed the freezing of spins at the lowest temperatures in the alloys which have SG (19,21) and mixed (23,26) phases at those temperatures. The role of the different magnetic phases (due to short and long – range spin orderings) on electronic transport has been throughly investigated using ρ(T) measurements[3, 4] in this system of alloys. In Table 5.1, we have listed the values of their magnetic transition temperatures (T$_c$, T$_f$ and T$_N$). It was found from low and intermediate–field magnetization[1, 2] studies that the alloy with x=30, behaves like a distorted or inhomogeneous FM unlike the conventional FM's. Isothermal magnetization curves, in the PM state of each alloy, have strong curvatures even at temperatures much higher than their respective transition temperatures. Also their M–H curves did not show any tendency of saturation even till 6 T and down to 4.2 K[2].

---

[1] This chapter is mainly based on the work by T. K. Nath, N. Sudhakar, E. J. Mcniff, and A.K. Majumdar, accepted for publication in *Phys. Rev. B*, 1997.

The motivation behind the present investigation is to seek answers to the following questions : What are the very high-field magnetic responses (χ_{HF}) of these wide varieties of magnetic phases (FM, mixed, SG and AFM) in these alloys which are very close to the critical concentration range and in which very strong competing exchange interactions exist ? Is it possible to find in them distinct functional relationships between the magnetization and the very strong magnetic field ? What is the saturation magnetization ($\overline{\mu}_s$) in this system and does it follow the Slater-Pauling curve ? What are the values of the saturation magnetic fields ($g\mu_B H \gg kT$) in these magnetic phases ? Whether the very high-field magnetization processes can be described resonably well with the law of approach to saturation ? What are the roles of the intrinsic fluctuation of material parameters as well as the magnetic and local anisotropy on the high-field magnetization processes ? What is the nature of ferromagnetism that exists in the alloys which are beyond the critical concentration range and in which long-range FM starts appearing (x = 30,26 and 23) ? Whether this kind of weak inhomogeneous FM can be described resonably well by the localized model or Stoner's itinerant electron model[5] ? Whether the temperature dependence of the demagnetization processes for the FM alloy with x = 30 can be described in terms of excitations of long–wavelength spin–waves at low temperature ranges ? What is the value of the spin–wave stiffness constant ($\mathcal{D}$) for this alloy and how does it compare with the standard FM's like Ni, Fe and strong FM amorphous metallic glasses ? Whether the Stoner single–particle excitations also contribute to the demagnetization process in this alloy together with spin–wave (magnon) excitation ? Is it a strong or weak FM ? Does the long-range FM ordering coexist with the SG freezing as envisaged in the G–T model[6] in the mixed phase alloys (x=23,26) below the second transition temperature or is it more likely to re–enter into the pure SG phase without any long-range ordering from the FM phase at higher temperatures ? Do the alloys which have pure SG freezing (x=19,21) at low temperatures are similar in response dynamics of the frozen spins as seen in *archtypical* spin-glass systems like CuMn, AuFe, etc. from dilute to critical concentration regime (14 at.%

of Mn and Fe)[7, 8] at 4.2 K ? What is the long-range AFM structure[9] in the case of the alloy with x=14 which has an fcc crystallographic structure (resembling γ–Fe[10, 11]) ? What are the effective molecular field coefficients (γ_i) for the 1st and 2nd nearest neighbours as well as the effective field exchange interaction (J_i) between the ith neighbours inside the different sublattices ? Does this AFM structure show any kind of *spin–flop* transition because of the canting of antiferromagnetic spins in the strong external magnetic field ? If yes, what is the nature of the magnetization process beyond the *spin–flop* transition ?

In this work we have performed a systematic isothermal high field dc–magnetization (M–H) measurements up to fields as high as 20 T at different temperatures between 4.2 to 60 K for the alloys under investigation as well as the strong amorphous FM $Fe_5Co_{50}Ni_{17}B_{16}Si_{12}$[12]. In addition to that we have also carried out M–H measurements with higher accuracy in the low-field region up to a field of 2 T at several temperatures between 19 and 300 K. We have performed low field M–T measurements in the temperature range between 19 and 700 K to examine the presence of any short-range clustering or frozen moments in PM states as well as to estimate the average magnetic moment per spin (q_c) at high temperatures when all the alloys are in purely PM state. For spin-wave analysis for the alloy with x = 30, we have carried out a very careful M–T measurements at each 100 mK in a magnetic field of 10 KOe.

5.1 RESULTS and DISCUSSION

5.1.1 General features of the high–field M–H curves between 4.2 and 60 K and low–field M–T curves between 19 and 700 K

In Fig.5.1 we show the high–field dc–magnetization (M–H) curves of substitutionally disordered γ–$Fe_{80-x}Ni_xCr_{20}$ alloys with x = 14, 19, 26 and 30 up to a field of 20 T at 4.2 K, which is much below their respective transition temperatures (T_c, T_f and T_N given in Table 5.1). We also show the M–H plots of the amorphous FM metallic glass $Fe_5Co_{50}Ni_{17}B_{16}Si_{12}$[12] at

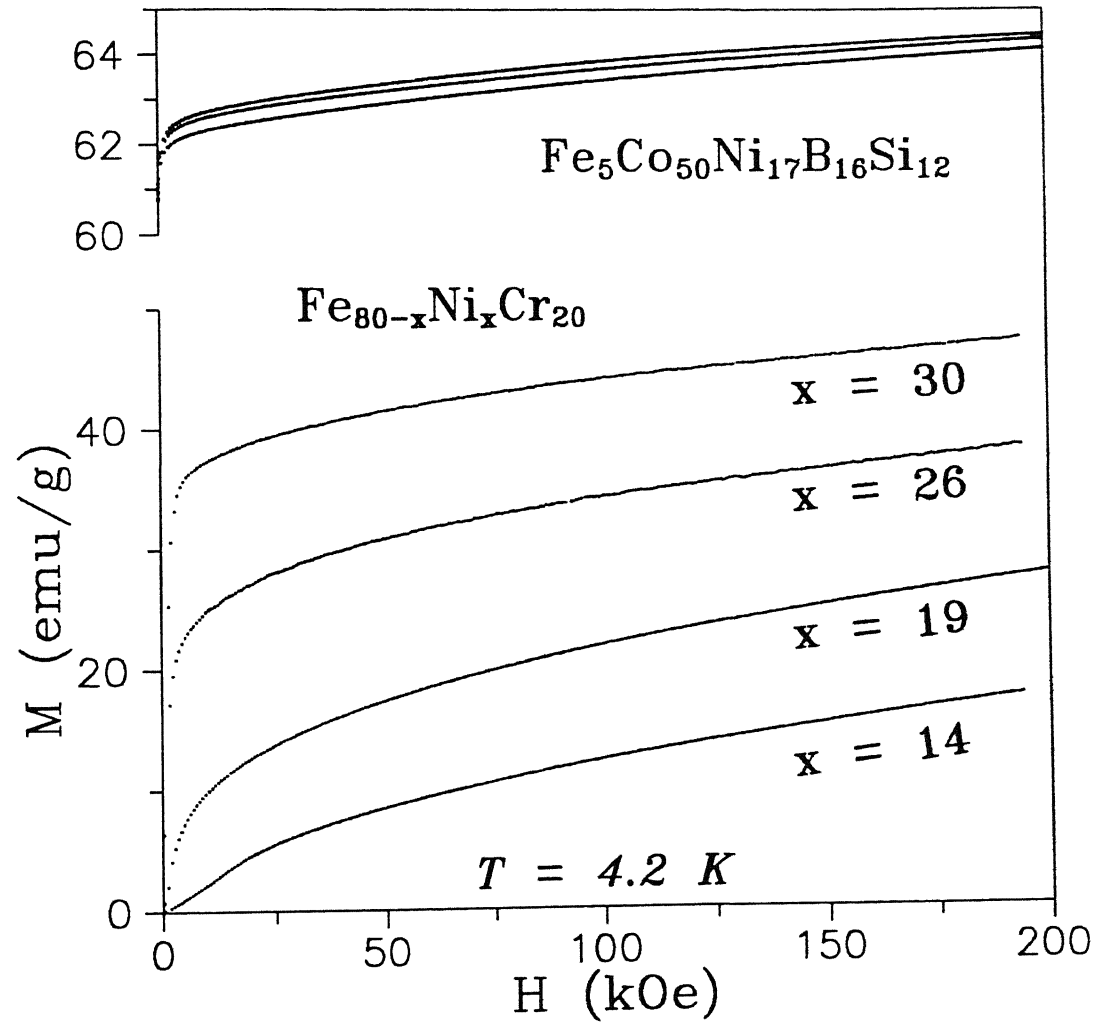

Figure 5.1: Experimental M(H) plots of $Fe_{80-x}Ni_xCr_{20}$ (x = 14,19,26 and 30) austenitic stainless steel alloys in the magnetic field range of 0 to 20 tesla at 4.2 K. The topmost 3 curves are the M–H plots of $Fe_5Co_{50}Ni_{17}B_{16}Si_{12}$ amorphous ferromagnetic metallic glass at 4.2, 8.1 and 20.1 K.

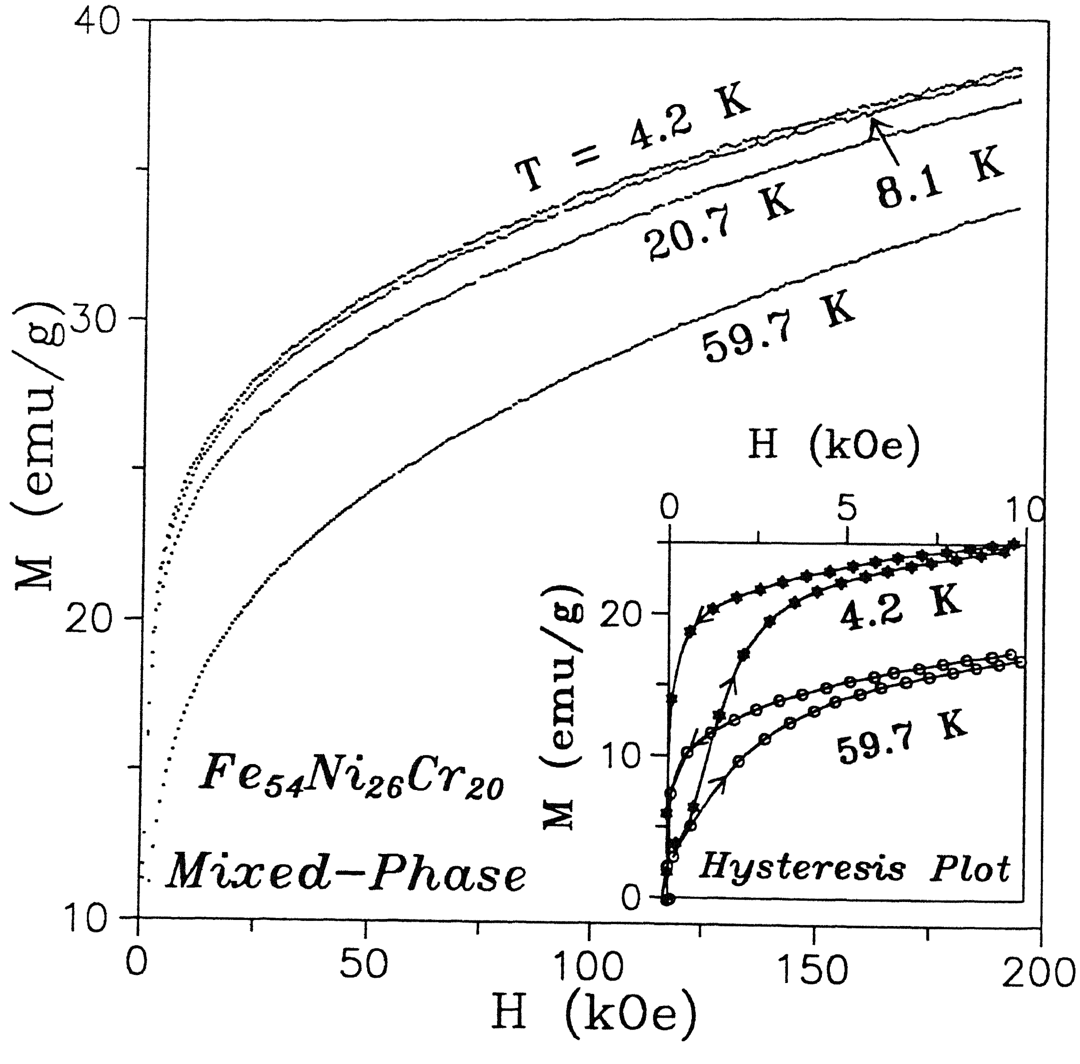

Figure 5.2: M–H isotherms of the mixed phase alloy $Fe_{54}Ni_{26}Cr_{20}$ at 4.2, 8.1, 20.7 and 59.7 K in the field range of 0 - 20 tesla. The inset shows its hysteresis plot which is a measure of the field-induced anisotropy energy at 4.2 and 59.7 K in the low-field range of 0 - 1 tesla.

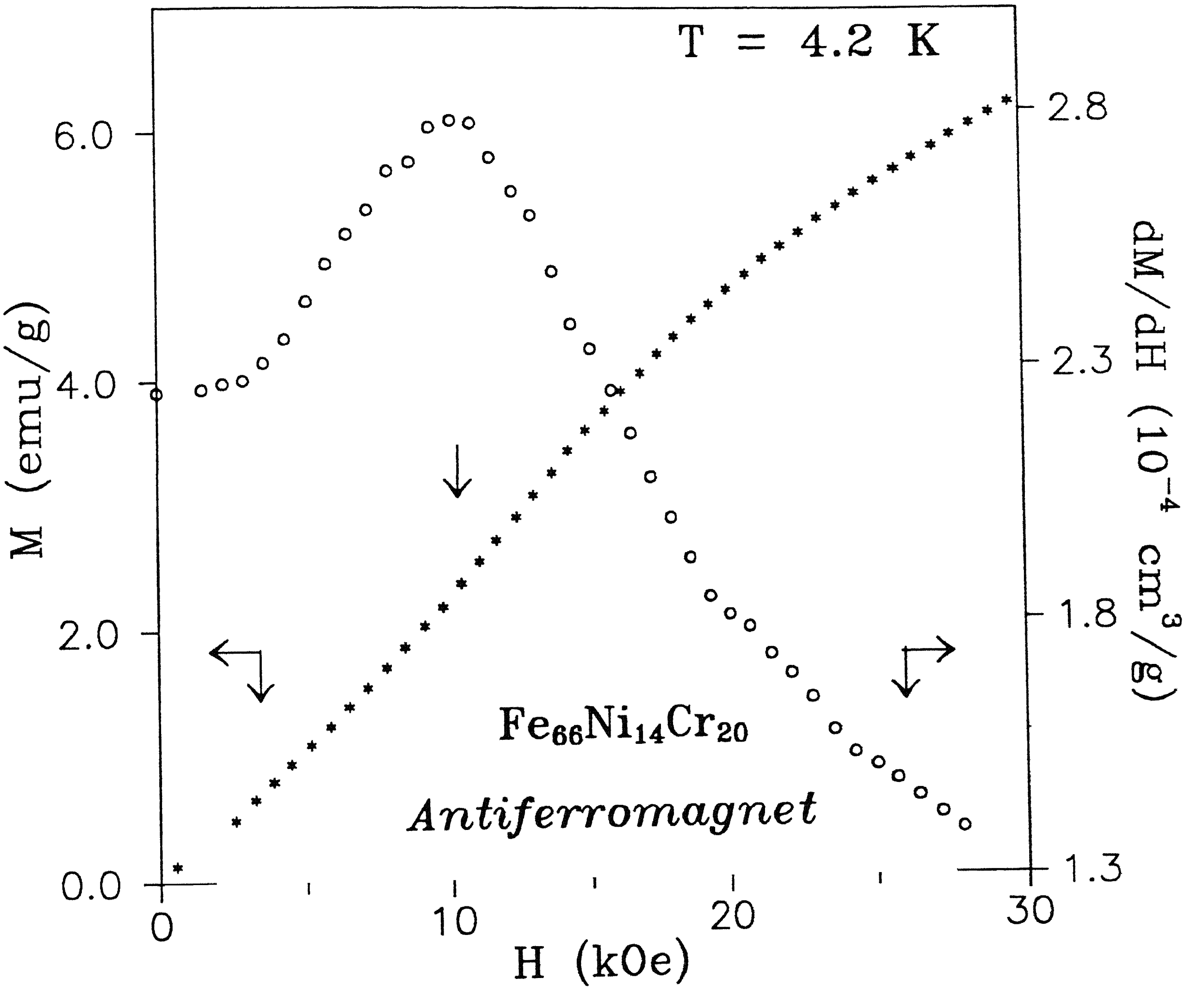

Figure 5.3: M–H and $\frac{dM}{dH}$ vs H plots of the AFM alloy Fe$_{66}$Ni$_{14}$Cr$_{20}$ at 4.2 K. The M–H plot shows a striking change of slope around 1 tesla (shown by an arrow) where $\frac{dM}{dH}$ shows a peak. This has been attributed to *spin–flop* transition at this field.

4 The M–H curve of the alloy with x = 14, which has an AFM ordering below $T_N = 26$ K, however, shows a striking change of slope at around 1 T at 4.2 K (Figs.5.1 and 5.3). This abrupt change of slope is more pronounced in the $\frac{dM}{dH}$ vs H plot (Fig.5.3) which shows a peak at 1 T. However, it vanishes completely at 35.3 K (not shown). This sudden change of slope may be attributed to a *spin-flop* transition because of the canting of the AFM spins in this alloy.

5. No abrupt change in the behaviour of the M–H curves is observed in the FM → AFM critical concentration range. The M–H curves of all the alloys have sufficient curvatures even at temperatures much higher than their respective transition temperatures. This may be due to the effect of clustering, short-range ordering or local frozen spin moments in the PM state.

We have made an attempt to fit all the high–field M–H curves of this series of alloys to some empirical relations. Non–linear log M vs. log H plots reveal that for the alloys with x = 30 and 26 , M is not solely dependent on a single term in H. However, the alloy with x = 19 shows a perfectly linear log–log plot implying M $\propto H^n$. The alloy with x = 14 also shows a linear log–log plot with two distinct slopes below and above the *spin–flop* transition. So we have taken a general empirical relation

$$M = M_0 + M_1 H^n \tag{5.1}$$

to fit all the M–H curves employing a non-linear least squares fitting program alongwith a EO4FDF NAG–Subroutine. We have kept M_0, M_1 and n as adjustable parameters to fit the M(H) data. In the case of alloys with x = 19 and 14, the values of M_0 are negligibly small and have been neglected. Table 5.1 gives the fitting parameters for all the alloys at several temperatures. From Table 5.1, the following inferences can be drawn :

In the case of the alloys with x=30 and 26, the inclusion of the additional constant term M_0 makes the quality of fit much better ($\chi^2 \sim 10^{-6}$ is comparable to the experimental accuracy). M_0 is maximum for the alloy with x = 30 at 4.2 K. In the case of the alloy with x=26, because

Table 5.1: Fit of the isothermal M–H curves of $Fe_{80-x}Ni_xCr_{20}$ alloys to several distinct fit functions till 20 T : compositions (x), fit parameters (M$_o$, M$_1$ and n), field range, temperature and the values of χ^2.

x (Ni conc.)	Fit function	M$_0$ $(\frac{emu}{g})$	M$_1$ $[\frac{emu}{gT^n}]$	n	Field range (T)	Temperature (K)	χ^{2^a} (10^{-6})
30	$M=M_0+M_1H^n$	32.0	5.4	0.35	1 – 20	4.2	1.2
(T_c=130 K)							
26	$M=M_0+M_1H^n$	18.7	7.0	0.38	2 – 20	4.2	1.8
(T_c & T_f		19.3	6.3	0.39	2 – 20	8.1	1.5
= 60 & 7K)		19 1	5.2	0.42	2 – 20	20.7	0.88
		11.2	6.9	0.40	2 – 20	59.8	0.72
19	$M = M_1H^n$		10.0	0.34	1 – 20	4.2	0.3
(T_f=12 K)			9.9	0.34	1 – 20	8.1	0.16
			9.1	0.36	1 – 20	20.2	0.17
14	$M = M_1H^n$		2.3	1.04	0 – 1.5	4.2	0.2
(T_N=26 K)			3.6	0.53	5 – 20	4.2	0.4
			3.5	0.54	5 – 20	11.2	1.9
			3.3	0.56	5 – 20	20.1	1.5
			2.7	0.60	5 – 20	35.3	2.5
			1.8	0.71	5 – 20	59.8	4.9

$^a\chi^2 = \frac{1}{N}\sum_{i=1}^{N}[Y^i_{expt.} - Y^i_{fit}]^2/(Y^i_{expt})^2$

of the freezing of the X-Y components of spins (GT model) below 7 K, the spontaneous moment (M_0) at 4.2 K has gone down slightly as compared to that at 8.1 K. This kind of observation could also be made from the M–T plots[2]. The decrease in M_0, above 8.1 K, due to the enhancement of thermal spin fluctuations as well as the spin–wave excitations, is quite reasonable. In the case of the alloys with x = 14 (AFM) and 19 (SG), M_0 is negligibly small. The M_0 term has been attributed physically to the spontaneous moments of these alloys. Its values are found to be consistent with their magnetic phases.

In the case of the alloy with x=30, the value of the exponent of H is n $\approx$ 1/3 at 4.2 K whereas for the alloy with x = 26 it is $\approx$ 3/7. Considering the infinite–range Ising interaction, Toulouse[15] had suggested a model for mixed phase systems where M $\sim$ $H^{3/7}$ which agrees with our observation. For x = 19, n $\approx$ 1/3. In the case of the alloy with x = 14, the exponents are n $\approx$ 1 and 1/2 in lower and higher field ranges, respectively. This implies that in the AFM state, below the *spin–flop* transition, M has a linear dependece on H whereas above it M $\propto$ $\sqrt{H}$.

As discussed earlier, in the γ–$Fe_{80-x}Ni_xCr_{20}$ ($14 \leq x \leq 30$) alloys, because of the presence of strongly competing exchange interactions between different pairs of magnetic atoms[2, 16], critical concentration is attained for this particular range of stoichiometry. As a result it hinders the rotation of the magnetic spins and so a saturation of the magnetization is hard to achieve (Figs.5.1 and 5.2) even at 20 T and 4.2 K. However, one cannot rule out the possibility of formation of either short-range clustering or clustering of local spin-freezing as well as the existence of local anisotropy and intrinsic fluctuation of the material parameters as in the case of AuFe[8], FeZr[17], etc..

We have also analysed the data in terms of the law of approach to saturation, given empirically by

$$M = M_s - \frac{a}{H} + b\,H, \tag{5.2}$$

where M_s is the saturation magnetization and the $\frac{a}{H}$ term is attributed to the intrinsic fluctuation of the material parameter, viz, presence of non-magnetic voids, inclusions and microstress.

Table 5.2: Concentration dependence of different fit parameters (M_s, a and b) of the law of approach to saturation (Eq.(5.2)), the values of χ^2, temperature and field ranges for several isothermal M–H curves of $Fe_{80-x}Ni_xCr_{20}$ alloys.

x (Ni conc.)	Temperature (K)	Field range (T)	M_s $(\frac{emu}{g})$	a $(\frac{emu\ T}{g})$	b $(\frac{emu}{g\ T})$	χ^2 (10^{-7})
30	4.2	3 - 20	42.6	13.00	0.30	7.4
26	4.2	5 - 20	32.6	17.64	0.40	0.18
	8.1	5 - 20	32.9	22.20	0.35	0.11
	20.7	5 - 20	31.9	23.78	0.38	7.9
	59.7	5 - 20	25.9	20.57	0.46	9.6
19	4.2	5 - 20	19.8	24.60	0.52	5.6
	8.1	5 - 20	19.6	24.40	0.47	4.8
	20.2	5 - 20	18.7	24.20	0.48	4.4
14	4.2	5 - 20	9.3	16.60	0.45	0.16
	11.2	5 - 20	9.3	17.62	0.47	0.21
	20.1	5 - 20	9.0	17.63	0.48	0.23
	35.3	5 - 20	8.0	17.26	0.48	0.28
	59.8	5 - 20	5.8	14.64	0.52	0.30

All our samples are cold rolled and after the final annealing process, to retain the γ phase, they had to be quenched from 1050^0 C to room temperature. This has caused mechanical hardening of the samples as a result of the microstress developed. The last term, bH, corresponds to the high-field susceptibility $\chi_{\rm HF}$ ($\approx \frac{\delta M}{\delta H} |_{\rm H \to \infty} \approx$ b). We have fitted all the M–H data to Eq.(5.2) employing a non-linear least squares fitting programme keeping M_s, a and b as adjustable parameters. In Table 5.2 we have summarized the values of the parameters alongwith the values of χ^2. From Table 5.2 a number of observations could be made. The quality of fit is good, the $\chi^2 \approx 10^{-7}$ is comparable to the experimental accuracy. The saturation magnetization (M_s) increases with Ni concentration (x) at a particular temperature whereas it decreases with temperature for the same x. The constant a and the high-field susceptibility b ($\approx \chi_{HF}$), both increase with x and attain maxima at around x = 19 (critcal concentration range) and then they decrease with further increase of x.

In Fig.5.4 we show the variation of M_s, a and b with x. This plot reveals that for the alloys with long-range FM (x = 30) and AFM (x = 14) orderings, the high-field susceptibility χ_{HF} is much smaller than those of the alloys which have SG and mixed phase orderings at low temperatures.

In Fig.5.5 we show the individual contributions of $M_s - \frac{a}{H}$ and bH terms alongwith the total M plotted against 1/H for x = 30 at 4.2 K. The figure shows how the magnetization approaches saturation in the high-field region ($\frac{1}{H} \to 0$). It is also clear from this analysis that even the 20 T field is not sufficient to align all the spins to reach saturation. The extrapolation with Eq.(5.2) (as shown in Fig.5.5) suggests that it may require a field as high as 100 T to align all the spins with a maximum saturation value of M $\approx$ 70 emu/gm.

Figure 5.6 is the Arrott–Belov–Kouvel (ABK) plot (using mean-field values of the critical exponents $\beta = 0.5$ and $\gamma = 1$) for x = 30, 26, 19 and 14 alloys at 4.2 K. This is a very important plot to confirm the presence of any FM phase from the finite value of the spontaneous moment in the absence of any internal magnetic field. In the high-field linear regions, we have fitted straight lines and estimated the spontaneous moments (M_0) from the positive intercepts. The alloy with x = 30 (FM) has a very high value of spontaneous moment as compared to those of

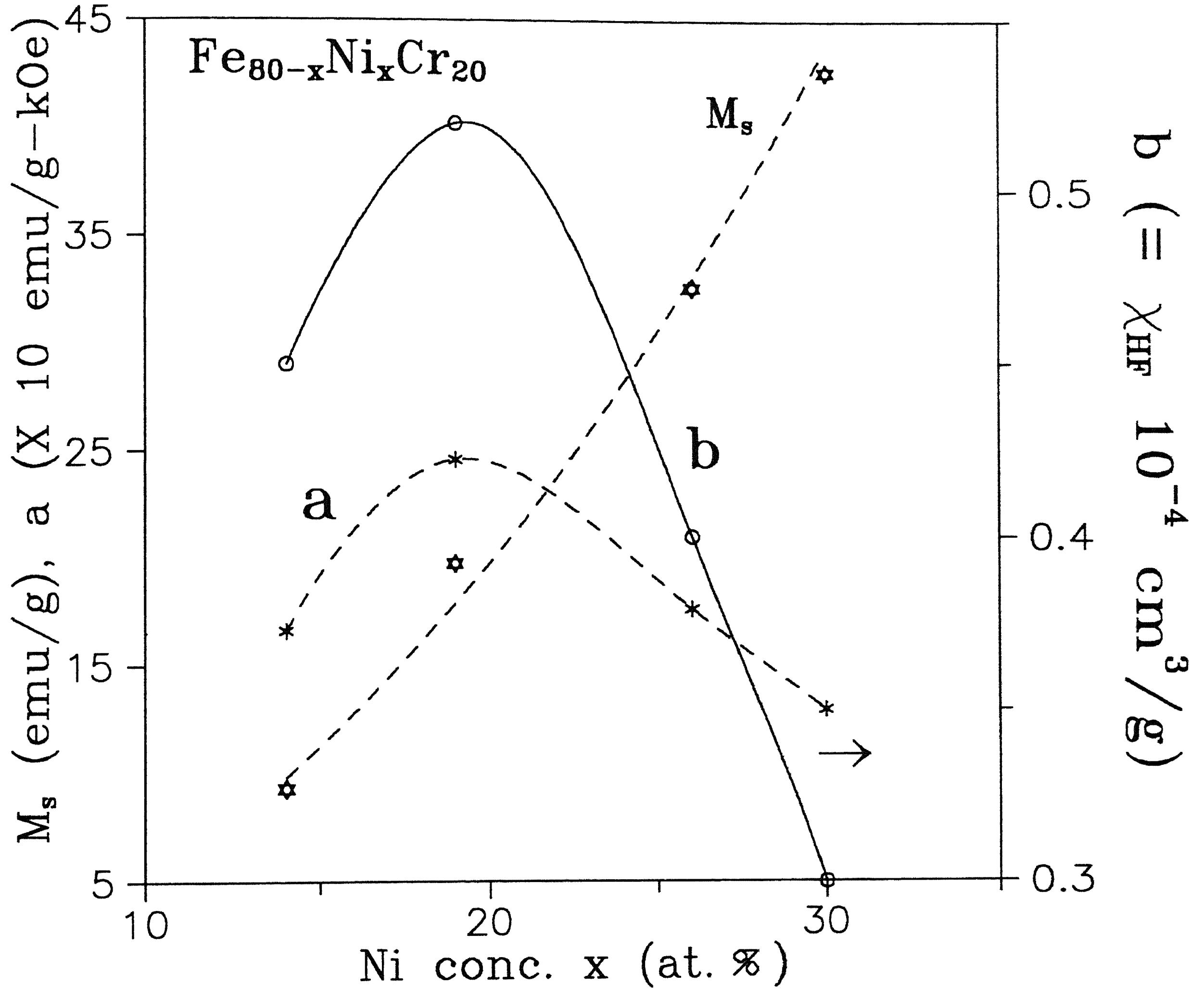

Figure 5.4: Ni concentration (x) dependence of fitting parameters M_s, a and b of the law of approach to saturation (Eq.(5.2)) for $Fe_{80-x}Ni_xCr_{20}$ alloys. The solid and the dashed lines are just guides to the eye.

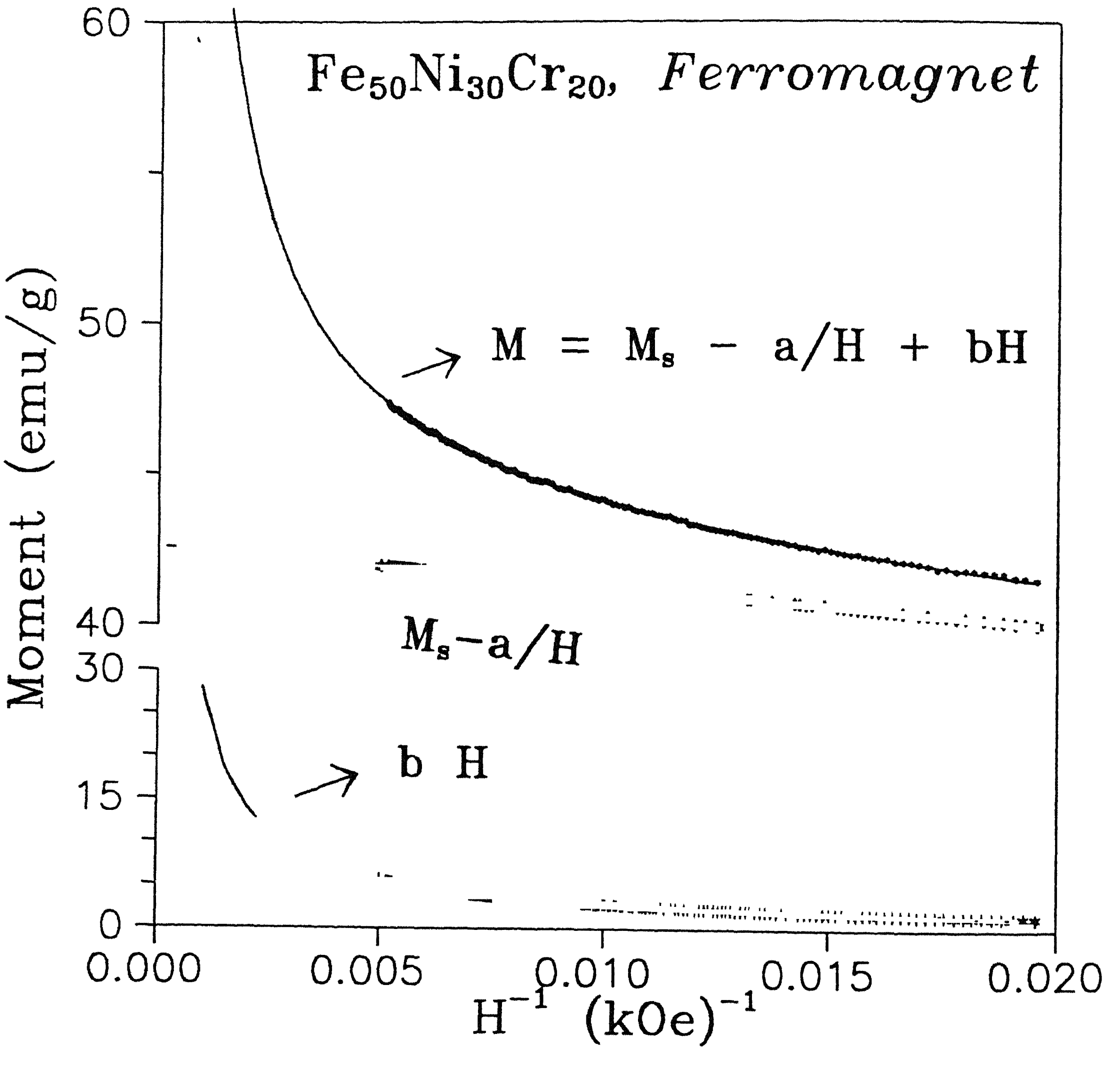

Figure 5.5: M vs. H^{-1} plot of $Fe_{50}Ni_{30}Cr_{20}$ (FM) alloy. The solid line is the extrapolation of the fit to Eq.(5.2) in the very high-field range. The other two curves are the resolved contributions.

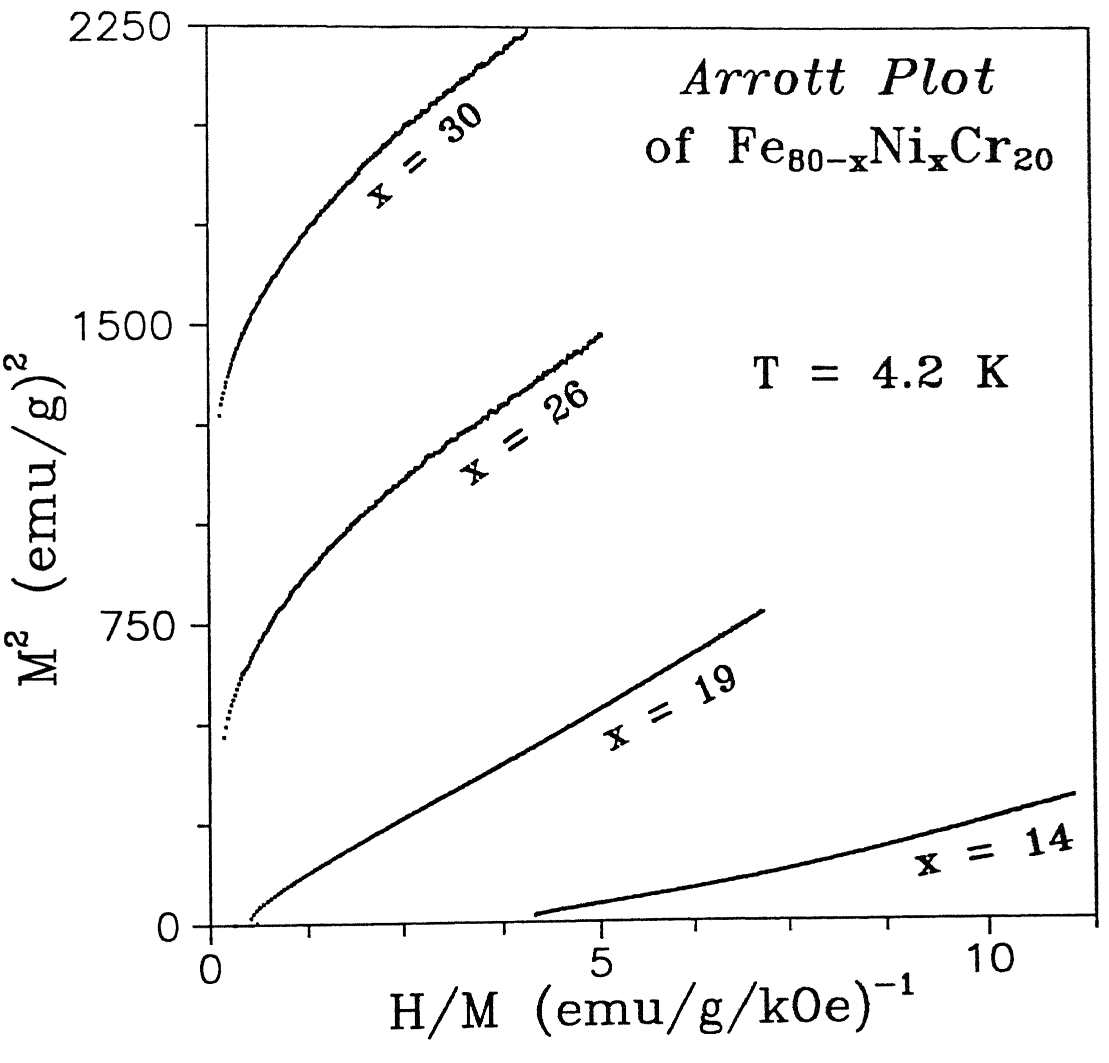

Figure 5.6: Arrott plots (M^2 vs H/M) for crystalline $Fe_{80-x}Ni_xCr_{20}$ (x = 14, 19, 26 and 30) alloys with wide varieties of magnetic phases at 4.2 K. The curvature changes (convex to concave) while passing through the critical concentration region.

the others. For the alloy with x = 26 (mixed) we confirm the persistence of the FM ordering even below the SG freezing temperature from the positive intercept on the M^2–axis. Had it been in a pure SG phase, it would not have shown any positive intercept. In our earlier work[1] we had confirmed the coexistence of FM and SG orderings in the alloy with x = 23 (mixed phase). In the case of the alloy with x = 19 (SG), the negative intercept on the M^2-axis even at 4.2 K rules out any possible FM ordering. For x = 14 (AFM), the ABK plot has a strong concave curvature in the low-field region as opposed to the convex ones for the FM and mixed phase alloys.

In the alloys with higher Ni concentraion, the FM states are either weak or inhomogeneous having very high values of χ_{HF}. The spontaneous moments (M_0) from the intercepts of the ABK plot at 4.2 K are 0.39, 0.27, and 0.13 μ_B/<atom>, respectively for x = 30, 26 and 23. These values strongly deviate from the Slater-Pauling curve for the 3d transition metals and alloys. This may be understood in the light of Friedel theory of the formation of VBS and the split–band model.

The Arrott plots for x = 26 at several higher temperatures (Fig.5.7) also show a change of curvature from concave to convex while passing through the Curie temperature from the high temperature side. So there exists a close analogy between what happens for a fixed concentration when the temperature is changed and the case where the temperature is fixed and the concentration is varied. There could be several reasons for the deviations from linearity of the ABK plots for all the alloys in the low-field range : (1) An inhomogeneous character of magnetization may be associated with such deviations (e.g.,amorphous Fe-Ni alloys near the critical concentration[18]). (2) According to Shtrikman and Wohlfarth[19], for heterogeneous weak itinerant magnetic alloys, the deviation from linearity is attributed to spatial inhomogenities of the magnetization due to fluctuations in concentration. (3) For a homogeneous magnetic system the Arrott plots give straight lines in the case of weak ferromagnetic materials except at the lowest fields where domain rotations occur[20]. The ABK plots for a SG or a mictomagnetic phase at high enough fields and temperatures as well as for a mixed phase, where FM

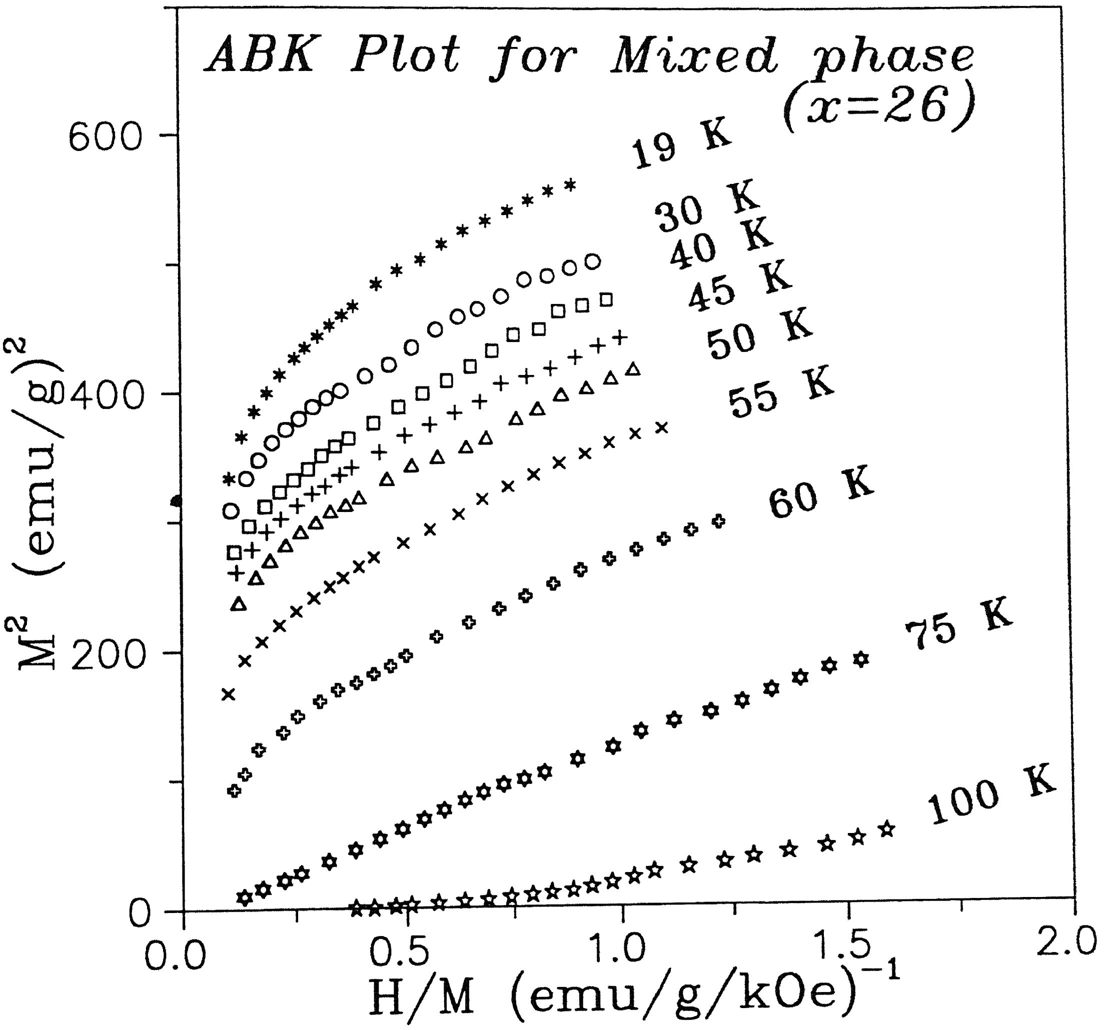

Figure 5.7: Arrott–Belov–Kouvel (ABK) plots at various temperatures in the low–field range for the mixed phase alloy $Fe_{54}Ni_{26}Cr_{20}$ confirming the presence of the FM ordering.

and cluster glass or SG coexist, should be rather curved[18]. Some experimental evidences in FeCr, FeMnPC, etc. alloys[21, 18] support this kind of behaviour.

Based on the Stoner model, Edwards, Wohlfarth and Mathon had applied the Landau–Ginzberg theory of second order phase trasition to FM metals and alloys whose magnetization M is low compared to that for complete alignment of spins and obtained

$$H/M(H,T,c) \;=\; A(T,c) \;+\; B(T,c)\,M^2(H,T,c)\;, \tag{5.3}$$

where A and B are the Landau coefficients and c is the concentration. We observe that the value of B^{-1} (120, 138 and 162 [(emu/g)^3/T], respectively for x=23, 26 and 30 after fitting the M–H data to Eq.(5.3) in the high–field linear regime (Fig. 5.6)) gradually increases with the increase in Ni concentration (x). Comparing the concentration dependence of the specific heat[22] which also increases with x, one can qualitatively argue that because of the increase of the density of states at Fermi level [N(E_F)] with x, the value of B^{-1} is enhanced. This result supports the Edwards and Wohlfarth's theoretical prediction[20]. We have also found (not shown) that for the alloys with x = 30, 26 and 23, $T_c^2 \sim$ x (Ni conc.), M^2(0,0,x) $\sim$ x and $\chi_0^{-1} \sim$ x $\sim$ |c - c_{crit} |. Experimental plots of these quantities are called Mathon plots, where c_{crit} is the critical concentration for weak itinerant ferromagnetism[23]. This provides us a better understanding of the weak itinerant type of FM ordering which exists in these disordered 3d transition metal alloys.

As mentioned earlier we have carried out dc magnetization measurements between 20 and 700 K in a constant dc–field of 0.2 T, to examine whether in the pure paramagnetic regime they follow the Curie–Weiss law. In Figs.5.8 and 5.9 we show typical $1/\chi$ vs. T plots for the alloys with x = 19, 30 and 14. We find that (Fig. 5.8) all the alloys obey the Curie–Weiss (CW) law in the high–temperature range. The deviation from the CW law starts at temperatures (T_d), much higher than their respective transition temperatures. This kind of behaviour also shows up in the non–linearity of the M–H curves (CW law gives M $\propto$ H at constant temperature) even much above their respective transition temperatures. This may be due to the persistence of some short-range ordering. From the high-temperature (T > T_d)

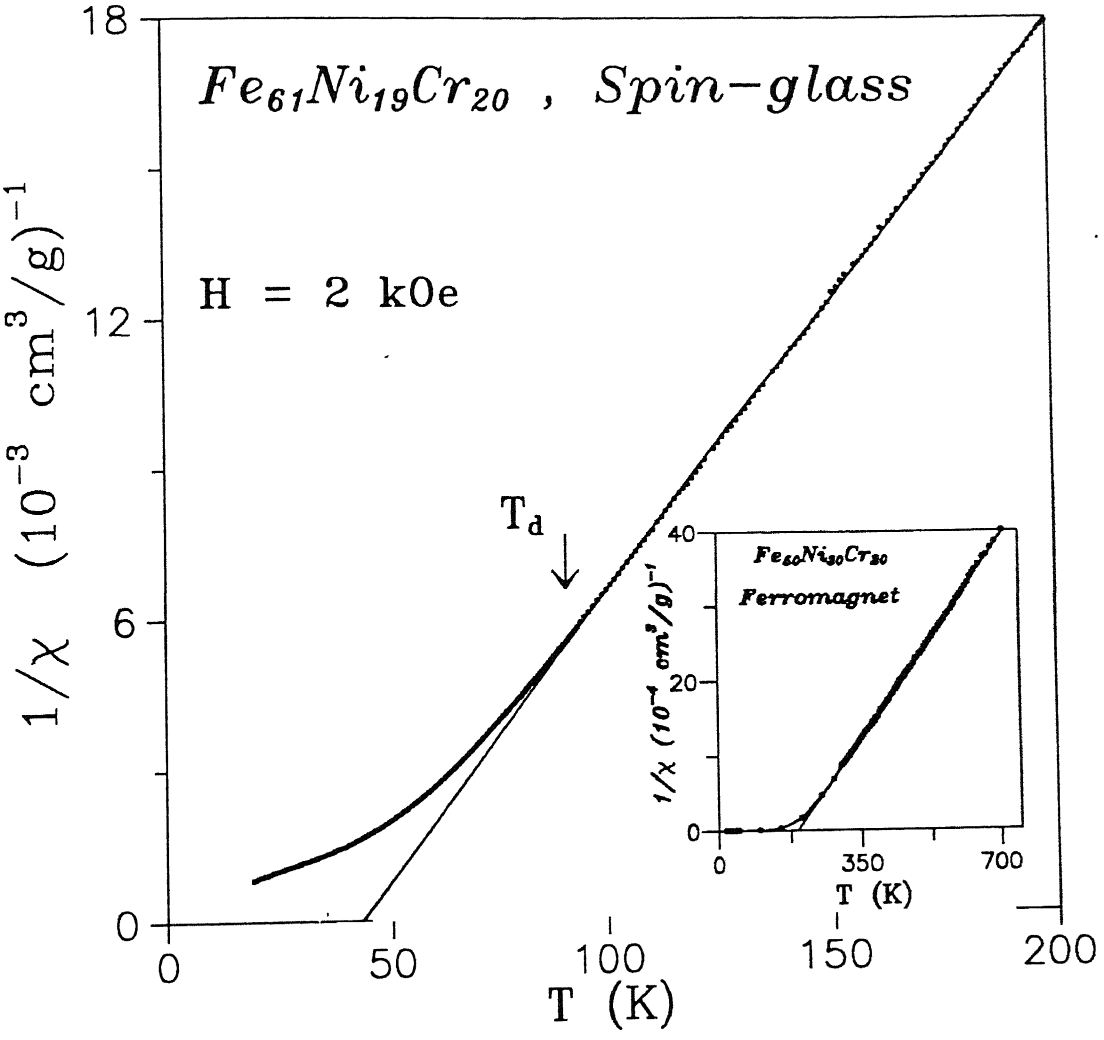

Figure 5.8: Reciprocal susceptibility (1/χ) vs temperature (T) for $Fe_{61}Ni_{19}Cr_{20}$ (SG) alloy at 0.2 tesla. The arrow shows the onset ($T_d \gg T_f$) of the deviation from the Curie–Weiss behaviour. The inset shows the same plot for $Fe_{50}Ni_{30}Cr_{20}$ (FM) alloy. The solid lines are the fits to Curie–Weiss law.

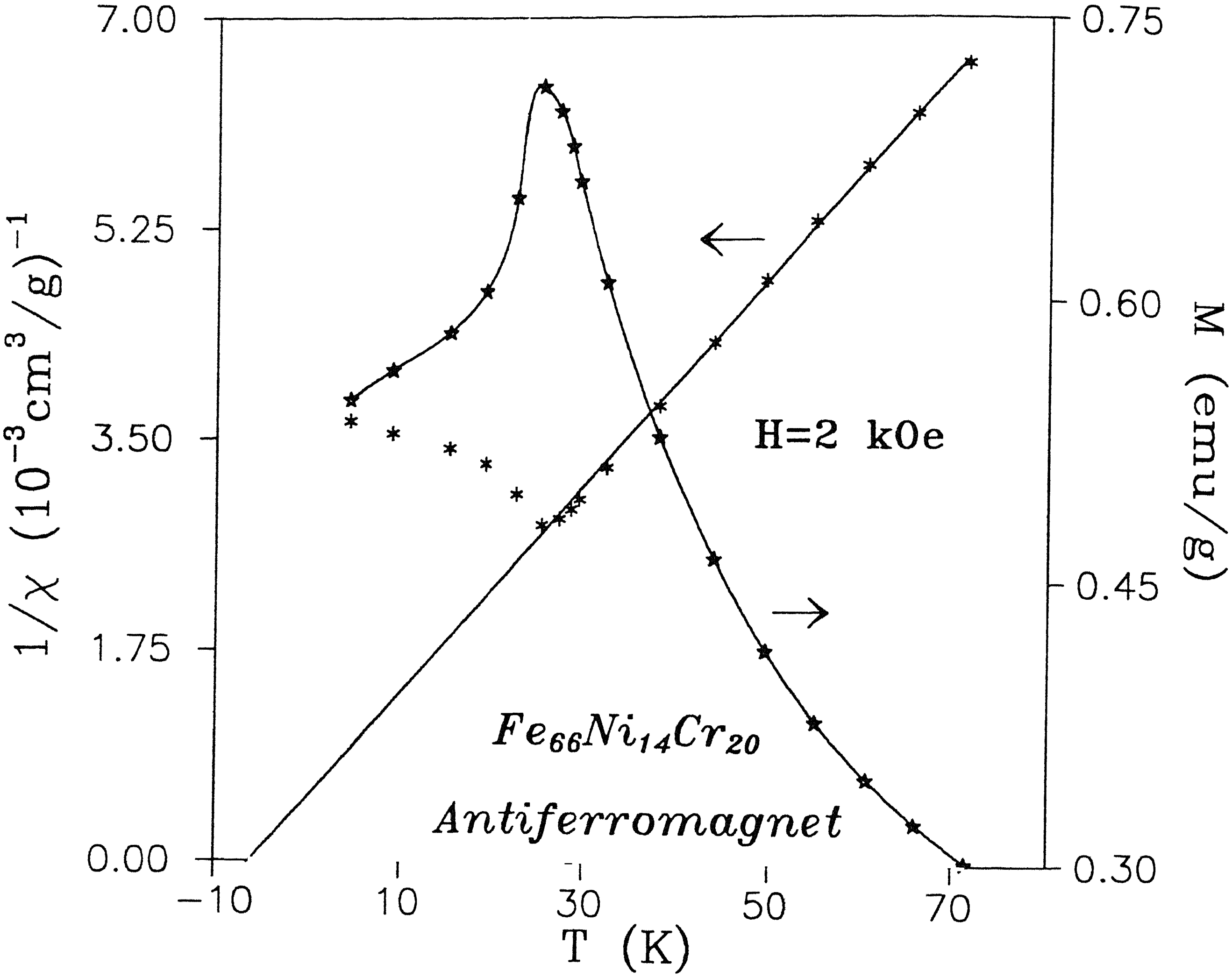

Figure 5.9: Reciprocal susceptibility ($1/\chi$) and magnetization (M) vs temperature (T) for $Fe_{66}Ni_{14}Cr_{20}$ alloy at 0.2 tesla. Θ is small but negative and the Néel temperature is (26±1) K.

data we have estimated the Curie constant (C) and the paramagnetic Curie temperature (Θ) for each alloy from the slopes and intercepts of the linear fits. Table 5.3 lists quantities like C, P_{eff}, Θ, etc , where P_{eff} is the effective Bohr magneton number given by

$$P_{eff} \;=\; g[J(J+1)]^{1/2} \;=\; \left[(3k_B)/(N_x\mu_B^2\frac{d}{dT}\left(\frac{1}{\chi}\right))\right]^{1/2} . \tag{5.4}$$

Here N_x is the average number of the three kinds of atoms (Fe, Ni and Cr) per gram, g the Landé g factor, J the total angular momentum, k_B the Boltzmann constant and μ_B the Bohr magneton.

Figure 5.9 clearly shows the AFM transition for the alloy with x=14 where a peak in M(T) occurs at T_N = (26±1) K. In Fig. 5.10 we show the variation of P_{eff} and Θ with the Ni concentration (x). The paramagnetic Curie temperature (Θ) increases roughly linearly with x. For the alloy with x = 14 (AFM), the value of Θ is negative (already shown in Fig.5.9). The variation of P_{eff} with x is rather small.

There is a subtle interplay between the effective number, n ($\approx$ <3d+4s>), of electrons per atom outside the closed argon shell and the type of magnetic ordering as well as their transition temperatures. In Table 5.3 we give the values of n for all the alloys. For n > 8, these alloys shift towards the FM state with increasing spontaneous moment (M_0) and T_c. On the other hand when n < 8, AFM ordering is established, while in the intermediate region the SG phase appears.

The above facts, namely, the non-integral values of $\bar{\mu}$ in Bohr magneton per atom, the strong deviation from Slater–Pauling curve, the curvature in the low-field region and a set of parallel lines in the high-field region of the ABK plots, the large values of χ_{HF} at 19 T and 4.2 K, and the Mathon plots indicate the possibility that the alloys with higher Ni concentration having FM ordering at lowest temperatures may be described within the framework of the itinerant model rather than the localized one.

We have examined the FM ordering in the light of the Rhodes–Wohlfarth[5] criteria :

(a) In the localized model the effective spin is the actual spin and hence $q_c/q_s = 1$, for all T_c, where $P_{eff} = \sqrt{q_c(q_c+2)}$ in the PM state and q_s is the average spontaneous moments

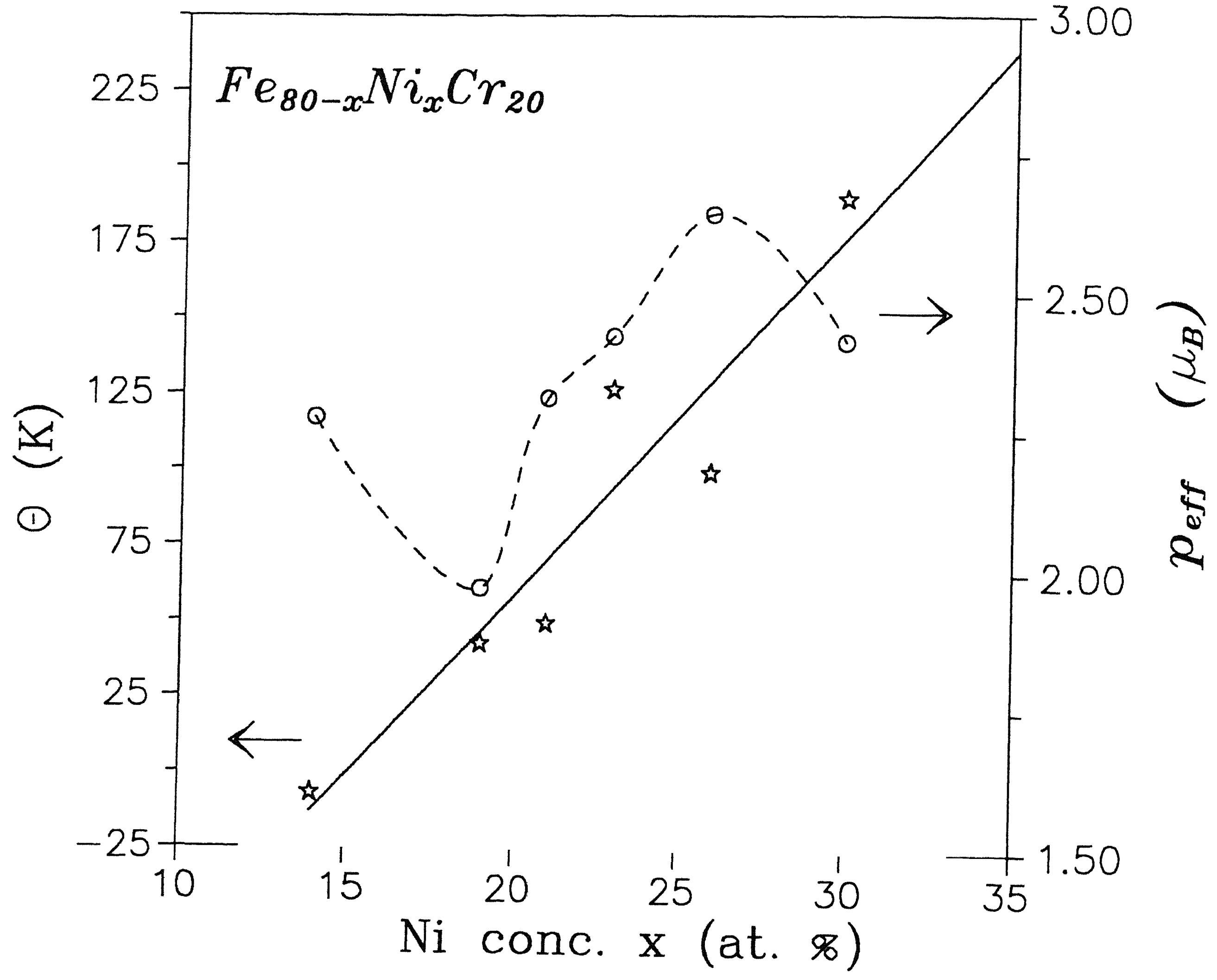

Figure 5.10: Ni conc. (x) dependence of the paramagnetic Curie temperature (Θ) and the effective Bohr magneton number (P_{eff}) (derived from Eq.(5.4)) for $Fe_{80-x}Ni_xCr_{20}$ alloys. The solid line is the best–fit straight line and the dashed one is a guide to the eye.

Table 5.3: Composition (x), Curie constant (C), effective Bohr magneton number (P_{eff}), Paramagnetic Curie temperature (Θ), q_c, q_s, temperature for the onset of deviation from Curie–Weiss law (T_d), and effective number of electrons per atom outside the closed argon shell [n ($\approx$ <3d+4s>] of $Fe_{80-x}Ni_xCr_{20}$ alloys.

x (Ni conc.)	C ($10^{-3}\ \frac{cm^3K}{g}$)	P_{eff} (μ_B)	Θ (K)	q_c (μ_B)	q_s (μ_B)	T_d (K)	n $\simeq$ <3d+4s>
14	11.7	2.28	-6.5	1.49		26	7.88
19	8.7	1 97	43	1.20		98	7.98
21	12.1	2.31	50	1.52		130	8.02
23	13.2	2.42	127	1.62	0.13	280	8.06
26	15.7	2.65	100	1.83	0.27	300	8.12
30	13.0	2.42	190	1.61	0.40	320	8.20

in units of μ_B and (b) In the itinerant model q_s might be less than the maximum possible value q_c, and hence $q_c/q_s > 1$ and its value (between 1 and ∞) gives a measure of the degree of itinerancy. In addition, $q_c/q_s \propto T_c^{-1}$ for itinerant electrons, i.e., larger the ratio (q_c/q_s), weaker is the FM The values of q_c and q_s are given in Table 5.3 for the alloys with x = 30, 26 and 23. It is quite apparent that q_c/q_s indeed shows a systematic increase with decreasing T_c and follows the relation $q_c/q_s \propto T_c^{-1}$. Moreover, q_c/q_s lies between 4 and 12 indicating moderate itinerancy. They also compare favourably with those of several other weak-itinerant FM alloys (e.g., FeCr, FeV, NiFeV,[24] ZrZn[25]). Thus we conclude that the alloys with higher x (23-30) are weak itinerant ferromagnets (WIF).

5.1.2 Spin–wave analysis of γ-$Fe_{50}Ni_{30}Cr_{20}$ alloy

There are reports on Fe-Ni based crystalline and amorphous alloys (e.g., $Fe_xNi_{80-x}B_{18}Si_2$[26], Ni-Fe-Cr and Ni-Fe-V[24], etc.) where the presence of both spin–wave and Stoner single-particle excitations were confirmed through bulk magnetization measurements. Inelastic neutron scattering[16] studies directly prove the presence of spin–wave excitations in these alloys. It was concluded for Ni–rich Ni-Fe-Cr and Ni-Fe-V alloys[24] that the addition of Cr and V enhances the Stoner term considerably, and drives these systems towards the weak-itinerant FM regime.

To examine contributions from various kinds of excitations to the temperature-dependent demagnetization process, we have carried out a very careful dc-magnetization M(T) measurements (accuracy 1 part in 10^4) at 100 mK temperature interval in a field of 1 tesla. In Fig.5.11, we show the M(T) data which have been analysed in the light of the spin–wave (SW) theory as well as the Stoner excitations[27–29]. At low temperatures, the change in magnetization due to spin–wave excitations is given by

$$\begin{aligned}\left[\frac{\Delta M(T)}{M(0)}\right]_{SW} &= \frac{M(T)-M(0)}{M(0)} \\ &= AT^{3/2}(1 - D_1T^2 - D_2T^{5/2})^{-3/2}\mathcal{Z}(3/2, T_g/T) \\ &+ BT^{5/2}\mathcal{Z}(5/2, T_g/T)\,. \end{aligned} \tag{5.5}$$

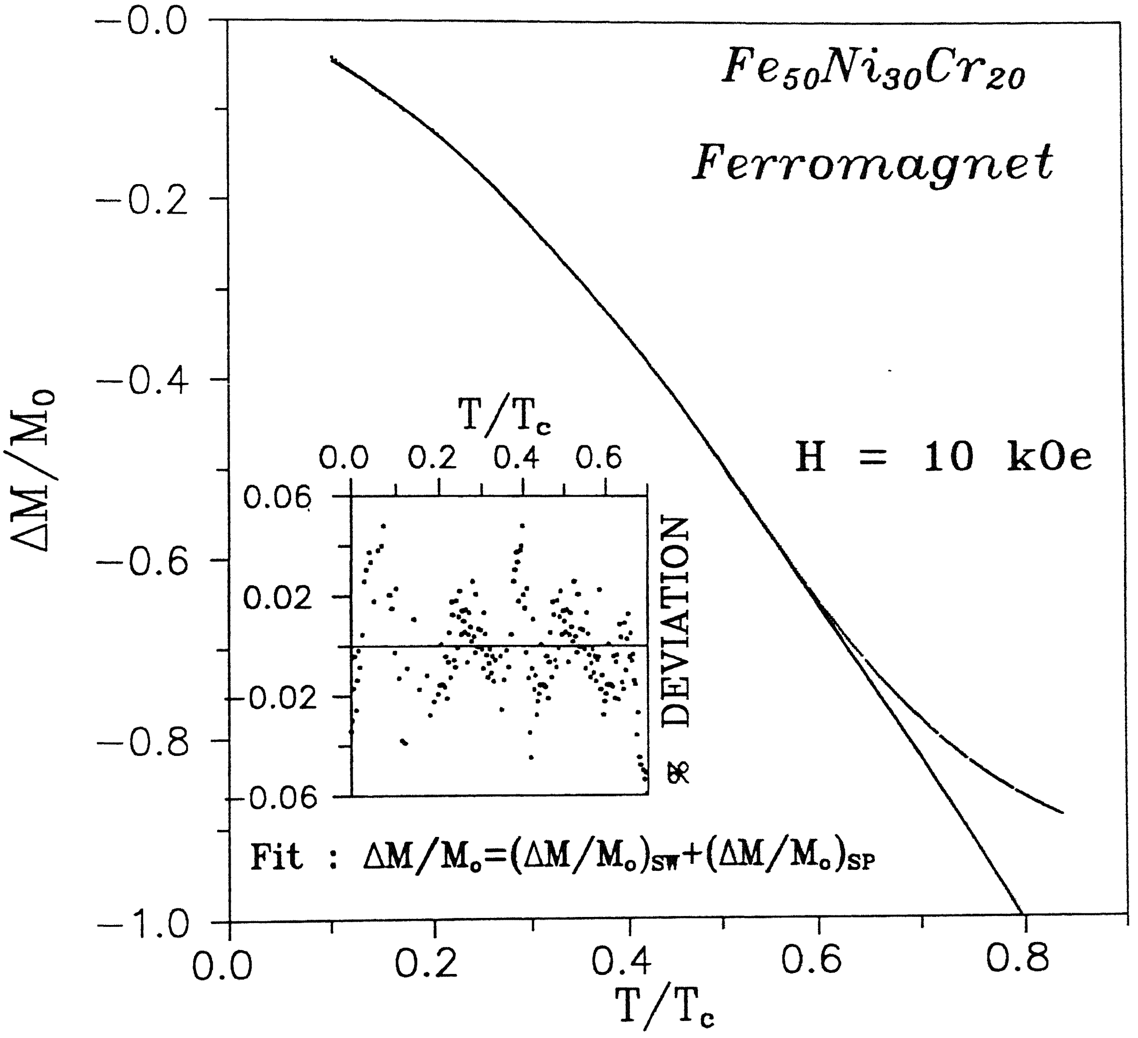

Figure 5.11: Change of reduced magnetization ($\frac{\Delta M}{M_o}$) as a function of reduced temperature (T/T_c) for $Fe_{50}Ni_{30}Cr_{20}$ (FM) alloy. The solid line is the non-linear least squares fit of the experimental data to the combination of *spin-wave* and Stoner *single-particle* excitations. The percentage deviation of the fit from the data, shown in the inset, indicates a very good quality of fit.

Here T_g is the gap temperature which is equal to $g\mu_B H_{int}/k_B$, $\mathcal{Z}(3/2\ ,\ T_g/T)$ and $\mathcal{Z}(5/2\ ,\ T_g/T)$ the Bose–Einstein integrals, and the coefficient A is related to the spin–wave stiffness constant $\mathcal{D}$, by

$$\mathcal{D}(=\mathcal{D}(0)) \;=\; \frac{k_B}{4\pi}\left(\frac{2.612 g\mu_B}{M(0)\rho A}\right)^{2/3} \;, \tag{5.6}$$

where ρ is the density. Thompson et al.[30] have calculated the change in reduced magnetization due to Stoner single- particle (SP) excitations only, given by

$$\left[\frac{\Delta M}{M(0)}\right]_{SP} \;=\; \alpha T^{3/2} e^{-\Delta/k_B T} \;, \tag{5.7}$$

for strong itinerant FM and

$$\left[\frac{\Delta M}{M(0)}\right]_{SP} \;=\; \beta T^2 \;, \tag{5.8}$$

for weak itinerant FM. Here α and β are related to various band parameters. Δ is the energy gap between the top of the full sub-band and the Fermi level (E_F) for a strong FM. It is 0 for a weak FM.

At low temperatures, when deviation from saturation magnetization at 0 K is small, the excitations from the SW and the SP are nearly independent and the thermal demagnetization is given by the the sum of both the contributions, i.e ,

$$\Delta M \;=\; [\Delta M]_{SW} \;+\; [\Delta M]_{SP} \;. \tag{5.9}$$

We used a non-linear least-squares fitting programme using the NAG library to fit the M(T) data for the alloy with x = 30. The fit to Eq.(5.5) excluding the $BT^{5/2}$ anharmonic term gives $\chi^2 = 6.8 \times 10^{-6}$ which is at least one order of magnitude higher than the experimental error. Inclusion of the anharmonic term yields an unphysical sign of the coefficient B. However, the data, when fitted to Eq.(5.9), a combination of Eqs.(5.5) and (5.8) but excluding the anharmonic $T^{5/2}$ term, yield a much improved $\chi^2 = 2.1 \times 10^{-7}$ with $A = 3.4 \times 10^{-4}\ K^{-3/2}$ and $\beta = 9.3 \times 10^{-7}\ K^{-2}$. As shown in Fig.5.11, the experimental data and the best-fitted curves are almost indistinguishable. But Eq.(5.9), when taken as a combination of Eqs.(5.5) and (5.7), gives unphysical values of α and the gap parameter Δ. In the inset of Fig.5.11 we have also shown the percentage deviation of the fit from the data which clearly reveals that a combination of both SW and SP excitations describes the thermal demagnetization process quite well in this FM alloy. The value of the coefficient of the SW term, A [$\approx 10^{-4}$ $K^{-3/2}$] is two orders of magnitude larger than those of pure Fe and Ni [$\approx 10^{-6}$ $K^{-3/2}$][28] and one order of magnitude larger than those of Ni-rich Ni-Fe-Cr and Ni-Fe-V alloys [$\approx 10^{-5}$ $K^{-3/2}$][24]. This implies that the spontaneous magnetization (M_0) of the alloy falls off with temperature at a faster rate and so it must have a weaker SW stiffness constant $\mathcal{D}(0)$. Using Eq.(5.6) we have estimated $\mathcal{D}(0)$ to be $\approx$ 40 meV Å^2 whereas it is 286, 100 and 46 meV Å^2 for pure Fe[28], Ni-rich $Ni_{67}Fe_{21}Cr_{12}$[24] and higher Cr-containing amorphous alloys like $Fe_5Co_{50}Ni_2Cr_{15}B_{16}Si_{12}$[12], respectively. It should be noted that with the addition of Cr in Ni-Fe binary alloys, $\mathcal{D}(0)$ falls off very rapidly[24, 12]. Moreover, so far as the magnetic properties are concerned there is not much difference between the crystalline and amorphous materials. Our estimated value of $\mathcal{D}(0)$ for the alloy with x = 30 seems rather reasonable. In addition to this there is also a strong experimental support to our result from the inelastic neutron scattering studies by Menshikov et al.[16] on Ni-rich Ni-Fe-Cr alloys from which the SW stiffness constant $\mathcal{D}(0)$ was estimated to be $\approx$ 50 meV Å^2. They also could not detect the presence of any higher order term apart from the quadratic one in the SW dispersion relation in good agreement with our result. Thus we conclude that the introduction of Cr suppresses the anharmonic term ($T^{5/2}$), similar to the earlier case[24]. Moreover, the Stoner single-particle excitation is present in this weak-itinerant FM. The constant β in the Stoner term is of the same order as in pure Ni[28] and Ni-rich Ni-Fe-Cr[24] alloys ($\approx 10^{-7}$ K^{-2}). Thus one finds that the addition of Cr enhances the Stoner term considerably.

5.1.3 x = 26 : Mixed-phase alloy

In Fig.5.12 the temperature dependence of the dc-susceptibility χ_{dc} ($= \frac{dM}{dH}$) is shown in a field of 0.6 T which is above the technical saturation for the alloy with x = 26. We find that there

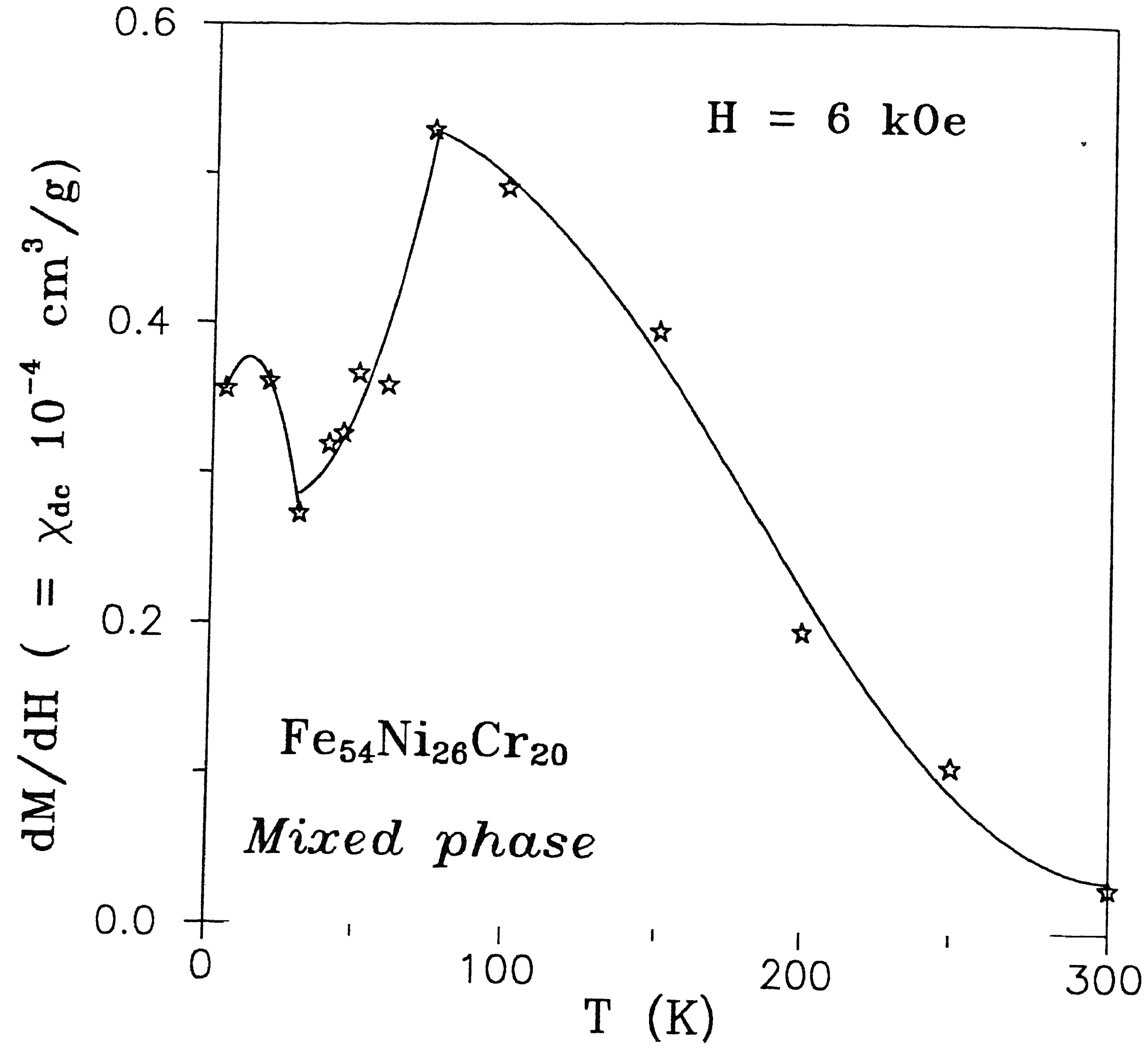

Figure 5.12: Temperature dependence of dc–susceptibility χ_{dc} (= $\frac{dM}{dH}$) for the mixed phase alloy $Fe_{54}Ni_{26}Cr_{20}$ at a field of 0.6 tesla. The solid line is a guide to the eye. The peaks appear at its two transition temperatures (T_c and T_f).

is a sharp peak in χ_{dc} at around T $\approx$ 60 K which is the PM $\rightarrow$ FM transition temperature (T_c) as reported earlier[2]. As the temperature decreases, χ_{dc} decreses continuously. But below some minimum temperature it again starts to increase significantly. In our earlier work[1] we made the same kind of observation for the alloy with x = 23 and 21 which have mixed phase and SG orderings, respectively at the lowest temperature. Hamzic and Campbell[31] also made exactly the same kind of observation for the variation of χ_{dc} with temperature in the case of *Au*19%Fe alloy which is beyond the percolation threshold where long-range FM appears alongwith SG freezing. In this alloy with x =26, there is a coexistence between FM and SG orderings at the lowest temperature. So this is a common feature of χ_{dc} which is observed in a number of alloys having either SG or mixed phase orderings.

The alloy with x = 26, below a temperature T_f = 7 K, has a SG ordering as reported in different investigations[2]. There is a long-standing controversy for this kind of mixed phase or re-entrant phase alloys[32] showing double transitions. Whether both kinds of ordering, namely, SG and FM co-exist below the second transition, is still debatable. From a number of experimental evidence[33–37] it was concluded that both the orderings do co-exist below the second transition. This kind of behaviour can be understood through the *semi–spin–glass* picture proposed by Villain[38]. Just below T_c these alloys behave as a standard FM with (for each spin) $m_z^i \neq 0$, $m_x^i = m_y^i = 0$. As the temperature drops, the degree of FM ordering increases continuously and hence χ_{dc} drops below T_c. But at a lower temperature the spins begin to acquire random uncorrelated canted moment with components m_x^i, $m_y^i \neq 0$ but $<m_x>$ $= <m_y> = 0$. At the lowest temperature (below the second transition) the conventional spin-wave theory totally breaks down. This has been clarified later in the Gabay - Toulouse (GT) model, which is a Heisenberg version of the Sherington - Kirkpatrick model, where below the second transition temperature there is an overall long-range order in a certain direction (say, z - direction) and a simultaneous existence of frozen spins in the transverse direction (x-y plane). So the temperature dependence of χ_{dc} of this mixed phase alloy can be understood in the light of the Villain as well as the G-T models. We have also seen from Arrott plots

(Fig.5.6) that at the lowest temperarure (4.2 K), FM ordering persists in this alloy. Moreover, thermoremanent history dependent FC magnetization[2] confirmed the SG ordering at 4.2 K. So our results for χ_{dc} as well as the Arrott plots definitely support the coexistence of both FM and SG orderings below the second transition.

5.1.4 x = 19 and 21 : Spin-glass alloys

A remarkable feature of the magnetization curves for the alloys with x = 19 and 21 is that the curves can be scaled on a single universal curve till very high fields as shown in Fig.5.13. Both the alloys have only one transition (PM → SG) at 12 and 10 K, respectively[2]. The magnetization curve for the higher concentration alloy (x = 21) can be brought into coincidence with that of x = 19 by using a scaling factor defined as : R_g = M(x) / M(x=19). The magnetization data for x = 21,[2] obtained by using the Faraday balance (FB), are also brought into coincidence on the same figure with the same scaling factor, i.e., irrespective of the measurement technique. The universality of the behaviour of the magnetization implies the same magnetization process, namely, the high-field response dynamics of the frozen spins. This kind of universal scaled magnetization curve was also observed in archetypical SG (CuMn and AuFe[7, 8]) systems below the critical concentration. For the alloys with x = 26, 23 and 14, the scaled magnetization curves have strong deviations from an universal one suggesting entirely different kinds of magnetization processess.

5.1.5 x = 14 : Antiferromagnetic alloy

As mentioned earlier, the M(H) curve at 4.2 K has an inflection point at around 1 T as shown in Fig.5.3 with an arrow. The figure also shows dM/dH vs. H plot which has a sharp peak at the same field. We have further observed that the point of inflection shifts slightly towards low fields at higher temperatures of 11.2 and 20.1 K. The M(H) curves (at T = 35.1 and 60 K) beyond the Néel temperature (T_N = 26 K) do not show any inflection point. The field H_c = 1 T can be taken as the critical field for the *spin-flop* transition below T_N. This alloy has a

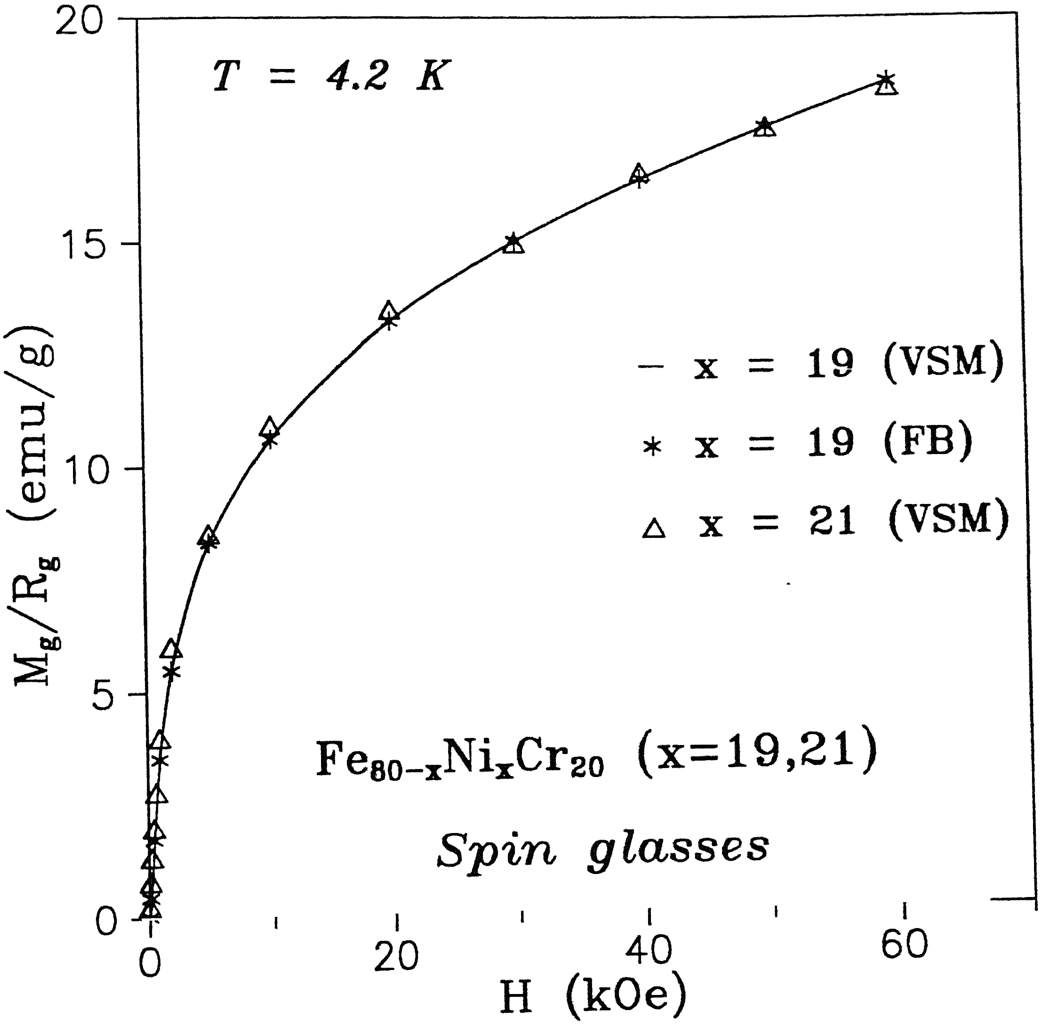

Figure 5.13: M-H plot of the alloy with x=21 is scaled on to that of x=19 implying the same kind of magnetization process at 4.2 K. The abbrebiations, VSM and FB stand for vibrating sample magnetometer and Faraday balance, respectively.

long-range AFM ordering with a resonably small value of Néel temperature (T_N = 26 K). A number of reports show that *spin-flopping* can be produced most easily if the Néel temperature is low and for them H_c will be relatively small (e.g.,$CuCl_2 \cdot 2H_20$ (T_N = 4.2 K),[39] MnF_2, Cr_2O_3. DyAg,[40] DyAu,[40] Au_3Mn, etc.).

Unlike the conventional AFM's, this alloy shows a high value of the field-induced moment at 19 T ($\approx$ 0 17 μ_B) and a tendency of saturation (Fig.5.1). Neutron scattering in AFM γ-$Fe_{0\,7}Ni_{0\,15}Cr_{0\,15}$[11] in magnetic fields of 5 T suggested that the induced moment can be interpreted in terms of the canting of the AFM spins. In the alloy with x = 14, the magnetization M induced in the high magnetic field H obeys the Landau relation of the form

$$M^2 \;=\; -A \;+\; BH/M \;, \tag{5.10}$$

with A = 308 $(emu/gm)^2$ and B = 560 $(emu/gm)^3$/T in the field range between 10 and 20 T at 4.2 K. This relation holds when the substance is close to a FM state but as a whole is an AFM. However, there may exist a positive interaction between the high-field-induced moments as had been concluded in the AFM γ-$Fe_{0.7}Ni_{0\,15}Cr_{0.15}$[41, 11] alloy. An itinerant AFM model[41] was proposed in which the effective magnetic interaction between the spins is always positive even in an AFM substance, and an AFM state can also be close to a FM state. The effect of magnetic field on the AFM structure was studied by neutron scattering measurements[11] on γ-$Fe_{0.7}Ni_{0.15}Cr_{0.15}$. It suggested that the induced moment could be explained by canting of the AFM spins by an angle θ.

We have used the experimentally – estimated parameters T_N ($\simeq$ 26 K), C ($\simeq 11.7 \times 10^{-3}$ cm^3 K /g) and the paramagnetic Néel temperature Θ ($\simeq$ -6.4 K) (some are shown in Table 5.3 and Fig.5.10) to evaluate J_1, J_2, γ_1 and γ_2 for this alloy with x = 14. Here J_i is the effective-field exchange interaction between the ith neighbours. Similarly, γ_1 and γ_2 are the first and second neighbour molecular field coefficients. In the light of Smart's model[9] for the generalized molecular field theory for an antiferromagnetic substance with n sublattices, the following relations can be written :

$$\gamma_{ij} \;=\; \frac{2nZ_{ij}J_{ij}}{Ng^2\mu_B^2} \;,\; i \neq j \;, \tag{5.11}$$

$$\Theta = \frac{C}{n}\sum_{j=1}^{n}\gamma_{ij} , \qquad (5.12)$$

and

$$T_{N_s} = \frac{C}{n}\sum_{j=1}^{n}\eta_{ij}J_{ij} , \qquad (5.13)$$

where Z_{ij} is the number of j neighbours of an i atom; J_{ij} the exchange interaction between an i atom and one of its j neighbours, γ_{ij} the molecular field coefficient for the field exerted on an atom on the ith sublattice by its neighbours on the j th sublattice, and μ_B the Bohr magneton. The present AFM alloy has an fcc structure. According to Smart[9], an AFM alloy with fcc structure can have maximum possible 3 types of antiferromagnetic ordering (Fig.5.14). Our calculation for the alloy with x = 14 is appropriate for the fcc structure with *type 1* antiferromagnetic ordering with 8 sublattices and 12 nearest as well as 6 next nearest neighbour atoms[9]. Using Eqs.(5.11) - (5.13) we have computed the following values: γ_1 = -20.8 × 10^5 kg/m^3, γ_2 = 15.3 × 10^5 kg/m^3, J_1/k = -1.29 K and J_2/J_1 = - 1.47. In this AFM alloy, Θ/T_N ($\simeq$ -0.25) is small and negative, in contrast to the large values (> 1) observed in the SG alloys (x = 19 and 21, Table 5.3). This indicates that frustration effects are minimal in this alloy with x = 14. From the above estimates, a number of important inferences could be drawn, e.g., negative values of J_1 and J_2/J_1 indicate that the first nearest–neighbour interaction is AFM and the second nearest–neighbour interaction is FM. $| J_2/J_1 | > 1$ implies that the second nearest–neighbour interaction is stronger than the first. The larger value of J_2 compared to J_1 does not affect the effective field approximation used here, because there are 12 nearest neighbours each contributing -$| J_1 |$ towards Θ, whereas there are only 6 next nearest neighbours each with a contribution of ≈ 1.5 J_1. Hence as a whole the paramagnetic Néel temperature Θ is still negative (antiferromagnetic) and has a small value as observed experimentally. Because of the fact that $| J_2/J_1 | > 1$, one concludes that this alloy must have a strong itinerant-electron contribution. Perhaps some of the outer 3d and 4s electrons are localized and some others are in the extended states. The nearest-neighbour molecular-field coefficient $\gamma_1 < 0$ implies the expected AFM interaction. The next-nearest-neighbour interaction $\gamma_2 > 0$ corresponds to the FM interaction. The values of Θ/T_N and γ_2/γ_1 are compatible

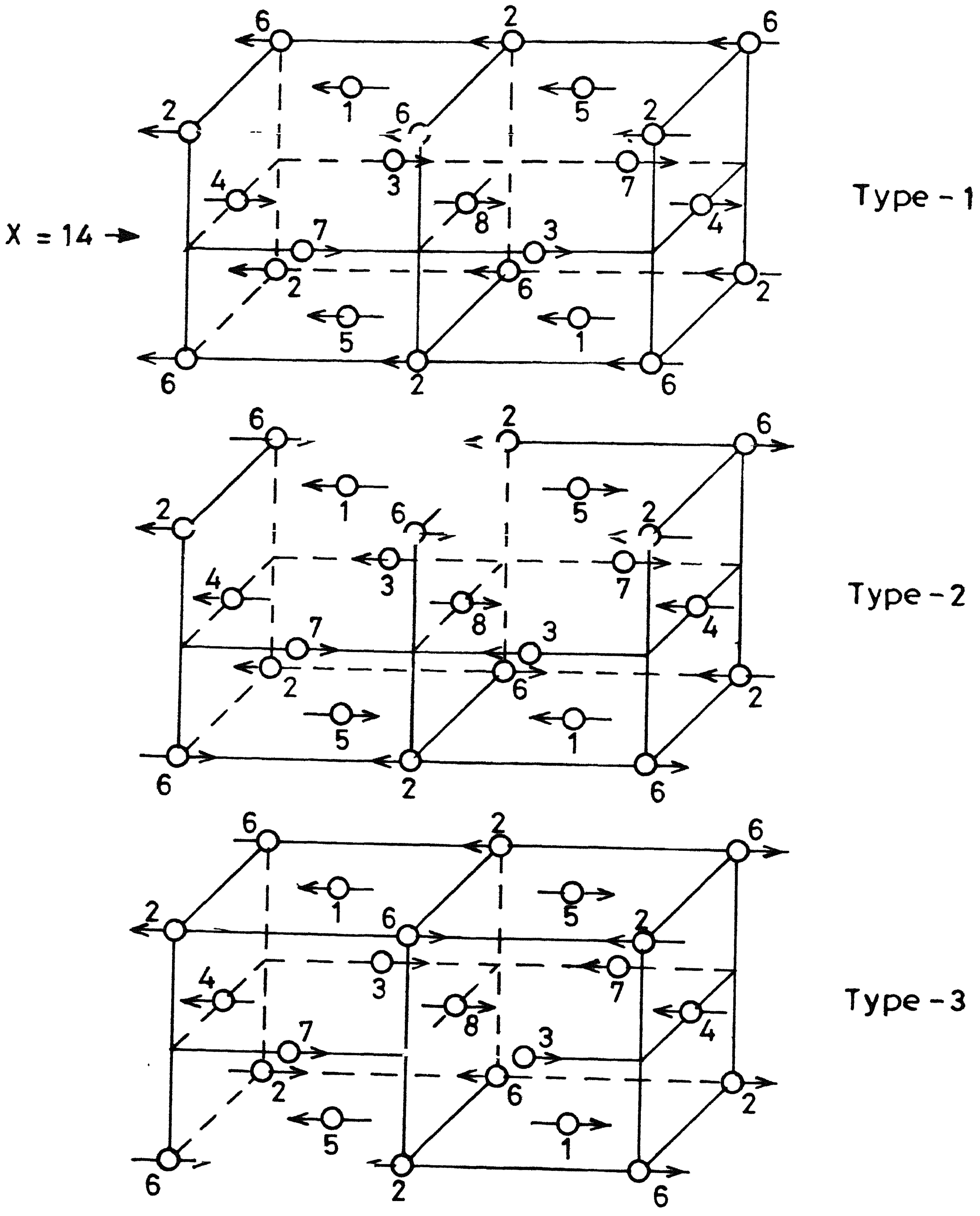

Figure 5.14: (a) First, (b) second, and (c) third kinds of antiferromagnetic orderings in f.c.c. lattice, after [9].

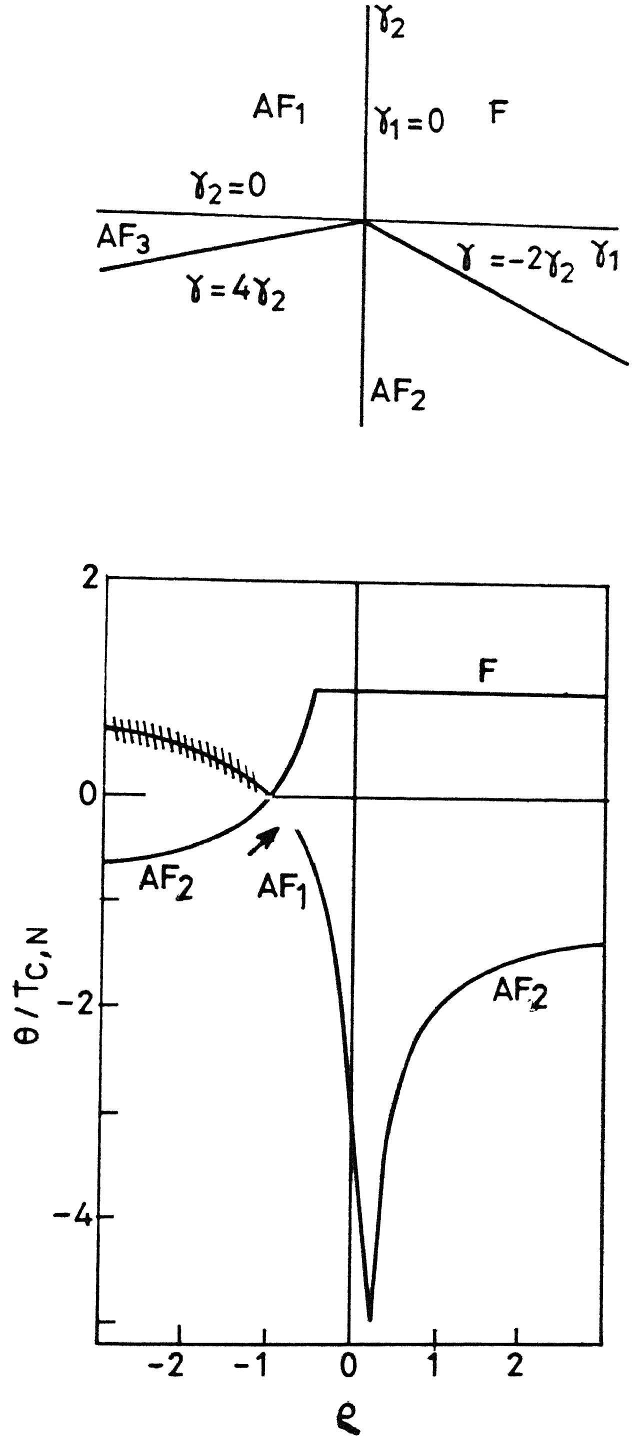

Figure 5.15: (a) Magnetic-ordering phase diagram in the γ_1–γ_2 plane for the antiferromagnetic f.c.c. lattice, after [9]. (b) Θ/T_N and Θ/T_C vs. ϱ (=γ_2/γ_1) for the f.c.c. lattice. The marked point is the position of the studied x=14 alloy.

only with the *type 1* AFM ordering in this alloy. In Fig.5.15(a), the magnetic-ordering phase diagram in the γ_1–γ_2 plane for the f.c.c. lattice has been shown[9]. According to the sign of γ_1 and γ_2, as computed from the magnetization study , it is clear from this phase diagram that the alloy with x=14 falls into the antiferromagetic ordering regime of *type 1* (AF_1). Figure 5.15(b) shows Θ/T_N and Θ/T_c vs. $\varrho(\simeq \gamma_2/\gamma_1)$ for the f.c.c. lattice[9]. The position of x=14 has been marked in this figure by a dot which lies on the AF_1 line with Θ negative and T_N positive. All these results agree with the neutron–diffraction–derived structural studies[41, 11] which revealed the *type 1* AFM ordering in alloys of similar composition

5.2 Conclusion

In this work we have carried out systematic high-field (0 - 20 T) dc-magnetization studies (M(H) and M(T) from 4.2 to 60 K and 19 to 700 K, respectively) on substitutionally disordered γ-$Fe_{80-x}Ni_xCr_{20}$ ($14 \leq x \leq 30$), austenitic stainless steel alloys having a very rich magnetic phase diagram at low temperatures. All the samples are at the vicinity of the critical concentration regime for long-range FM and AFM orderings and have strong competing interactions between different kinds of magnetic atoms. We find a number of distinct functional relationships M(H) in different magnetic phases below their respective magnetic transition temperatures. Because of the very large χ_{HF} compared to that of a conventional FM, we conclude that the nature of ferromagnetism in the case of the alloys with x = 30, 26 and 23 in their FM phase is unlike that of a standard FM. They are very hard to saturate even at a field of 19 tesla at 4.2 K. The law of approach to saturation reproduces the high-field M(H) data in the saturation regime resonably well. In the light of the *Rhodes-Wohlfarth* criterion the alloys with x = 30, 26 and 23 in their FM regime are of weak - itinerant type. The non-integral values of the number of Bohr magneton per atom ($\overline{\mu}$) and the strong deviation from the Slater-Pauling curve support this weak-itinerant picture. In the FM alloy with x = 30, the combination of long wave–length *spin-wave* and *Stoner single-particle* excitations describes the thermal demagnetization process quite well till 0.5 T_c. We conclude that the introduction of Cr in this alloy substantially reduces the *spin-wave stiffness constant* $\mathcal{D}(0)$, suppresses the anharmonic term ($T^{5/2}$) and enhances the Stoner term.

In the case of the alloys with x = 26 and 23 (mixed phase), this particular study, alongwith our earlier studies, corroborate that below the second transition the long-range FM ordering coexist with the transverse SG freezing supporting the G-T model. Neutron-depolarization studies coupled with small-angle neutron scattering would be able to provide a complete picture of the transverse spin component in the FM domain (which might be of vortex-like spin structure), the nature of the domain-wall motion and the spin-modulated structure. In the concentrated SG alloys (x = 21 and 19) the high–field response dynamics of the frozen spins is similar to that of the *archtypical* spin glasses.

Our analysis on x = 14 (AFM) alloy shows that the long - range AFM structure of this alloy is of *type 1* where the 1st nearest neighbour interaction (J_1) is AFM and the 2nd one is FM (J_2). Since $\mid J_2/J_1 \mid > 1$, we conclude that this alloy must have a strong itinerant–electron–AFM contribution. Our estimated molecular field coefficents γ_1 and γ_2 for the 1st and 2nd nearest neighbour interaction in different sublattices are also compatible with the *type 1* kind of AFM structure. The latter shows a *spin-flop* transition at 1 T due to the canting of the AFM spins in the strong external magnetic field. Beyond this transition a square-root dependence of magnetization with external field is found whereas below it the dependence is linear.

At present as there is no band structure (electronic or magnetic) calculation in these alloys, it is very difficult to estimate and correlate anything in more quantitative terms. Greater attention must be paid in this direction for better correlation of the transport and magnetic properties of these ternary alloys.

Bibliography

[1] T. K. Nath and A. K. Majumdar, J. Appl. Phys. **70**, 5828 (1991).

[2] A. K. Majumdar and P. v. Blanckenhagen, Phys. Rev. B **29**, 4079 (1984).

[3] T. K. Nath and A. K. Majumdar, Phys. Rev. B, May B **53**, 12148 (1996).

[4] S. Banerjee and A. K. Raychaudhuri, Phys. Rev. B **50**, 8195 (1995).

[5] P. Rhodes and E. P. Wohlfarth, Proc. Roy. Soc. London, Ser. A **273**, 247 (1963); E. P. Wohlfarth, J. Magn. Magn. Mater. **7**, 113 (1978).

[6] M. Gabay and G. Toulouse, Phys. Rev. Lett. **47**, 201 (1981).

[7] J. J Smit, G. J. Nieuwenhuys, and L. J. de Jongh, Solid State Commun. **31**, 265 (1979).

[8] J. J. Smit, G. J. Nieuwenhuys, and L. J. de Jongh, Solid State Commun. **32**, 233 (1979).

[9] J. S. Smart, *Effective Field Theories of Magnetism* (Saunders, Philadelphia, 1966).

[10] A. K. Majumdar and P. v. Blanckenhagen, J. Magn. Magn. Mater. **40**, 227 (1983).

[11] Y. Ishika, M. Kohgi, and Y. Noda, J. Phys. Soc. Japan **39**, 675 (1974).

[12] A. Das and A. K. Majumdar, J. Magn. Magn. Mater. **128**, 47 (1993).

[13] T. Sakakibara, T. Goto, and Y. Miyako, Soild State Commun. **58**, 563 (1986).

[14] H. Hiroyoshi and K. Fukamichi, J. Appl. Phys. **53**, 2226 (1982); S. N. Kaul, Phys. Rev. B **27**, 6923 (1983); H. Hiroyoshi, N. Saito, K. Fukamichi, and Y. Nakagawa, Sci. Rep. RITU, Japan **33**, 58 (1986).

[15] G. Toulouse, J. Physique Lett. **41**, L447 (1980).

[16] A. Z. Men'shikov, N. N. Kuz'min, V. A. Kazantsev, S. K. Sidorov, and V. N. Kalinin, Phys. Metal. Metalloved. **40**, 174 (1975).

[17] H. Hiroyoshi, K. Fukamichi, A. Hoshi, and Y. Nakagawa, *High Field Magnetism* , edited by M. Date (North-Holland, Amsterdam, 1983), p.113.

[18] J. Schneider, Physica **91B**, 185 (1977); J. de Phys. C **8**, 682 (1980); J. Schneider, A. Handstein, and K. Zaveta, J. Magn. Magn. Mater. **42**, 73 (1984).

[19] S. Shtrikman and E. P. Wohlfarth, Physica **60**, 427 (1972).

[20] D. M. Edwards and E. P. Wohlfarth, Proc. Roy. Soc. A **303**, 127 (1968).

[21] R. D. Shull and P. A. Beck, AIP Conf. Proc. **24**, 95 (1975).

[22] V. I. Pecherskaya, D. N. Bol'shutkin, A. V. Butenko, V. N. Beilinson, V. I. Ovcharenko, V. A. Pervakov, and N. Yu. Tyutryumova, Sov. J. Low Temp. Phys. **14**, 505 (1988).

[23] J. Mathon, Proc. Roy. Soc. A **306**, 355 (1968); J. Mathon and E. P. Wohlfarth, Phys. Status Solidi **30**, K 131 (1968).

[24] A. K. Gangopadhyay, R. K. Ray, and A. K. Majumdar, Phys. Rev. B **30**, 6693 (1984).

[25] D. A. Reed, E. H. Thomas, and J. B. Forsythe, J. Phys. Chem. Solids **29**, 1569 (1968); G. S. Knapp, F. Y. Fradin, and H. V. Culbert, J. Appl. Phys. **42**, 1341 (1971).

[26] E. Babic, Z. Marohnic and E. P. Wohlfarth, Phys. Lett. **95** A, 335 (1983).

[27] F. Keffer, *Handbuch der Physik*, edited by S. Flügge (Springer, Berlin, 1966), Vol. XVIII/2.

[28] B. E. Argyle, S. H. Charap, and E. W. Pugh, Phys. Rev. **132**, 2051 (1963).

[29] C. Herring in *Magnetism*, edited by G. T. Rado and H. Suhl, (Academic Press, New York, 1966) Vol. IV; W. Marshall and S. W. Lovesey, *Theory of Thermal Neutron Scattering* (Oxford, 1971).

[30] E. D. Thompson, E. P. Wohlfarth, and A. C. Bryan, Proc. Phys. Soc. London **83**, 59 (1964).

[31] A. Hamzic and I. A. Campbell, J. Physique Lett. **42** L-309 (1981).

[32] G. Aeppli, S. M. Shapiro, H. Maletta, R. J. Birgeneau, and H. S. Chen, J. Appl. Phys. **55**, 1628 (1984), and the references therein.

[33] B. R. Coles, B.Sarkissian, and R. H. Taylor, Phil. Mag. B **37**, 489 (1978); B. V. B. Sarkissian, J. Phys. F **11**, 2191 (1981).

[34] H. Kunkel, R. M. Roshko, W. Ruan, and G. Williams, Phil. Mag. B **64**, 153 (1991).

[35] W. Abdul-Razzaq and J. S. Kouvel, Phys. Rev. B **35**, 1764 (1987); J. S. Kouvel and W. Abdul-Razzaq, J. Magn. Magn. Mater. **53**, 139 (1985).

[36] M. Avirovic, P. Ziemann, B. Huck, and J. Hesse, Europhys. Lett. *8*, 281 (1989).

[37] B. H. Verbeek, G. J. Nieuwenhuys, H. Stocker, and J. A. Mydosh, Phys. Rev. Lett. **40**, 586 (1978).

[38] J. Villain, Z. Phys. **33**, 31 (1979).

[39] N. J. Poulis, J. van den Handel, J. Ubbink, J. A. Poulis, and C. J. Gorter, Phys. Rev. **82**, 552 (1951); C. J. Gorter, Rev. Mod. Phys. **25**, 277 (1953).

[40] T. Kaneko, Shunya Abe, H. Yamauchi, H. Hiroyoshi, and Akira Hoshi in *High Field Magnetism*, edited by M. Date (North-Holland, Amsterdam, 1983), p.108.

[41] Y. Ishikawa, Y. Endoh, and T. Takimoto, J. Phys. Chem. Solids **31**, 1225 (1970).

Chapter 6

Quantum corrections to Boltzmann conductivity in Cu-Zr-Al and Ni-Zr -Al amorphous alloys

6.1 Introduction

In the last few years studies of transport properties of strongly disordered crystalline and amorphous materials have generated considerable interest. The occurrence of negative temperature coefficient of resistivity (TCR $\sim \rho^{-1}d\rho/dT$) giving rise to resistivity minima at low temperatures, has stimulated many investigators to explore various scattering mechanisms in disordered systems, both crystalline and amorphous. Controversy arises in interpreting the resistance minima[1–3]. The increase of ρ(T) below T_{min} was initially attributed to scattering from the structural two-level states ($\approx -ln(T^2 + \Delta^2)$) or from magnetic impurities of the Kondo type ($\approx -lnT$)[4]. However, the validity of either one of the above mechanisms is debatable since they are found in magnetic alloys[3, 1] as well as those without any magnetic

---

[1] This chapter is mainly based on the work by T. K. Nath and A.K. Majumdar, accepted for publication in *Phys. Rev. B* (1997) and *J. Phys.: Condensed Matter* (communicated).

by Howson *et al.*[5, 9–11], Cochrane *et al.*[16], Bieri *et al.*[17], Schulte *et al.*[18], and Hickey *et al* [19] have more or less confirmed the prediction of the theories based on quantum corrections to the Boltzmann transport equations valid for disordered materials[7, 8, 14, 20].

In this particular investigation, we have reported a systematic high -resolution ρ(T) measurements in the temperature range of 1.2 to 300 K in a series of melt-spun non-magnetic transition-metal-based amorphous $(Cu_{0.36}Zr_{0.64})_{1-x}Al_x$ and $(Ni_{0.5}Zr_{0.5})_{1-x}Al_x$ alloy ribbons with $0 \leq x \leq 0.2$. We find that all of them show negative TCR till the highest temperature (300 K) except at very low temperatures where each of them shows a tendency of superconductivity. The primary motivation behind the present work is to check whether the scattering mechanisms in all these highly disordered non-magnetic alloys can be well described by quantum interference effects (QIE), viz, the weak localization and the electron–electron interaction (EEI). Moreover, theoretically[7, 9, 20] it has been predicted that in a strongly disordered system a sequence of $\sqrt{T}$, T , and $\sqrt{T}$ dependence of conductivity (σ) could be observed at low, intermediate and high temperature ranges because of QIE effects. Till now, there is only one report[3] on Co-rich ferromagnetic bulk (3-dimensional) alloys where the full sequence was observed in the *same specimen.* However, since ferromagnetism may destroy localization[7, 14], the interpretation could be erroneous. Moreover, all earlier works on non-magnetic CuTi, CuHf, etc., (for example, M. A. Howson and D. Grieg, *J. Phys. F : Met. Phys.* **16**, 989 (1986)) showed only two regions (either $\sqrt{T}$ and T or T and $\sqrt{T}$) in the same specimen. Agreement with any theory is most satisfactory if predictions are checked on the same specimen. In the present study all the alloys under investigation are non-magnetic having temperature-indepedent Pauli paramagnetism ($\chi \sim 10^{-5}$ - 10^{-6} emu/mol). Also, all of them have a negative TCR in a very wide range of temperature (till 300 K) and provide us an opportunity to observe the full sequence of $\sqrt{T}$, T, and $\sqrt{T}$ of conductivity (σ) in three distinct regions of temperatures.

6.2 Results and Discussions

The temperature dependence of the resistivity (ρ(T)) between 1.2 and 300 K for $(Cu_{0.36}Zr_{0.64})_{1-x}Al_x$ and $(Ni_{0.5}Zr_{0.5})_{1-x}Al_x$ ($0 \leq x \leq 0.2$) non-magnetic metallic glasses is shown in Figs. 6.1 and 6.2, respectively. The composition dependence of ρ_{300K} is shown in the inset of each figure. In Table 6.1 we have listed some useful physical properties of all the alloys under investigation. From a detailed inspection of all the ρ(T) curves, the following salient features emerge :

1. The room–temperature values of the resistivity (ρ_{300K}) for all the alloys are high (> 165 $\mu\Omega$ cm) and they increase with the Al concentration (x) (inset of Figs. 6.1 and 6.2).

2. The TCR of all the alloys are negative for the entire range of temperature which is the signature of the strong–scattering metallic glass alloys[5].

3. In the case of $(Cu_{0.36}Zr_{0.64})_{1-x}Al_x$ metallic glass system ρ(T)/ρ(300K) at 4.2 K lies between 1.02 and 1.045 whereas for $(Ni_{0.5}Zr_{0.5})_{1-x}Al_x$ system it lies between 1.03 and 1.05.

4. The nature of the ρ–T curves of all the alloys are of E-type which is found only in all group(4) d-electron-dominated non-magnetic metallic glasses[1, 15].

5. In each alloy the superconducting fluctuations are already noticeable around 4 K (Figs. 6.3 and 6.4). The superconducting transition temperature (T_c) and its onset are found to decrease with increasing Al concentration.

6.2.1 Superconducting Fluctuations

Figures 6.3 and 6.4 clearly show superconducting fluctuations in $(Cu_{0.36}Zr_{0.64})_{1-x}Al_x$ and $(Ni_{0.5}Zr_{0.5})_{1-x}Al_x$ amorphous alloys below 4 K. We could estimate the T_c's (Table 6.1) for x = 0.0 (for both the systems) from the peak of the dρ/dT vs. T plot as shown in the inset of Fig. 6.3 for $Cu_{0.36}Zr_{0.64}$. The onset of T_c (Table 6.1) for the rest of them could be clearly seen (Figs. 6.3 and 6.4) to decrease with the increase of the Al (x) concentration. But their

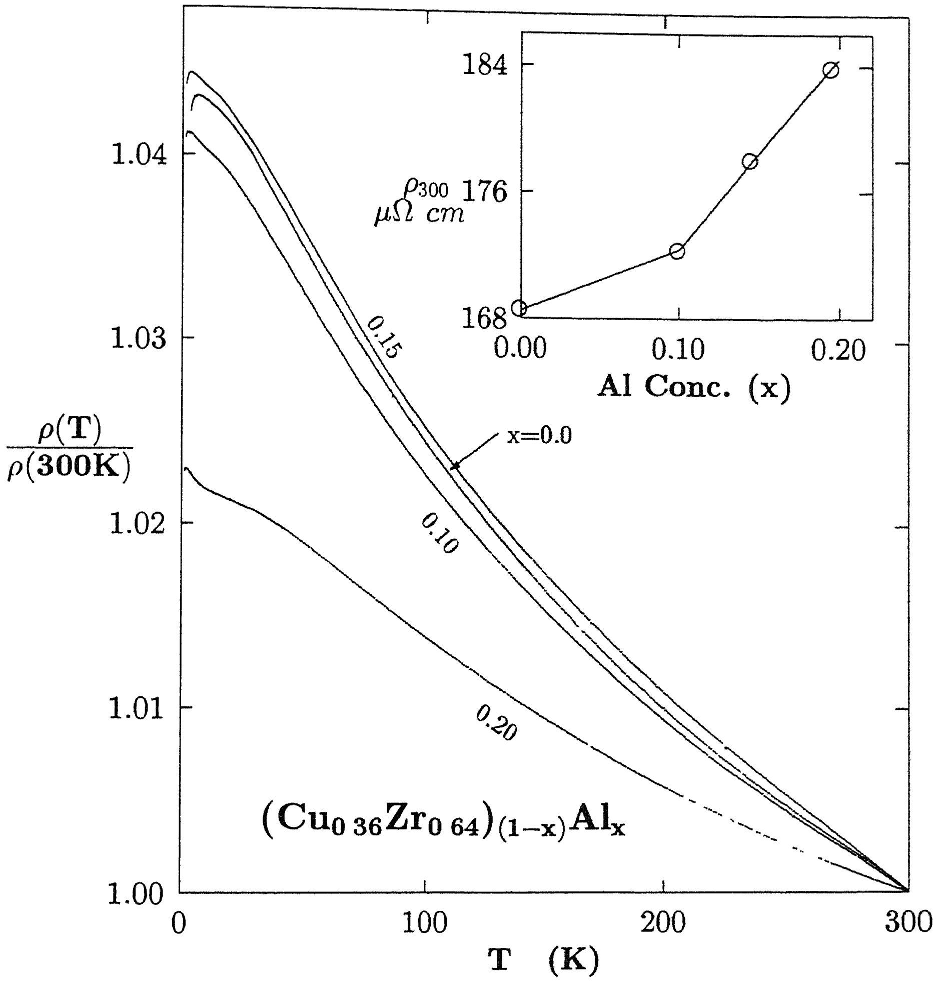

Figure 6.1: Temperature dependence of the normalized electrical resistivity of $(Cu_{0.36}Zr_{0.64})_{1-x}Al_x$ ($0 \leq$ x ≤ 0.2) amorphous ribbons. The resistivity is normalized with respect to that at 300 K. The resistivity at 300 K is shown in the inset as a function of Al concentration.

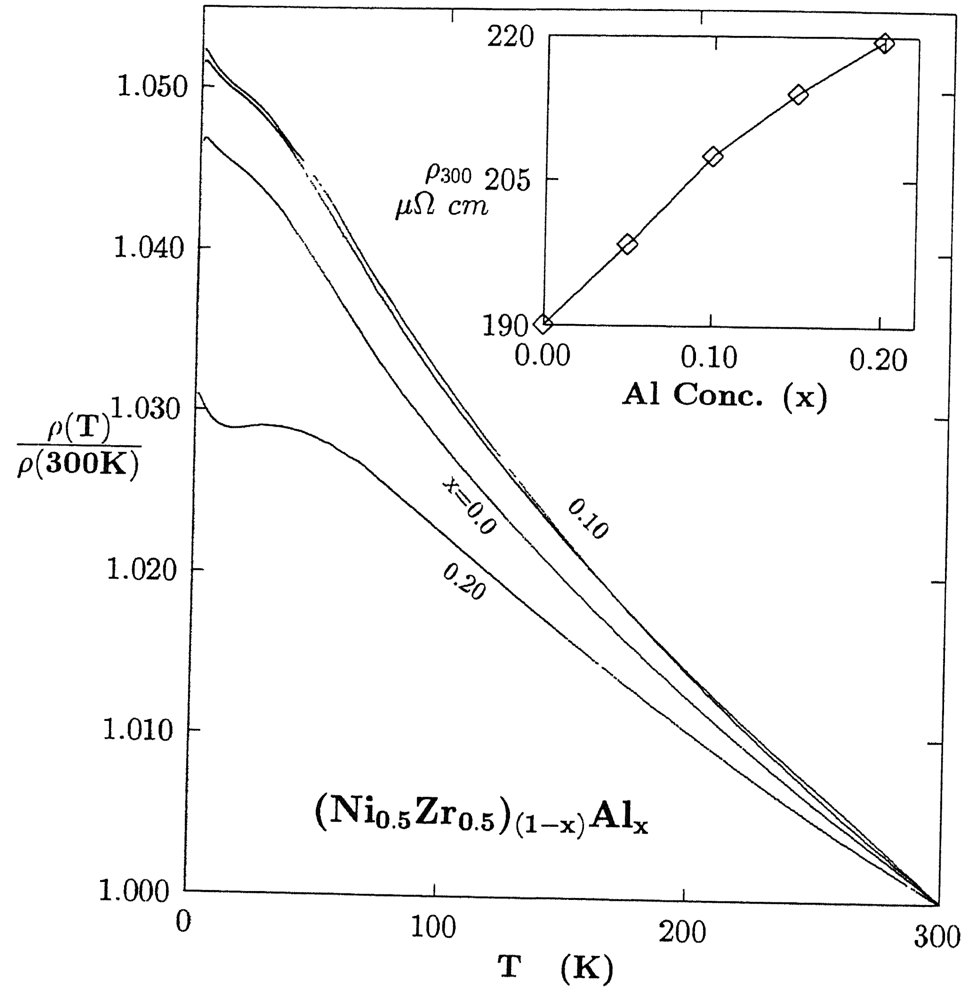

Figure 6.2: Temperature dependence of the normalized electrical resistivity of $(Ni_{0.5}Zr_{0.5})_{1-x}Al_x$ ($0 \le x \le 0.2$) amorphous ribbons. The resistivity is normalized with respect to that at 300 K. The resistivity at 300 K is shown in the inset as a function of Al concentration.

actual T_c's are lower than 1.2 K which is not attainable in our experiments. The transition width (ΔT_c) of these amorphous superconducting alloys is found to be around 0.25 K (Fig. 6.3)

As mentioned earlier, all these amorphous alloys under investigation fall into the strong-scattering regime ($\rho_{300} > 165\ \mu\Omega$ cm) with negative TCR as expected from the Mooij correlation. As a consequence, the only relevant length scale describing the disorder is the electron mean-free path. Mizutani[15] has estimated mean-free path ($l_F \sim$ 3-5 Å) and Fermi velocity ($v_F \sim 0.25 \times 10^8$ cm/sec.) of Cu-Zr-Al and Ni-Zr-Al metallic glasses taking into account the possible contribution of both sp and d electrons. Electron mean-free path (l_F) of these systems are comparable with the avarage atomic distance ($< a >$) leading to the breakdown of the generalized Faber-Ziman theory (within the Boltzmann transport framework). The increase of ρ_{300K} with Al concentration in both the alloy systems may be attributed to the enhancement of the degree of disorder. Generally in the case of strongly disordered systems, as disorder increases, the electronic states near E_F start getting localized, superconductive coherence is destroyed and the system goes insulating[21]. One thus expects an interesting competition between localization (exponentially) and superconductivity. In a large number of intermediate and high-T_c superconductors [A-15 compounds (Nb_3Ge), cluster compounds ($ErRh_4B_4$), layered cuprate oxides ($Bi_2Sr(Er,Gd)_2Ca\ Cu_3O_y$)] strong disorder reduces T_c drastically.

The present transition-metal-based amorphous systems exihibit an extremely dirty type-II superconductivity in an isotropic and highly disordered metallic phase. Typical Ginzburg-Landau parameter κ ($\sim \lambda/\xi$) is > 80 for this kind of d-band amorphous metal alloys (e.g., CuZr, NiZr)[22] and they fall into the type-II regime ($\kappa > 1/\sqrt{2}$). In the "*dirty limit*" ($1/\xi_{BCS} << 1$), for very small free path (l), using Ginzburg-Landau-Abrikosov-Gorkov (GLAG) theory, the product of the BCS coherence length (ξ_{BCS}) and l of the electrons has been estimated in the case of $Cu_{0.35}Zr_{0.65}$[22] to be $\approx 1.64 \times 10^4$ Å^2. Generally, in the case of strongly disordered materials, transport properties are more sensitive to the disorder. In the "*dirty limit*" the penetration depth of the electromagnetic field is increased by $\sqrt{\xi_{BCS}/l_e}$ over its

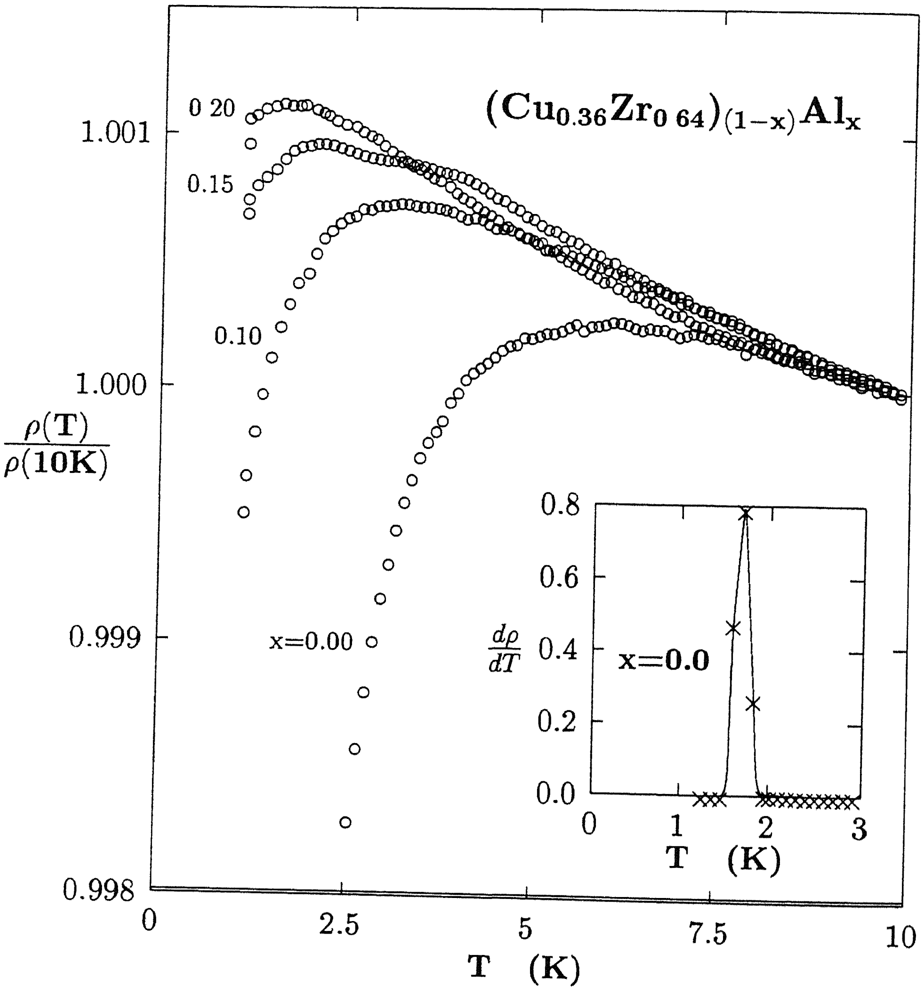

Figure 6.3: Plot of normalized resistance ($\rho(T)/\rho(10K)$) versus T for $(Cu_{0.36}Zr_{0.64})_{1-x}Al_x$ ($0 \leq x \leq 0.2$) amorphous alloys each of which shows onset of superconducting transition. The inset shows $d\rho/dT$ versus T of x=0.0 alloy from which the T_c is estimated to be 1.7 K.

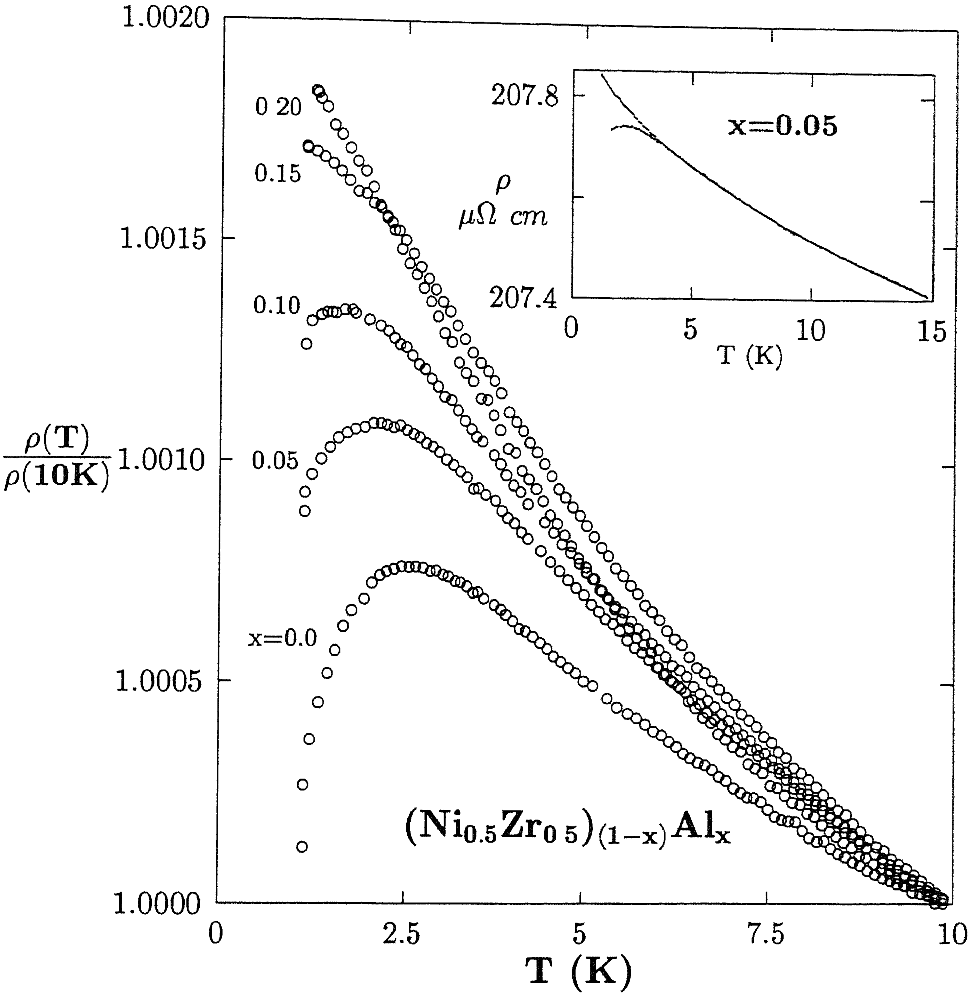

Figure 6 4: Plot of normalized resistance $(\rho(T)/\rho(10K))$ versus T for $(Ni_{0.5}Zr_{0.5})_{1-x}Al_x$ ($0 \leq x \leq 0.2$) amorphous alloys each of which shows onset of superconducting transition. The inset shows excellent fit with *EEI theory* (Eq.(6.3)) for x=0.05 alloy. A strong deviation from the fit is observed below 5 K because of the superconducting fluctuations.

Table 6.1: Values of density, resistivity (ρ_{300}), temperature coefficient of resistance (ρ^{-1} dρ/dT), crystallization temperature ($T_{crystal}$), susceptibility (χ), superconducting transition temperature (T_c), T_c(onset), electron-phonon coupling constant (Λ), Hall coefficient (R_H) and Debye temperature (Θ_D) for $(Cu_{0.36}Zr_{0.64})_{1-x}Al_x$ and $(Ni_{0.5}Zr_{0.5})_{1-x}Al_x$ alloys.

x Al conc	Density ($\frac{gm}{cm^3}$)	ρ_{300} ($\mu\Omega$cm)	$\left(\frac{1}{\rho}\frac{d\rho}{dT}\right)_{300K}$ 10^{-4} (K^{-1})	$T_{crystal}$ (K)	χ 10^{-6} ($\frac{emu}{mole}$)	T_c (K)	T_c(onset) (K)	Λ	R_H 10^{-11} ($\frac{m^3}{C}$)	Θ_D (K)
$(Cu_{0.36}Zr_{0.64})_{1-x}Al_x$										
0.00	6.97[b]	168.5	-1.2	710[f]	94.3[b]	1.7	4.0	0.53	5.3[b]	221±1[f]
0.10	6.75[b]	172.4	-1.1		93.0[b]	<1.2	3.0		5.0[b]	226±1[e]
0.15	6.53[b]	178.5	-1.0		85.1[b]	<1.2	1.9		8.9[b]	
0.20	6.35[b]	184.5	-0.6		80.1[b]	<1.2	1.4		6.8[b]	217±1[e]
$(Ni_{0.5}Zr_{0.5})_{1-x}Al_x$										
0.00	7.46[a]	190.1		772[c]	88.9[b]	1.25	2.53	0.48	-1.2[a]	314±2[d]
0.05	7.37[a]	198.4	-1.2	793[c]	84.8[b]	<1.2	2.13		-1.0[a]	
0.10	7.19[a]	207.5	-1.3	811[c]	79.0[b]	<1.2	1.5		0.0[a]	313±2[d]
0.15	6.83[a]	214.1	-1.2	822[c]	75.0[b]	<1.2	<1.2		0.6[a]	
0.20	6.77[a]	219.5	-0.9	836[c]	71.2[b]	<1.2	<1.2		1.1[a]	346±3[d]

[a] Rhie *et al* Ref. 38.
[b] Rhie *et al* Ref 37
[c] Bhatnagar *et al* Ref 44
[d] Mizutani *et al* Ref 31.
[e] Mizutani *et al* Ref 15
[f] Samwer and Löhneysen Ref. 22.

value in pure system (clean limit). However, in that limit, the Ginzburg–Landau coherence length ξ_{GL} is reduced to

$$\xi_{GL} = 0.85\ [\xi_{BCS}(0)\ l_e]^{1/2} \left(\frac{T_c}{T_c - T}\right)^{1/2}. \tag{6.1}$$

Using the value of $\xi_{BCS}l$ we estimate the GL coherence length from Eq.(6.1) and find ξ_{GL}(T=0) $\approx$ 108 Å in the dirty limit for $(Cu_{0.36}Zr_{0.64})_{1.0}Al_{0.0}$ alloy. Near T_c, the coherence length ξ_{GL} increases tremendously.

The electron – phonon coupling constant Λ in this kind of d-band dominated amorphous Cu-Zr-Al and Ni-Zr-Al alloys can be estimated using the relation $\Lambda = 2\int_0^\infty(\alpha^2F(\omega)d\omega)/\omega$

where F(ω) is the spectral function which describes the density of phonon states, $\alpha^2(\omega)$F(ω) is called the Eliashberg function[23]. The Eliashberg function can be estimated from good tunneling data which are still awaited for these alloys. However, using McMillan's[24] expression for T$_c$, a way to estimate the electron–phonon coupling, Λ, is provided by

$$\Lambda = \frac{1.04 + \mu\ ln(\Theta_D/1.45T_c)}{(1-0.62\mu)ln(\Theta_D/1.45T_c) - 1.04} \quad , \tag{6.2}$$

where μ is the effective Coulomb coupling constant which is set at 0.13 for transition metals. Inserting the values of T$_c$ and Θ_D from Table 6.1 in Eq.(6.2), we have found Λ = 0.48 and 0.53 for $Cu_{0.36}Zr_{0.64}$ and $Ni_{0.5}Zr_{0.5}$ alloys, respectively. With the addition of a simple metal (Al) in both these amorphous systems, T$_c$ and hence Λ reduce drastically. This can be associated with the increase of the degree of disorder. The reduction of T$_c$ with increasing ρ_{300K} can be attributed to the QIE effects[5, 25, 26].

For glassy CuZr and NiZr alloys,[22, 27] the electronic density of states $N_\gamma(E_F)$ is comparable with that of pure crystalline Zr. This implies that $N_\gamma(E_F)$ is mainly dominated by 4d-Zr band in CuZr and NiZr. Using the electron–phonon enhancement factor (1 + Λ), the bare density of states can be written as $N_b(E_F) = N_\gamma(E_F)/(1+\Lambda)$. For glassy CuZr and NiZr systems, $N_b(E_F) \approx 1$ states/(ev atom) for both the spin directions. The value of Λ for these amorphous alloys is found to be very small ($\Lambda < 1$) and is significantly smaller than the value generally observed for simple (non–transition metal) amorphous superconductors ($\Lambda \approx 2$, strong coupling)[28]. The microscopic origin of superconductivity in this transition-metal-based type-II dirty superconductors can be explained through the BCS weak–coupling theory where spin singlet state s-wave (orbital angular momentum ($\mathcal{L} = 0$) pairing (superconducting gap $\Delta \neq 0$) holds, unlike the Heavy Fermions (e.g., UPt_3)[29] and probably the high–T$_c$ cuprate type–II superconductors where non-BCS d-state ($\mathcal{L} = 2$) pairing ($\Delta = 0$) holds[30].

Superconducting fluctuation effects in bulk amorphous superconductors are strongly enhanced by the short electron mean–free path ($l \sim< a >$) as well as the small coherence length whereas in pure crystalline bulk superconductors these fluctuation effects are very small. From Figs. 6.3 and 6.4 it is obvious that in both the amorphous alloy systems the fluctuation region is observed up to several degrees above T$_c$. Superconducting fluctuation study (paraconductivity) using Aslamazov–Larkin (AL) and Maki–Thomson (MT) theories in the presence of QIE effects could be very interesting in this 3-dimensional amorphous superconductors.

6.2.2 Quantum Correction Analysis

(a) Electron–electron interaction effects (T$_c$ $\leq$ T $\leq$ 15 K)

The ρ(T) behaviour of the strong scattering (TCR > 150 $\mu\Omega$-cm) non-magnetic transition-metal-based group(4) amorphous metallic glasses can not be explained[5, 13, 15, 31] through the generalised Faber-Ziman theory within the framework of Boltzmann transport. In this limit of $K_F l \geq 1$, electron mean-free path ($l \sim< a >$) becoming comparable with the interatomic distance raises the possibility of (a) an incipient weak-localization along with (b) enhanced electron–electron interaction. This provides quantum corrections to the Boltzmann conductivity. Howson[9] and Howson and Greig[5, 10, 11] have confirmed the need of quantum corrections to the Boltzmann conductivity in these highly resistive group(4) alloys. In this regime a significant interference between the scattered partial waves takes place as the electrons propagate between two scattering events. In such highly disordered environments, the motion of the conduction electrons becomes diffusive from site to site rather than ballistic (classical trajectory). The wavefunctions are not composed of plane waves but waves multiply scattered from the random potential. The eigenstates of different energies experience the same random potential and so they are correlated in space. The spatial correlation enhances the amplitude of scattering of any two electrons of similar amplitude. In fact, the amplitude becomes singular as the difference between the energies of the two electrons goes to zero[14, 12]. This is the so-called EEI effect. To explain the electron–electron correlation effects two theoretical approaches exist which predict a low-temperature $\sqrt{T}$ variations of conductivity (σ) : a scaling theory and a perturbative one which are valid in the limits of strong and weak scattering, respectively.

In the strong-scattering limit the scaling theory of metal-insulator transition, proposed by McMillan[32], yields for the conductivity on the metallic side of the transition $\sigma(T) = \sigma(0)[1 + (T/\Delta)^{1/2}]$, where Δ denotes the correlation gap in the density of states at E_F. Cochrane and Strom–Olsen[16] deduced a quasi-universal temperature variation of conductivity $\sigma(T) - \sigma(0) = \Delta\sigma(T) = (500 \pm 100)\sqrt{T}(\Omega m)^{-1}$, which is valid for a large number of highly resistive metallic glasses having a wide range of $\sigma(0)$ values.

The perturbative interaction approach[7, 8] considers the modification of the effective Coulomb interaction in the presence of structural disorder. In the lowest order quantum correction this leads to a change in the density of states around the Fermi level, $\delta N(E) \sim \sqrt{E}$. The characteristic temperature dependence of the conductivity $\sigma(T)$, calculated using the Kubo formula and valid for 3-dimensional weak-scattering materials, is given by[7, 8]

$$\Delta(\sigma) \;=\; \sigma(T) - \sigma(0) = \frac{1.3}{\sqrt{2}}\frac{e^2}{4\pi\hbar}\left(\frac{4}{3} - \frac{3}{2}F_\sigma\right)\sqrt{\frac{k_B T}{\hbar D}} = m_\sigma\sqrt{T}\,, \qquad (6.3)$$

where D is the diffusion constant, and F_σ the screening factor for the Coulomb interaction.

Howson[5, 9, 11] and Mott and Kaveh[33] suggested that, while weak localization effect dominates the conductivity above 20 K, at lower temperatures EEI effect is very important for these highly resistive metallic glasses. Later on a number of workers[10, 11, 16, 34] observed a $(-\sqrt{T})$ dependence of resistivity in the low–temperature range in metallic glasses and attributed it to the EEI effects.

Along the same line we have interpreted σ(T) of our alloys in terms of EEI effects in the temperature range $T_c < T < 15$ K. The data for $(Cu_{0.36}Zr_{0.64})_{1-x}Al_x$ alloys could not be fitted at all to Eq.(6.3), viz, $\sigma(T) = \sigma(0) + m_\sigma\sqrt{T}$ except for x = 0.20. However, the data for $(Ni_{0.5}Zr_{0.5})_{1-x}Al_x$ alloys fit the above equation very well. The coefficients of the fits, the values of χ^2 (quality of fit), and the ranges of fit are summarized in Table 6.2. Figure 6.5 and its inset clearly show this low temperature $\sqrt{T}$ dependence of the conductivity of $(Cu_{0.36}Zr_{0.64})_{0.8}Al_{0.2}$ and all the $Ni - Zr - Al$ alloys. The quality of fit ($\chi^2 \sim 10^{-11}$) is extremely good and consistent with the very high experimental resolution. The coefficient of the $\sqrt{T}$ term [$m_\sigma \approx$ (360–460) $(\Omega\ m)^{-1}\ K^{-1/2}$] is in good agreement with the near-universal

Table 6 2: Fit to $\sigma(T) = \sigma_0 + m_\sigma\sqrt{T}$ in the temperature range ($T_c \leq T \leq 15$ K) : Al conc.(x), parameters, χ^{2^b}, range of fit, diffusion constant(D), and density of states at the Fermi level [N(E_F)] for $(Cu_{0\,36}Zr_{0.64})_{1-x}Al_x$ and $(Ni_{0\,5}Zr_{0\,5})_{1-x}Al_x$ alloys.

x Al conc.	σ_0 $(\Omega m)^{-1}$	m_σ $(\Omega m)^{-1}K^{-1/2}$	χ^{2^b} (10^{-10})	Range of T (K)	D 10^{-5} (m²/s)	N(E_F (atom e
$(Cu_{0\,36}Zr_{0.64})_{1-x}Al_x$						
0.20	529262	375	0.3	4–8	5.2	1.10
$(Ni_{0\,5}Zr_{0\,5})_{1-x}Al_x$						
0.00	530079	359	0.2	4–11	5 8	0.95
0.05	480734	366	0.5	4–15	5.5	0.88
0.10	457690	379	0.7	3–15	5.1	0.89
0.15	443267	438	1.0	3–10	3.8	1.18
0.20	441340	459	1.0	2–8	3.5	1.20

$^b\chi^2 = 1/N\sum_{i=1}^{i=N}[Y_i(data) - Y_i(fit)]^2/[Y_i(data)]^2$

value of (500±100) $(\Omega\ m)^{-1}\ K^{-1/2}$. Similiar values have also been obtained by Thummes *et al.*[2] and Das and Majumdar[3] in ferromagnetic metallic glasses.

We have mentioned in the earlier section that both these metallic glass systems have superconducting fluctuations in the low–temperature range and with the addition of Al (x), T_c drops significantly (Figs. 6.3 and 6.4). Superconducting fluctuation in Cu-Zr-Al alloys starts around 10 K (Fig 6.3) and the resulting drops in resistivity (ρ(T)) could very well mask the increase in ρ due to the EEI effects in this low-temperature range. On the other hand, in $(Cu_{0\,36}Zr_{0.64})_{0\,8}Al_{0\,2}$ alloy, T_c is much below 1 K and hence the EEI effect could be observed. In Ni-Zr-Al alloys, as T_c drops significantly with the addition of Al (x), the range of fit also extends to lower temperatures (Table 6.2). The inset of Fig. 6.4 shows how the experimental curve deviates below 4 K from the $\sqrt{T}$ fit because of the superconducting fluctuations. At these low temperatures Cooper pairs start forming and they affect the normal electron–electron interaction in the presence of weak localization.

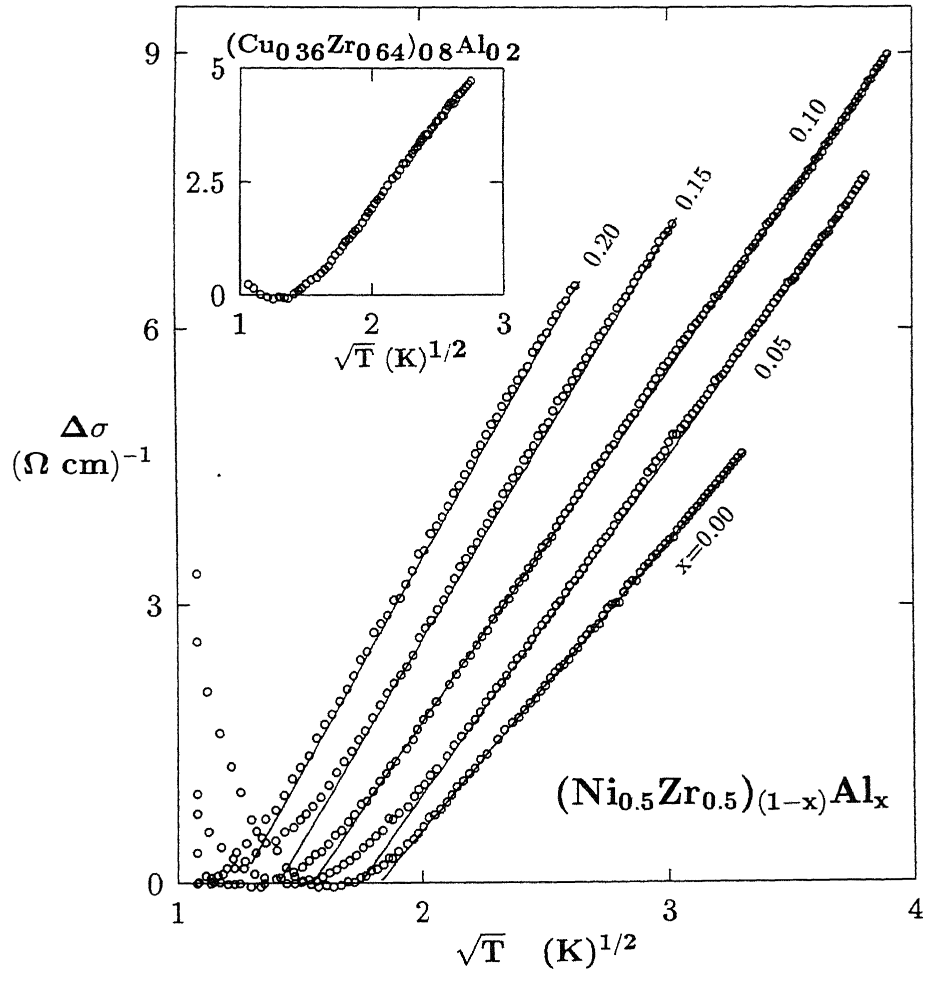

Figure 6.5: Plot of $\Delta\sigma$ vs $\sqrt{T}$ for $(Ni_{0.5}Zr_{0.5})_{1-x}Al_x$ alloys and the best-fitted straight lines (Table 6.2) as predicted by the *EEI theory*. The inset shows the same for $(Cu_{0.36}Zr_{0.64})_{0.8}Al_{0.2}$ alloy.

For all these alloys $K_F l \sim$ 4–5 and so one should expect the screening parameter F_σ in Eq.(6.3) to be negligibly small. The diffusion constant (D), obtained from the slope (m_σ) of σ(T) and Eq.(6 3) keeping $F_\sigma = 0$, is in the range (3.5-5.5) $\times 10^{-5}$ (m^2/s) for all the 6 samples (Table 6 2). It is this D which carries the signature of disorder and we find that $\rho_{300} \propto 1/D$ for our alloys. The values are similar to those obtained by Howson and Greig ($\approx 2.0 \times 10^{-5}$ m^2/s for CuTi, CuZr, and CuHf alloys[10, 11]), Oliver *et al.*[35] ($\approx 3.0 \times 10^{-5}$ m^2/s) and Das and Majumdar[3] ($\approx$ (0.4-4.0) $\times 10^{-5}$ m^2/s). Consequently, the value of the density of states ($N(E_F)$), calculated using Einstein relation $D = [\rho(0)\ e^2\ N(E_F)]^{-1}$, is about 1.0 (atom-ev)$^{-1}$ (Table 6.2) for all the 6 alloys. This value is in excellent agreement with those found in CuZr and NiZr non-magnetic metallic glasses[22, 27] after taking into account the electron-phonon mass enhancement factor ($1+\Lambda$), where we used $\Lambda = 0.5$, as found in the previous subsection

All these results lead to the conclusion that the measured slope (m_σ) of the $\sqrt{T}$ dependence of σ(T) can be very well explained in terms of the electron–electron interaction (EEI) theory. This provides the most significant correction to the Boltzmann conductivity in these NiZrAl and CuZrAl alloys at lower temperatures.

(b) Quantum interference effect (20 K $\leq$ T $\leq$ 300 K)

Tsuei[36] suggested that in strongly disordered crystalline and amorphous alloys the electron localization plays a significant role in determining the sign and magnitude of the TCR at temperatures even as high as the room temperature. Here the mean-free path of the conduction electrons is of the order of average interatomic spacing ($l \sim < a >$) and the electron motions become diffusive. This results in a mutual interference between waves elastically scattered from nearby ions and leads to a phase coherence between the scattered partial waves. As a consequence, the probability for an electron to return to its origin is enhanced which implies a tendency of localization. In Fig. 6.6(a) diffusive paths of two counter propagating partial waves of a conduction electron under the influence of elastic scattering from ions have been shown.

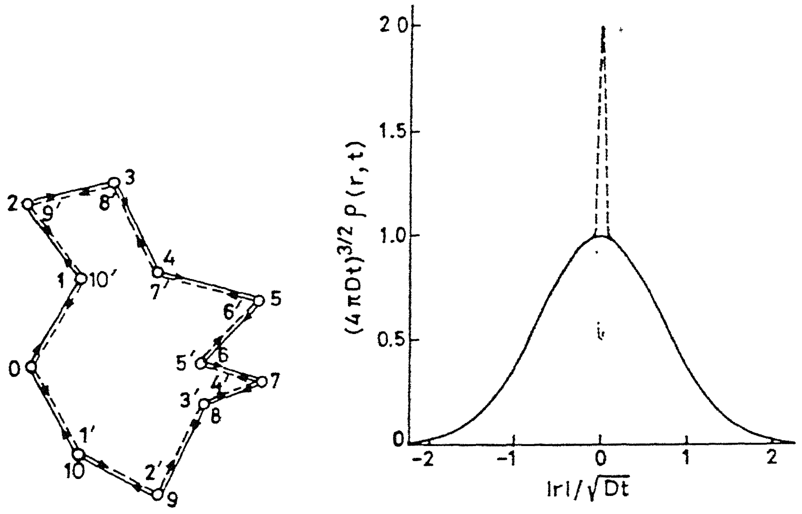

Figure 6.6: (a) Diffusive paths of a conduction electron in a disordered system. The electron with two time reversal partial waves propagates in both directions (full and dashed lines). (b) The classical probability distribution of a diffusing electron (full curve) which starts at r=0 at time t=0. In quantum diffusion (dashed peak) it is twice whereas in the presence of large spin-orbit scattering (dot peak) it becomes half of the classical case.

The probability distribution of a diffusing electron which starts at r=0 at time t=0 is shown in Fig. 6.6(b). In quantum diffusion (dashed peak) the probability to return to the origin is twice as great as in classical diffusion (full curve). Large spin-orbit scattering reduces the probability by a factor of two (dotted peak) and yields a weak antilocalization. Altshuler and Aronov[8], Lee and Ramakrishnan[7], and Dugdale[14] have given detailed theoretical and physical interpretations of weak-localization and EEI effects. Generally, two processes, namely, temperature-dependent inelastic scattering and presence of magnetic field can destroy the phase coherence and reduce the additional resistivity, contributed by the quantum correction to the Boltzmann transport.

Using the scaling approach of Abraham *et al.*[20] to localization and further simplification by Howson[9], the correction to the Boltzmann conductivity is given by

$$\Delta\sigma(T) = \frac{e^2}{\pi^2\hbar}\,\frac{1}{L_\imath(T)}\,, \tag{6.4}$$

where L_i is the inelastic diffusion length $L_i^2(T) = \frac{1}{2}l_e l_i(T)$, where l_e and l_i are elastic and inelastic mean-free paths. This was shown[9] to lead to temperature dependence in amorphous alloys of forms

$$\Delta\sigma \propto T \,, \qquad \Theta_D/10 < T < \Theta_D/3 \tag{6.5}$$

and

$$\Delta\sigma \propto \sqrt{T} \,, \qquad \Theta_D/3 < T < \Theta_D \,. \tag{6.6}$$

It is interesting to note that the localization correction to the conductivity (Eqs.(6.5) and (6.6)) appears to describe adequately the temperature dependence from 20 K to 300 K in a number of non–magnetic transition metal based alloys[11, 9, 5], e.g., $Cu_{50}Ti_{50}$, $Cu_{50}Zr_{50}$, $Cu_{50}Hf_{50}$, $Ti_{50}Be_{40}Zr_{10}$, etc. At higher temperatures, other possible contributions which need to be considered (e.g., phonon assisted tunneling, broadening of Fermi surface, thermal expansion effect, etc.) were ruled out in those alloys. Moreover, there are some recent reports on magnetic amorphous alloys[2, 3] where the localization effect could be detected even till 300 K and Eqs.(6.5) and (6.6) could successfully reproduce the experimental data in intermediate and high temperature ranges. As mentioned earlier, none of our alloys show resistivity minimum till 300 K and they have negligibly small Pauli paramagnetic susceptibility (10^{-6} emu/mol)[37, 38] (Table 6.1).

The Debye temperature (Θ_D) of all these alloys are in the range of 250 - 350 K (Table 6.1). The region roughly between $\Theta_D/10$ and $\Theta_D/3$ clearly shows a linear temperature dependence of σ(T) as given in Eq.(6.5) for all the alloys. Figures 6.7 and 6.8 show this linear dependence for *CuZrAl* and *NiZrAl* alloys, respectively. In Table 6.3 all the fitting parameters, the values of χ^2, and the ranges of fit are given. The values of χ^2 are consistent with the experimental resolution indicating excellent quality of fit. In the region between $\Theta_D/3$ and Θ_D, a $\sqrt{T}$ behaviour, as given by Eq.(6.6) is found for all these alloys. Figures 6.9 and 6.10 clearly show the $\sqrt{T}$ dependence for *CuZrAl* and *NiZrAl*, respectively and Table 6.3 gives the relevant parameters. In this regime as well the fits are excellent ($\chi^2 \approx 10^{-10}$). The values of $\sigma(0)$

Table 6.3: Fit in the temperature ranges $\Theta_D/10 \leq T \leq \Theta_D/3$ and $\Theta_D/3 \leq T \leq \Theta_D$: Al conc.(x), parameters, χ^2, range of fit, inelastic mean–free path (l_i), equations used, and inelastic relaxation time (τ_i) for $(Cu_{0.36}Zr_{0.64})_{1-x}Al_x$ and $(Ni_{0.5}Zr_{0.5})_{1-x}Al_x$ alloys.

x Al Conc	σ_0 $(\Omega m)^{-1}$	m'_σ $(\Omega m)^{-1}K^{-1}$ or $(\Omega m)^{-1}K^{-1/2}$	χ^2 (10^{-10})	Range of T (K)	l_i $10^{-4}(mT^{-2})$ or $10^{-6}(mT^{-1})$	Fit of σ to	τ_i $(10^{10}T^2)^{-1}$ s or $(10^{13}T)^{-1}$ s
$(Cu_{0.36}Zr_{0.64})_{1-x}Al_x$							
0.0	566961	129	0.3	30-60	2.4	$\sigma_0 + m'_\sigma T$	
	558871	2037	4.7	70-180	0.9	$\sigma_0 + m'_\sigma \sqrt{T}$	
0.10	554037	123	3.9	30-80	2.7	$\sigma_0 + m'_\sigma T$	
	546654	1932	6.4	100-220	1.1	$\sigma_0 + m'_\sigma \sqrt{T}$	
0.15	536881	113	3.9	28-70	3.1	$\sigma_0 + m'_\sigma T$	
	529941	1779	7.4	80-170	1.3	$\sigma_0 + m'_\sigma \sqrt{T}$	
0.20	530127	29.6	2.4	11-28	4.1	$\sigma_0 + m'_\sigma T$	32.8
	524253	1036	6.4	75-230	3.8	$\sigma_0 + m'_\sigma \sqrt{T}$	26.7
$(Ni_{0.5}Zr_{0.5})_{1-x}Al_x$							
0.00	529617	112	1.7	30-75	3.2	$\sigma_0 + m'_\sigma T$	2.1
	522612	1741	8.4	105-250	1.3	$\sigma_0 + m'_\sigma \sqrt{T}$	8.7
0.05	479911	108	1.3	35-70	3.5	$\sigma_0 + m'_\sigma T$	2.4
	471749	1838	9.1	100-250	1.2	$\sigma_0 + m'_\sigma \sqrt{T}$	8.1
0.10	456949	106	8.9	40-80	3.6	$\sigma_0 + m'_\sigma T$	2.6
	447619	1954	4.3	120-250	1.1	$\sigma_0 + m'_\sigma \sqrt{T}$	7.7
0.15	443280	87.8	3.7	25-50	5.2	$\sigma_0 + m'_\sigma T$	5.1
	432921	1967	4.1	100-300	1.0	$\sigma_0 + m'_\sigma \sqrt{T}$	10.1
0.20	440091	54.8	1.2	80-140	13.4	$\sigma_0 + m'_\sigma T$	14.3
	430475	1448	9.4	150-300	1.9	$\sigma_0 + m'_\sigma \sqrt{T}$	20.5

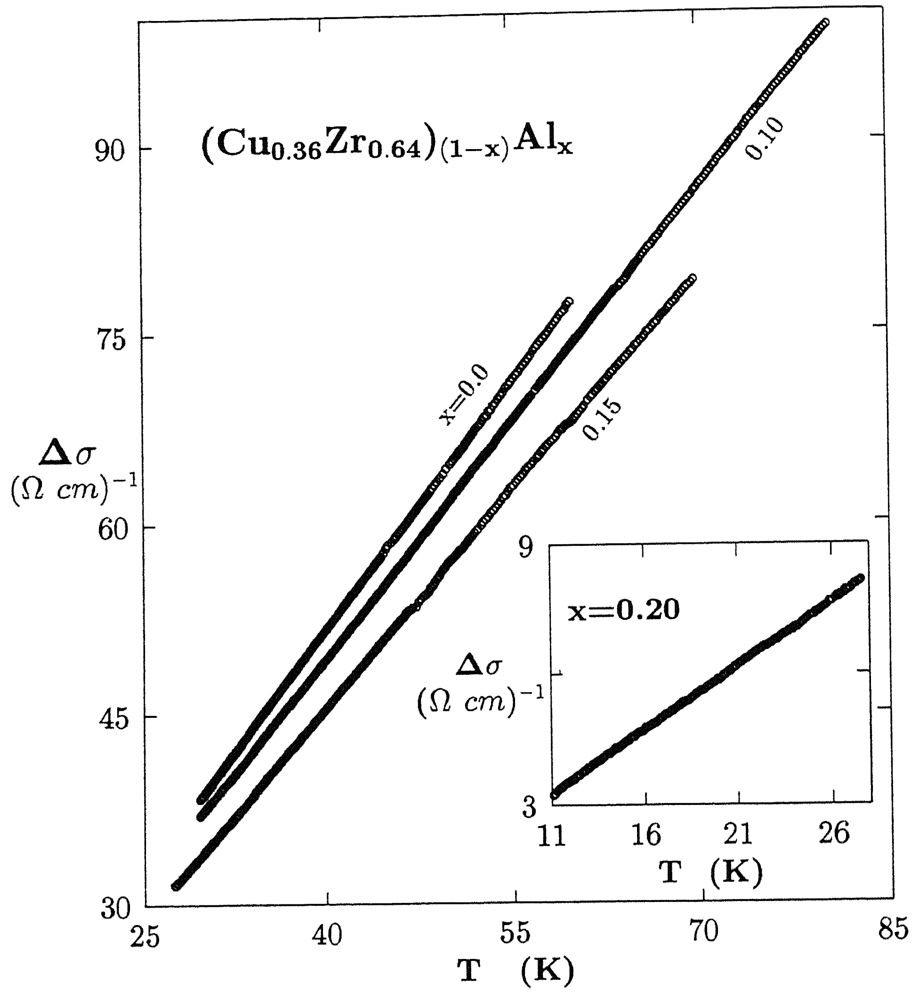

Figure 6.7: Linear dependence of $\Delta\sigma$ on T in the intermediate range (Table 6.3) for $(Cu_{0.36}Zr_{0.64})_{1-x}Al_x$ amorphous alloys as predicted by the localization theory.

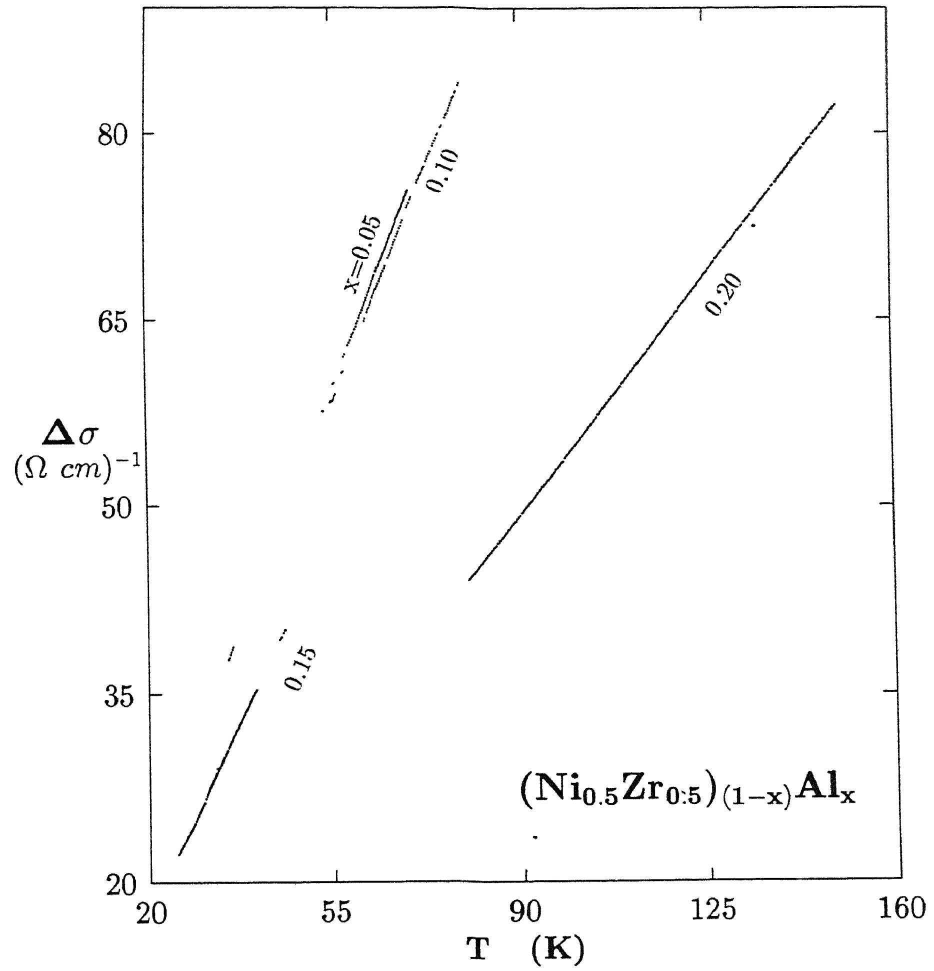

Figure 6.8: Linear dependence of $\Delta\sigma$ on T in the intermediate range (Table 6.3) for $(Ni_{0.5}Zr_{0.5})_{1-x}Al_x$ amorphous alloys as predicted by the localization theory.

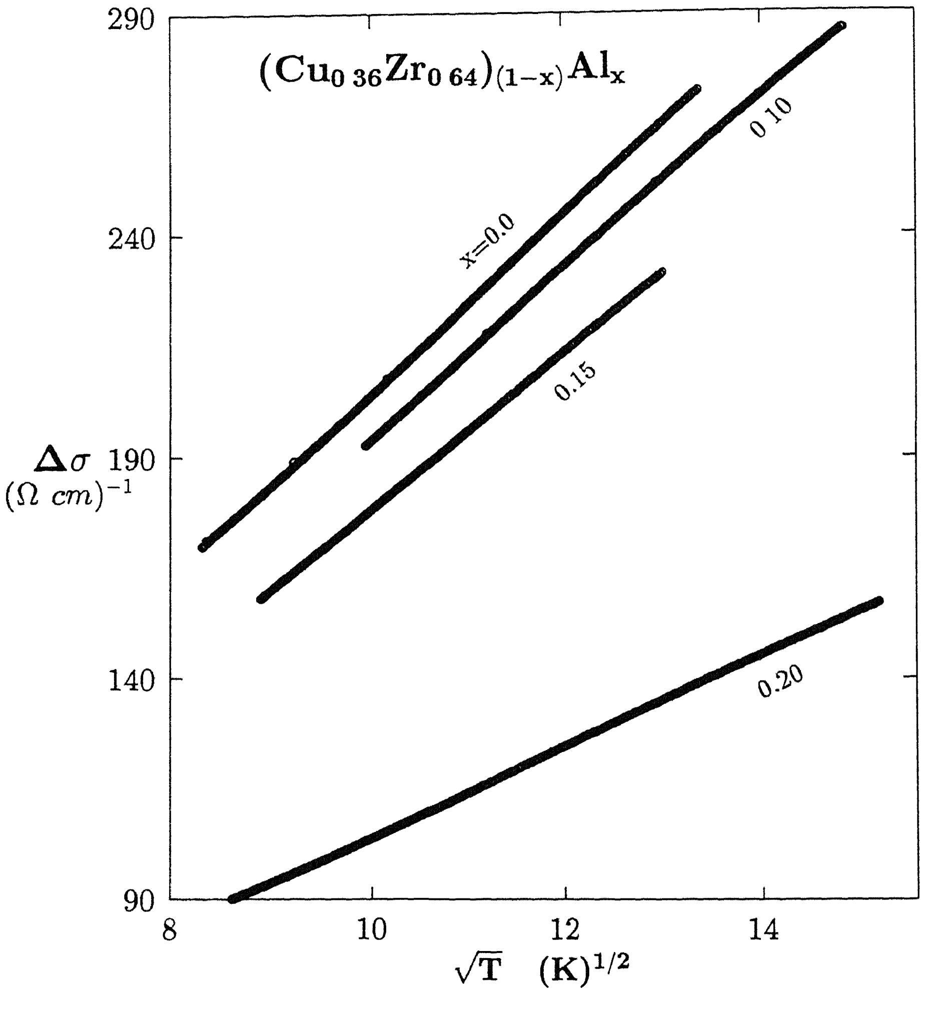

Figure 6.9: Linear dependence of $\Delta\sigma$ on $\sqrt{T}$ in the high-temperature range (Table 6.3) for $(Cu_{0.36}Zr_{0.64})_{1-x}Al_x$ amorphous alloys as predicted by the localization theory.

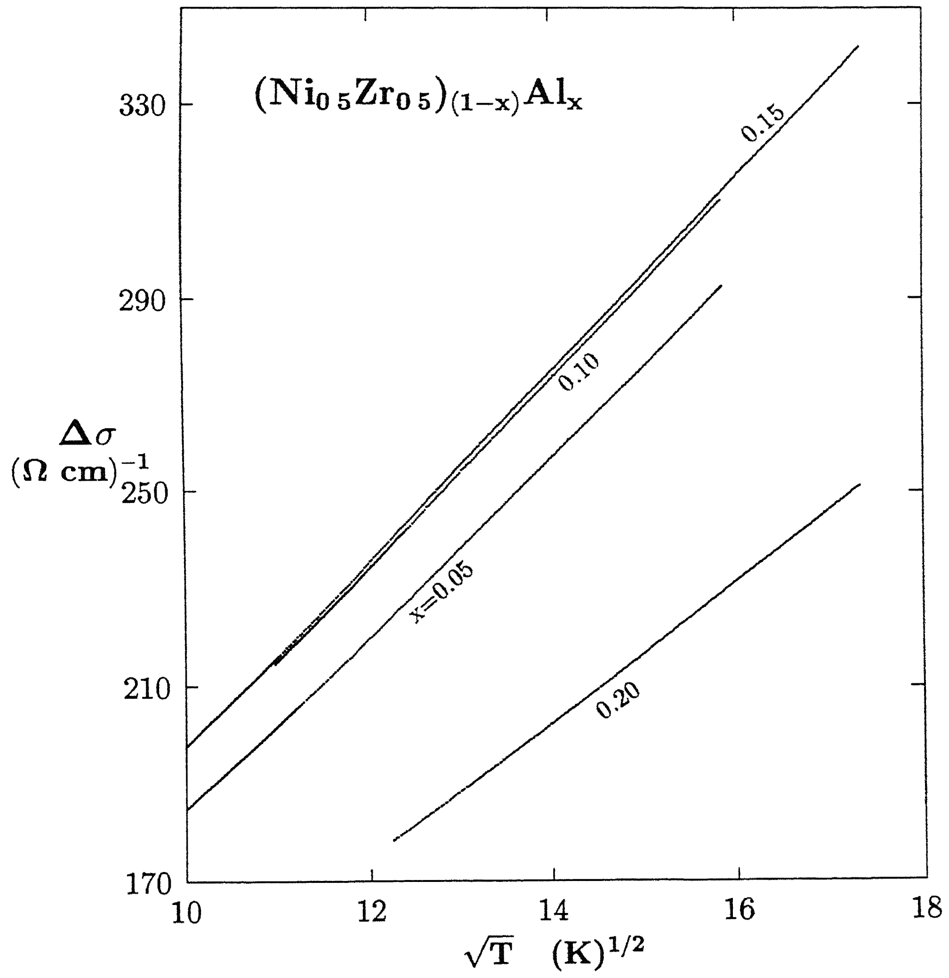

Figure 6.10: Linear dependence of $\Delta\sigma$ on $\sqrt{T}$ in the high-temperature range (Table 6.3) for $(Ni_{0.5}Zr_{0.5})_{1-x}Al_x$ amorphous alloys as predicted by the localization theory.

[which is the extrapolated value of σ at T = 0 K] are not exactly the same (Tables 6.2 and 6.3). This kind of behaviour of $\sigma(0)$ was also obtained by Howson and Greig[9] for non-magnetic transition–metal–based alloys where the temperature dependence in the two distinct temperature regions does not extrapolate to the same value of $\sigma(0)$. Das and Majumdar[3] also found different values of $\sigma(0)$ from extrapolations of three distinct regions in the case of Co-rich ferromagenetic metallic glasses. The reason for this is not clear. However, in our case the variation in $\sigma(0)$ does not in any way influence the analysis. In Figs. 6.11 and 6.12 we have shown separately the three distinct regions of ($\sqrt{T}$/T/$\sqrt{T}$) on the same log-log plot for $(Cu_{0.36}Zr_{0.64})_{1-x}Al_x$ and $(Ni_{0.5}Zr_{0.5})_{1-x}Al_x$ alloys, respectively as predicted by weak localization and EEI effects. The parallelism of the lines is rather striking. In Figs. 6.11 and 6.12 the transitions region (in temperature) are intentionally left out. The plots are shown only in those temperature regions where $\sqrt{T}, T$, and $\sqrt{T}$ dependences are found through non-linear least-squares fit (the regions are specified in Table 6.2 and 6.3). Thus the plots for each sample look discontinuous.

Taking the elastic mean-free path length (l_e) $\sim$ 3 Å, which is of the same order as the interatomic spacing for all our alloys[15], we obtain (shown in Table 6.3) from Eq.(6.4) and the slope of the σ(T) curves, the inelastic mean-free path length l_i(T) = (2.4-3.1) × 10^{-4} T^{-2} (m) for the CuZrAl and (3.5-13.4) × 10^{-4} T^{-2} (m) for the NiZrAl alloys in the temperature range $\Theta_D/10 < T < \Theta_D/3$. In the region $\Theta_D/3 < T < \Theta_D$, the same l_i(T) = (0.9-3.8) × 10^{-6} T^{-1} (m) for the CuZrAl and (1.0-1.9) × 10^{-6} T^{-1} (m) for the NiZrAl alloys. All these values are very much similar to those of 7.7 × 10^{-4} T^{-2} (m) for $T \leq \Theta_D/3$ and 1.8 × 10^{-6} T^{-1} (m) for $T > \Theta_D/3$ reported in the case of non-magnetic transition–metal–based alloys[9]. Above Θ_D there is a significant departure from both T and $\sqrt{T}$ behaviour for all the alloys.

To interpret the quantum interference in the presence of structural disorder (weak localization), several theories[7, 8] predict the lowest order quantum correction to the Boltzmann conductivity of a 3-dimensional disordered system in zero magnetic field as

$$\Delta\sigma_L = \frac{e^2}{2\pi^2\hbar}\,(D\tau_i)^{-1/2}\,, \qquad (6.7)$$

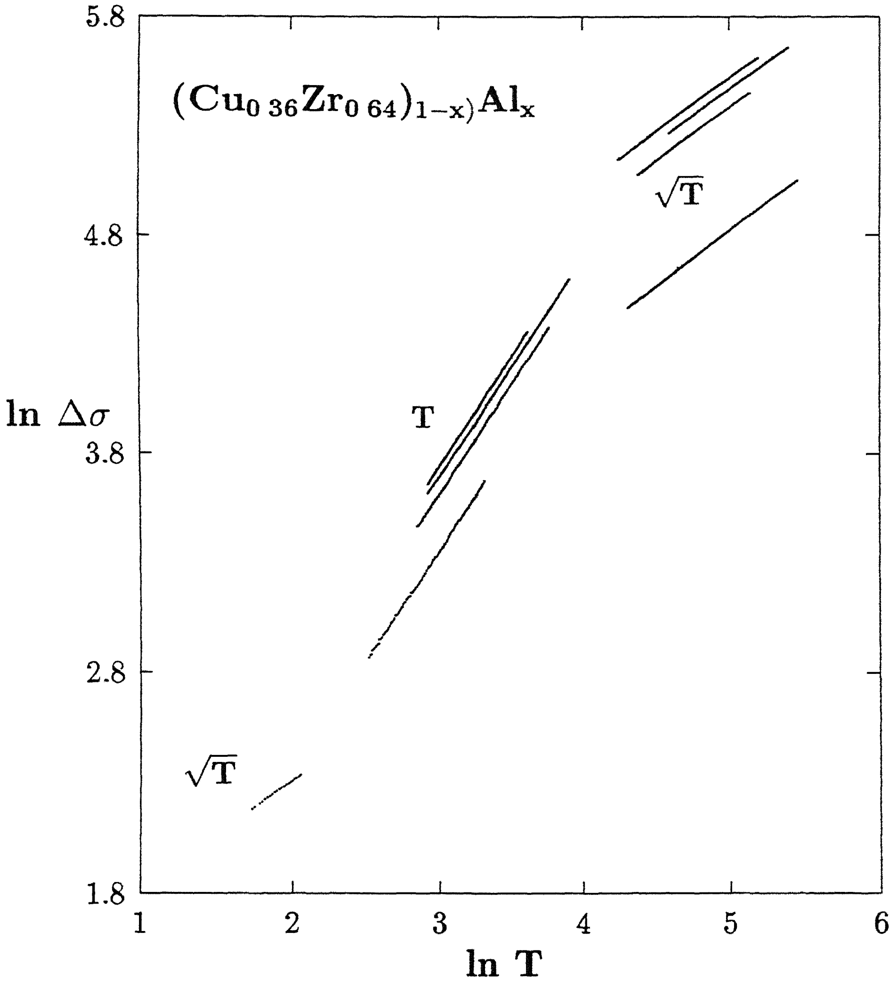

Figure 6.11: Plot of ln($\Delta\sigma$) vs ln T for $(Cu_{0.36}Zr_{0.64})_{1-x}Al_x$ amorphous alloys depicting three distinct regions of $\sqrt{T}$, T and $\sqrt{T}$ dependence in agreement with QIE.

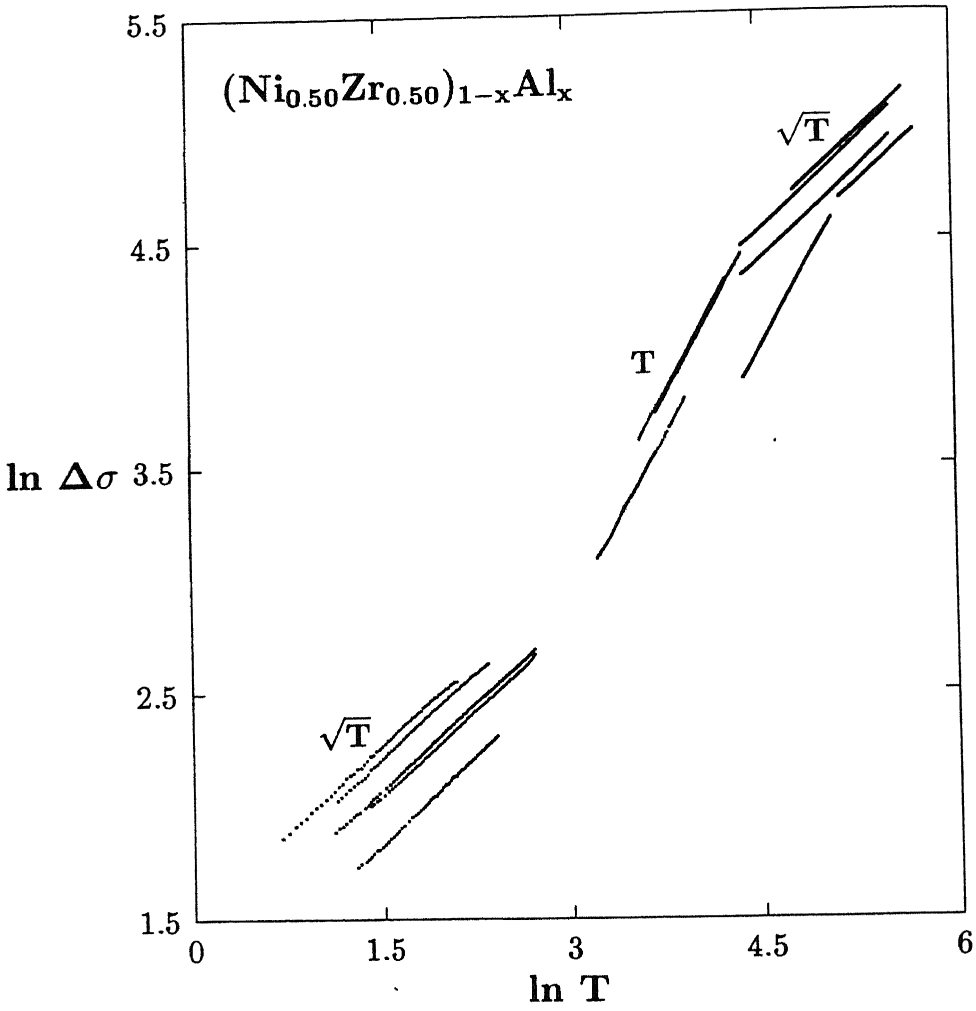

Figure 6.12: Plot of ln(Δσ) vs ln T for $(Ni_{0.5}Zr_{0.5})_{1-x}Al_x$ amorphous alloys depicting three distinct regions of $\sqrt{T}$, T and $\sqrt{T}$ dependence in agreement with QIE. Only raw data are shown in Figs. 6.7-6.12.

where τ_i is the inelastic scattering time. Poon *et al* [39] have shown that the τ_i^{-1} increases with T^2 in the low-temperature range. We have estimated the inelsatic scattering time in our alloys in the two distinct temperature regimes using Eqns. (6.5), (6.6) and (6.7) and the values of D found from the low-temperature range (Table 6.2). Table 6.3 lists all the values of τ_i which are $(2.3\text{-}14.3) \times 10^{-10}\ T^{-2}$ (s) for $T < \Theta_D/3$ and $(7.7\text{-}20.5) \times 10^{-13} T^{-1}$ (s) for $T > \Theta_D/3$. Many experimental investigators[14, 39] found τ_i of the order of $2.0 \times 10^{-10}\ T^{-2}$ (s) in CuZr, CuHf, and CuTi systems in the low-temperature range. These values agree quite well with our estimated values. Generally the elastic scattering time (τ_0) is of the order of ($\sim 10^{-15}$–10^{-16}) s in these highly resistive alloys. This is much smaller than the inelastic scattering time ($\tau \sim (10^{-12}$–$10^{-14})$ s) even in the higher temperature range which strongly suggests the finite probability of electron localization in our alloys.

As mentioned earlier, in all group(4) non-magnetic transition–metal–based alloys the Fermi level (E_F) lies in the d-band. Photoemission spectroscopy measurements coupled with band structure calculations in CuTi, NiZr, and CuZr metallic glasses revealed that the valence band is split into two peaks, one near E_F dominated by the 4d-states of the early transition metal and the other one at higher binding energy[40]. Mizutani suggested[15, 41] that in all group(4) non-magnetic metallic glasses the behaviour of $\rho(T)$ between 30 K and 300 K could be described by the empirical relation

$$\frac{\rho}{\rho_{300}} = A + B\, exp\left(-\frac{T}{\Delta}\right), \tag{6.8}$$

where A, B and Δ are fitting parameters and ρ_{300} is the resistivity at 300 K. Mizutani[15] has found that the characteristic temperature Δ in Eq.(6.8) is strongly correlated with the Debye temperature (Θ_D), and an increase in Θ_D leads to an increase in Δ. Along the same line we have also examined whether the above empirical relation can describe the present data. In Table 6.4 we have summarized all the fitting parameters, the values of χ^2, and the range of fit. Figures 6.13 and 6.14 show the fitted curves along with the experimental data for *CuZrAl* and *NiZrAl* alloys, respectively. It is quite clear that Eq.(6.8) fails to explain the data below

Table 6.4: Parameters A, B, and Δ, obtained from the fit to Eq.(6.8), χ^2, range of fit for $(Cu_{0.36}Zr_{0.64})_{1-x}Al_x$ and $(Ni_{0.5}Zr_{0.5})_{1-x}Al_x$ alloys.

x (Al conc.)	A	B	Δ (K)	χ^2 (10^{-8})	Range (K)
$(Cu_{0.36}Zr_{0.64})_{1-x}Al_x$					
0.0	0.985	0.0630	218	0.8	30–300
0.10	0.983	0.0654	232	3.6	30–300
0.15	0.986	0.0585	217	1.6	30–300
0.20	0.986	0.0391	290	0.4	30–300
$(Ni_{0.5}Zr_{0.5})_{1-x}Al_x$					
0.0	0.971	0.0812	327	2.1	45–300
0.05	0.965	0.0839	344	2.2	50–300
0.10	0.963	0.0922	336	2.8	30–300
0.15	0.961	0.0951	338	0.6	40–300
0.20	0.938	0.0990	645	0.9	100–300

$\simeq$ 40 K. Table 6.4 shows that Δ is typically of the same order as the Debye temperature (Θ_D) of the alloys.

It was believed[42] that the coefficient B is a better parameter for expressing the overall change in resistivity compared to the TCR at 300 K. We find that the fit to each curve (Figs. 6.13 and 6.14) is at least one to two orders of magnitude poorer ($\chi^2 \sim 10^{-8}$-10^{-9}) compared to our experimental resolution as well as that for the quantum correction analysis.

Recently Bhatnagar *et al.*[43] also could not fit the ρ(T) data of some non-magnetic transition–metal–based metallic glasses with the same empirical Eq.(6.8). In addition, they could not find even unique values of the fitting parameters A, B and Δ. However, they could successfully interpret their data in terms of QIE. Moreover, to the best of our knowledge, so far there is no physical or theoretical justification of this empirical exponential law.

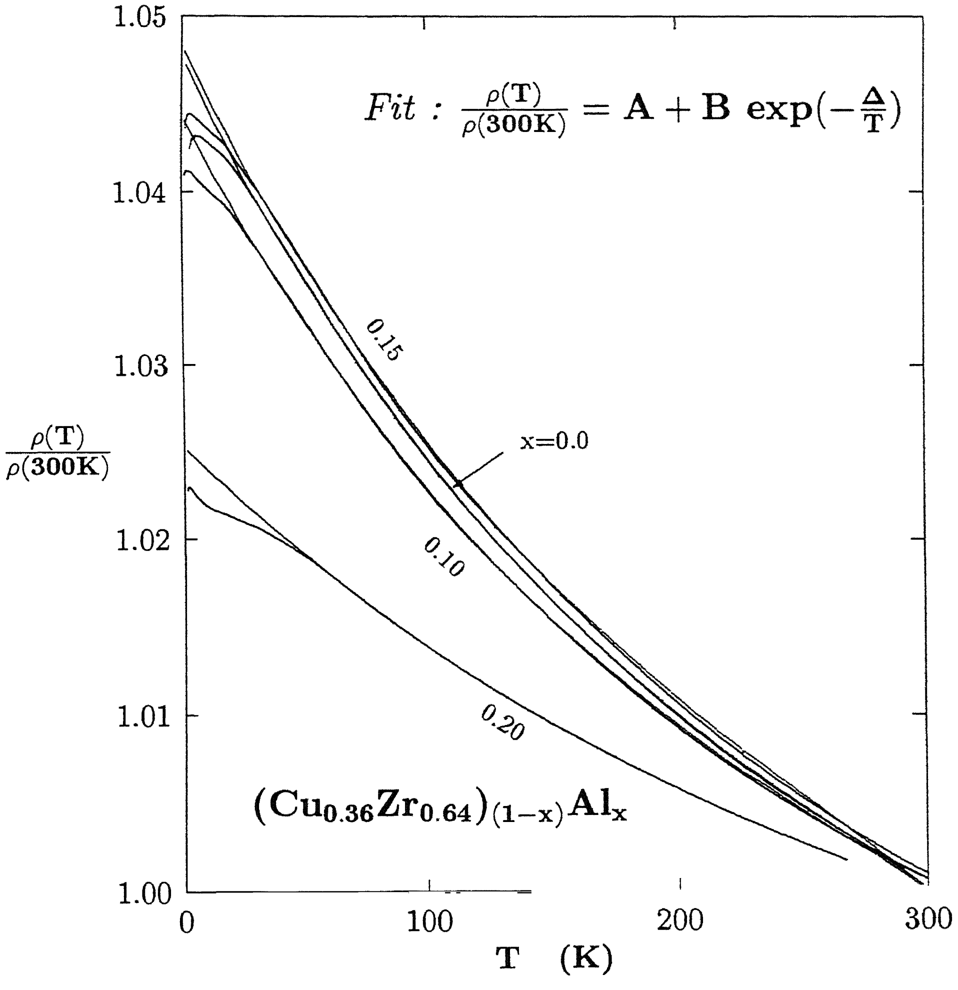

Figure 6.13: Plots of the normalized resistivity ($\rho(T)/\rho(300K)$) and the fit to Eq.(6.8) as a function of T for $(Cu_{0.36}Zr_{0.64})_{1-x}Al_x$ amorphous alloys.

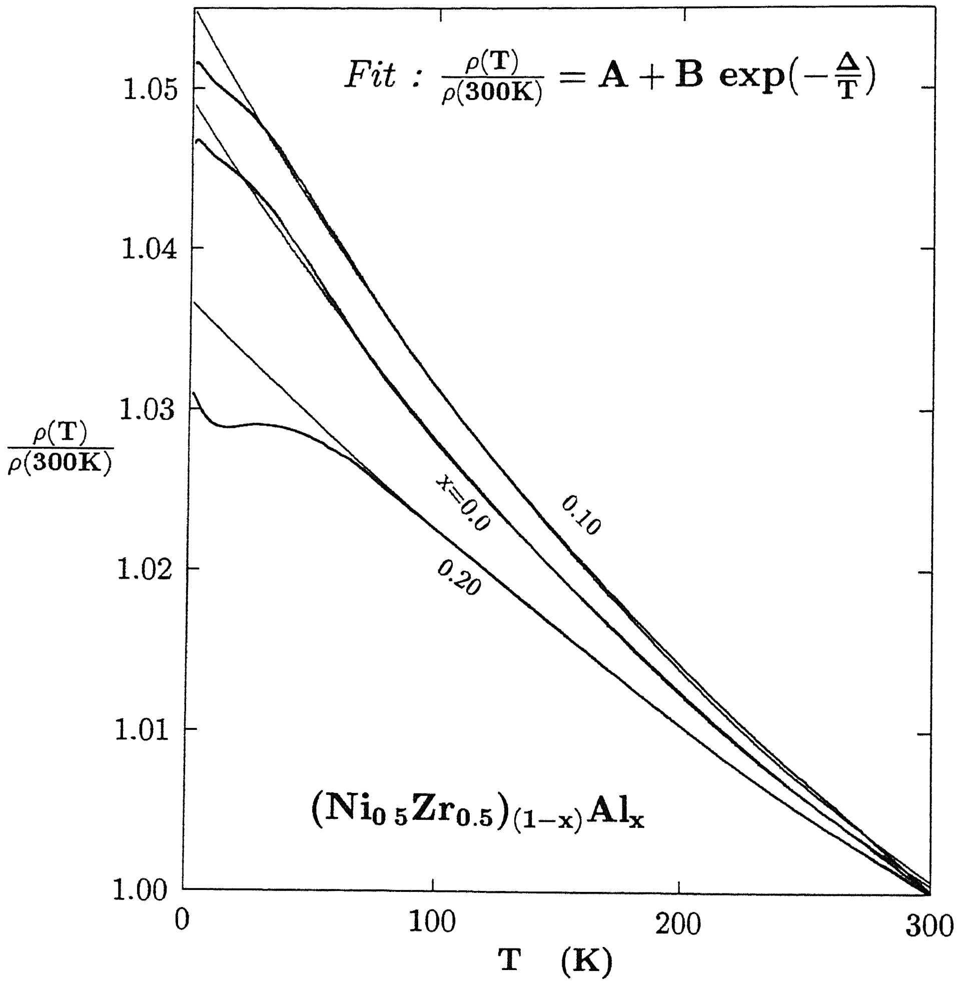

Figure 6.14: Plots of the normalized resistivity ($\rho(T)/\rho(300K)$) and the fit to Eq.(6.8) as a function of T for $(Ni_{0.5}Zr_{0.5})_{1-x}Al_x$ amorphous alloys.

So we conclude that the weak localization and the electron-elecrton interaction theories give a much better and consistent description of the present ρ(T) data.

6.2.3 Thermoelectric Power

The thermoelectric power (S), which is essentially the entropy per unit charge transported by an electric current, is small, positive and of the order of μV/K in all our alloys at 300 K. In Fig. 6.15 we have shown the variation of S/T for both $(Cu_{0.36}Zr_{0.64})_{1-x}Al_x$ (shown as curve a) and $(Ni_{0.5}Zr_{0.5})_{1-x}Al_x$ (curve b) alloys with Al concentration (x). Initially, it increases with x, attains a maximum around x = 0.1 and then it decreases. This is very similar to the result reported by Mizutani[31] on Ni–rich ($\mathrm{Ni_{0.67}Zr_{0.33}Al_x}$) alloys (Fig. 6.15, curve c) where they found a peak at x = 0.3. However, in the case of Zr–rich $(\mathrm{Zr_{0.64}Ni_{0.36}})_{1-x}\mathrm{Al}_x$, S/T continuosly decreases with x as reported by Bhatnagar *et al.*[43] (Fig. 6.15, curve d). So, we infer that the peak shifts towards the lower concentration of Al (x) as the alloys pass from the Ni-rich side to the Zr-rich side. In a simple naive approach, ignoring any s-d hybridization contribition, we have made an attempt to find a qualitative explanation of the variation of S/T with Al concentration (x). Applying Mott's s-d scattering model the expression for S/T is given by

$$\frac{S}{T} = \frac{\pi^2 k_B^2}{3\,|\,e\,|}\left[-\frac{3}{2\epsilon_F} + \frac{1}{N_d}\frac{\partial N_d}{\partial \epsilon}\bigg|_{\epsilon=\epsilon_F}\right]T, \tag{6.9}$$

where N_d is the d-band density of states and ϵ_F the Fermi energy. We believe that the density of states at ϵ_F in $\mathrm{Cu_{0.36}Zr_{0.64}}$ and $\mathrm{Ni_{0.5}Zr_{0.5}}$ is dominated by the Zr–4d states and the addition of Al reduces both Cu and Zr, and Ni and Zr concentration in the two systems. From the XPS spectra[31] the same conclusion could be drawn. The typical behaviour of S/T with x in our alloys mainly depends on the relative change of the two terms in Eq.(6.9), namely, the negative term due to the free electron (s-electron) contribution and the positive term due to the variation of the d-band density of states at the Fermi level.

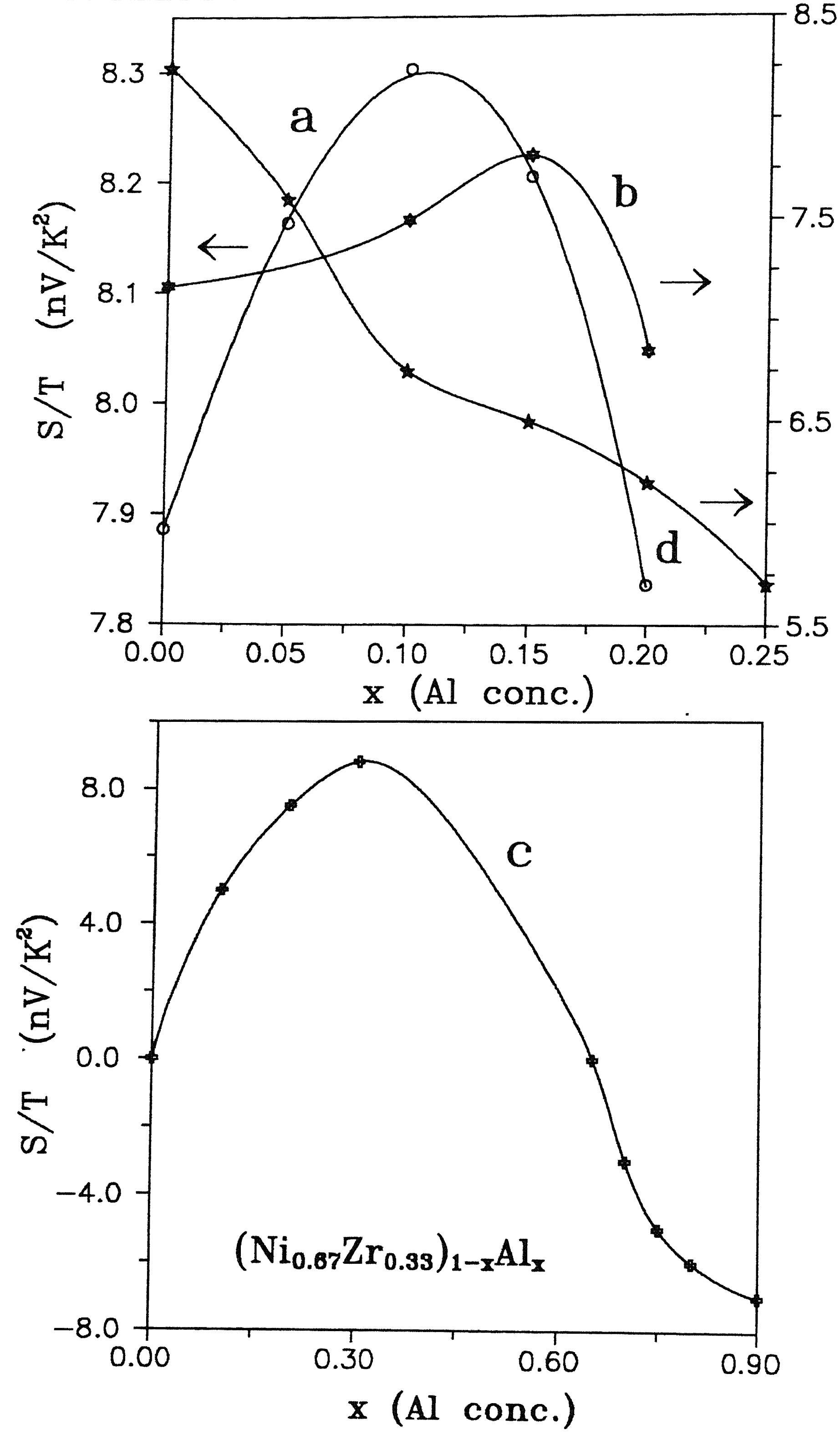

Figure 6.15: Al concentration dependence of thermopower divided by temeperature (S/T) near 300 K for (a) $(Cu_{0.36}Zr_{0.64})_{1-x}Al_x$ (b) $(Ni_{0.5}Zr_{0.5})_{1-x}Al_x$ (c) (c)$(Ni_{0.67}Zr_{0.33})_{1-x}Al_x$ and (d) $(Ni_{0.64}Zr_{0.36})_{1-x}Al_x$ metallic glasses.

6.3 Conclusion

We have systematically studied the electrical resistivity ρ(T) of Zr-rich $(Cu_{0.36}Zr_{0.64})_{1-x}Al_x$ with x = 0, 0.1, 0.15, and 0.2 and $(Ni_{0.5}Zr_{0.5})_{1-x}Al_x$ with x = 0, 0.5, 0.1, 0.15, and 0.2 non-magnetic transition–metal–based amorphous alloys. We find that all these alloys fall into the strong-scattering regime ($\rho_{300} > 165\ \mu\Omega$ cm) with negative TCR till the highest measuring temperature (300 K). In both the systems, addition of Al, enhances ρ_{300}. In the very low-temperature region each alloy shows a tendency of superconductivity. They are found to be highly disordered, extremely dirty type–II BCS superconductors. The electron–phonon coupling constant is found to be very small ($\Lambda \sim 0.5$) unlike the simple (non-transition metal) amorphous superconductors ($\Lambda \sim 2$). We also find that with the increase of the degree of disorder with Al concentration (x), the superconducting transition temperature (T$_c$) gets suppressed.

In regions $T_c < T < 15$, $\Theta_D/10 < T < \Theta_D/3$, and $\Theta_D/3 < T < \Theta_D$, in $(Cu_{0.36}Zr_{0.64})_{1-x}Al_x$ system we could observe only T and $\sqrt{T}$ dependence at intermediate and high temperature ranges except for $(Cu_{0.36}Zr_{0.64})_{0.8}Al_{0.2}$ alloy where the low–temperature $\sqrt{T}$ regime was also seen. This is clearly because of the superconducting fluctuations which appear even much above their T$_c$'s and overshadow the $\sqrt{T}$ dependence of σ in the low temperature range. However, the conductivity in $(Ni_{0.5}Zr_{0.5})_{1-x}Al_x$ alloys, varies as $\sqrt{T}$, T, and $\sqrt{T}$, respectively, due to electron–electron interaction and weak localization effects. Thus we are able to observe three distinct regions of conductivity in the same alloy, hitherto only theoretically predicted. This is the first such report (*three distinct regions in each specimen*) in a non-magnetic clean system, the earlier one on the ferromagnetic Co-rich alloys[3] is somewhat controversial because quantum correction has been applied in the presence of spontaneous moment. The coefficient of the $\sqrt{T}$ term at low temperatures [(360–460) $(\Omega m)^{-1}K^{-1/2}$]is in good agreement with the near-universal value of (500±100) $(\Omega m)^{-1}K^{-1/2}$, obtained by Cochrane and Strom-Olsen[16] for many amorphous systems. Also the diffusion constant of electrons [D ~ (0.4-4.0) × 10^{-5} m^2/s] is in good agreement with those of the binary non-magnetic transition–metal–based alloys[10, 11, 5], e.g., CuTi, CuHf, and CuZr (D $\sim 2 \times 10^{-5}$ m^2/s). The density of states at the Fermi level, calculated from D, is in excellent agreement with those obtained from specific heat measurements[27, 22]. Inelastic mean-free path length (l_i) and inelastic relaxation time (τ_i), estimated using weak localization theory, agree very well with the experimental results for CuTi, CuHf, and CuZr systems as reported by Howson[9, 11, 5], Dugdale[14], and Poon *et al.*[39].

A number of experimental results based on high–field magnetoresistance measurements in non-magnetic amorphous alloys Cu-Zr, Cu-Ti, Ti-Be-Zr, etc. by Howson *et al.*[11], Bieri *et al.*[17], Schulte *et al.*[18], and Hickey *et al.*[19] have confirmed the contribution of superconducting fluctuations, weak localization and EEI in the presence of spin–orbit interactions. High–field magnetoresistance measurements on this alloy system will be useful to single out the effects from localization in the presence of spin-orbit interaction, superconducting fluctuation and electron–electron interaction.

Our results provide further evidence that the low–temperature electrical transport in non-magnetic transition–metal–based alloys can be better described by quantum corrections to the Boltzmann conductivity rather than the empirical exponential form given by Mizutani. The addition of Al seems to behave like metalloid addition enhancing the stability against crystallization.

Bibliography

[1] U. Mizutani, Prog. Mater. Sci. **28**, 97 (1983).

[2] G. Thummes, J. Kötzler, R Ranganathan, and R. Krishnan, Z. Phys. B – Condensed Matter **69**, 489 (1988).

[3] A. Das and A. K. Majumdar, Phys. Rev. B **43**, 6042 (1991).

[4] R. Harris and J. O. Strom-Olsen, *in Glassy Metals II*, edited by H. beck and H. J. Güntherodt (Springer-Verlag, New York,1983), p.325.

[5] M. A. Howson and B. L. Gallagher, Physics Reports **170**, 265 (1988).

[6] O. Rapp, S. M. Bhagat, and H. Gudmundsoon, Solid State Commun. **42**, 741 (1982), and references 5-11 therein.

[7] Patrick A. Lee and T. V. Ramakrishnan, Rev. Mod. Phys. **57**, 287 (1985).

[8] B. L. Altshuler and A. G. Aronov, *in Electron-Electron Interaction in Disordered Systems*, edited by A. L. Efros and M. Pollak (Elsvier, New York, 1985), p. 1.

[9] M. A. Howson, J. Phys. F **14**, L25 (1984).

[10] M. A. Howson and D. Greig, Phys. Rev. B **30**, 4805 (1984).

[11] M. A. Howson and D. Greig, J. Phys. F **16**, 989 (1986).

[12] B. L. Altshuler and Patrick A. Lee, Physics Today, 36 (December 1988).

[13] D. G. Naugle, J. Phys. Chem. Solids **45**, 367 (1984).

[14] J. S. Dugdale, Contemp. Phys. **28**, 547 (1987).

[15] U. Mizutani, Mater. Sci. Eng. **99**, 165 (1988).

[16] R. W. Cochrane and J. O. Strom-Olsen, Phys. Rev. B **29**, 1088 (1984)

[17] J. B. Bieri, A. Fert, G. Creuzet, and J. C. Ousset, Solid State Commun. **49**, 849 (1984).

[18] A. Schulte and G. Fritsch, J. Phys. F **16**, L55 (1986); A. Schulte, Solid State Commun. **60**, 99 (1986).

[19] B. J. Hickey, D. Greig, and M. A. Howson, J. Phys. F **16**, L13 (1986); Phys. Rev. B **36**, 3074 (1987).

[20] E. Abrahams, P. W. Anderson, D. C. Licciardello, and T. V. Ramakrishnan, Phys. Rev. Lett. **42**, 673 (1979).

[21] T. V. Ramakrishnan in *Electron Localization*, Les Houches, Session XLVI–1986, edited by J. Souletie, J. Vannimenus and R. Stora (Elsevier, North Holland, 1987).

[22] K. Samwer and H. v. Löhneysen, Phys. Rev. B **26**, 107 (1982).

[23] G. M. Eliashberg, Zh. Eksp. Teor. Fiz. **38**, 966 (1960).

[24] W. L. McMillan, Phys. Rev. **167**, 331 (1968).

[25] L. Coffey, K. A. Muttalib, and K. Levin, Phys. Rev. Lett. **52**, 783 (1984).

[26] S. J. Poon, Phys. Rev. B **31**, 7442 (1985).

[27] Makoto Matsuura and Uchiro Mizutani, J. Phys. F **16**, L183 (1986).

[28] G. Bergmann, Phys. Rep. **27C**, 159 (1976).

[29] Gerald Burns, in *High Temperature Superconductivity* (Academic Press, San Diego, 1992).

[30] C. C. Tsuei, J. R. Kirtley, M. Rupp, J. Z. Sun, A. Gupta, M. B. Ketchen, C. A. Wang. Z. F. Ren, J. H. Wang, and M. Bhushan, Science **271**, (1996).

[31] U. Mizutani, S. Ohashi, T. Matsuda, K. Fukamichi, and K. Tanaka, J. Phys.: Condensed Matter **2**, 541 (1990).

[32] W. L. McMillan, Phys. Rev. B **24**, 2739 (1981).

[33] N. F. Mott and M. Kaveh, J. Phys. C **15**, L707 (1982).

[34] M. Olivier, J. O. Strom-Olsen, Z. Altounian, R. W. Cochrane and M. Trudeau, Phys. Rev. B **33**, 2799 (1986).

[35] M. Olivier, J. O. Strom-Olsen and Z. Altounian, Phys. Rev. B **35**, 333 (1987).

[36] C. C. Tsuei, Phys. Rev. Lett. **57**, 1943 (1986).

[37] K. Rhie, D. G. Naugle, Beom-hoan O, and J. T. Markert, Phys. Rev. B **48**, 5973 (1993).

[38] K. Rhie and D. G. Naugle, Phys. Lett. A **149**, 301 (1990).

[39] S. J. Poon, K. M. Wong, A. J. Drehmann, Phys. Rev. B **31**, 1668 (1985).

[40] P. Oelhafen, E. Hauser, and H. J. Güntherodt, Solid State Commun. **35**, 1017 (1980).

[41] S. Kanemaki, M. Suzuki, Y. Yamada, and U. Mizutani, J. Phys. F **18**, 105 (1988).

[42] U. Mizutani, M. Tanaka, and H. Sato, J. Phys. F **17**, 131 (1987).

[43] A. K. Bhatnagar, R. Pan, and D. G. Naugle, Phys. Rev. B **39**, 12460 (1989).

[44] A. K. Bhatnagar, K. W. Rhie, D. G. Naugle, A. Wolfenden, B. H. Zhang, T. O. Callaway, W. D. Bruton, and C. R. Hu, J. Phys.: Condensed Matter 2, 2625 (1990).

Chapter 7

Conclusions

In this chapter we summarize briefly some of the important observations and conclusions from the present study. In this thesis we have made an attempt to understand the transport and magnetic properties of some highly resistive crystalline and amorphous alloys and to indentify the dominant physical processes responsible for their behaviour.

In the case of the Fe-Ni-Cr alloys what distinct features does this system show in electronic transport, magneto - transport and magnetization when it undergoes a gradual change for long-range FM to long-range AFM with intermediate SG and RSG phases *within the same crystallographic phase* have been studied thoroughly. Moreover, how the electronic transport properties are affected by short-range magnetic ordering, clustering or setting in of long-range FM or AFM order or frozen-in frustrated spins (arising out of strong competing FM and AFM interactions) with no long - range order have also been investigated.

Fe-Ni-Cr

(a) Resistivity

We have performed systematic electrical resistivity measurements on γ-$Fe_{80-x}Ni_xCr_{20}$ (14 $\leq$ x $\leq$ 30) substitutionally disordered, crystalline, austenitic stainless steel alloys in different magnetic states in the temperature range between 10 and 600 K. The value of ρ_{300K} for all these alloys lie between 90 and 120 $\mu\Omega$ cm. All of them show positive TCR with decreasing magnitude at higher temperatures.

At low temperatures, we conclude that the T^2 dependence of ρ of these magnetic alloys in the long-range (FM or AFM) regime mainly arises from the electron - magnon (spin wave) scattering. The latter also provides a more consistent picture for the entire range of x. We also find that the Baber mechanism is too small to explain this low - temperature T^2 behaviour. We further conclude that for the alloys (x = 19 and 21) in the SG regime, the T^2 contribution becomes somewhat smaller (as it should be) and an additional T^3 contribution, which arises from the electron - phonon scattering in the presence of s-d interaction, plays an important role in the behaviour of the low-temperature ρ(T).

The most important observation made in each alloy (in Chapter 3) is the strong deviation from linearity (DFL) of ρ, which is an indication of resistivity saturation at high temperatures, irrespective of its low - temperature magnetic state. The TCR vs ρ curves for all the alloys merge in the temperature range of 100 - 600 K, showing a striking correlation. This behaviour indicates that both thermal and compositional disorders are equally important in determining the resistivity saturation. Our study provides a rigorous test of some theoretical models. In conclusion, we argue that the particular way in which the alloys approach saturation can be understood quite well on the basis of the parallel – resistor model. The phonon – ineffectiveness model has failed to explain this strong downward DFL of ρ at high temperatures, atleast in our alloys. The ion – displacement model also provides a consistent explanation of the DFL of ρ at high temperatures. However, every model has its own limitations. None of them provide a single constant saturation resistivity derived from the experimental data. Also one does not know whether a unique saturation resistivity or a number of them is desirable for the entire range of concentration (x) of this particular alloy system because of insufficient theoretical inputs. To the best of our knowledge very few studies have been made on highly resistive crystalline alloys to resolve this open problem of resistivity saturation. Further works are needed in this directon. We also conclude that the σ_{sat} in these alloys are much higher than those expected if this system approached the region of minimum metallic conductivity

(σ_{min}). Thus the two situations, namely, the conductivity 'σ' when the electron mean free path approaches the lattice spacing ($l \approx$ a) and the minimum metallic conductivity, are not alike. Greater attention should be paid in the direction of the band - theory calculations in ternary 3d-transition metal alloys which ultimately will help in understanding the transport properties of these systems in a more quantitative manner.

(b) Magnetoresistance

The most important observation made in the low-field magnetoresistance (MR) studies (Chapter 4) is that all the alloys show negative (anomalous) MR (with large isotropic part) (except x = 14 (AFM) alloy) below 50 K. Above 50 K all of them show Kohler type (quadratic in H) normal MR. This Fe-Ni-Cr series exhibits small MR (maximum $\frac{\Delta\rho}{\rho} \sim 1\%$) and also a positive contribution at high fields and temperatures. At the lowest field and temperature the FM (x = 30) alloy does show a small FAR because of the domain orientation like a conventional FM.

The MR of all the alloys has a large isotropic part. The magnitude of anisotropy MR $[(\frac{\Delta\rho}{\rho})_{\|}$ - $(\frac{\Delta\rho}{\rho})_{\perp}]$ decreases as this system moves away from the long-range ordered phases (x = 30 (FM) or x = 14 (AFM)). In the low-field regime below 50 K, the MR data of all the alloys have been well described by an empirical relation $\frac{\Delta\rho}{\rho} = -\alpha(T)H^n$ with distinct values of α and n for different magnetic phases. In the case of the concentrated SG alloy (x = 21), n is found to be $\frac{3}{4}$ whereas for the mixed phase alloy (x = 23) it is $\frac{2}{3}$ and they remain temperature independent below 50 K. From these results we claim that these are the characteristics of the field dependence of MR in the concentrated SG and re-entrant SG phases, respectively. Definite trends of MR, α and n with composition (x) have been obtained as the Fe-Ni-Cr system evolves from the long-range AFM ordering to the long-range FM ordering passing through the critical concentration (x $\approx$ x$_c$) where the maximum change of all the three quantities occurs.

In the case of the SG alloy (x = 21), the MR correlates very well with M as $\frac{\Delta\rho}{\rho} \propto M^{2\,5}$ over a wide range of temperature and field. The isotropic part of MR $[(\frac{\Delta\rho}{\rho})_{iso}]$ correlates with M in distinct fashions in different magnetic phases in the presence of either short or long-range ordering. For the SG alloys with no long-range ordering it correlates very well with M satisfying an empirical relation $[(\frac{\Delta\rho}{\rho})_{iso}] = -\alpha[M(H)]^2$. As the system approaches towards the long-range FM ordering from the SG and RSG regimes, a distinct deviation from the above relation has been observed and finally in the case of long-range FM alloy (x = 30) the relationship of $[(\frac{\Delta\rho}{\rho})_{iso}] = -\alpha[M^2(H) - M^2(0)]$ holds.

We thus conclude that the RSG (x=23 and 26) phase is the precursor to the FM ordering. For the RSG alloys there is a short - range FM ordering on the scale of electron mean - free path (~ 10 - 20 Å). For the FM alloy (x = 30), a homogeneous canted FM phase sets in. At low fields alignment of domains produces a rapid increase in M without affecting the resistivity as the domain size is much greater than the electron mean-free path. At higher fields (beyond technical saturation) once a single domain structure is established, the progressive alignment of individual moments of canted spins (which is manifested in the high-field slope of the M-H curve (Fig.4.3) beyond the technical saturation) dominates the MR behaviour and the M^2 dependence.

So a gradual evolution of MR occurs as one goes from the long-range FM ordering towards the critical region ($x \approx x_c$) close to the SG regime.

At low temperatures and very high fields beyond 4-5 tesla the observed upturn in the negative MR in these Fe-Ni-Cr alloys has been attributed to the positive (normal) contribution having a quadratic field dependence $[(\frac{\Delta\rho}{\rho})_n \sim aH^2]$. The negative (anomalous) contribution mainly arises from the suppression of the spin - flip scattering in these alloys in different magnetic states.

The contribution to MR from QIE is found to be very small (if present at all) compared to the magnetic contribution. Moreover, a very important point to be mentioned here is that the presence of any ferromagnetic impurity can destroy weak localization. In all these random magnetic alloys Ni is ferromagnetic and there are also strong FM interactions among some other pairs. It is very unlikely that weak localization can persist in these magnetic alloys. So one has to be very careful in invoking QIE in these Fe-Ni-Cr alloys.

To our knowledge, very few MR studies have been done on similar type of highly resistive crystalline alloys. More work is needed to understand anisotropies, QIE, magnetic effect, etc. in these magnetic alloys.

(c) Magnetization

A systematic high-field (0 - 20 T) dc-magnetization measurements, M(H) and M(T) have been carried out between 4.2 and 60 K, and 19 and 700 K, respectively in these Fe-Ni-Cr alloys. All these samples are at the vicinity of the critical concentration regime for long-range FM and AFM orderings and have strong competing interactions between different kinds of magnetic atoms. We find a number of distinct functional relationships M(H) in different magnetic phases below their respective magnetic transition temperatures. Because of the very large χ_{HF} compared to that of a conventional FM, we conclude that the nature of ferromagnetism in the case of the alloys with x = 30, 26 and 23 in their FM phase is unlike that of a standard FM. They are very hard to saturate even at a field of 19 tesla at 4.2 K. The law of approach to saturation reproduces the high-field M(H) data in the saturation regime resonably well. In the light of the *Rhodes-Wohlfarth* criterion, the alloys with x = 30, 26 and 23 in their FM regime are of weak - itinerant type. The non-integral values of the number of Bohr magneton per atom ($\overline{\mu}$) and the strong deviation from the Slater-Pauling curve support this weak-itinerant picture. In the FM alloy with x = 30, the combination of the long wave–length *spin wave* and *Stoner single particle* excitations describes the thermal demagnetization process quite well till 0.5 T_c. We conclude that the introduction of Cr in this alloy system substantially reduces the *spin-wave stiffness constant* $\mathcal{D}(0)$, suppresses the anharmonic term ($T^{5/2}$) and enhances the Stoner term.

In the case of the alloys with x = 26 and 23 (mixed phase), this particular study confirms that below the second transition the long-range FM ordering coexist with the transverse SG freezing supporting the G-T model. *Neutron-depolarization* studies coupled with *small-angle neutron scattering* would be able to provide a complete picture of the transeverse spin component in the FM domain (which might be of vortex-like spin structure), the nature of the domain-wall motion and the spin-modulated structure. In the concentrated SG alloys (x = 21 and 19) the high-field response dynamics of the frozen spins is similar to that of the *archtypical* spin glasses.

Our analysis on x = 14 (AFM) alloy shows that the long - range AFM structure of this alloy is of *type 1* where the 1st nearest neighbour interaction (J_1) is AFM and the 2nd one is FM (J_2). Since $| J_2/J_1 | > 1$, we conclude that this alloy must have a strong itinerant–electron–AFM contribution. Our estimated molecular field coefficents γ_1 and γ_2 for the 1st and 2nd nearest neighbour interaction in different sublattices are also compatible with the *type 1* kind of AFM structure. The latter shows a *spin-flop* transition at 1 T due to the canting of the AFM spins in the strong external magnetic field. Beyond this transition a square-root dependence of magnetization with external field is found whereas below it the dependence is linear.

At present, as there is no band structure (electronic or magnetic) calculation in these alloys, it is very difficult to estimate and correlate anything in more quantitative terms. Greater attention must be paid in this direction for better correlation of the transport and magnetic properties of these ternary alloys.

Moreover, a few more experimental techniques which could be the tools to study magnetism on a short length scale (i.e., rather local to the probing atom) should be employed on this ternary magnetic alloys to supplement our present investigations. μSR, neutron depolarization, Mössbauer spectroscopy, and time differential angular distribution / correlation (TDPAD/TDPAC) techniques using heavy-ion beams would throw more light on the understanding of these exotic magnetic phases with short or long-range ordering.

Cu/Ni-Zr-Al

We have also systematically studied the electrical resistivity ρ(T) of Zr-rich $(Cu_{0.36}Zr_{0.64})_{1-x}Al_x$ with x = 0, 0.1, 0.15, and 0.2 and $(Ni_{0.5}Zr_{0.5})_{1-x}Al_x$ with x = 0, 0.5, 0.1, 0.15, and 0.2 non-magnetic transition–metal–based amorphous alloys We find that all these alloys fall into the strong-scattering regime ($\rho_{300} > 165$ $\mu\Omega$ cm) with negative TCR till the highest measuring temperature (300 K). In both the systems, addition of Al, enhances ρ_{300}. In the lowest temperature region each alloy shows a tendency of superconductivity. They are found to be highly disordered, extremely dirty type–II BCS superconductors. The electron–phonon coupling constant is found to be very small ($\Lambda \sim 0.5$) unlike the simple (non-transition metal) amorphous superconductors ($\Lambda \sim 2$). We also find that with the increase of the degree of disorder with Al concentration (x), the superconducting transition temperature (T_c) gets suppressed.

In regions $T_c < T < 15$ K, $\Theta_D/10 < T < \Theta_D/3$, and $\Theta_D/3 < T < \Theta_D$, in $(Cu_{0.36}Zr_{0.64})_{1-x}Al_x$ system we could observe only T and $\sqrt{T}$ dependences at intermediate and high temperature ranges except for $(Cu_{0.36}Zr_{0.64})_{0.8}Al_{0.2}$ alloy where the low–temperature $\sqrt{T}$ regime was also seen. This is clearly because of the superconducting fluctuations which appear much above their T_c's and overshadow the $\sqrt{T}$ dependence of σ in the low-temperature range. However, the conductivity in $(Ni_{0.5}Zr_{0.5})_{1-x}Al_x$ alloys, varies as $\sqrt{T}$, T, and $\sqrt{T}$, respectively, due to electron–electron interaction and weak localization effects. Thus we are able to observe three distinct regions of conductivity in the same alloy, hitherto only theoretically predicted. This is the **first such report** (*three distinct regions in each specimen*) in a non-magnetic clean system, the earlier one on the ferromagnetic Co-rich alloys is somewhat controversial because quantum corrections have been applied in the presence of spontaneous magnetic moment. The coefficient of the $\sqrt{T}$ term at low temperatures [(360–460) $(\Omega m)^{-1}K^{-1/2}$]is in good agreement with the near-universal value of (500±100) $(\Omega m)^{-1}K^{-1/2}$, obtained by Cochrane and Strom-Olsen for many amorphous systems. Also, the diffusion constant of electrons [$D \sim (0.4\text{-}4.0) \times 10^{-5}$ m^2/s] is in good agreement with those of the binary non-magnetic transition–metal-based alloys, e.g., CuTi, CuHf, and CuZr ($D \sim 2 \times 10^{-5}$ m^2/s). The density of states at the Fermi level, calculated from D, is in excellent agreement with those obtained from specific heat measurements. Inelastic mean-free path length (l_i) and inelastic relaxation time (τ_i), estimated using weak localization theory, agree very well with the experimental results for CuTi, CuHf, and CuZr systems as reported earlier.

High–field magnetoresistance measurements in this alloy system will be useful to single out the effects from localization in the presence of spin-orbit interaction, superconducting fluctuations and electron–electron interaction.

Our results provide further evidence that the low–temperature electrical transport in non-magnetic transition–metal–based alloys can be better described by quantum corrections to the Boltzmann conductivity than the empirical exponential form given by Mizutani.

APPENDIX A

Software developed for data aquisition for electrical transport measurements in the temperature range of 1.2 - 300 K employing different IEEE interfaceble devices (PID-temperature controller, current source, digital multimeter adapted with 20 channel scanner, etc.) with IBM compatible PC/AT (80386).

```
    program Resistivity_measurement;
    uses gpib,dos,crt;
   type
       read=array[1..100] of real;
   var
     vbuf,cbuf,tbuf,sbuf,s1buf:iobuf;
     g1,g2,g3,g4,n,prema,cs,temc,l:integer;
     ti,tu:iobuf;
     v,t:read;
     fname,date,usr,time,stg,sh,strg,ts,ts1,sampl1,sampl2:string;
    t1,init,finit,heat,incr,icr,cur,toll,tol:real;
     num,sum,sumsq,meansq,dev,stdev,mean:real ;
     bkground:boolean;
   procedure
    Settings( var init, finit, tol,incr,cur: real; var N:integer);
   var
     T:real;
     y:integer;
     cr,lf:char;
   begin
      clrscr;
      window(1,1,80,25);
     write('INITIAL TEMPERATURE  ');
     readln(init);
     write('FINAL TEMPERATURE  ');
     readln(finit);
     If init > finit then
     begin
       T:= init;
       init:= finit;
       finit:= T;
     end;
     writeln(#7,#7,'PLEASE GIVE TEMP.INCREMENT (In Kelvin) ');
     readln(incr);
              if incr< 0.1 then
     begin
            writeln(#7,#7,'NOT ACCEPTABLE!! TAKING INCREMENT = 0.1 K');
           incr :=0.1;
        end ;
     writeln(#7,#7,'GIVE TEMPERATURE TOLERANCE FOR TAKING DATA ');
     readln(tol);
     If tol > 1 then
     begin
      tol:= 1;
       writeln('Your value was too large. Taking it to be 1.00.');
end;
    clrscr;    delay(500);
    writeln(#7,#7,#7,'PLEASE GIVE SAMPLE CURRENT IN Amp ( e.g. 100mA as 0.1) ');
    readln(cur);
             if cur< 0.001 then
    begin
            writeln(#7,#7,'NO SAMPLE CURRENT? TAKING CURRENT = 0.001 Amp');
            cur:=0.001;
       end
    else
       if cur>0.101 then
      begin
         writeln(#7,#7,'VERY HIGH CURRENT!! TAKING CURRENT = 0.1 Amp');
         cur:=0.1
    end;
    writeln('HOW MANY DATA TO BE AVERAGED ?   ');
    readln(N);
if N < 3 then
    begin
     writeln(#7,'That was too small. Taking it to be 3.');
      N:= 3;
```

```
  end
  else if N > 100 then
  begin
   writeln('That was too large. Adjusting it to be 100.');
    N:= 100;
  end;
  clrscr;
  writeln('OUTPUT FILE NAME :  ',fname);
  writeln('INITIAL TEMPERATURE=',init:4:2,'     ','FINAL TEMPERATURE=',finit:4:2);
  writeln('TOLERANCE:=',tol:1:3,'     ' ,'TEMP. INCREMENT:=',incr:2:2,'K');
  cr:=chr(13); lf:=chr(10);
  writeln('PRESS:',cr,lf,' Q : To Exit',cr,lf,'  C: To Change TempTol', '   ',
  'I: TO CHANGE INCR');
  gotoXY(58,4);
  textcolor(15);
  writeln('USER NAME :=> ');
  gotoXY(73,4);
  textcolor(15+16);
  writeln(usr);
  gotoXY(53,6);
  textcolor(15);
  writeln('STARTING TIME : ');
  gotoXY(70,6);
  writeln(time);
  gotoXY(44,8);
  writeln(sampl1);
  gotoXY(44,9);
  writeln(sampl2);
  gotoXY(56,11);
  writeln('DATE :=  ',date);
  gotoxy(3,14);
  writeln('SL.NO.','  ','TEMP.','     ','RESTNC-IN-CHANL-2','         '
  ,'SDV2','     ','RESTNC-IN-CHANL-6','      ','SDV6');
  textcolor(14);
  window(1,16,80,25)
end;
procedure newtol(var tol:real);
var
  y:integer;
  begin
    writeln(#7,#7,#7'GIVE NEW TEMPTOLERENCE  VALUE (0=QUIT)');
    readln(toll);y:=wherey;
   if toll = 0 then
   tol:=tol+toll
   else
   tol:=toll;  window(1,1,80,6);
   gotoxy(1,3);writeln('TOLERANCE:=',tol:1.3) ;
   window(1,16,80,25);
   gotoxy(1,y);
       end;
  PROCEDURE nuincr(var incr:real);
 var
      y:integer;
 begin
        writeln (#7,#7,#7'GIVE TEMP. INCREMENT (0=QUIT)');
        readln(icr);y:=wherey;
        if icr=0 then
        incr:=incr+icr
        else  incr:=icr;
        window(1,1,80,6);
        gotoxy(21,3);writeln ('TEMP. INCREMENT :=', incr:1:2,'K');
        window(1,16,80,25);gotoxy(1,y);
        end;
 procedure escape;
 begin
   writeln('PROGRAMME TERMINATED'),
   bkground:=true;
   halt
   end;
  procedure check;
 var ch:char;
 begin
     if keypressed then begin
     ch:=readkey;
     case ch of
       'q','Q': escape;
```

```
        'c','C': newtol(tol);
        'i','I': nuincr(incr);
      end;      end      end;
  procedure statistics(data:read; var N:integer,var mean,stdev:real);
  var
    i:integer;
    begin
         sum:=0;
         sumsq:=0;
   for  i:= 1 to N do
     begin
         num =data[i];
         sumsq:=sumsq+sqr(num);
         sum =sum+num;
         end;
         meansq:=sumsq/N;
         mean:=abs(sum/N);
         dev:=abs(meansq-sqr(mean));
         stdev:=sqrt(dev);
         end;
 procedure convert(s1.string;var buf:iobuf,n:integer);
    var
      i:integer;
   begin
          for i:=1 to n do
          buf[i]:=s1[i];
          end;
 procedure change (var buf:iobuf; var str:string; var g1.integer);
     var
     i,k :integer;
     begin
       k:=1;
       str:='';
       for i:=1 to g1 do
       begin
       str:=str+buf[k];
       k:=k+1;
       end;
     end;
 procedure initialise;  { initialises GPIB instruments }
   var
   strng,st,strg,strn:string;
 begin
   prema:=ibfind('sdv182');
   temc:=ibfind('temp');
   cs:=ibfind('cs220');
   ibclr(prema),    ibclr(temc);
   ibclr(cs);
    st:='DOF1R0V10G1X';
    convert(st,cbuf,12);
    ibwrt(cs,cbuf,12);
    strng:='VDA1T4M2';
    convert(strng,vbuf,9);
    ibwrt(prema,vbuf,9);
    strng:='M1P90I35D30R5ASX';
    convert(strng,tbuf,16);
    ibwrt( temc,tbuf,16);
  end;
procedure settem(var init:real);
begin
  str(init:3:1,ts1);
      ts1:='S'+ ts1  ;
      l:=length(ts1);
      convert(ts1,s1buf,l);
      ibwrt(temc,s1buf,l);
    end;
procedure forcur(var cur:real);
var
  i:integer;
  st:string[8];
  ibuf:iobuf;
begin
    str(cur:1:3,st);
    st:='I' + st+'X';
     i:=length(st),
     convert(st,ibuf,i);
     ibwrt(cs,ibuf,i);
 end;
 procedure revcur(var cur:real),
 var
     st:string[8];
     i:integer;
     r,re:real;
     ibuf:iobuf;
  begin
    r:=cur;
    re:= - r ;
    str(re:1:3,st);
    st:='I'+st+'X';
    i:=length(st);
    convert(st,ibuf,i);
     ibwrt(cs,ibuf,i);
  end;
 procedure command1;
var
sttrg:string;
kbuf:iobuf;
begin
 sttrg:='VDA1T4M2';
 convert(sttrg,kbuf,9);
 ibwrt(prema,kbuf,9);
end;
 procedure command2;
var
sttrgg:string;
kkbuf:iobuf;
begin
 sttrgg:='VDA1T4M6';
 convert(sttrgg,kkbuf,9);
 ibwrt(prema,kkbuf,9);
end;
 function voltage(var prema:integer):real;
 var
   vobuf:iobuf;
   strg,strg1:string;
   v:real;
   code,tap:integer;
     begin
     g2:=32;
     ibrd(prema,vobuf,32);
     change(vobuf,strg,g2);
     tap:=pos('V',strg);
     strg1:=copy(strg,0,(tap-1));
     val(strg1,v,code);
     voltage:=abs(v);
   end;
 function temperature(var temc:integer):real;
 var
     st:string;
     code:integer;
  begin
      g3:=64;
     ibrd(temc,tu,64);
     change(tu,strg,g3);
     stg:=copy(strg,1,6);
     val(stg,t1,code);
     temperature:=t1;
     end;
 procedure resistance(var ohm,sdv:real),
 var
    i:integer;
    volt:real;
 begin
   for i:=1 to n do
    begin
     v[i]:=voltage(prema);
     end;
     statistics(v,n,volt,sdv);
     ohm:=volt/cur;
     sdv:=sdv/cur;
     end;
 procedure kelvin(var temp,sdt:real);
```

```
var
  i:integer;
begin
   for i:=1 to n do
   begin
    t[i]:=temperature(temc);
    end;
    statistics(t,n,temp,sdt);
    end;
{************************************************************}
                {MAIN PROGRAMME}
  label
    filename,exit;
 var
      cibuf,vobuf:iobuf;
 ohm1,ohm2,temp1,temp2,temp3,res1,res2,temp,diff,sdt,sdt1,
 sdt2,sdv1,sdv2,sdv:real;
 ohm3,ohm4,sdv3,sdv4,vmean3,vmean4,sdvv:real;
   stt,st:string;
    y,i,j,k,z,code:integer;
    t2,v2,v3,v4:read;
    phile,outf:text;
    settle,good,steady,error:boolean;
    up:real;
begin
  clrscr;
   {$i-}
 writeln('WRITE YOUR OUTPUT FILE NAME ');
  filename :
  readln(fname);
  fname:=fname+'.PRN';
  assign(phile,fname);
  reset(phile);
  if ioresult<>0 then rewrite(phile)
  else
 begin
  writeln(#7,#7,#7,'File already exists');
  goto filename;
 y:=ioresult;       {$i+}     end;
close(phile);
writeln (#7,#7,'WRITE THE SAMPLE NAME 1');
 repeat
  readln(sampl1);
   until sampl1<> '';
  sampl1:='SAMPLE NAME (A) IN CHANNL 2:= '+sampl1;
   append(phile);
  writeln(phile,sampl1);
  close(phile);
writeln (#7,#7,'WRITE THE SAMPLE NAME 2');
 repeat
  readln(sampl2);
   until sampl2<> '';
  sampl2:='SAMPLE NAME (B) IN CHANNL 6:= '+sampl2;
   append(phile);
  writeln(phile,sampl2);
  writeln('DATE :=    ');
  readln(date);
  writeln(phile,'DATE :    ',date);
  writeln('USER NAME (INTL.) :   ');
  readln(usr);
  writeln('STARTING TIME := ');
  readln(time);
  writeln(phile,'STARTING TIME := ' ,time);
  writeln(phile,'  ','TEMP.','    ','RESTNC-IN-CHANL-2','     ',
  'SDV2','    ','RESTNC-IN-CHANL-6','     ','SDV6');
  close(phile);
  k:=0;
  settings(init,finit,tol,incr,cur,n);
  initialise;
  delay(1000);
  while init<= finit do
  begin
  error:=false;bkground:=false;
  settem(init);
  if (incr <= 0.5) then  delay(25000)
  else
       delay(30000);
  for j:=1 to 1 do
  begin
    exit:
     check;
    temp:=0;
    res1:=0;
    res2:=0;
    forcur(cur);
     delay(5000);
   kelvin(temp1,sdt);
   temp:=temp+temp1;
   if sdt>tol then goto exit;
   command1;
   delay(5000);
   resistance(ohm1,sdv1);
    command2;
    delay(5000);
   resistance(ohm2,sdv2);
   kelvin(temp2,sdt1);
    good:= (abs(sdt1)<=tol) and (abs(temp2-temp)<=tol);
    if good then
    begin
    temp:= temp+temp2;
    temp:=temp/2;
    res1:=res1+ohm1;
    res2:=res2 +ohm2;
   end
     else
     goto exit;
    revcur(cur);
    delay(5000);
    command1;
    delay(5000);
    resistance(ohm3,sdv3);
    command2;
    delay(5000);
    resistance(ohm4,sdv4);
    kelvin(temp3,sdt2);
    diff:=abs(temp3-temp);
    steady:= (abs(sdt2)<=tol) and (diff<=tol );
    if steady then
    begin
    temp:=temp+temp3;
    temp:=temp/2;
    res1:=res1+ohm3;
    res2:=res2+ohm4;
    sdv:=(sdv1+sdv3)/2;
    sdvv:=(sdv2+sdv4)/2;
  res1:=res1/2;
  res2:=res2/2;
   k:=k+1;
  append(phile),
  writeln(k:5,'     ',temp:4:3,'     ',res1:3:8,'     ',sdv:3:9,'     '
,res2:3:8,'     ',sdvv:3:9);
  writeln(phile,temp:4:3,'     ',ohm1:3:8,'     ',sdv:3:9,'     ',ohm2:3:8,'     '
 ,sdvv:3:9);
  close(phile)
    end
        else
          goto exit;
  end;
  init.=init+incr;
  end;
  ibclr(prema);ibclr(temc);ibclr(cs);
  ibloc(temc);ibloc(prema);ibloc(cs);
   clrscr;
end.
```

APPENDIX B(1)

Software developed to evaluate the BLOCH-WILSON [Eq.(3.)] integral, employing DO1AHF (1-D quadrature, adaptive, finite interval and strategy due to Patterson) NAG Routine which is suitable for any well-behaved function.

```
C     PROGRAM INTEGRATION USING D01AHF (NAG ROUTINE)
      implicit real*8 (a-h, o-z)
      dimension c(500), d(500), t(500), tr(500)
      common t
      external         d01ahf,fun
      open (unit=23, file = 'r21m.prn',status='unknown')
      open (unit=25, file = '/b1/tapan/3int/r21.int3',status='unknown')
      a=0.0d0
      m=0
      mn=1
      nlimit=0
      epsr=1.0d-6
      ifail=1
      write (*,*) 'give lower and upper limits of temperature'
      read  (*,*) anmin, anmax
      do i = 1,500
      read (23,*,end=56) c(i),d(i)
      if (( c(i) .ge. anmin).and.(c(i).le.anmax))then
      tr(mn)=c(i)
      t(mn) = 400.0/c(i)
      mn = mn+1
      m = m+1
      endif
      enddo
      56     endfile 23
C     if (ifail .ne. 0) then
C     write (25,80) 'ifail = ' , ifail
C    80      format (1x,  i4)
C           endif
    if (ifail . le . 2) then
    do i = 1,m
    ti=t(i)
    ans = d01ahf( a, ti, epsr, n, relerr, fun, nlimit, ifail)
       write (25,100) c(i),  ans*((tr(i)/400.0)**3), 1/d(i)
     100     format ( 5x, f8.3, 5x, f21.18, 5x, f18.8)
    enddo
    endif
    stop
     end
C     ****************************************************************
C     FUNCTION TO BE INTEGRATED
C     ****************************************************************
      double precision function fun(x)
      double precision   x
C     FUNCTION TO BE INTEGRATED (GIVEN  BELOW)
      fun = (x**3)/((exp(x)-1.)*(1.-exp(-x)))
      return
      end
C     ****************************************************************
c     SUBROUTINE USED D01AHF (NAG-LIBRARY) FOR INTEGRATION
C     ****************************************************************
      DOUBLE PRECISION FUNCTION D01AHF(A,B,EPR,NPTS,RELERR,F,NL,IFAIL)
C     MARK 8 RELEASE. NAG COPYRIGHT 1979.
C     MARK 8A REVISED. IER-254 (AUG 1980).
C     MARK 11.5(F77) REVISED. (SEPT 1985.)
C     MARK 12B REVISED. IER-525 (FEB 1987)
C     MARK 13 REVISED. USE OF MARK 12 X02 FUNCTIONS (APR 1988).
C     MARK 14 REVISED. IER-819 (DEC 1989).
C
C     THIS FUNCTION ROUTINE PERFORMS AUTOMATIC INTEGRATION OVER A
C     FINITE INTERVAL USING THE BASIC INTEGRATION ALGORITHMS D01AHY
C     AND D01AHX, TOGETHER WITH, IF NECESSARY, AN ADAPTIVE
C     SUBDIVISION PROCESS.
C
C     INPUT ARGUMENTS
C     ----- ----------
C     A,B       -  LOWER AND UPPER INTEGRATION LIMITS.
C     EPR       -  REQUIRED RELATIVE ACCURACY.
C     NL        -  APPROXIMATE LIMIT ON NUMBER OF INTEGRAND
C                  EVALUATIONS. IF SET NEGATIVE OR ZERO THE
C                  DEFAULT IS 10000.
C     F         -  THE USER NAMED AND PREPARED FUNCTION  F(X)
C                  GIVES THE VALUE OF THE INTEGRAND AT X.
```

```
C      IFAIL       INTEGER VARIABLE
C               - 0  FOR HARD FAIL REPORT
C               - 1  FOR SOFT FAIL REPORT
C
C      OUTPUT ARGUMENTS
C      ------ ---------
C      NPTS    -   NUMBER OF INTEGRAND EVALUATIONS USED IN OBTAINING
C                  THE RESULT.
C      RELERR  -   ROUGH ESTIMATE OF RELATIVE ACCURACY ACHIEVED.
C      IFAIL   -   VALUE INDICATES THE OUTCOME OF THE INTEGRATION -
C                  IFAIL  = 0  CONVERGED
C                  IFAIL  = 1  INTEGRAND EVALUATIONS EXCEEDED  NL.
C                              THE RESULT WAS OBTAINED BY CONTINUING
C                              BUT IGNORING ANY NEED TO SUBDIVIDE.
C                              RESULT LIKELY TO BE INACCURATE.
C                  IFAIL  = 2  DURING THE SUBDIVISION PROCESS
C                              THE STACK BECAME FULL
C                              (PRESENTLY SET TO HOLD 20
C                              LEVELS OF INFORMATION.  MAY BE
C                              INCREASED BY  ALTERING  ISMAX
C                              AND THE DIMENSIONS OF STACK
C                              AND ISTACK). RESULT IS
C                              OBTAINED BY CONTINUING BUT
C                              IGNORING CONVERGENCE FAILURES
C                              ON INTERVALS  WHICH CANNOT BE
C                              ACCOMMODATED ON THE STACKS.
C                              RESULT LIKELY TO BE
C                              INACCURATE.
C                  IFAIL  = 3  INVALID ACCURACY REQUEST.
C
C      THE SUBDIVISION STRATEGY IS AS FOLLOWS -
C      AT EACH STAGE AN INTERVAL IS PRESENTED FOR SUBDIVISION
C      (INITIALLY THE WHOLE INTERVAL). THE POINT OF SUBDIVISION IS
C      DETERMINED BY THE RELATIVE GRADIENT OF THE INTEGRAND
C      AT THE END POINTS (SEE D01AHZ) AND MAY BE IN THE
C      RATIO 1/2, 1/1 OR 2/1.D01AHY IS THEN APPLIED TO EACH
C      SUBINTERVAL.  SHOULD IT FAIL TO CONVERGE ON THE LEFT
C      SUBINTERVAL THE SUBINTERVAL IS STACKED FOR FUTURE
C      EXAMINATION AND THE RIGHT SUBINTERVAL IMMEDIATELY
C      EXAMINED. SHOULD  IT FAIL ON THE RIGHT SUBINTERVAL
C      SUBDIVISION IS IMMEDIATELY PERFORMED AND THE WHOLE
C      PROCESS REPEATED. EACH CONVERGED RESULT IS
C      ACCUMULATED AS THE PARTIAL VALUE OF THE INTEGRAL.
C      WHEN THE LEFT  AND RIGHT SUBINTERVALS BOTH CONVERGE
C      THE INTERVAL LAST STACKED IS SUBDIVIDED AND THE
C      PROCESS REPEATED.
C      A NUMBER OF REFINEMENTS ARE INCLUDED.  ATTEMPTS ARE MADE TO
C      DETECT LARGE VARIATIONS IN THE INTEGRAND AND
C      TRANSFORMATIONS ARE MADE IF ENDPOINT VARIATION IS
C      EXTREME. THIS DEPENDS ON THE RATE OF CONVERGENCE OF
C      D01AHX AND ON THE END POINT RELATIVE GRADIENTS OF THE
C      INTEGRAND FOR THE NON-SUBDIVIDED INTERVAL.  RANDOM
C      TRANSFORMATIONS ARE ALSO APPLIED TO IMPROVE THE
C      RELIABILITY.  THE  RELATIVE ACCURACY REQUESTED ON
C      EACH SUBINTERVAL IS ADJUSTED IN ACCORDANCE WITH ITS
C      LIKELY CONTRIBUTION TO THE TOTAL INTEGRAL.
C
C      .. Parameters ..
       CHARACTER*6                      SRNAME
       PARAMETER                        (SRNAME='D01AHF')
C      .. Scalar Arguments ..
       DOUBLE PRECISION                 A, B, EPR, RELERR
       INTEGER                          IFAIL, NL, NPTS
C      .. Function Arguments ..
       DOUBLE PRECISION                 F
       EXTERNAL                         F
C      .. Scalars in Common ..
       DOUBLE PRECISION                 AFLOW, ALP, AV, CRATE, EPMACH,
      *                                 UFLOW
       INTEGER                          IR, MRULE, NT
C      .. Local Scalars ..
       DOUBLE PRECISION                 QSUBND
       DOUBLE PRECISION                 AMAXL, AMAXR, C2, COMP, EPS,
      *                                 EPSIL, EPSR, FACTOR, SUB1, SUB2,
      *                                 SUB3, TEST, V
       INTEGER                          IC, ICQ, IL, IS, ISI, ISMAX, IT,
      *                                 K, KK, NF, NLIM, NLIMIT, NTMAX
C      .. Local Arrays ..
       DOUBLE PRECISION                 RESULT(8), STACK(120)
       INTEGER                          ISTACK(20)
       CHARACTER*1                      P01REC(1)
C      .. External Functions ..
       DOUBLE PRECISION                 D01AHU, D01AHZ, X02AJF, X02AMF
       INTEGER                          P01ABF
       EXTERNAL                         D01AHU, D01AHZ, X02AJF, X02AMF,
      *                                 P01ABF
C      .. External Subroutines ..
       EXTERNAL                         D01AHY
C      .. Intrinsic Functions ..
       INTRINSIC                        ABS, LOG, MAX, MIN, SIGN
C      .. Common blocks ..
       COMMON                           /AD01AH/CRATE, MRULE
      COMMON                          /CD01AH/ALP, AV, NT, IR
      COMMON                          /DD01AH/EPMACH, UFLOW, AFLOW
C     .. Data statements ..
      DATA                            ISMAX, NLIM, NTMAX, TEST/116,
     *                                10000, 10, 0.25D0/
C     .. Executable Statements ..
      IL = 3
      ICQ = IFAIL
      IF (EPR.LE.0.0D0) GO TO 220
C     EPMACH SHOULD BE SLIGHTLY LARGER THAN THE RELATIVE
C     MACHINE ACCURACY.
      EPMACH = 1.1D0*X02AJF()
C     UFLOW IS THE SMALLEST POSITIVE REAL NUMBER REPRESENTABLE
C     ON THE MACHINE WHICH CAN BE INVERTED WITHOUT OVERFLOW.
      UFLOW = X02AMF()
      AFLOW = LOG(X02AMF())
      CRATE = 0.0D0
      EPSR = EPR/10.0D0
      NLIMIT = NL
      IF (NLIMIT.LE.0) NLIMIT = NLIM
      EPSIL = MIN(EPSR,1.0D-3)
      CALL D01AHY(A,B,RESULT,K,EPSIL,NPTS,IFAIL,F,AMAXL,AMAXR,A,0)
      D01AHF = RESULT(K)
      RELERR = ABS(RESULT(K)-RESULT(K-1))
      IF (ABS(D01AHF).GT.100.0D0*UFLOW) RELERR = RELERR/D01AHF
      RELERR = MAX(RELERR,0.5D0*EPMACH)
C
C     CHECK IF SUBDIVISION IS NEEDED
      IF (IFAIL.EQ.0) RETURN
C
C     SUBDIVIDE
      EPSIL = EPSIL*0.5D0
      FACTOR = 1.0D0
      NT = 1
      RELERR = 0.0D0
      QSUBND = 0.0D0
      D01AHF = 0.0D0
      IS = 1
      ISI = 1
      IC = 1
      SUB1 = A
      SUB3 = B
   20 IF (ABS(SUB1-SUB3).LT.20.0D0*EPSIL*(ABS(SUB1)+ABS(SUB3))) THEN
         K = 1
         RESULT(K) = F((SUB1+SUB3)/2.0D0)*(SUB3-SUB1)
         COMP = 0.0D0
         NPTS = NPTS + 1
         GO TO 160
      END IF
      SUB2 = D01AHZ(SUB1,SUB3,AMAXL,AMAXR)
      EPS = MIN(0.5D-3,FACTOR*EPSIL)
C
C     PROCESS SUBINTERVAL (SUB1,SUB2)
      IT = 0
      IF (AMAXL.GT.TEST .AND. CRATE.LE.21.0D0) IT = 1
      V = AMAXR
      C2 = CRATE
      CALL D01AHY(SUB1,SUB2,RESULT,K,EPS,NF,IFAIL,F,AMAXL,AMAXR,SUB1,IT)
      NPTS = NPTS + NF
      IF (NPTS.LE.NLIMIT) GO TO 40
      IC = SIGN(2,IC)
   40 COMP = ABS(RESULT(K)-RESULT(K-1))
      IF (IFAIL.EQ.0) GO TO 100
      IF (ABS(IC).EQ.2) GO TO 100
      IF (IS.GE.ISMAX) GO TO 80
C
C     STACK SUBINTERVAL (SUB1,SUB2) FOR FUTURE EXAMINATION
      IF (RESULT(K).EQ.0.0D0) RESULT(K) = D01AHF
      STACK(IS) = MAX(1.0D0,ABS(D01AHF/RESULT(K))*0.1D0)
      IS = IS + 1
      STACK(IS) = SUB1
      IS = IS + 1
      STACK(IS) = SUB2
      IS = IS + 1
      STACK(IS) = AMAXL
      IS = IS + 1
      STACK(IS) = AMAXR
      IS = IS + 1
      STACK(IS) = CRATE
      IS = IS + 1
      KK = NT
      IF (IT.EQ.0) GO TO 60
      IF (IFAIL.EQ.4) GO TO 60
      IF (NT.GE.NTMAX) GO TO 60
      KK = NT + 1
   60 ISTACK(ISI) = KK
      ISI = ISI + 1
      GO TO 120
   80 IC = -ABS(IC)
  100 QSUBND = QSUBND + RESULT(K)
      D01AHF = QSUBND
      RELERR = RELERR + COMP
C
C     PROCESS SUBINTERVAL (SUB2,SUB3)
  120 IT = 0
      IF (V.GT.TEST .AND. C2.LE.21.0D0) IT = 1
      CALL D01AHY(SUB2,SUB3,RESULT,K,EPS,NF,IFAIL,F,AMAXL,AMAXR,SUB3,IT)
      NPTS = NPTS + NF
      IF (NPTS.LE.NLIMIT) GO TO 140
      IC = SIGN(2,IC)
  140 COMP = ABS(RESULT(K)-RESULT(K-1))
      IF (IFAIL.EQ.0) GO TO 160
      IF (ABS(IC).EQ.2) GO TO 160
C
C     SUBDIVIDE INTERVAL (SUB2,SUB3)
      IF (IT.EQ.1 .AND. IFAIL.NE.4) NT = NT + 1
      SUB1 = SUB2
      IF (RESULT(K).EQ.0.0D0) RESULT(K) = D01AHF
      FACTOR = MAX(1.0D0,ABS(D01AHF/RESULT(K))*0.1D0)
      GO TO 20
  160 QSUBND = QSUBND + RESULT(K)
      D01AHF = QSUBND
      RELERR = RELERR + COMP
      IF (IS.EQ.1) GO TO 180
C
C     SUBDIVIDE THE DELINQUENT INTERVAL LAST STACKED
      ISI = ISI - 1
      NT = ISTACK(ISI)
      IS = IS - 1
      CRATE = STACK(IS)
      IS = IS - 1
      AMAXR = STACK(IS)
      IS = IS - 1
      AMAXL = STACK(IS)
      IS = IS - 1
      SUB3 = STACK(IS)
      IS = IS - 1
      SUB1 = STACK(IS)
      IS = IS - 1
      FACTOR = STACK(IS)
      GO TO 20
C
C     SUBDIVISION RESULT
  180 IF (ABS(D01AHF).GT.100.0D0*UFLOW)
     *    RELERR = ABS(RELERR/D01AHU(D01AHF))
      RELERR = MAX(RELERR,0.5D0*EPMACH)
      IF (IC.NE.1) GO TO 200
      IFAIL = 0
      RETURN
  200 IL = 2
      IF (IC.LT.0) GO TO 220
      IL = 1
  220 IFAIL = P01ABF(ICQ,IL,SRNAME,0,P01REC)
      RETURN
      END
```

APPENDIX B(2)

Software developed for non-linear least-squares fitting using the results of BLOCH-WILSON integral [APPENDIX B(1)], employing E04FDF (unconstrained minimum of a sum of squares, combined Gauss-Newton and modified Newton algorithm using function values only) NAG Routine.

```
c     NON-LINEAR LEAST-SQUARES FIT PROGRAMME USING NAG (E04FDF) ROUTINE
c     ******************************************************************
c     ******************************************************************
c     double precision
      implicit real*8 ( a-h, o-z )
      real*8 x(10), b(500),s(500),r(500)
      real*8 y(500), w(1000000), a(500,2), t(500,2)
      real*8 fsumsq, ymean, f, rm
      integer iw(1), mn, nmin, nmax
      common t, y, s, mean
c     n = 300
      f = 0.0
      m = 0
      mn = 1
      scl = 1.
      sft = 0.
c     nmin = 200
c     nmax = 300
      open ( unit = 23, file = 'r30.intv5')
      open ( unit = 25, file = 'funy.ot')
      write  (6,60)
      read ( 5,* ) nmin, nmax
      do 20 i = 1, 500
      read ( 23,*,end = 21 ) ( a ( i, j ), j = 1, 2 ),b ( i )
      if (a(i,1) .LT. nmin) go to 20
      if ( a ( i, 1) .gt. nmax ) go to 25
      t ( mn, 1) = a ( i, 1 )
      t ( mn, 2) = a ( i, 2 )
      y ( mn ) = b ( i )
      y ( mn ) = ( y ( mn ) * scl ) - sft
      mn = mn + 1
      m = m + 1
      write (6,76) (a (i,j), j=1,2), b(i)
20    continue
21    endfile 23
25    continue
      write ( 6, 80 )
      read ( 5, * ) n
      write ( 6, 70 )
      read ( 5, * ) ( x ( i ), i = 1, n )
c     x ( 1 ) = 0.0
c     x ( 2 ) = 0.0
c     x ( 3 ) = 0.0
      ymean = 0.0
      do 1 i = 1, m
      ymean = ymean + y ( i )
1     continue
      rm = m
      ymean = ymean / rm
      ymean = ymean * ymean
      liw = 1
      lw = 1000000
      ifail = 1
      call e04fdf ( m, n, x, fsumsq, iw, liw, w, lw, ifail )
      if ( ifail . ne . 0 ) write ( 25, 8 ) ifail
      f = fsumsq / ( ymean * rm )
c     write ( 25, 7 ) fsumsq
      write ( 25, 7 ) f
      do 10 j = 1, n
      x ( j ) = ( x ( j ) + sft ) / scl
10    continue
      write ( 25, 6) ( x ( j ), j = 1, n )
      write ( 25, 100 ) m
      write ( 25, 9 )
      do 15 i = 1, m
      s ( i ) = ( s ( i ) + sft ) / scl
      y ( i ) = ( y ( i ) + sft ) / scl
      r ( i ) = y ( i ) - s ( i )
      write ( 25, 90 ) t ( i, 1 ), t ( i, 2 ), y ( i ), s ( i ), r ( i )
15    continue
      rewind 23
      stop
8     format (///' error exit type ' , i2 , ' see routine document' )
6     format ( 1x , ' at the point ' , 20 ( / 4e15.5 ) )
7     format (///1x, ' on the exit sum of squares is = ', d29.15 )
9     format ( ///1x,'fitted values for comparision, ')
60    format ( 1x, ' give the lower and upper limits of temperature' )
70    format ( 1x, ' give the approximate values of parameters ' )
76    format ( 3(5x, f20.10 ))
80    format ( 1x, ' give the # of parameters ' )
90    format ( 1x, f7.3, 2x, f11.9, 2x, f18.8, 2x, f18.8, 2x, f15.8 )
100   format ( / 10x, '  # of data points : ', 5x, i4 )
      end
c     ***************************************************************
c     ***************************************************************
      subroutine lsfun1 ( m, n,xc, fvecc )
c     double precision ( a-z )
      implicit real*8 ( a-h, o-z )
      real*8 fvecc(1000000), y(500), s(500), xc(4), d(500), t(500,2)
      common t, y, s
      do 20 i = 1, m
      d(i) = xc(1)+xc(2)*t(i,2)+xc(3)*(t(i,1)**2)
      fvecc(i) = d(i) - y(i)
      s(i) = fvecc(i) + y(i)
20    continue
      return
      end
C     *******************************************************************
      SUBROUTINE E04FDF(M,N,X,FSUMSQ,IW,LIW,W,LW,IFAIL)
C     MARK 13 RE-ISSUE. NAG COPYRIGHT 1988.
C
C     ***************************************************************
C
C     E04FDF IS AN EASY-TO-USE ALGORITHM FOR FINDING
C     AN UNCONSTRAINED MINIMUM OF A SUM OF SQUARES OF M NONLINEAR
C     FUNCTIONS IN N VARIABLES (M .GE. N).  NO DERIVATIVES ARE
C     REQUIRED.
C
C     THE ROUTINE IS ESSENTIALLY IDENTICAL TO THE SUBROUTINE LSNDN1
C     IN THE NPL ALGORITHMS LIBRARY (REF. NO. E4/26/F) AND CALLS
C     E04FCZ WITH SUITABLE DEFAULT SETTINGS FOR PARAMETERS. IT CALLS
C     THE USER-SUPPLIED ROUTINE LSFUN1.
C
C     N.B. LSFUN1 IS A DESIGNATED NAME.
C     --------------------------------
C
C     GIVEN AN INITIAL APPROXIMATION TO THE MINIMUM, E04FDF COMPUTES
C     THE POSITION OF THE MINIMUM AND THE CORRESPONDING FUNCTION
C     VALUE.  THE REAL ARRAY W AND THE INTEGER ARRAY IW ARE USED
C     AS WORKSPACE.  W MUST BE DIMENSIONED AT LEAST
C     7*N + N*N + 2*M*N + 3*M + N*(N - 1)/2 OR 9 + 5*M IF N = 1
C     AND IW MUST HAVE AT LEAST ONE ELEMENT.
C
C     PHILIP E. GILL, WALTER MURRAY, SUSAN M. PICKEN,
C     NICHOLAS I. M. GOULD AND ENID M. R. LONG
C     D.N.A.C., NATIONAL PHYSICAL LABORATORY, ENGLAND
C
C     ***************************************************************
C
C     Modified to call BLAS.
C     Peter Mayes, NAG Central Office, October 1987.
C
C     Modified to output explanatory messages.
C     Peter Mayes, NAG Central Office, December 1987.
C
C     .. Parameters ..
      CHARACTER*6       SRNAME
      PARAMETER         (SRNAME='E04FDF')
C     .. Scalar Arguments ..
      DOUBLE PRECISION  FSUMSQ
      INTEGER           IFAIL, LIW, LW, M, N
C     .. Array Arguments ..
      DOUBLE PRECISION  W(LW), X(N)
      INTEGER           IW(LIW)
C     .. Local Scalars ..
      DOUBLE PRECISION  EPSMCH, ETA, GTG, PEPS, RTEPS, STEPMX, U, XTOL
      INTEGER           IPRINT, LFJAC, LFVEC, LG, LS, LV, LW1, LW2,
     *                  MAXFUN, NFTOTL, NH, NITER, NREC, NWHY
C     .. Local Arrays ..
      CHARACTER*80      P01REC(2)
C     .. External Functions ..
      DOUBLE PRECISION  DDOT, X02AJF
      INTEGER          P01ABF
      EXTERNAL         DDOT, X02AJF, P01ABF
C     .. External Subroutines ..
      EXTERNAL         E04FCW, E04FCZ, E04FDY, E04FDZ
C     .. Intrinsic Functions ..
      INTRINSIC        ABS, SQRT
C     .. Executable Statements ..
      EPSMCH = X02AJF()
      RTEPS = SQRT(EPSMCH)
      PEPS = EPSMCH**0.66666D+0
C
C     CHECK THAT THE WORKSPACE HAS BEEN ALLOCATED CORRECTLY.
C
      NWHY = 1
      NH = 1
      IF (N.GE.2) NH = N*(N-1)/2
      IF (LW.LT.7*N+3*M+2*M*N+N*N+NH .OR. LIW.LT.1 .OR. M.LT.N)
     *    GO TO 20
      NWHY = 0
C
C     SET UP THE INPUT PARAMETERS FOR E04FCZ.
C
C     SUPPRESS THE PRINT FREQUENCY.
C
      IPRINT = 0
C
C     SET THE MAXIMUM NUMBER OF FUNCTION EVALUATIONS ALLOWED
C     AS 400*N.
C
      MAXFUN = 400*N
C
C     SET THE LINEAR SEARCH PARAMETER.
C
      ETA = 5.0D-1
      IF (N.EQ.1) ETA = 0.0D+0
C
C     SPECIFY THE OVERALL CONVERGENCE CRITERION.
C
      XTOL = 1.0D+1*RTEPS
C
C     SPECIFY THE BOUND ON THE STEP LENGTH.
C
      STEPMX = 1.0D+1
C
C     COMPUTE THE ADDRESSES FOR THE ARRAYS USED IN E04FCZ.
C
      LS = 6*N + 2*M + M*N + NH + 1
      LV = LS + N
      LFVEC = LV + N*N
      LFJAC = LFVEC + M
C
C     CALL SUBROUTINE E04FCZ TO MINIMIZE THE FUNCTION.
C
      CALL E04FCZ(M,N,E04FCW,E04FDY,E04FDZ,IPRINT,MAXFUN,ETA,XTOL,
     *            STEPMX,X,FSUMSQ,W(LFVEC),W(LFJAC),M,W(LS),W(LV),N,
     *            NITER,NFTOTL,NWHY,IW,LIW,W,LW)
      IF (NWHY.LE.2) GO TO 20
      U = 1.0D+0 + ABS(FSUMSQ)
      U = PEPS*U*U
      LG = 5*N + M + M*N + NH + 1
      GTG = DDOT(N,W(LG),1,W(LG),1)
C
C     ATTEMPT TO DETERMINE IF FAILURE WAS DUE TO TOO SMALL A SETTING
C     FOR XTOL.  THE FOLLOWING RULE IS USED -
C
C     NWHY = 3  -  THE MINIMIZATION HAS FAILED.
C     NWHY = 5  -  THE MINIMIZATION HAS PROBABLY WORKED.
C     NWHY = 6  -  THE MINIMIZATION HAS POSSIBLY WORKED.
C     NWHY = 7  -  THE MINIMIZATION IS UNLIKELY TO HAVE WORKED.
C     NWHY = 8  -  THE MINIMIZATION IS VERY UNLIKELY TO HAVE WORKED.
C
      IF (GTG.LE.1.0D+3*U) NWHY = 8
      IF (GTG.LE.1.0D+2*U) NWHY = 7
      IF (GTG.LE.1.0D+1*U) NWHY = 6
      IF (GTG.LE.U) NWHY = 5
   20 IF (NWHY.EQ.1) THEN
         LW1 = 7*N + N*N + 2*M*N + 2*M + N*(N-1)/2
         LW2 = 9 + 5*M
         IF (N.LT.1) THEN
            WRITE (P01REC,FMT=99999) N
            NREC = 1
         ELSE IF (M.LT.N) THEN
            WRITE (P01REC,FMT=99998) M, N
            NREC = 1
         ELSE IF (LIW.LT.1) THEN
            WRITE (P01REC,FMT=99997) LIW
            NREC = 1
         ELSE IF (LW.LT.LW1 .AND. N.GT.1) THEN
            WRITE (P01REC,FMT=99996) LW, LW1
            NREC = 2
         ELSE IF (LW.LT.LW2 .AND. N.EQ.1) THEN
```

```
             WRITE (P01REC,FMT=99995) LW, LW2
             NREC = 2
          END IF
      ELSE IF (NWHY.EQ.2) THEN
         P01REC(1) = ' ** There have been 400*N calls to LSFUN1'
         NREC = 1
      ELSE IF (NWHY.EQ.3) THEN
         P01REC(1) =
     *   ' ** The conditions for a minimum have not all been satisfied,'
         P01REC(2) = ' ** but a lower point could not be found'
         NREC = 2
      ELSE IF (NWHY.EQ.4) THEN
         P01REC(1) =
     *        ' ** Failure in computing SVD of estimated Jaobian matrix'
         NREC = 1
      ELSE IF (NWHY.EQ.5) THEN
         P01REC(1) =
     *         ' ** It is probable that a local minimum has been found,'
         P01REC(2) = ' ** but it cannot be guaranteed'
         NREC = 2
      ELSE IF (NWHY.EQ.6) THEN
         P01REC(1) =
     *         ' ** It is possible that a local minimum has been found,'
         P01REC(2) = ' ** but it cannot be guaranteed'
         NREC = 2
      ELSE IF (NWHY.EQ.7) THEN
         P01REC(1) =
     *          ' ** It is unlikely that a local minimum has been found'
         NREC = 1
      ELSE IF (NWHY.EQ.8) THEN
         P01REC(1) =
     *    ' ** It is very unlikely that a local minimum has been found'
         NREC = 1
      END IF
      IFAIL = P01ABF(IFAIL,NWHY,SRNAME,NREC,P01REC)
      RETURN
C
C     END OF E04FDF   (LSNDN1)
C
99999 FORMAT (' ** On entry, N must be at least 1: N =',I16)
99998 FORMAT (' ** On entry, M must be at least N: M =',I16,', N =',I16)
99997 FORMAT (' ** On entry, LIW must be at least 1: LIW =',I16)
99996 FORMAT (' ** On entry, LW must be at least 7*N + N*N + 2*M*N + 2',
     *       '*M + N*(N-1)/2 if N.gt.1:',/' ** LW =',I16,', LW must be',
     *       ' at least',I16)
99995 FORMAT (' ** On entry, LW must be at least 9 + 5*M if N.eq.1:',
     *       /' ** LW =',I16,', LW must be at least',I16)
      END
```

APPENDIX (3)

Software (*in Turbo Pascal*) developed to find the temperature coefficient of resistivity (TCR) at any temperature and for any composition (x) used in Chapter 3, employing an interpolation technique.

```
PROGRAM INTERPOLATION_OF_DATA;
uses crt,dos;
type
venus = array[1..358,1..2] of real;
  mars = array[1..500,1..2] of real;
var
n,m : integer;
  vs : venus;
mas : mars;
fil_dat,out_fil : text;
name,infile : string[20];

function res(tm : real; vs : venus) : real;

var
t1,tu,tp : integer;
tp1 : real;
found : boolean;

begin
  if vs[1,1] = tm then res := vs[1,2] else
  if vs[243,1] = tm then res := vs[243,2]
  else
   begin
     t1 := 1; tu := 243;
      found := false;
      while (not(found) and (tu > t1 + 1)) do
       begin
         tp := trunc((t1 + tu)/2);
          tp1 := vs[tp,1];
          if tp1 = tm then
           begin
             res := vs[tp,2];
              found := true
            end
          else
           if tp1 < tm then t1 := tp
            else tu := tp
        end;
      if not(found) then
       res := vs[t1,2] + (vs[tu,2]-vs[t1,2])*(tm-vs[t1,1])
              /(vs[tu,1]-vs[t1,1])
        end
    end;

procedure table(var vs : venus);
var
t : integer;
tx : text;
begin
assign(tx, 'c:\20.dat');
  reset(tx);
  for t := 1 to 243 do read(tx, vs[t,1], vs[t,2]);
  close(tx);
end;

{main programme}
{$I MSC.INC}
begin
  clrscr;
  gotoxy(5,10),
write('enter name of the drvtv of data file to be read : ');
  readln(infile);
  assign(fil_dat,infile);
  gotoxy(5,16);
  write('enter name of interpltd output file :');
  readln(name);
  assign(out_fil, name);
  reset(fil_dat);
  n := 0;
  while not (eof(fil_dat)) do
   begin
     n := n + 1;
for m := 1 to 2 do
read (fil_dat, mas[n,m]);
    end;
close(fil_dat);

table(vs);
clrscr;
rewrite(out_fil);
writeln (out_fil,'Interpolated resistivity data of    ', infile);
writeln(out_fil);
writeln(out_fil);
writeln(out_fil,'Temp.(K)','      ','1st Dervtv','    ','Intrpltd Restvty');
writeln(out_fil);
for m := 1 to (n-1) do
 begin
    writeln(out_fil, mas[m,1]:8:3,'    ', mas[m,2]:4:15,'    ',
            res(mas[m,1],vs):5:15);
  writeln(m,'     ', mas[m,1]:8:3,'    ', mas[m,2]:4:15,'    ',
            res(mas[m,1],vs):5:15);
 end;
close(out_fil);
Anthem;
clrscr;
gotoxy(15,10);
textcolor(15);
writeln('INTERPOLATION DONE SUCCESSFULLY !');
readln;
end.
```